

**INTERFACIAL CHARACTERIZATION OF POLYHEDRAL
OLIGOMERIC SILSESQUIOXANE (POSS) AMPHIPHILES
AND POLYMER BLENDS: THERMODYNAMICS,
MORPHOLOGY, AND RHEOLOGY**

Jianjun Deng

A thesis submitted to the faculty of the
Virginia Polytechnic Institute and State University
in partial fulfillment of the requirements for the degree of

**Doctor of Philosophy
in
Chemistry**

Alan R. Esker, Chair

T. Daniel Crawford

John G. Dillard

Herve Marand

Thomas C. Ward

April 18, 2005

Blacksburg, Virginia

Keywords: Langmuir monolayers, Polyhedral oligomeric silsesquioxane (POSS),
Nanofiller, Polymer blends

Copyright 2005, Jianjun Deng

**INTERFACIAL CHARACTERIZATION OF POLYHEDRAL OLIGOMERIC
SILSESQUOXANE (POSS) AMPHIPHILES AND POLYMER BLENDS:
THERMODYNAMICS, MORPHOLOGY, AND RHEOLOGY**

Jianjun Deng

(Abstract)

Over the past two decades one class of oligomers, polyhedral oligomeric silsesquioxanes (POSS), has attracted considerable attention because of their unique hybrid organic/inorganic molecular structures and nanoscopic sizes. While surface and interfacial properties may play a key role in many potential POSS applications, relatively little is actually known about the surface properties of POSS. This dissertation provides studies of the interfacial aspects of both POSS molecules and POSS/polymer blends at the air/water interface (A/W) through surface pressure-area per molecule (Π -A) isotherm, Brewster angle microscopy (BAM), and interfacial stress rheometry (ISR) studies.

Results for POSS Langmuir thin films at A/W show that trisilanol-POSS derivatives are a new class of amphiphiles, that exhibit multiple phase transitions in going from traditional 2D Langmuir monolayers (1 POSS molecule thick) to various 3D multilayer films upon compression. With small length/diameter ratios and bulky shapes, the monolayer phase behavior and packing states of different POSS are simpler than the traditional rod-like lipids. Meanwhile trisilanol-POSS derivatives have very different collapse behavior and multilayer organization showing strong substituent effects even though they have similar molecular sizes. While trisilanolisobutyl-POSS (TiBuP) monolayers undergo collapse around $\Pi \approx 18 \text{ mN}\cdot\text{m}^{-1}$ and form various ordered or disordered solid-like 3D aggregates at different compression rates, trisilanolcyclohexyl-

POSS (TCyP) monolayers collapse into trilayers via instantaneous nucleation with hemispherical edge growth around $\Pi \approx 3.7 \text{ mN}\cdot\text{m}^{-1}$. ISR results reveal three different non-Newtonian flow regimes that correlate with phase transitions in the Π - A isotherms. Further symmetric compression after trilayer formation induces TCyP thin films to self-assemble into highly ordered crystalline-like hydrophobic multilayers (≈ 8 POSS molecule thick) with unique rod-like morphologies, which are dramatically different from “collapsed” morphologies seen in other systems.

By treating POSS derivatives as ideal nanofiller for studying confinement effects on filled polymer systems, amphiphilic poly(dimethylsiloxane) (PDMS) derivatives with different polar functional groups are studied as blends with TiBuP and octaisobutyl-POSS at A/W to resolve one of the key challenges for current nanocomposite applications: How to control nanofiller dispersion in polymer matrices? The results in this dissertation reveal that introducing polar groups into polymeric matrix polymers is a good way to control dispersion.

Table of Contents

Abstract	ii
Table of Contents	iv
List of Figures	viii
List of Tables	xii
Acknowledgments	xiii
Dedication	xv
CHAPTER 1: Introduction and Review	
1.1 General Introduction for Molecular Films	1
1.2 Historical Background of Langmuir and Langmuir-Blodgett (LB) Films	2
1.3 Langmuir Monolayer Formation	4
1.4 Surface Pressure (Π)–Area per Molecule (A) Isotherms	6
1.4.1 Surface Pressure (Π) vs. Surface Tension (γ)	6
1.4.2 Langmuir Trough and Π - A Isotherms	9
1.4.3 Limitations of Π - A Isotherms	14
1.5 Brewster Angle Microscopy	15
1.5.1 Background	15
1.5.2 Principle of Brewster Angle Microscopy	17
1.5.3 Experimental Setup of BAM	19
1.5.4 Applications of BAM	21
1.6 Phase Diagrams of Langmuir Monolayers	22
1.6.1 Monolayer Phases	22
1.6.2 Chain-length Dependence of Monolayer Phase Diagrams	23
1.7 Interfacial Shear Rheological Measurements	25
1.7.1 General Introduction	25
1.7.2 Magnetic Needle Shear Viscometer	26
1.7.3 Interfacial Stress Rheometer (ISR)	27
1.8 Polyhedral Oligomeric Silsesquioxanes (POSS) As Hybrid Nanofiller	29
1.8.1 Overview of Hybrid Nanocomposite Materials	29
1.8.2 Polyhedral Oligomeric Silsesquioxanes (POSS)	30
1.8.3 Synthesis of POSS Macromers	33
1.8.4 Applications of POSS	34
1.8.5 The Future of POSS	36
1.9 General Overview of this Dissertation	36
CHAPTER 2: Materials and Experimental Methods	
2.1 Materials	40
2.1.1 Polyhedral Oligomeric Silsesquioxanes (POSS)	40
2.1.2 Poly(dimethylsiloxane) (PDMS) Derivatives	40
2.2 Experimental Methods	41
2.2.1 Langmuir Trough and BAM Configuration	41
2.2.2 Constant Compression Rate Experiments	43
2.2.3 Compression and Expansion Isotherms: Hysteresis Loops	43
2.2.4 Stepwise or “Quasi-static” Compression Experiments	44
2.2.5 Surface Pressure Relaxation Experiments	44

2.2.6 Isobaric Area Relaxation Experiments	44
2.2.7 Successive Addition Experiments	45
2.2.8 Brewster Angle Microscopy (BAM)	45
2.2.9 Interfacial Stress Rheometry (ISR)	47
CHAPTER 3: Polyhedral Oligomeric Silsesquioxanes: A New Class of Amphiphiles at the Air/Water Interface	
3.1 Abstract	48
3.2 Introduction	48
3.3 Experimental	49
3.4 Results and Discussion	50
3.5 Conclusions	52
CHAPTER 4: Isotherm and Brewster Angle Microscopy Studies of Trisilanolisobutyl-POSS at the Air/Water Interface	
4.1 Abstract	54
4.2 Introduction	55
4.3 Experimental	57
4.3.1 Materials	57
4.3.2 Isotherm Studies	58
4.3.3 Brewster Angle Microscopy (BAM)	59
4.4 Results and Discussion	59
4.4.1 Π -A Isotherms of Trisilanolisobutyl-POSS	59
4.4.2 Morphology of Trisilanolisobutyl-POSS Films by BAM	65
4.4.3 Schematic Depiction of the Phase Behavior in a Trisilanolisobutyl-POSS Compression Isotherm	66
4.4.4 Viscoelastic Effects on Trisilanolisobutyl-POSS Films at A/W	69
4.4.5 Surface Pressure and Morphological Stability and Reversibility of Trisilanolisobutyl-POSS Films at A/W	72
4.5 Conclusions	81
CHAPTER 5: Blends of Amphiphilic PDMS and Trisilanolisobutyl-POSS at the Air/Water Interface	
5.1 Abstract	82
5.2 Introduction	83
5.3 Experimental	84
5.3.1 Materials	84
5.3.2 Isotherm Studies	84
5.3.3 Brewster Angle Microscopy (BAM)	86
5.4 Results and Discussion	86
5.4.1 Compression Isotherm Studies of the Pure Components	86
5.4.2 Compression Isotherm Studies of the Blends	88
5.4.3 The Monolayer Regime	89
5.4.4 PDMS Collapse	92
5.4.5 The Non-equilibrium "Monolayer" Regime	95
5.4.6 Collapse of the POSS Component	97
5.4.7 Hysteresis Studies	100
5.4.8 Addition Experiments	102

5.4.9 Relaxation Phenomena	104
5.5 Conclusions	113
CHAPTER 6: Blends of Phosphine Oxide Substituted Poly(dimethylsiloxane) and Amphiphilic Trisilanolisobutyl-POSS at the Air/Water Interface	
6.1 Abstract	114
6.2 Introduction	115
6.3 Experimental	117
6.3.1 Materials	117
6.3.2 Isotherm and Brewster Angle Microscopy (BAM) Studies	118
6.4 Results and Discussion	120
6.4.1 Isotherms of the Single Component Silicone Films	120
6.4.2 Compression Isotherms of PDMS-PO/TiBuP Mixed Films	124
6.4.3 Hysteresis and Dynamic Behavior of PDMS-PO/Trisilanolisobutyl-POSS Mixed Films	128
6.4.4 Thermodynamic Analyses of the Isotherm Studies	134
6.4.5 A Model for Aggregation in PDMS-PO/TiBuP Blends	140
6.5 Conclusions	143
CHAPTER 7: Blends of Amphiphilic Poly(dimethylsiloxane) and Non-Amphiphilic Octaisobutyl-POSS at the Air/Water Interface	
7.1 Abstract	144
7.2 Introduction	145
7.3 Experimental	147
7.3.1 Materials	147
7.3.2 Isotherm Studies	147
7.3.3 Brewster Angle Microscopy (BAM)	148
7.4 Results and Discussion	150
7.4.1 Compression Isotherm Studies of the Blends	150
7.4.2 BAM Image Analyses for Compression Isotherms	159
7.4.3 Hysteresis Experiments	163
7.4.4 Relaxation Experiments	172
7.4.5 Addition Experiments	175
7.5 Conclusions	180
CHAPTER 8: Phase Behavior, Morphologies, and Viscoelastic Properties of Trisilanolcyclohexyl-POSS at the Air/Water Interface	
8.1 Abstract	181
8.2 Introduction	182
8.3 Experimental	187
8.3.1 Materials	187
8.3.2 Surface Pressure Measurements	188
8.3.3 Brewster Angle Microscopy (BAM)	190
8.3.4 Interfacial Stress Rheometry (ISR)	190
8.4 Results and Discussion	191
8.4.1 Comparison between TCyP and TiBuP	191

8.4.2 Nucleation and Growth of 3D Domains from TCyP Monolayer Films During Isothermal Compression Experiments	202
8.4.3 Nucleation and Growth of 3D Domains from TCyP Monolayers During Isobaric Area Relaxation Experiments	211
8.4.4 Surface Rheology of TCyP Films at A/W	215
8.4.5 Schematic Depiction of the Phase Behavior from a Monolayer to a Trilayer in a TCyP Film During a Compression Experiment	225
8.4.6 Unique Rod-like Surface Morphologies in Highly Ordered TCyP Multilayers	226
8.5 Conclusions	230
CHAPTER 9: Conclusions and Suggestions for Future Work	
9.1 Overall Conclusions	232
9.1.1 POSS at A/W	232
9.1.2 POSS/Polymer Blends at A/W	234
9.2 Suggestions for Future Work	238
9.2.1 Trisilanophenyl-POSS (TPP) at A/W	238
9.2.2 Fluorinated POSS derivatives (<i>F</i> -POSS) at A/W	247
Bibliography	257
Curriculum Vitae	276

List of Figures

Chapter 1

Figure 1.1: Some frequently used lipid molecules to form Langmuir monolayers at A/W	5
Figure 1.2: Measurement of surface pressure (Π) with the Wilhelmy plate technique	9
Figure 1.3: A schematic diagram of a Langmuir trough	10
Figure 1.4: Comparison between 3D and 2D isotherms	11
Figure 1.5: Comparison of first- and second-order phase transitions between a low-density tilted phase and a higher-density untilted phase	13
Figure 1.6: Comparison of the reflectivity of <i>s</i> and <i>p</i> -polarized light at Θ_B	16
Figure 1.7: Experimental setup for a typical BAM experiment	20
Figure 1.8: Experimental Π - <i>T</i> phase diagram for an eicosanoic acid Langmuir film	23
Figure 1.9: The chain-length dependence of the phase diagram for fatty acids	24
Figure 1.10: Schematic diagram of an interfacial stress rheometer (ISR)	28
Figure 1.11: Schematic diagram describing hybrid nanocomposites	31
Figure 1.12: Schematic diagram of POSS-based nanocomposites	32
Figure 1.13: Different Π - <i>A</i> isotherms of some trisilanol-POSS derivatives obtained at 22.5 °C by constant compression at 20 cm ² •min ⁻¹	37
Figure 1.14: Comparison between a rod-like model for traditional fatty acid and essentially spherical POSS	37

Chapter 2

Figure 2.1: Schematic diagram of a Langmuir trough and BAM configuration	42
Figure 2.2: Schematic representation of the trough area changing with time in different Langmuir monolayer measurements	46

Chapter 3

Figure 3.1: Generic structure of closed (T ₈ R ₈) and open cage (T ₇ R ₇ (OH) ₃) POSS	49
Figure 3.2: Π - <i>A</i> isotherms of T ₈ R ₈ and T ₇ R ₇ (OH) ₃ , R = isobutyl	51
Figure 3.3: BAM images of T ₈ R ₈ and T ₇ R ₇ (OH) ₃ and T ₈ R ₈	52

Chapter 4

Figure 4.1: Different Π - <i>A</i> isotherms for TiBuP measured at T = 22.5 °C	61
Figure 4.2: Different presentations of molecular models of TiBuP	63
Figure 4.3: Compression BAM images obtained at different <i>A</i> at 10 cm ² •min ⁻¹	67
Figure 4.4: Proposed organization of TiBuP films at A/W	68
Figure 4.5: The compression rate effect on isotherms of TiBuP at T = 22.5 °C	69
Figure 4.6: BAM images acquired at $A \approx 70 \text{ \AA}^2 \cdot \text{molecule}^{-1}$ and T = 22.5 °C for different compression rates	73
Figure 4.7: Compression Π - <i>A</i> isotherms collected as a function of temperature at a constant compression rate of 20 cm ² •min ⁻¹	74
Figure 4.8: Π vs. time (<i>t</i>) curves for three different TiBuP films compressed to different surface concentrations	75
Figure 4.9: Relaxed BAM images obtained at T = 22.5 °C after compression at 20 cm ² •min ⁻¹ to an area of 40 $\text{\AA}^2 \cdot \text{molecule}^{-1}$	76
Figure 4.10: Π - <i>A</i> isotherms obtained at T = 22.5 °C showing hysteresis behavior for compression and expansion at 20 cm ² •min ⁻¹	78
Figure 4.11: BAM images obtained for a compression/expansion loop at 20 cm ² •min ⁻¹ for T = 22.5 °C	80

Chapter 5

Figure 5.1: Π - $\langle A \rangle$ compression isotherms for TiBuP blends with PDMS	88
Figure 5.2: $\langle A(\Pi) \rangle$, ΔG_{excess} and ΔG_{mix} as a function of X_{POSS} , or ϕ_{POSS}	91
Figure 5.3: $\Pi_{transition}$ for PDMS multilayer formation as a function of the mole fraction of POSS on a per monomer basis	93
Figure 5.4: BAM images upon compression for different POSS/PDMS blends	96
Figure 5.5: Π - $\langle A \rangle$ hysteresis loops for different POSS/PDMS blends	98
Figure 5.6: BAM images upon expansion for different POSS/PDMS blends	99
Figure 5.7: A Π - $\langle A \rangle$ isotherm comparison between addition and compression for a 60 wt% TiBuP blend with PDMS	102
Figure 5.8: BAM morphologies obtained by addition and compression of a 60 wt% TiBuP blend with PDMS	106
Figure 5.9: Relaxation, Π vs. t , curves for blends of TiBuP with PDMS	107
Figure 5.10: Morphologies obtained from a relaxation experiment for 90 wt% TiBuP blend with PDMS at a constant area, $\langle A \rangle = 28.5 \text{ \AA}^2 \cdot \text{monomer}^{-1}$	108
Figure 5.11: Film morphologies after 5 minutes of relaxation for different TiBuP/PDMS blends	109

Chapter 6

Figure 6.1: A model of hydrogen bonding between the phosphine oxide moiety and (A) a silica surface of a semiconductor, and (B) a model silica nanoparticle of TiBuP	117
Figure 6.2: The molecular structure of PDMS-PO	118
Figure 6.3: Π - A isotherms of PDMS and PDMS-PO obtained by compression and PDMS-PO by addition at A/W and 22.5 °C	122
Figure 6.4: Π - A isotherms of PDMS-PO/TiBuP blends at 22.5 °C	123
Figure 6.5: BAM images for different blends of TiBuP and PDMS-PO at $A_{POSS} = 40 \text{ \AA}^2 \cdot \text{monomer}^{-1}$	127
Figure 6.6: Π - A isotherms for a 76 wt% trisilanolisobutyl-POSS blend with PDMS-PO at A/W and 22.5 °C	130
Figure 6.7: BAM images obtained from a 76 wt% TiBuP blend with PDMS-PO at 22.5 °C by different methods for controlling the surface concentration	131
Figure 6.8: Composition dependence of $\Pi_{collapse,POSS}$ for TiBuP blends with PDMS-PO obtained by compression and addition at A/W and 22.5 °C	137
Figure 6.9: $\langle A(\Pi) \rangle$ and ΔG_{excess} of trisilanolisobutyl-POSS/ PDMS-PO blends	140
Figure 6.10: A proposed aggregation mechanism of mixed thin films of PDMS-PO:trisilanolisobutyl-POSS at A/W for $A_{POSS} = 120 \text{ \AA}^2 \cdot \text{monomer}^{-1}$	142

Chapter 7

Figure 7.1: Π - $\langle A \rangle$ compression isotherms for octaisobutyl-POSS blends with PDMS at 22.5 °C and a compression rate of $15 \text{ cm}^2 \cdot \text{min}^{-1}$	149
Figure 7.2: BAM images upon compression of a pure octaisobutyl-POSS Langmuir film at 22.5 °C and a compression rate of $15 \text{ cm}^2 \cdot \text{min}^{-1}$	151
Figure 7.3: Separated replots of each isotherm in Figure 7.1	153
Figure 7.4: Π_C and 1 st "PDMS" $\Pi_{plateau}$ value as a function of wt% POSS	154
Figure 7.5A: Π - A_{PDMS} compression isotherms for octaisobutyl-POSS /PDMS	156
Figure 7.5B: Θ_{POSS} , $\Theta_{POSS,ideal}$ and $\langle d_{POSS} \rangle$ as a function of wt% POSS	156

Figure 7.6: BAM images upon compression for different octaisobutyl-POSS/PDMS blends	161
Figure 7.7: BAM images obtained during a hysteresis experiment at 22.5 °C and a compression rate of 15 cm ² •min ⁻¹ for a 90wt% octaisobutyl-POSS blend with PDMS	162
Figure 7.8: BAM images obtained during a hysteresis experiment at 22.5 °C and a compression rate of 15 cm ² •min ⁻¹ for a 70wt% octaisobutyl-POSS blend with PDMS	167
Figure 7.9: BAM images obtained during a hysteresis experiment at 22.5 °C and a compression rate of 15 cm ² •min ⁻¹ for a 70wt% octaisobutyl-POSS blend with PDMS	168
Figure 7.10: BAM images upon expansion for different octaisobutyl-POSS/PDMS blends with PDMS at $\Pi = 4 \text{ mN}\cdot\text{m}^{-1}$	169
Figure 7.11: BAM images upon expansion for different octaisobutyl-POSS/PDMS blends with PDMS at $\Pi = 0 \text{ mN}\cdot\text{m}^{-1}$	170
Figure 7.12: Representative $\Pi - A_{PDMS}$ hysteresis loops for octaisobutyl-POSS blends with PDMS for compression up to $\Pi_C (\approx 7 \text{ mN}\cdot\text{m}^{-1})$ and for compression into the collapsed regime of the PDMS component ($A_{PDMS} \approx 10 \text{ \AA}^2\cdot\text{monomer}^{-1}$)	171
Figure 7.13: Relaxation, Π vs. t , curves for blends of octaisobutyl-POSS with PDMS at 22.5 °C	174
Figure 7.14: BAM images during relaxation for different octaisobutyl-POSS/PDMS blends	175
Figure 7.15: $\Pi - A_{PDMS}$ addition isotherms for octaisobutyl-POSS blend with PDMS at 22.5 °C	178
Figure 7.16: BAM images obtained upon successive addition of spreading solution for octaisobutyl-POSS blends with PDMS	179
Chapter 8	
Figure 8.1: Generic structure and space-filling model of TCyP at A/W	187
Figure 8.2: $\Pi - A$ isotherms comparison between trisilanolisobutyl-POSS (TiBuP) and trisilanocyclohexyl-POSS (TCyP) measured at room temperature, $T = 22.5 \text{ °C}$, with a constant compression rate of 20 cm ² •min ⁻¹	193
Figure 8.3: $\epsilon_s - A$ for TiBuP and TCyP at $T = 22.5 \text{ °C}$ with a constant compression rate of 20 cm ² •min ⁻¹ up to the collapse point and for the entire A range of TCyP	196
Figure 8.4: Comparison of hysteresis curves of TiBuP and TCyP	200
Figure 8.5: Different $\Pi - A$ isotherms for TCyP at $T = 22.5 \text{ °C}$	201
Figure 8.6: Typical BAM images obtained for TCyP at $T = 22.5 \text{ °C}$ with a compression rate of 20 cm ² •min ⁻¹ after spreading the film at room temperature	204
Figure 8.7: BAM images for different A for a TCyP film prepared by "homogeneous" spreading conditions at $T = 22.5 \text{ °C}$ with a compression rate of 20 cm ² •min ⁻¹	209
Figure 8.8: BAM images for different A for a TCyP film prepared by "heterogeneous" experimental conditions at $T = 22.5 \text{ °C}$ with a compression rate of 20 cm ² •min ⁻¹	210
Figure 8.9: $A(t)$ versus t for TCyP during isobaric area relaxation experiments at $\Pi = 3.7 \text{ mN}\cdot\text{m}^{-1}$ along with the fitting result for instantaneous nucleation with hemispherical edge growth at 22.5°C	214
Figure 8.10: BAM images of TCyP acquired at $\Pi = 3.7 \text{ mN}\cdot\text{m}^{-1}$ and $T = 22.5 \text{ °C}$ for the isobaric area relaxation experiment in Figure 8.9	215
Figure 8.11: G_s' and G_s'' measured at a low frequency ($\omega = 0.92 \text{ rad}\cdot\text{s}^{-1}$, $T = 22.5 \text{ °C}$) for TCyP as a function of A	217

Figure 8.12: $\tan\delta$ vs. A for TCyP ($T = 22.5\text{ }^\circ\text{C}$, $\omega = 0.92\text{ rad}\cdot\text{s}^{-1}$)	218
Figure 8.13: $\tan\delta$ as a function of ω for TCyP at the different A $T = 22.5\text{ }^\circ\text{C}$	220
Figure 8.14: $ \mu_s^*(\omega) $ at different A values	222
Figure 8.15: Proposed organization of trisilanolcyclohexyl-POSS films going from 2D to 3D films at A/W during symmetric compression	224
Figure 8.16: BAM images for TiBuP at different areas per molecule smaller than $A_c/3$ for the compression/expansion rate of $20\text{ cm}^2\cdot\text{min}^{-1}$ and $T = 22.5\text{ }^\circ\text{C}$	229

Chapter 9

Figure 9.1: Summary of compression Π - A isotherms of different trisilanol-POSS molecules at room temperature, $T = 22.5\text{ }^\circ\text{C}$, with compression rates of $20\text{ cm}^2\cdot\text{min}^{-1}$	236
Figure 9.2: A comparison of cross-sectional areas from modeling results (A_{MM2}) or XRD data (A_{XRD}) and limiting area (A_o) obtained from compression Π - A isotherms	237
Figure 9.3: BAM images obtained from a hysteresis loop at different A for a TPP film with a constant compression/expansion rate of $20\text{ cm}^2\cdot\text{min}^{-1}$ at $T = 22.5\text{ }^\circ\text{C}$	241
Figure 9.4: A demonstration of “interdigitating” or “interlocking” phenyl groups for TPP molecules at A/W	242
Figure 9.5: Proposed organization of TPP films at A/W	246
Figure 9.6: BAM images obtained from a hysteresis loop for different A for a F(13)DCpP film with a constant compression/expansion rate of $20\text{ cm}^2\cdot\text{min}^{-1}$ at $T = 22.5\text{ }^\circ\text{C}$	249
Figure 9.7: Proposed phase transitions and organization of F(13)DCpP films at A/W	251
Figure 9.8: BAM images obtained at surface concentrations around $A = 85\text{ \AA}^2\cdot\text{molecule}^{-1}$ for F(13)DCpP films at $T = 22.5\text{ }^\circ\text{C}$ with different compression rates	252
Figure 9.9: An enlarged rhombus dimer domain obtained at a low compression rate ($8\text{ cm}^2\cdot\text{min}^{-1}$) at $A = 86\text{ \AA}^2\cdot\text{molecule}^{-1}$ for a F(13)DCpP film	255
Figure 9.10: The morphology change of F(13)DCpP dimer aggregates at $A \approx 80\text{ \AA}^2\cdot\text{molecule}^{-1}$ transferred from A/W by the LB and LS techniques onto hydrophilic and hydrophobic glass surface, respectively	256

List of Tables

Table 1.1: A summary of Langmuir Monolayer phases observed in Figure 1.8	23
Table 4.1: Experimental and calculated size parameters for TiBuP	64
Table 5.1: Important Π values for TiBuP/PDMS blends at A/W	110
Table 5.2: Parameters used to fit the relaxation of TiBuP/PDMS blends	111
Table 7.1: Area fractions and average thicknesses of octaisobutyl-POSS blends with PDMS at $\Pi = 5 \text{ mN}\cdot\text{m}^{-1}$	158

ACKNOWLEDGEMENTS

I am grateful to Professor Alan R. Esker for the opportunity to work in his group as his first Ph. D student. Alan encouraged me to set the direction of my own research and to pursue the questions that I found most interesting, while patiently providing guidance all along the way. He also has involved me in many of the non-laboratory aspects of scientific research, such as writing articles and grant proposals. Alan's clarity and skills of presentation, both written and oral, will always serve as a goal to which I will aspire. I know that the skills that I have learned from him will serve me well in my future career. Most importantly, I thank Alan for creating a pretty friendly lab atmosphere.

Alan's gift of choosing intelligent students who integrate well into the group's culture has provided me with a great set of coworkers. In the POSS projects I have benefited from collaboration with Catherine E. Farmer-Creely, Joseph T. Polidan, John R. Hottle, Benjamin A. Vastine, Kevin J. Dawson, Sarah M. Huffer, Wen Yin, and Dr. Hyong-Jun Kim (POSS team). I also have benefited at least as much from my interactions with my other "group pals", Sheila E. Gradwell, Bingbing Li, Rituparna Paul, Ufuk Karabiyik, and Abdulaziz Kaya on other projects. I've enjoyed my one-week opportunity to use ISR in Professor Gerald G. Fuller's laboratory at Stanford University with Jay W. Anseth. I also wish to thank Dr. Brent D. Viers at Virginia Tech and Dr. Shawn Phillips at the Air Force Research Laboratories at Edward's Air Force Base, without their generous POSS supply, the POSS experiments would never have been possible.

Although the instrumental construction of Surface Light Scattering (SLS) was painful, I still wish I could express my thanks to the machine shop in the Department of Physics at Virginia Tech, whose delicate effort at least helped me fulfill my assignment. At this point, I also would like to thank the generous donation of electronic and optical parts of SLS from Professor Hyuk Yu at the University of Wisconsin, Madison. Without those magic parts, SLS could never have worked during my residence in the Esker group.

I would like to thank the members of my committee, Professors T. Daniel Crawford, John G. Dillard, William Ducker, Herve Marand, and Thomas C. Ward for their many helpful conversations over the course and projects of my graduate school career.

I would especially like to thank my family for their support over the years. We have gone through many difficult times, and their love and understanding have helped me make it to this point. I am lucky to have my wife Hongyan, whose love and support during the difficult portions of my graduate school career are the only reasons that I was able to make it through this long process. I only wish that I could return to her one tenth of the favor, which she has given me.

Finally, I am grateful to financial support for my partial research assistantship from the Thomas F. Jeffress and Kate Miller Jeffress Memorial Trust (J-553), 3M Untenured Faculty Program, the Virginia Tech Aspires Program, and the National Science Foundation (CHE-0239633).

To my wife Hongyan,
whose love and care helped me through my Ph. D studies,
and to my father and sister,
without them I never would have gone to college.

谨以此博士文献给我的妻子, 薛宏艳,
她对我的爱和照顾是我能在异国他乡完成博士学位的基础;
还有我的父亲和姐姐,
没有他们, 我甚至不可能完成我的大学学业.

CHAPTER 1

Introduction and Review

1.1 General Introduction for Molecular Films

In general, molecular films, ordered thin organic films with a thickness ranging from several nanometers (a monolayer) to several hundred nanometers, are expected to serve as useful components in many practical and commercial applications such as sensors, detectors, displays and electronic circuit components,¹⁻⁵ and further scientific investigation on these systems could prove to be very fruitful. With the almost unlimited possibility to synthesize organic molecules with desired structure and functionality, a sophisticated thin film deposition technology can provide considerable promise to fabricate electrically, optically and biologically active components on a nanometer scale.² An organic thin film can be deposited on a solid substrate by various techniques such as thermal evaporation, sputtering, electrodeposition, molecular beam epitaxy, adsorption from solution, the Langmuir-Blodgett (LB) technique, self-assembly (SAM), spin coating, etc.⁶ Among them, the Langmuir-Blodgett (LB) technique is one of the best techniques for preparing complex architectures as it enables (1) the precise control of the monolayer thickness, (2) homogeneous deposition of the monolayer over large areas, (3) the possibility to make multilayer structures with varying layer composition, and (4) the possibility to deposit monolayers onto almost any kind of hydrophilic or hydrophobic solid substrate.

Before going further, the difference in terminology between *Langmuir films* and *Langmuir-Blodgett (LB) films* should be clarified. Following the most widely used terms, *Langmuir films* or *Langmuir monolayers* are defined as the spread films formed by

certain insoluble amphiphilic molecules while monomolecular films of soluble amphiphiles are known as *Gibbs monolayers*. *Langmuir films* are most commonly formed on the surface of water by lipid molecules, such as fatty acids, which have two dissimilar parts: a hydrophilic (water-loving) headgroup to anchor the molecule on an aqueous surface and a hydrophobic (water-hating) tail to keep the molecule from dissolving into the aqueous bulk.¹ The term of *Langmuir-Blodgett (LB) films* is pointed to the molecular films, which can be either single layers or multilayers, on solid supporting substrates transferred by the Langmuir-Blodgett and Langmuir-Schaeffer techniques.³ Most of the work in this dissertation focuses on the characterization of the physical properties of *Langmuir monolayers*.

1.2 Historical Background of Langmuir and Langmuir-Blodgett (LB) Films

The earliest records of spreading of oil on water, which was used by Babylonians as one of their forms of divination, were written on clay tablets around the 18th century BC. Babylonians used the observation of the spreading behavior of an oil layer on water to predict success, marriage, birth of a child, recovery, or bad luck, sickness, death, etc.⁷ Furthermore, one ancient Orient marble sculpture art, *suminagashi*, which literally means ‘ink-float’ or ‘ink-stream’, was developed in China over 2000 years ago and is regarded as the earliest technical application of Langmuir films.⁸

Benjamin Franklin, an American statesman and scientist, is the first person to introduce the concept of spread monolayers into the scientific field with his famous Clapham pond experiment in 1774.⁹ It was not until a hundred years later when Lord Rayleigh measured the lowering of the water surface tension quantitatively due to spreading of olive oil and suspected that the maximum extension of an oil film on water

Chapter 1

represents a layer one molecule thick.¹⁰ At the same time a German woman, Agnes Pockles, set up the foundation for our ability to characterize monolayers at the air/water interface. She developed a rudimentary surface balance in her kitchen sink and made a systematic study by compressing films containing different amounts of oil on the water surface with ‘barriers’, thus observing that the surface tension fell rapidly when the monolayer was compressed below a certain area.¹¹ It was later speculated by Lord Rayleigh¹² that at this area, the oil molecules were closely packed and this speculation actually became the basis for the subject of modern monolayer research.

In the early 1900s, Irving Langmuir designed a number of new devices for measuring the surface pressures of spread monolayers; one such device was later named as the Langmuir film balance. By using chemically pure substances instead of the oils used by his forerunners, he presented the evidence for the monomolecular nature of the film as well as the orientation of the molecules at A/W.¹³ Three years later, Langmuir showed how these monomolecular films could be transferred as single monomolecular films onto solid substrates.¹⁴ Seventeen years later, Katharine Blodgett demonstrated the first successive or multiple transfer of long aliphatic carboxylic acids monolayers onto a solid substrate.¹⁵ These films are now referred to as Langmuir–Blodgett (LB) films.

It took almost 50 years before people began to realize the advantages and opportunities provided by the LB-technique after Langmuir and Blodgett’s work. While the early investigations were mainly related to the interfacial phenomena, nowadays the interest has shifted to functional LB-films for various applications.² If the term “Langmuir and Langmuir-Blodgett” is input for literature survey in SciFinder[®] engine, there are still nearly 700 new entries every year.

For the sake of creating desired supramolecular architectures and optimizing the transfer conditions through the Langmuir-Blodgett technique to study biomimetic,¹⁶⁻¹⁹ electronic,^{4,20,21} and optical^{22,23} processes in ultra thin films, Langmuir monolayers, which are the precursors of LB-films, have attracted considerable attention over the past two decades. In addition, Langmuir monolayers at A/W serve as important chemical and physical model systems for the basic understanding of two-dimensional (2D) ordering, phase transitions, wetting, and interfacial rheology due to their confined 2D-geometry²⁴ and as interesting models for biological membranes.²⁵

1.3 Langmuir Monolayer Formation

In general, molecules that form Langmuir monolayers are amphiphiles with a polar head group (such as an acid or alcohol) and a long hydrophobic tail (such as a hydrocarbon chain). For the monolayer to be stable, an amphiphile must have very low solubility in water and a small enough vapor pressure so that it does not dissolve or evaporate. Classes of molecules that are commonly used to form Langmuir monolayers include long-chain fatty acids, alcohols, esters, and phospholipids as shown in Figure 1.1. Each of these traditionally and frequently studied Langmuir monolayer molecules consists of one or several long hydrocarbon chain(s) having more than 14 carbon atoms and a polar hydrophilic head group.

While some insoluble amphiphiles can naturally spread into Langmuir monolayers, others only form drops on the water surface and need to be dissolved into a volatile solvent such as chloroform, which completely spreads on water. When a drop of the dilute chloroform solution is placed on the water, it spreads over the surface of the water promptly and leaves the amphiphiles behind to form a monolayer after solvent

Chapter 1

evaporation. After the formation of a monolayer, the basic and widely used technique to characterize Langmuir monolayers is the surface pressure (Π)–area per molecule (A) isotherm measurement, by which the monolayer characteristics of a compound can easily be obtained.

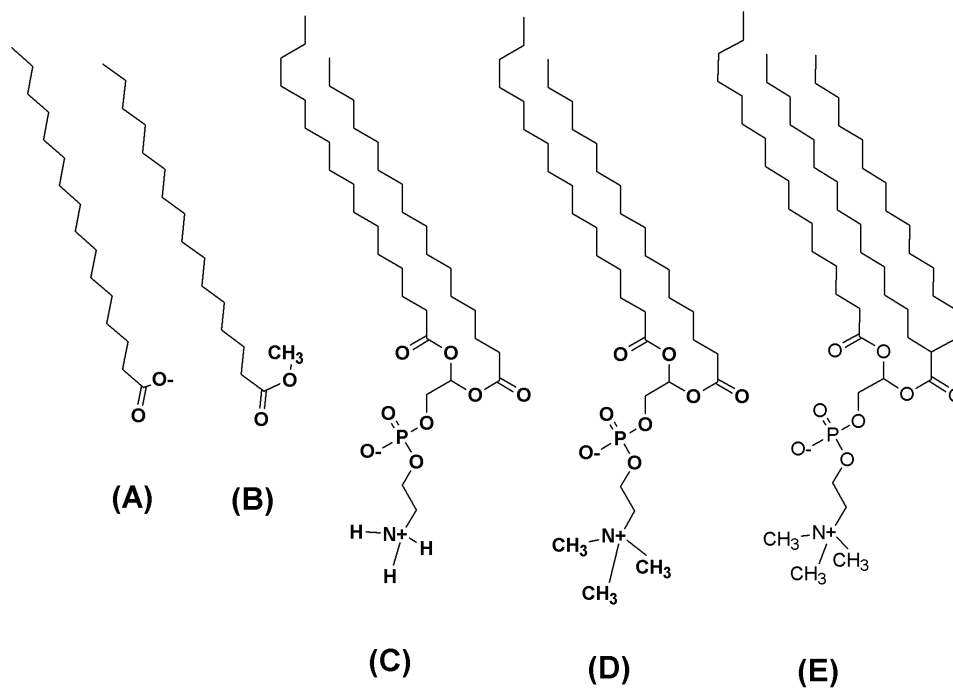


Figure 1.1: Some frequently used lipid molecules to form Langmuir monolayers at A/W: (A) Ionized n-hexadecanoic (palmitic) acid, (B) n-hexadecanoic methyl ester, and various phospholipids: (C) palmitoylphosphatidylethanolamine, (D) palmitoylphosphatidylcholine, and (E) palmitoylphosphatidylcholine with an aliphatic branch.

1.4 Surface Pressure (Π)–Area per Molecule (A) Isotherms

1.4.1 Surface Pressure (Π) vs. Surface Tension (γ)

The air/water interface (A/W) possesses an excess free energy originating from the difference in environment between the surface molecules and those in the bulk. This interfacial free energy can be accessed by measurements of the surface tension, γ . At thermodynamic equilibrium, the surface tension of a planar interface can be related to the partial derivatives of the free energy function with respect to the area of the surface as eq 1.1.

$$\gamma = \left(\frac{\partial F}{\partial A}\right)_{T,V,n} = \left(\frac{\partial G}{\partial A}\right)_{T,P,n} \quad [1.1]$$

where F and G , are the Helmholtz and Gibbs free energies, respectively, and A is the surface area. To minimize its energy, the system will try to minimize its surface area, whereby surface tension, γ , also manifests itself as a force per unit length. Due to the strong hydrogen bonding between water molecules, water has a high surface tension relative to organic liquids of about $73 \text{ mN}\cdot\text{m}^{-1}$ at $20 \text{ }^\circ\text{C}$, which consequently makes water a very good subphase for Langmuir monolayer studies.

When a monolayer is spread at A/W, the interaction of water molecules with the hydrophilic head groups of amphiphiles lowers the energy cost for a water molecule to be at A/W, which means they decrease the surface tension of water. If the monolayer molecules are compressed to pack closely with one another, the steric or repulsive interactions between them produces the force that opposes the contracting tendency of the water surface, thereby further lowering the surface tension. This change in the surface

Chapter 1

tension is usually defined as the surface pressure, Π , which is the two-dimensional analog of an ordinary bulk pressure, P ,

$$\Pi = \gamma_0 - \gamma \quad [1.2]$$

where γ_0 is the surface tension of pure water and γ is the surface tension of water covered by a monolayer. Before further discussion of the monolayer behavior, it is informative to set up the correspondence between surface pressure (Π) values and ordinary bulk pressure (P) values. One may consider that although Π has dimensions of force per unit length, it actually is a pressure distributed over the thickness of thin films. By the way of that interpretation, we could have eq. 1.3:

$$P(\text{mN} \cdot \text{m}^{-2}) = \frac{\Pi(\text{mN} \cdot \text{m}^{-1})}{\text{thickness}(\text{m})} \quad [1.3]$$

Assuming the thickness of a monolayer is on the order of 1 nm, $\Pi = 1 \text{ mN} \cdot \text{m}^{-1}$ will give a corresponding $P = 10 \text{ atm}$. From the above point, almost all the physical quantities in 3D bulk systems can have corresponding counterparts in 2D monolayer systems. For example, there is an expression of bulk modulus, K , in 3D bulk systems as

$$K = -V \left(\frac{\partial P}{\partial V} \right)_T \quad [1.4]$$

and its corresponding one in 2D monolayer systems will be a 2D lateral modulus, ε_s , shown as:

$$\varepsilon_s = -A \left(\frac{\partial \Pi}{\partial A} \right)_T \quad [1.5]$$

In general, there are two methods for measuring surface pressure, a Langmuir balance and the Wilhelmy plate technique.¹ For the first one a clean water surface is separated from the surface covered with the monolayer by a float connected to a

conventional balance that measures the force acting on the float. For the more commonly used Wilhelmy plate method, the forces acting on a piece of platinum or filter paper plate immersed in the water are measured by a high-sensitivity electrobalance shown as Figure 1.2 and 1.3. Such forces are downward forces, such as the gravitational force (W) and surface tension (γ), and upward forces, such as buoyancy. If the buoyant force is small enough, it is negligible, and the surface tension (γ) and surface pressure (Π) can be calculated by the following equations,

$$\gamma = \frac{F_{obs, film} - W}{2(L + t)\cos\theta} \quad [1.6]$$

$$\Pi = \gamma_0 - \gamma = \frac{F_{obs,0} - F_{obs, film}}{2(L + t)\cos\theta} \quad [1.7]$$

where F_{obs} is the observed force read by the electrobalance, W is the gravitational force, L is the length of plate and t is thickness of the plate, which is usually negligible compared to the scale of L . θ is the contact angle between the liquid subphase and the plate at the interface as shown in Figure 1.2. When using filter paper, essentially perfect wetting is observed, and the contact angle can be regarded as zero, which gives a practical surface pressure measurement equation as eq 1.8.

$$\Pi = \frac{F_{obs,0} - F_{obs, film}}{2L} \quad [1.8]$$

While the measurement software always assumes the contact angle is zero, θ actually can deviate from zero during the film compression due to the adsorption of hydrophobic materials on the surface of the plate or increases in a films' rigidity. To avoid the above-mentioned drawback, a fresh and clean filter paper plate is used for each isotherm experiment.

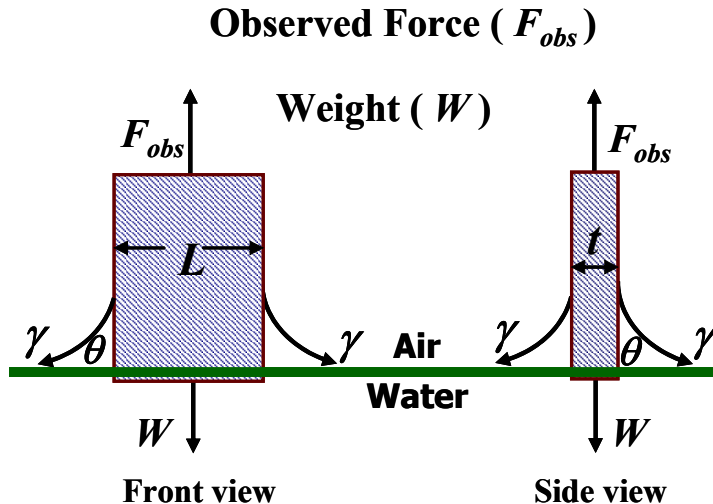


Figure 1.2: Measurement of surface pressure (Π) with the Wilhelmy plate technique.

1.4.2 Langmuir Trough and Π - A Isotherms

Normally Langmuir monolayers are spread and characterized in an apparatus traditionally referred to as a Langmuir trough (Figure 1.3). A Langmuir trough consists of a chemically inert trough, usually made up of hydrophobic materials such as TeflonTM (PTFE) to contain the aqueous subphase. Movable hydrophilic (DelrinTM) or hydrophobic (PTFE) barrier(s) are used to control the surface concentration of the amphiphiles.

Area per molecule or monomer (A), which is commonly used to express the surface concentration in the studies of Langmuir monolayers, is defined as the average area available to or occupied by each insoluble amphiphile on the water subphase surface. It is simply calculated by dividing the trough area by the number of spread amphiphile number, so that a small area per molecule (A) means a high surface concentration ($\Gamma = 1/A$). For a single component monolayer, area per molecule can provide direct

information about the size of a molecule, monolayer structures, monolayer phase transitions, and monolayer to multilayer collapse behavior. In particular, the limiting area (A_0) obtained by extrapolating the steepest portion of an isotherm back to the x-axis can be used to estimate the actual cross-sectional area (A_c) of a molecule and set up the basis for further isotherm analysis.

A schematic diagram of a Langmuir trough is shown in Figure 1.3. The monolayer samples and water subphase are held in a Langmuir trough; the movement of the barriers, which blocks off the surface of the water while allowing the bulk water to pass underneath, controls the surface density of a monolayer. By moving the barriers forward or backward a monolayer at A/W can be compressed or expanded, without causing the height of the water subphase to change. By continuously compressing or expanding the monolayer while monitoring the surface pressure (Π), plots of the change in surface pressure (Π) as a function of the area per molecule, Π - A isotherms, are obtained.

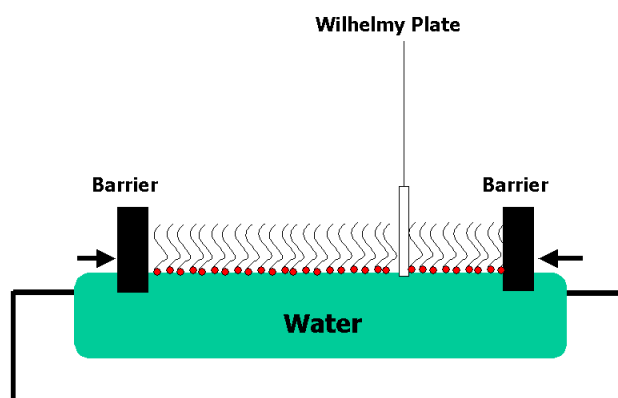


Figure 1.3: A schematic diagram of a Langmuir trough.

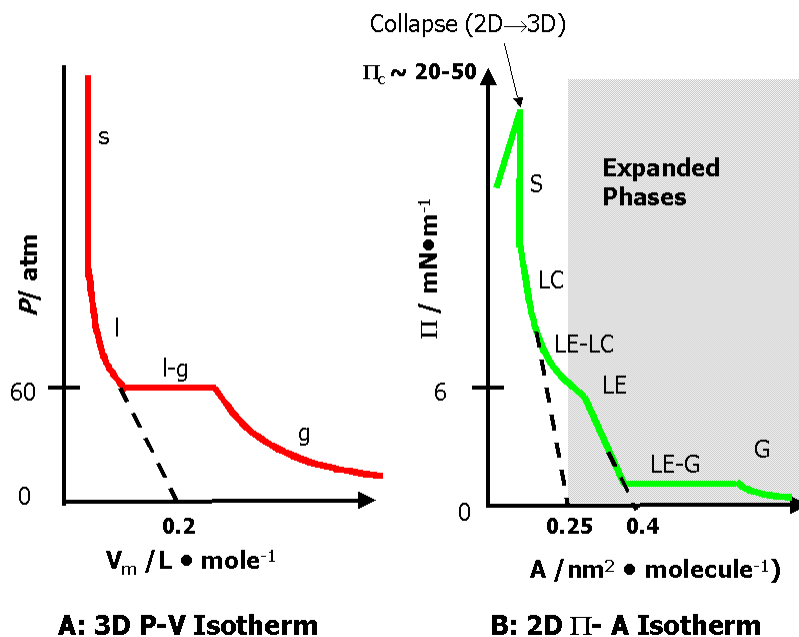


Figure 1.4: Comparison between 3D and 2D isotherms. (A) P - V isotherm of carbon dioxide (CO_2) at $20\text{ }^\circ\text{C}$;²⁶ g: gas phase; l-g: liquid and gas phase coexistence; l: liquid phase; s: solid phase; (B) Π - A isotherm for n-pentadecanoic acid at $25\text{ }^\circ\text{C}$ on a subphase of 10^{-2} M HCl .²⁷ G: gaseous phase; LE-G: liquid expanded and gas phase coexistence; LE: liquid expanded phase; LE-LC: liquid expanded and liquid condensed phase coexistence; LC: liquid condensed phase; S: solid phase; Π_c : 2D \rightarrow 3D collapse point.

As a function of temperature (T) and surface pressure (Π), in different area per molecule or monomer (A) monolayers undergo phase transitions that are similar to those occurring in 3D bulk systems as shown in Figure 1.4. As described in Figure 1.4B, measuring the surface pressure as a function of area per molecule at constant temperature yields a Π - A isotherm similar to a P - V isotherm as shown in Figure 1.4A. Such Π - A

isotherms can be used to elucidate the phase behavior of the monolayers.²⁸ For example, at large A , the distance between adjacent amphiphiles is large and their interactions are very weak. Under these conditions the monolayers have little effect on the surface tension of water, hence, they exhibit very low surface pressures on the order of $0.1 \text{ mN}\cdot\text{m}^{-1}$. At this state the monolayer can be regarded as a two-dimensional (2D) gas (G) when compared to 3D bulk systems (Figure 1.4). Upon further compression, the distance between amphiphiles decreases and at a certain point after a low Π plateau (LE-G or L_1 -G) the molecules start to feel each other and the surface pressure increases with the enhancement of repulsive interactions. Next, the monolayer enters an expanded liquidlike region called a liquid expanded phase (LE or L_1). Upon further compression, monolayers undergo very complicated condensed phase transitions with the appearances of various short plateaus or “kinks”. While the appearance of plateaus in Π - A isotherms (Figures 1.4B and 1.5) simply indicate first-order phase transitions, the “kinks” actually represent second-order phase transitions. The difference between a first- and a second-order transition between two monolayer phases will be clarified shortly.²⁹

In a first-order phase transition, the densities of the two phases are different from one another during the transition plateau. When the density of the system is intermediate between the densities of the two phases, the system displays phase coexistence with a heterogeneous surface morphology. In a second-order phase transition, the transition between the two phases is continuous; at the transition point the densities of the two phases are the same. In contrast to first-order transitions, second-order transitions never exhibit coexistence between two phases and the resulting surface morphology is homogeneous. Instead, as the density of the system is increased, for example in the case

Chapter 1

of fatty acids, the tilt angles of the molecules become increasingly smaller, going smoothly to zero; therefore the isotherm displays a “kink” at the density at which the tilt angle becomes zero, indicating a second order transition as shown in Figure 1.5.

From the results of Π - A isotherm analyses at different temperatures, condensed monolayer phases with different orientational order can be roughly identified as liquid condensed (LC or L_2), solid (S) and finally a collapse regime with 3D structures at different surface pressures. A generalized Π - A isotherm with different monolayer phases is summarized in the left side of Figure 1.5 for an amphiphilic fatty acid.

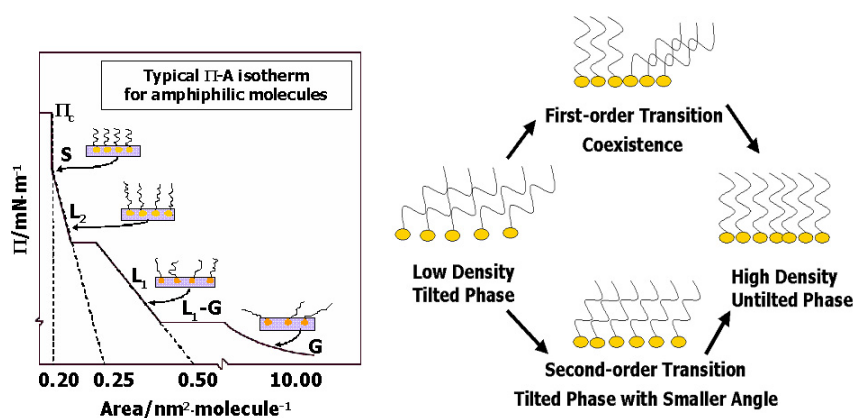


Figure 1.5: Comparison of first- and second-order phase transitions between a low-density tilted phase and a higher-density untilted phase. For the first-order transition there is a region where the two phases coexist. For the second-order transition the tilted phase changes continuously into the untilted phase. (A generalized ideal Π - A isotherm for an amphiphilic fatty acid molecule is provided on the left side of the figure. Horizontal sections (plateaus) of isotherm are phase coexistence regions at a first-order transition, and the “kink” from L_2 -S indicates a continuous second-order phase transition.)

1.4.3 Limitations of Π - A Isotherms

While Π - A Isotherms are very helpful for characterizing phases and phase transitions in Langmuir monolayers, isotherm studies are often ambiguous, and lead to controversies that can only be resolved with more sophisticated techniques. For example, for the isotherm of n-pentadecanoic acid (Figure 1.4B), the nature of the LE \rightarrow LC phase transition was a matter of dispute for several years. During continuous compression, there is only a “kink” and not a plateau, observed in the isotherm around $0.30 \text{ nm}^2 \cdot \text{molecule}^{-1}$. This “kink” seems to indicate a second-order phase transition, rather than a first-order phase transition. Although some researchers argued that the LE \rightarrow LC transition is second-order, it was observed that the isotherm actually showed a short plateau if additional care was taken to remove impurities and if compression was carried out at a slower rate.¹ Subsequently, Brewster angle microscopy and fluorescence microscopy studies clearly showed phase coexistence in this region, that is consistent with a first-order phase transition.²⁹ As a result of these studies, one may conclude that dynamic isotherm measurements alone are insufficient to reveal delicate condensed monolayer phase transitions. Many similar examples in the field of monolayer research require the need for experimental methods more sophisticated than Π - A isotherms to study Langmuir monolayers.

Over the past two decades a number of *in situ* techniques have been developed to elucidate various aspects of monolayer condensed phase behavior. These include x-ray diffraction techniques (XRD),^{30,31} fluorescence microscopy (FM),^{32,33} Brewster angle microscopy (BAM),^{34,35} surface light scattering (SLS),³⁶⁻³⁸ interfacial stress rheometer (ISR),³⁹ and non-linear optical techniques.⁴⁰⁻⁴² In the remainder of this chapter we will

Chapter 1

mainly focus on one powerful optical technique for deducing monolayer morphology, Brewster angle microscopy (BAM) and a technique for measuring interfacial rheology, the interfacial stress rheometer (ISR). BAM allows for the visualization of phase behavior in two-dimensional systems. ISR provides the shear viscoelastic properties of Langmuir monolayers.

1.5 Brewster Angle Microscopy

1.5.1 Background

Many questions about Langmuir monolayers can easily be addressed if the morphology of the monolayers can be directly imaged. For example, if a microscope image shows two phase coexistence, it is clear that the phase transition being studied is first-order. One other microscopy method that yields images of monolayer morphology is fluorescence microscopy (FM),^{32,33} which involves the addition of an insoluble amphiphilic fluorescent dye molecule into the monolayer. The solubility of these amphiphilic fluorescent dyes depends upon the densities of the monolayers phase: the more ordered or condensed a monolayer phase is, the smaller the solubility of the fluorescent probe. For a coexistence region, the dye is preferentially soluble in the less dense monolayer phase. Hence, imaging the fluorescence of the dye yields images of the monolayer morphologies. However, this technique has the disadvantage that it requires the addition of an extra fluorescent dye, which contains the samples and may affect the monolayer phase behavior. To avoid using fluorescent dyes, it is preferable to use a direct microscopy technique that images light reflected by the monolayers.

When *p*-polarized light impinges on a water surface at Brewster's angle ($\Theta_B=53.1^\circ$ for water), very little incident light is reflected from the air ($n_l = 1$) and water

($n_2 = 1.33$) interface according to Fresnel's law (Figure 1.6). Under the condition of a constant incident angle, the introduction of a Langmuir monolayer at A/W modifies the conditions for Brewster's angle, and light can be reflected thereby allowing imaging of the morphology. Different domain shapes are usually observed with different reflection density or gray levels, which are related either to refractive index differences of different monolayer phases, such as liquid-expanded, liquid-condensed and solid phases, or to the thickness change due to the formation of three-dimensional aggregates.

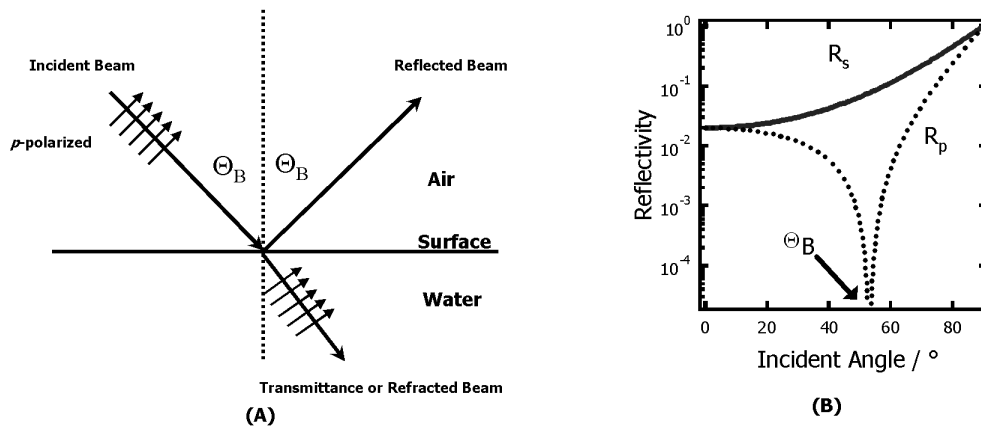


Figure 1.6: Comparison of the reflectivity of s and p -polarized light at Θ_B : (A) Scheme indicating how the reflectivity vanishes at Brewster's angle for the p polarized light; (B) calculated reflectivity of a Fresnel interface between air ($n_1 = 1$) and water ($n_2 = 1.33$) for p -polarized (in the plane of incidence) light and s -polarized (perpendicular to this plane) light according to eqs. 1.9 & 1.10. At Brewster's angle ($\Theta_B = 53.1^\circ$ for water), the reflectivity (R_p) for p -polarized light vanishes.

1.5.2 Principle of Brewster Angle Microscopy

David Brewster was a 19th century Scottish physicist who investigated the reflection of light from polished surfaces and discovered that the reflected light is always partially polarized with polarization of its electric field vector either normal to (s -polarization) or parallel to (p -polarization) the plane of incidence. According to Fresnel's law, the reflectivity (R) of light from a surface mainly depends on its angle of incidence θ and its polarization as follow,

$$R_s = \left(\frac{n_i \cos \theta_i - n_t \cos \theta_t}{n_i \cos \theta_i + n_t \cos \theta_t} \right)^2 = \frac{\sin^2(\theta_t - \theta_i)}{\sin^2(\theta_i + \theta_t)} \quad [1.9]$$

$$R_p = \left(\frac{n_t \cos \theta_i - n_i \cos \theta_t}{n_i \cos \theta_t + n_t \cos \theta_i} \right)^2 = \frac{\tan^2(\theta_i - \theta_t)}{\tan^2(\theta_i + \theta_t)} \quad [1.10]$$

where the subscripts s , p , r , i , and t represent s -polarization, p -polarization, reflection, incident, and transmitted or refracted light, respectively; n means refractive index, and $\theta_i + \theta_t = 90^\circ$ at Brewster's angle.

For a Fresnel interface, which is an ideal isotropic interface without roughness possessing an abrupt refractive index change from n_1 to n_2 , the normal reflectivity (R_s) of light increases continuously with the angle of incidence and approaches unity at the total reflection angle as shown in Figure 1.6. Compared to R_s , the parallel reflectivity (R_p) has a very sharp minimum, which reaches zero at Brewster's angle θ_B . By using Snell's refraction law, Brewster's angle can be correlated with the indices of refraction of the media as $\tan \theta_B = n_2/n_1$. Basically, the reflectivity of a real interface at Brewster's angle for p -polarized light has three origins:

(1) The thickness of the interface: the refractive index of a real interface does not change abruptly at $z = 0$, where z is the distance from the average interfacial position. The refractive index is different from either n_1 or n_2 , and is equal to $n(z)$, over the range of the interface. Drude has calculated the reflectivity for the amplitude of an electromagnetic wave with polarization p (parallel to the plane of incidence).⁴³ For an interfacial layer with a small thickness, h , which is small compared to the incident wavelength, λ_o , and possesses a refractive index profile $n(z)$,

$$R_p(\Theta_B) = R_s(\Theta_B) \overline{\rho_B}^{-2} \quad [1.11]$$

where $R_s(\Theta_B)$ is the reflectivity of a Fresnel interface at the Brewster's angle for s -polarized light, and $\overline{\rho_B}$ is the ellipticity given as:^{34,35}

$$\overline{\rho_B} = \frac{\pi}{\lambda_o} \frac{\sqrt{n_1^2 + n_2^2}}{n_1^2 - n_2^2} \int_{-\infty}^{+\infty} \frac{[n(z)^2 - n_1^2][n(z)^2 - n_2^2]}{n(z)^2} dz \quad [1.12]$$

where n_1 and n_2 correspond to the refractive indices of the upper medium (air) and the lower medium (water), respectively. A dense monolayer of amphiphilic molecules can introduce a variation of the refractive index $n(z)$, which depends on the properties of the phase domain, over a thickness of about 20 Å; therefore, two different monolayer phase domains could have very different parallel reflectivity, $R_p(\Theta_B)$, which means the phases with higher $R_p(\Theta_B)$ will appear much brighter than the phases with lower $R_p(\Theta_B)$ when observed with an imaging detector, such as a CCD camera, at Brewster's angle.⁴⁴ Furthermore, if the thin film's refractive index $n(z)$ can be assumed to be uniform, one obtains

$$I_r = I_i R_p(\theta_B) \propto \rho_B^{-2} \approx \left(\pi \frac{h}{\lambda_o} \frac{\sqrt{n_1^2 + n_2^2}}{n_1^2 - n_2^2} \frac{[n^2 - n_1^2][n^2 - n_2^2]}{n^2} \right)^2 \quad [1.13]$$

To a first approximation, the reflected intensity, I_r , at Brewster's angle is proportional to the square of film thickness, h^2 . Hence a quantitative determination of the relative thickness, not the exact thickness, can be made from the relative reflectivity data of BAM images as a function of molecular area (A). As an example, a layer with a thickness of 10 Å and a uniform refractive index of 1.4 can increase reflectivity for p -polarized light by a factor of 35 at the Brewster's angle.

(2) The roughness of real interfaces:^{45,46} At liquid interfaces, the origin of the roughness is thermal fluctuations. For monolayers at the free surface of water, the surface tension is large; so that the surface thermal fluctuations are small enough to be neglected to a first approximation. However roughness still introduces a small error on the thickness of the monolayer (~ 3 Å).⁴⁷

(3) The anisotropy of monolayers: Some concentrated phases in monolayers are optically anisotropic.⁴⁸ This anisotropy can greatly increase the reflected intensity which can be calculated using the 4×4 matrix method. If the optically anisotropic monolayer does not have an axis of vertical symmetry, the reflected light is a function of the orientation of the monolayer in its plane.

1.5.3 Experimental Setup of BAM

A typical BAM instrument consists of a laser source, a Glan-Thompson polarizer with the field polarized parallel to the plane of incidence, and a light detector (such as a CCD camera) as shown in Figure 1.7. The incident light source in a BAM is provided by a laser, which is the only possible light source because the incident beam must have a

high intensity and a well-defined polarization (p) to provide uniform illumination. The polarizer can be placed either in the path of the incident beam to polarize the radiation in the p direction before it contacts the surface, as in traditional BAM, or it can be placed in the path of the reflected beam to filter out any residual s component before the reflected p radiation reaches the CCD detector, as is the case for the Mini-BAM used in this dissertation. By placing the polarizer in the path of the reflected beam, better resolution can be achieved than by the traditional method. To prevent the light from randomly scattering from the subphase and trough, a black flat glass plate is normally placed underneath the water surface. A set of lenses is used to direct the reflected beam to a CCD camera for imaging.

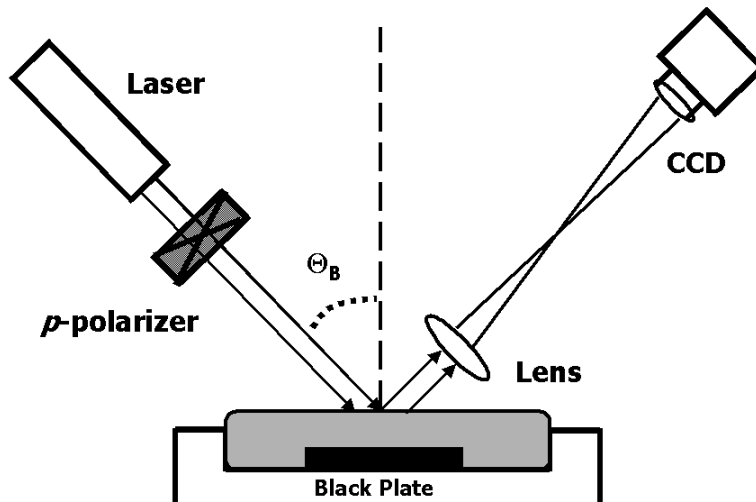


Figure 1.7: Experimental setup for a typical BAM experiment. A p -polarized light beam is incident on the water surface at Brewster's angle for water ($\Theta_B = 53.1^\circ$). Light reflected by the monolayer is imaged onto a CCD camera.

1.5.4 Applications of BAM

After the invention of BAM, numerous standard monolayers including fatty acids, esters and phospholipids as well as mixed monolayers were studied and an unexpected richness of morphologies in monomolecular films were revealed.²⁴ A multiplicity of domain shapes were observed directly, including simple circles, vague hexagons, two-dimensional foams spiral and branched shapes, and labyrinthine structures.²⁴ The monolayers were typically very heterogeneous, including both very large and small domains, whose shapes are very sensitive to experimental conditions, including the method of film spreading, the presence of any impurities, change in temperature, compression and expansion rate, subphase compositions, and possibly humidity.⁸

When combined with the traditional Π - A isotherm measurements and other surface sensitive techniques, such as X-ray and neutron reflectivity,^{49,50} ellipsometric measurements,⁵¹⁻⁵³ infrared reflection-absorption spectroscopy,⁵⁴ Brewster angle microscopy not only provides rich information on the morphology of amphiphilic monolayers,⁵⁵⁻⁶⁵ but also provides information about two-dimensional phase transitions. This information includes the internal structure of condensed domains and phase transitions in condensed monolayers,^{29,63,66} the orientational order of the monolayer domains,⁶⁶⁻⁶⁸ deformation⁶⁹⁻⁷² and relaxation phenomena in monolayer domains caused by compression-expansion cycles or by interfacial flow,^{57,73,74} etc. As the light intensity at each point in the BAM image depends on the local thickness and monolayer optical properties, BAM also can be applied to determine the thickness of film regions, even when the optical properties of the film are unknown.^{68,75,76}

BAM is not only an excellent tool for the direct observation of macroscopic structures in Langmuir monolayers, but also for the illustration of monolayer molecules' orientation, tilt azimuth or rotational degrees of freedom in various phases. Through BAM and fluorescence microscopy studies, the phase behavior of long-chain monolayers were much more complicated than the classification implied by Π - A isotherms as shown in Figure 1.4 & 1.5.

1.6 Phase Diagrams of Langmuir Monolayers

1.6.1 Monolayer Phases

Although one can easily extract several overall descriptions of different monolayer phases by analyzing Π - A isotherm results, the complexity of monolayer phase diagrams came as a surprise after the invention of FM and BAM.

An experimental Langmuir monolayer phase diagram for a fatty acid (eicosanoic acid)⁷⁷ derived mainly by locating the phase boundaries via BAM and FM observations is shown in Figure 1.8. In general, it shows two "expanded" phases, gas (G) and "liquid-expanded" (L_1 or LE), and many other "condensed" phases. The condensed phases can be separated into tilted phases, in which the molecular axes are tilted with respect to the surface normal, and untilted phases, in which the axes are perpendicular to the interface. In Figure 1.8, the phases labeled L_2 , L_2' , L_2'' and O_v are tilted phases. In L_2 , L_2'' , the tilt directions are toward nearest neighbors (NN, see the summary in Table 1.1), and in L_2' and O_v toward next-nearest neighbors (NNN, see Table 1.1). While herringbone (V-shaped) order has been observed in the untilted phases CS and S, the LS phase is an untilted hexatic phase.

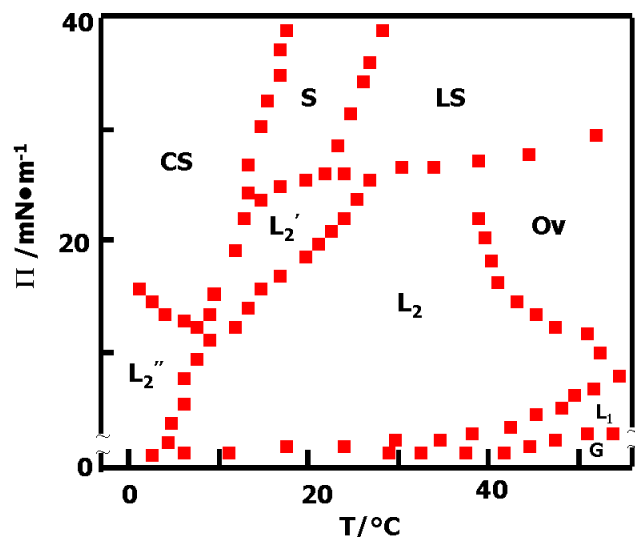


Figure 1.8: Experimental Π - T phase diagram for an eicosanoic acid Langmuir film. The phase boundaries have been determined primarily by BAM and FM measurements. Reconstructed from reference 77.

Table 1.1: A summary of Langmuir monolayer phases observed in Figure 1.8:

	Gas	Liquid Expanded	Liquid Condensed			Super-liquid	Solid		
Notation	G	L ₁	L ₂	Ov	L ₂ '	L ₂ ''	LS	S	CS
Azimuth of tilt	---	---	NN	NNN	NNN	NN	U	U	U

*NN = tilt to the nearest-neighbor molecule, NNN = tilt to the next-nearest neighbor, U = untilted hexagonal.

1.6.2 Chain-length Dependence of Monolayer Phase Diagrams

While fatty acids and molecules with similar structures show various condensed phases that reflect different orientations for closely packed side chains,^{29,77,78} they actually show degrees of universal behavior.⁷⁹ Figure 1.9 summarizes phase diagrams for the Langmuir films of fatty acids (C₁₄-C₂₄) at different subphase temperatures ranging

from 2 to 45 °C.^{29,80,83,84} Figure 1.9 is constructed from the combination of Π - A isotherms, BAM, X-ray diffraction, and theoretical studies.²⁴ The phase diagrams were superimposable with the phase transition temperatures shifted to higher values by 5-10 °C per additional methylene group.^{79,80} Other amphiphilic substances, which have different headgroup structures compared to fatty acids such as alcohols, esters, and acetates, also form stable Langmuir monolayers if they have sufficiently hydrophobic tails with the phase diagrams of alcohols being quite similar to those of the fatty acids.^{73,81} The phase diagram of Figure 1.9 is still under construction and is not final. In particular, Durbin *et al.*⁸² recently found a new phase lying in a narrow region between L_2 and L_2' phases in eicosanoic (C_{20}) and nonadecanoic (C_{19}) acid monolayers.

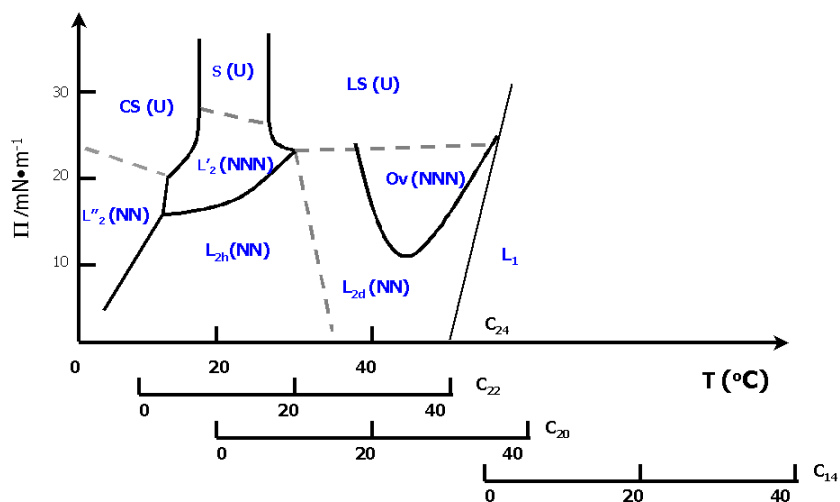


Figure 1.9: The chain-length dependence of the monolayer phase diagram for fatty acids. Solid lines represent first-order transitions and dashed lines correspond to second-order transitions.^{29,80,83,84}

1.7 Interfacial Shear Rheological Measurements

1.7.1 General Introduction

Rheological measurements (viscosity and flow behavior) of Langmuir monolayers have been an important subject of interfacial research. They play an important role in the dynamic characterization of surfaces in industries ranging from food and pharmaceuticals to petroleum.⁸⁵ The measurement of surface shear viscosities was pioneered in the last century. Over the latter decades a variety of techniques for the measurement of interfacial shear viscosity and viscoelasticity have been proposed. Most of those may be classified into two broad categories:

(1) *Indirect shear rheometers*, where the displacement of tracer particles placed at the interface are recorded and evaluated using image analysis. The flow type in these rheometers is either surface pressure driven, such as in rectangular channel rheometers⁸⁶⁻⁸⁸ or drag flow as in deep channel rheometers.⁸⁹ For these types of viscometers, it is necessary to determine the flow profile of the monolayer, using tracer particles, fluorescence microscopy,⁹⁰ or Brewster angle microscopy.⁹¹ The surface shear viscosity is then evaluated by comparing the flow profiles to solutions of the Navier-Stokes equation that are appropriate for the corresponding geometry.^{86,92,93} Devices such as the deep channel or the knife-in-wall rheometer offer high sensitivity even at low interfacial viscosities.⁹⁴⁻⁹⁶ However, the necessity to introduce and observe tracer particles makes measurements with channel-type rheometers practically difficult and time consuming.

(2) *Direct shear rheometers*, which are based on directly measuring the response of a monolayer to a torsion pendulum, or other oscillator. This category includes rotating disk geometries⁹⁶ and knife-edge or ring-type setups.⁹⁷⁻¹⁰⁰ One of the main goals in these

designs is to provide adequate sensitivity to detect stresses in the surface film in the presence of stresses from the underlying subphase. Recently interest has moved toward non-symmetric needle-shaped rheometers based on the belief that a needle-shaped oscillator should have some advantages due to their high sensitivity to the surface shear viscosity compared to the subphase is background rheological force.

1.7.2 Magnetic Needle Shear Viscometer

The needle oscillators, compared to the rotating disks and other oscillators with cylindrical symmetry, have a lower ratio (P_n/A_n) between the area of the needle facing the subphase (A_n) and the perimeter of the monolayer/needle boundary (P_n) and thereby a higher Boussinesq number. Therefore the sensitivity of a needle viscometer for the measurement of surface shear rheological properties should be better than that of a disk viscometer of comparable size.^{39,101}

The magnetic needle viscometer, first developed by Shahin,¹⁰² recently modified by Brooks *et al.*,³⁹ and further simplified by Ding *et al.*¹⁰¹ is a relatively new and sensitive method for measuring monolayer viscosity and has the following advantages when compared to other existing techniques in addition to its expected high sensitivity: (1) the interfacial stresses can be measured in real time, allowing the study of time-dependent flows, and subsequently the determination of the elasticity and viscosity of the monolayer; (2) the frequency of the applied force can be readily changed without having to change the elements of the rheometer, e.g., the torsion wire in some of the torsion-bob-based devices; (3) the strain rate is determined from the position of the rod, avoiding the need to use tracer particles to analyze velocity profiles, as is required in the deep channel surface viscometer; (4) non-Newtonian surfaces can be examined since no assumptions

regarding the constitutive behavior are required to analyze the flow response, unlike some channel flow methods; and (5) the surface pressure and temperature can be readily changed without having to change the geometry of the flow cell.^{39,103} By following the authors' terminology, the magnetic needle shear viscometer designed by the Fuller group and used in this dissertation is called an "interfacial stress rheometer (ISR)".

1.7.3 Interfacial Stress Rheometer (ISR)

In general, this instrument has a simple design that is based on applying a controlled shear stress via a magnetized probe at A/W and measuring the resulting deformation (strain). The rheological probe for this surface rheometer is a piece of slender magnetized PTFE coated needle confined in a well defined glass flow cell. The hydrophilic nature of the glass surface produces a meniscus that aids in aligning the magnetic rod along the channel's centerline. The needle remains at A/W because of surface tension (Figure 1.10A). The magnetized probe undergoes oscillatory translational motion at different angular frequencies (ω) along the long axis of an applied sinusoidal magnetic field gradient generated by a pair of AC controlled Helmholtz coils. The position of the needle is monitored as a function of time using a modified inverted microscope (Figure 1.10B). The image is projected onto a linear image sensor and the array output is analyzed to detect the edge motion of the needle. The amplitude and the phase of the needle's motion relative to the applied force is measured to determine the complex surface shear modulus (G_s^*) comprised of an elastic modulus (G_s') and a loss modulus (G_s''). In addition, a dynamic viscosity, μ_s^* , can be derived from the dynamic surface moduli to describe the general flow behavior of complex materials.

$$G_s^*(\omega) = G_s'(\omega) + iG_s''(\omega) \quad [1.14]$$

$$\mu_s^*(\omega) = \frac{G_s^*(\omega)}{i\omega} = \frac{G_s''(\omega)}{\omega} - i \frac{G_s'(\omega)}{\omega} \quad [1.15]$$

As one might expect, the combination of the interfacial stress rheometer with Π - A isotherm measurements and BAM observations can provide us a relationship between morphological and mechanical properties of amphiphiles.^{39,103-108} More importantly, these measurements may also lead to new insights into molecular interactions under dynamic conditions, such as hydrogen bonding between neighboring molecules, physical entanglement, and covalent cross-linking.¹⁰⁹⁻¹¹³

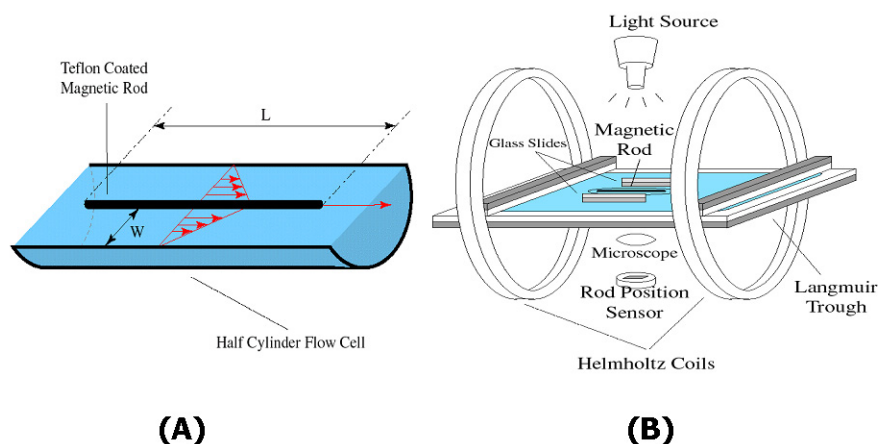


Figure 1.10: Schematic diagram of an interfacial stress rheometer (ISR). (A) Enlarged view of the magnetic rod between the glass slides of the flow cell (not to scale). The meniscus formed between the glass slides (not shown) aligns the rod along the centerline, and surface tension supports the rod. (B) Schematic diagram of the magnetic rod interfacial stress rheometer (ISR) apparatus showing the main elements of the device. The trough is surrounded by a pair of Helmholtz coils to create a magnetic field gradient, which applies a force on the rod to shear the film. It is assumed that the drag experienced by the rod predominantly arises from shear stresses developed between the glass slides and the rod. The position of the rod is detected by tracking the end of the needle. An inverted microscope is focused on the end of the needle, and the resulting image is projected onto a photodiode array. Modified from reference 39.

1.8 Polyhedral Oligomeric Silsesquioxanes (POSS) As Hybrid Nanofillers

1.8.1 Overview of Hybrid Nanocomposite Materials

*“It has been said the 19th century was the Ceramic Age, and the 20th century was the Polymer Age. The 21st century may well become the Hybrid Age.”*¹⁴

Hybrid materials, which contain both inorganic and organic molecules, lie at the interface of the organic and inorganic realms and occupy a unique property “space” as shown in Figure 1.11A. These hybrid materials are believed to offer exceptional opportunities not only to combine the important properties from both groups but also to create entirely new compositions with unique properties. Among these hybrid materials, polyhedral oligomeric silsesquioxanes (POSS, as shown in Figure 1.12) are a new class of lightweight, high-performance hybrid materials containing both inorganic silsesquioxane cores and organic alkyl groups, meanwhile they also fall in the category of nanostructured materials with sizes around 1-2 nm and have the potential to be used as nanofillers for the preparation of high-performance polymer nanocomposites.

The demand for advances in performance and properties of polymeric and composite materials has driven the research for new technologies and methods for improving the properties of existing plastics. As a result, the field of nanocomposites has been developed with the goal of reinforcing polymer chains at the molecular level. In the mid-1970s, people applied sol-gel technologies to form homogeneous dispersions of inorganic domains throughout a polymeric matrix (Figure 1.11B). In such systems, the inorganic phase may not be chemically attached to the organic phase, which results in limited material strength. The second-generation nanocomposite technology emerged with a resurgence in the use of surface-modified clay fillers (Figure 1.11C). The obstacle

for the application of clay nanofillers lies in the difficulty to form homogeneous dispersions of nanofillers via exfoliation or intercalation mechanisms into polymeric matrices. In 1995, a third-generation nanocomposite technology was developed based on one class of nanostructured, silicon-based oligomers, polyhedral oligomeric silsesquioxane (POSS) molecules (Figure 1.11D). In this technology, dissolving, standard polymerization, compounding, and coating techniques allows one to incorporate POSS nanofillers into well-defined polymeric materials. When incorporated into polymers, POSS nanostructured chemicals provide nanocomposite properties while maintaining or improving product processability. Meanwhile the versatile chemistry of POSS as shown in Figure 1.12A leads to an almost infinite group of chemically diverse POSS materials apart from other nanostructured fillers.

1.8.2 Polyhedral Oligomeric Silsesquioxanes (POSS)

Polyhedral Oligomeric Silsesquioxanes (POSS) are a family of important hybrid organic-inorganic materials that have been used in the last two decades for the preparation of polymeric nanocomposites. Based on their polyhedral structures that are topologically equivalent to a sphere, POSS derivatives are referred to as *spherosiloxanes*¹¹⁵ and are the smallest possible silicas due to their nano-scale size.¹¹⁶

There are two main POSS derivatives, the fully functional octasubstituted-POSS (R_8T_8) shown in Figure 1.12B (I) and the heptasubstituted trisilanol-POSS ($R_7T_7(OH)_3$) also shown in Figure 1.12B (II). These two POSS derivatives are the products of a hydrolysis and condensation of trichlorosilanes or trialkoxysilanes.¹¹⁷⁻¹¹⁹ The R_8T_8 can be hydrolyzed to form $R_7T_7(OH)_3$, but it is stable at room temperature in an environment with relatively high humidity (up to 70%).¹²⁰

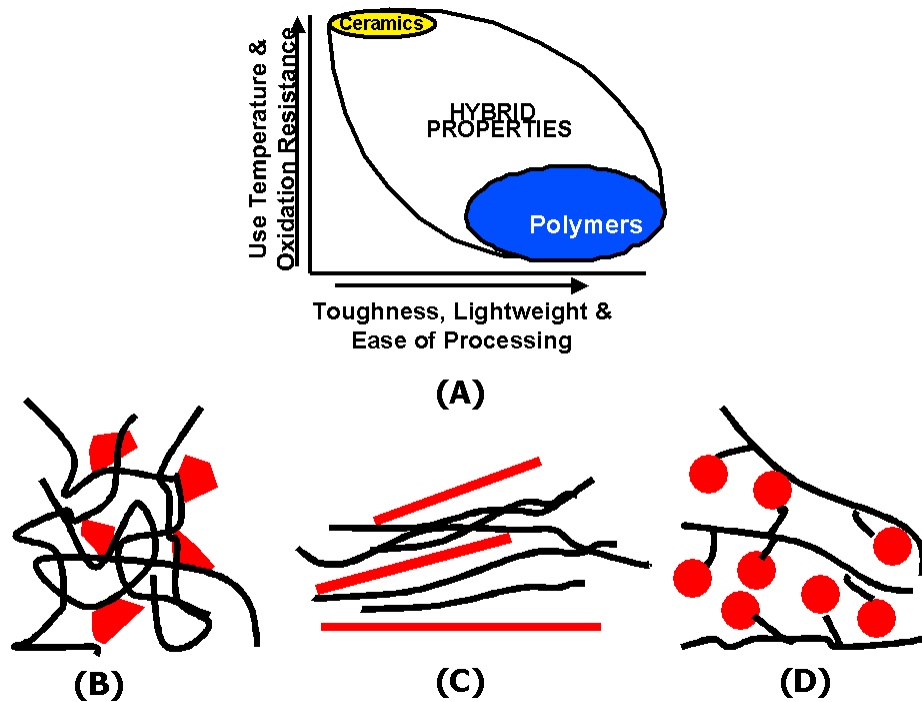
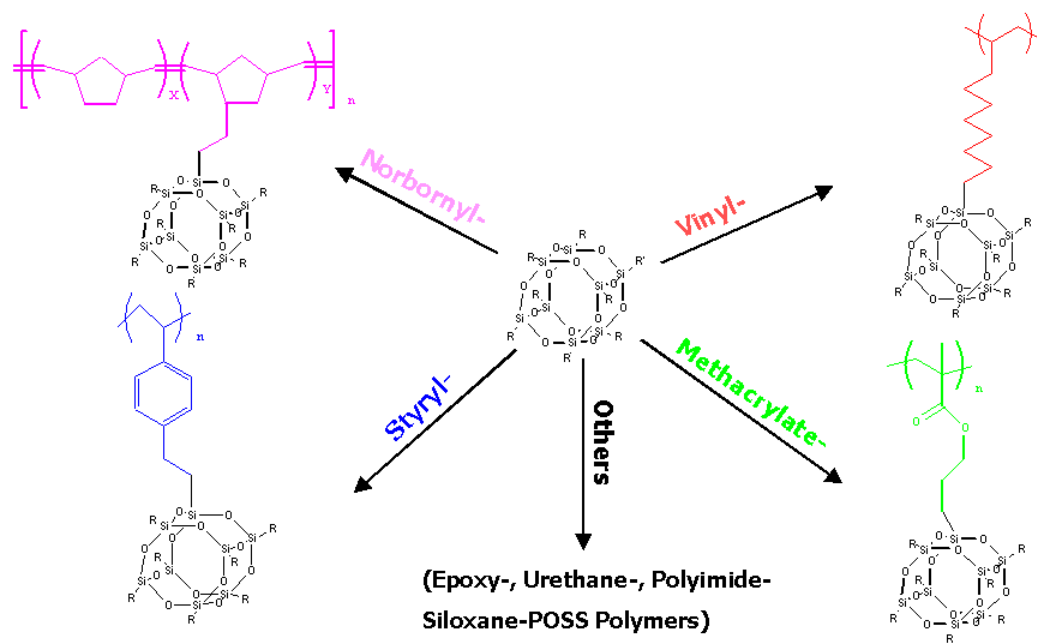
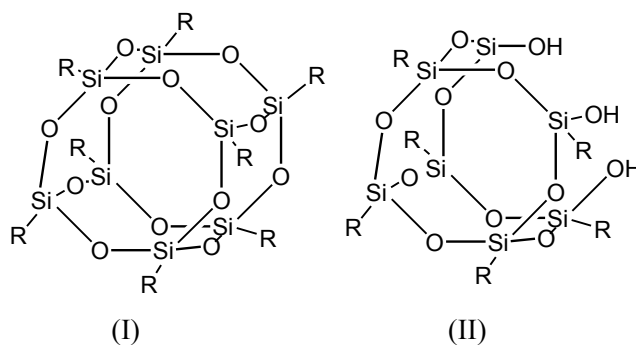


Figure 1.11: Schematic diagram describing hybrid nanocomposites: (A) The unique “space” of hybrid nanocomposite properties, which bridge the gap between polymers and ceramics; (B)→(D) the evolution of nanocomposite plastics: (B) composites were prepared by physically dispersing particulates within a polymeric matrix or via sol-gel routes; (C) composites were prepared by dispersing a clay filler within a polymer matrix via intercalation and exfoliation; (D) composites are prepared by dissolving, copolymerizing, or grafting nanostructured chemicals onto polymer chains.



(A)



(B)

Figure 1.12: Schematic diagram of POSS-based nanocomposites: (A) Different POSS-based nanocomposites with various building blocks; (B) two main POSS cages (I) T_8R_8 and (II) $T_7R_7(OH)_3$, where R is an alkyl group, H, Cl, or a variety of other organic groups.

1.8.3 Synthesis of POSS Macromers

There are different strategies for the synthesis of POSS.¹²¹ The most general route is the hydrolysis and condensation of trialkoxysilanes or trichlorosilanes.¹¹⁷⁻¹¹⁹ However this method frequently leads to a distribution of different products that depends on the nature of the starting silane, solvent, catalyst, their relative concentrations, the amount of added water, the selected temperature cycle, and the solubility of the final products. $R_7T_7(OH)_3$ can be isolated in moderate yields from the hydrolytic condensation of silanes under strictly controlled conditions.^{122,123} Corner capping of this precursor can be carried out using a variety of trichlorosilane coupling agents.^{119,124} This approach leads to an $R'R_7T_8$ with one corner that may be functionalized with a graftable or polymerizable group. Lichtenhan *et al.*¹²⁵⁻¹²⁷ have used this approach to synthesize and characterize a variety of linear polymers modified with POSS building blocks tethered to the polymer backbone. Feher *et al.*¹²⁸ developed a strategy for preparing functionalized POSS from fully condensed T_8 frameworks. They used a general and remarkably selective method for the effective cleavage of a single framework siloxane linkage, opening the possibility of introducing desired functional groups into the new structure. Fasce *et al.*¹²⁹ developed a simple but cheap route to synthesize R_8T_8 by the hydrolytic condensation of modified aminosilanes. The starting material was N-(β -aminoethyl)- γ -aminopropyltrimethoxysilane, a trifunctional aminosilane, which was reacted with a stoichiometric amount of phenylglycidyl ether in sealed ampules at 50 °C for 24 h, leading to the $R_7T_7(OH)_3$ product plus a series of oligomers. When this product was subjected to hydrolytic condensation using a variety of catalysts (HCl, NaOH, HCOOH)

and a thermal cycle reaching 150 °C, R_8T_8 was obtained. This process opens an efficient and direct path to synthesize functionalized POSS that may be used as cross-linking agents or as additives for a variety of polymers.

The POSS macromers can be polymerized or copolymerized using standard techniques to yield inorganic-organic hybrid homopolymers and copolymers.^{130,131} Depending on their functionality (Figure 1.12A), 3-D networks, bead or pendant type-POSS based polymeric nanocomposites can be synthesized. For example, the propylmethacryl-POSS monomer undergoes free radical polymerization to give POSS macromers,¹²⁶ and the hydrido-POSS monomer can undergo hydrosilylation reactions to give oligomers and polymers.^{132,133} Therefore POSS has the potential to be designed for products with specific nanostructures for specific end-use applications.

1.8.4 Applications of POSS

As mentioned before, the advantage of POSS technology is that it fills the property space between petroleum based plastics and ceramics, thereby improving the mechanical, electrical, and thermal characteristics of many polymers as well as reducing their density. Hence, it is not surprising to find numerous applications of POSS in both fields.

(1) *Applications in functional inorganic materials*: There are numerous applications of substituted silsesquioxanes as inorganic chemical reagents and functional materials precursors, including their use as Wittig reagents,¹²⁴ precursors to silicon carbide (SiC) powders,^{134,135} nitrided glass,¹³⁶ low dielectric constant materials,¹³⁷ silica-reinforced composites,^{138,139} and a variety of microporous materials.^{140,141}

(2) *Applications in polymer systems*: Unlike silica or modified clays, each POSS molecule can contain covalently bonded reactive functional groups suitable for polymerization or grafting POSS monomers to polymer chains. POSS molecules can also contain non-reactive organic functionalities for solubility and compatibility of the POSS segments with the various polymer systems. Hence, POSS can be used in the same manner as common organics, in either monomer or polymeric (resin) form and can be added to nearly all types of polymers (glassy, elastomeric, rubbery, semicrystalline and crystalline) in varying compositions. Because of its chemical nature, POSS is easily incorporated into common plastics via copolymerization or blending and results in a nanostructured organic-inorganic hybrid polymer.^{114,142} Meanwhile it requires little or no alteration of existing manufacturing processes. POSS additives can radically improve the thermal and physical properties of many plastics.¹⁴³ Enhancements in the physical properties of polymers containing POSS segments come from its ability to control the motion of the polymer chains while still maintaining the processability and mechanical properties of the base resin. Property enhancements observed in POSS-copolymers and blends include increased thermal decomposition temperatures T_{dec} ,¹⁴⁴⁻¹⁴⁶ increased glass transition temperature T_g ,¹⁴⁷⁻¹⁵⁰ reduced flammability and heat evolution,^{151,152} lower thermal conductivity,^{150,153} expanded useable temperature ranges,^{121,154} increased oxygen permeability,¹⁵⁵ better thermoplastic and curable properties,¹⁵⁶ enhanced blend miscibility,¹⁵⁷ increased oxidation resistance,¹⁵⁵ reduced viscosity,¹⁵⁸ and improved mechanical properties.^{155,159,160}

1.8.5 The Future of POSS

What makes POSS technology so unique and advantageous lies in that it is made directly from precipitated silica instead of from petroleum.¹²¹ Ironically, POSS will become cheaper since it is a byproduct of most petrochemical refining. Another advantage is that POSS has no Volatile Organic Components (VOCs) and thereby produces no odor or air pollution. Because POSS materials are truly nanoscopic they can be used as direct replacements for hydrocarbon-based plastics or as additives in traditional plastics.¹²¹ Moreover, since these hybrid nanochemicals are also biocompatible, they push the technology into new organic areas such as soluble yet biologically inert delivery vehicles for pharmaceuticals and biocompatible prosthetics and other medical devices.^{161,162}

1.9 General Overview of this Dissertation

While numerous POSS-based nanocomposite applications are emerging, most of them are focused on materials synthesis and surprisingly very little is known about the interfacial properties of the POSS materials.¹⁶³⁻¹⁶⁵ Understanding interfacial properties is required for their future applications as nanofillers.

Looking at the structure of open-cage trisilanol-POSS in Figure 1.12B, it is very obvious that this group of silanol derivatives could possess amphiphilic character. Meanwhile most POSS derivatives are water insoluble. For these reasons it was reasonable to believe that trisilanol-POSS molecules could be spread at A/W and form stable Langmuir monolayers. Thus far, Langmuir film studies have proven to be very successful and fruitful.¹⁶⁶⁻¹⁷² Moreover, structural changes in POSS derivatives lead to dramatic changes in interfacial properties.

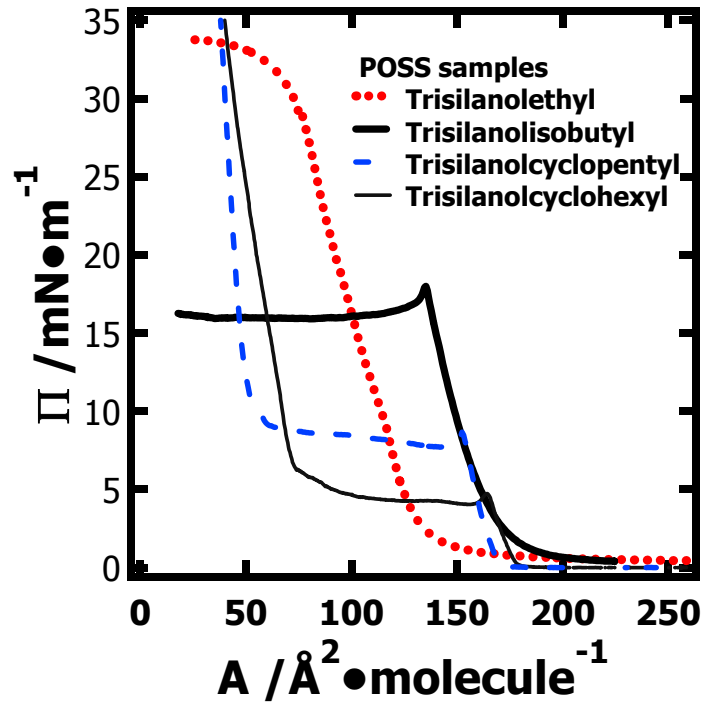


Figure 1.13: Different Π - A isotherms of some trisilanol-POSS derivatives obtained at 22.5°C by constant compression at 20 cm²•min⁻¹.

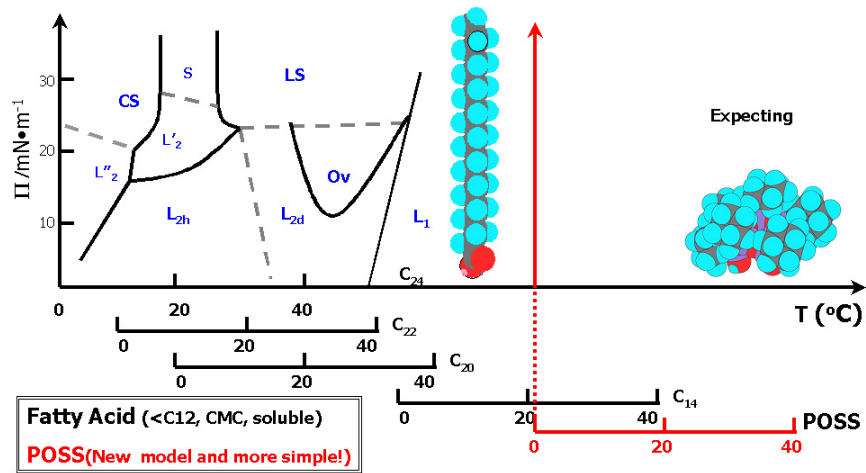


Figure 1.14: Comparison between a rod-like model for traditional fatty acid and essentially spherical POSS.

From Figure 1.13, it is noted that with the different R groups as coronae, trisilanol-POSS derivatives can have very different Π - A isotherm shapes. Furthermore, morphology results obtained from BAM revealed very interesting information that was dramatically different from traditional lipid studies at A/W. In other words, POSS represents a totally new class of Langmuir monolayer forming materials. In retrospect, it is not surprising that POSS molecules differ from a traditional Langmuir monolayer model, fatty acids (Figure 1.14). The traditional Langmuir model for fatty acids can be simplified as rod-like objects due to their large length/diameter ratio. As the length/diameter ratio decreases, the traditional amphiphiles become water-soluble (for fatty acids, C13 is the lower limit for insoluble monolayers) leading to Gibbs monolayers. Additionally, the complicated regions of the monolayer phase diagram shifts to temperatures that are experimentally inaccessible as shown in Figures 1.9 & 1.14. As a result, short chain fatty acids only exhibit a liquid-expanded monolayer phase. From POSS' topological features, with small length/diameter ratios and bulky shapes, it is not surprising that trisilanol-POSS also exhibit simple monolayer phase behavior within the experimentally accessible temperature window like short chain fatty acids. This feature arises from a lack of side chains that can form tilted phases in densely packed states. While the monolayer phases will be simple, the trisilanol-POSS Langmuir thin films exhibit rich multilayer phase transitions, which originate from its interesting dimer formation in the solid state.¹¹⁹ Dimer formation in trisilanol-POSS derivatives arises from strong intermolecular hydrogen bonding and bulky shapes. One focus of this dissertation is to understand how organic substituents on POSS derivatives affect interfacial thermodynamics, dynamics, and morphology. In Chapters 3, 4, and 8,

Chapter 1

published interfacial characterization results for two different trisilanol-POSS derivatives: trisilanolisobutyl-POSS (TiBuP) and trisilanolcyclohexyl-POSS (TCyP) will be discussed.

While trisilanol-POSS can be regarded as a novel Langmuir monolayer model, it also affords a good opportunity to study interactions between polymers and nanofillers. The other objective of this dissertation was to examine “two-dimensional” nanofiller systems by blending POSS with an amphiphilic polymer, such as poly(dimethylsiloxane) (PDMS) and poly(*t*-butyl)acrylate (PtBA). Efforts exploring trisilanol-POSS as a 2D nanofiller appear in Chapters 5 and 6, where trisilanolisobutyl-POSS was blended with PDMS and another polar PDMS derivative, PDMS-PO. For the sake of comparison, a closed-cage non-amphiphilic POSS, octaisobutyl-POSS, was blended with amphiphilic PDMS. The octaisobutyl-POSS/PDMS system required a totally new route to do the experimental data analysis. Those results are reported in Chapter 7.

In order to aid reading, each chapter (3→8) will be organized into journal article format, which has its own introduction, experimental details, results, and conclusions sections.

Chapter 9 includes overall conclusions and some unpublished, yet interesting results with suggestions for future work for trisilanolphenyl-POSS (TPP) and some fluorinated POSS-derivatives (*F*-POSS).

CHAPTER 2**Materials and Experimental Methods****2.1 Materials****2.1.1 Polyhedral Oligomeric Silsesquioxanes (POSS)**

A series of polyhedral oligomeric silsesquioxanes (POSS) obtained from Hybrid Plastics, Inc. and dried in a vacuum oven for 3 days at 40 °C were used without further purification. All POSS samples were dissolved in chloroform (0.02-0.5 mg•g⁻¹, HPLC grade). Due to slow POSS dissolution, the samples were sealed in special glass vials and sonicated (Fisher Scientific FS140H) for more than 1 hour at room temperature. Next, the solutions were allowed to dissolve for 24-36 hours at room temperature. Replicates for all the measurements discussed below were done in two or three days to guarantee reproducible results.

2.1.2 Poly(dimethylsiloxane) (PDMS) Derivatives

A non-polar “regular” PDMS sample ($M_n = 7.5 \text{ kg}\cdot\text{mol}^{-1}$, $M_w/M_n = 1.09$, Polymer Source, Inc.) was used to prepare POSS/PDMS blend spreading solutions without further purification. Spreading solutions were made by dissolving the predetermined weight ratio of pure components (POSS and PDMS) in chloroform ($\approx 0.5 \text{ mg}\cdot\text{g}^{-1}$, HPLC grade). Another polar PDMS derivative, poly(dimethyl-co-methylvinyl-co-methyl, 2-diphenyl phosphine oxide ethyl) siloxane (PDMS-PO) containing about 15 mol% of the phosphine oxide repeating unit ($M_n = 3.7 \text{ kg}\cdot\text{mol}^{-1}$ by NMR, $T_g = -48 \text{ }^\circ\text{C}$) was obtained from Prof. Judy S. Riffle’s group (Department of Chemistry, Virginia Tech) and was used as the polar silicone to prepare POSS/PDMS-PO chloroform solutions ($\approx 0.5 \text{ mg}\cdot\text{g}^{-1}$, HPLC

Chapter 2

grade) without further purification. All of the samples were allowed to dissolve for at least 24 hours prior to use.

2.2 Experimental Methods

2.2.1 Langmuir Trough and BAM Configuration

Most of the results presented in this dissertation were obtained with a standard Langmuir trough (500 cm², NIMA Technology, 601BAM) equipped with a Brewster angle microscope (MiniBAM, NanoFilm Technologie GmbH, Linear resolution (≤ 20 μm) as shown in Figure 2.1. The instruments are housed in a Plexiglas[®] box to maintain a relative humidity of 70–75 % and a dust free environment. The Plexiglas[®] box and instrument are placed on a floating optical table with black curtains on all sides to minimize stray light and mechanical vibrations (Newport RS-2000 & I-2000). The Langmuir trough is constructed of strongly hydrophobic Teflon[®] and can be cleaned by dichloromethane or chloroform without any chemical reaction or degradation. The Langmuir trough was filled with ultrapure 18.2 M Ω water (Milli-Q Gradient A-10). The barriers are made of either a hydrophilic acetal resin polymer (Delrin[®]) or hydrophobic Teflon[®] and need to be cleaned with isopropanol or dichloromethane, respectively. The barriers sweep the water surface during compression of the monolayer to vary the surface area as illustrated in Figure 2.1. The highly hydrophobic Teflon[®] trough supports an approximately 1 mm brim of water above the top of the trough edges. The anti-overflow container around the trough was used to maintain a clean environment. In the ISR measurements, a commercial Teflon[®] Langmuir trough (KSV Instruments, Helsinki, Finland) was used for all measurements. The trough dimensions were 33.0 \times 7.5 cm², and it was equipped with a quartz window (30 mm in diameter) flush with the bottom of the

trough. Two hydrophilic Delrin[®] barriers were moved symmetrically to change the surface concentration of the surfactant molecules at the interface.

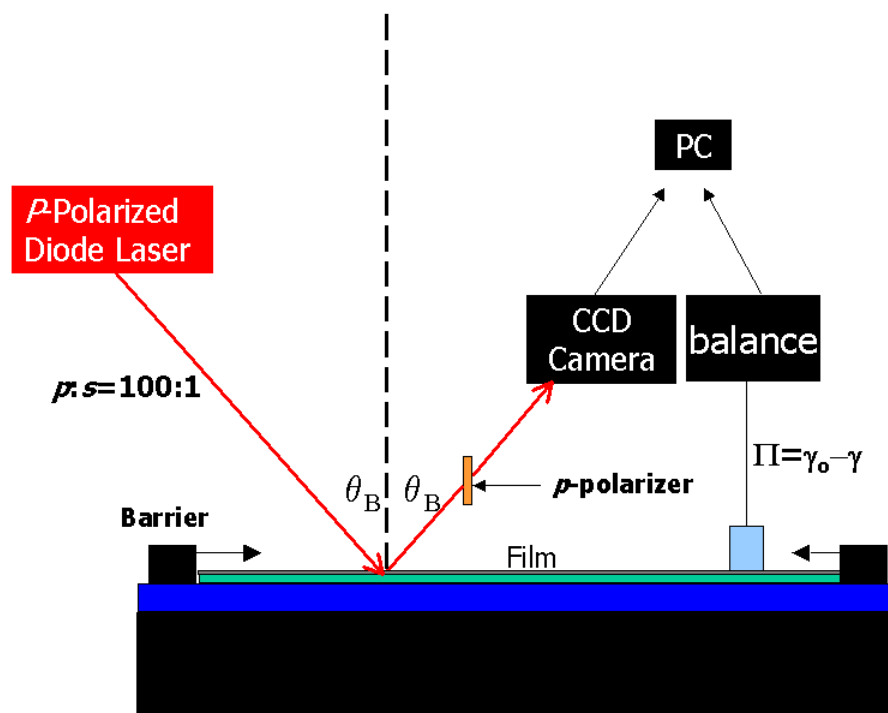


Figure 2.1: Schematic diagram of a Langmuir trough and BAM configuration.

Before spreading the monolayer, the barriers were automatically moved toward each other thereby collecting dust and surface-active contaminants into the center of the trough. Next a clean pipette connected to a vacuum pump was used to suction off surface-active contaminants. The cleaning procedure was repeated multiple times until the surface pressure at the minimum trough area was zero and no floating dust was observed by BAM monitor.

A predetermined mass of spreading solution based on solution concentration and the desired initial area per molecule was spread onto the clean surface using a micro

Chapter 2

syringe (Hamilton). A minimum of 30 min was allowed after spreading to ensure that the volatile solvent, chloroform, evaporated before all measurements.

During all isotherm measurements, the surface pressure was recorded by the Wilhelmy plate technique to $\pm 0.1 \text{ mN}\cdot\text{m}^{-1}$. A completely wetted filter paper plate or surface-roughened platinum plate was used in the Nima Mini-BAM instrument or ISR KSV trough, respectively. Trough temperature was controlled by using a circulating bath (Neslab RTE-111). Surface pressure-area per monomer (Π - A) isotherms were recorded by a computer via an interface unit (Nima IU4), which controlled the barrier positions and compression/expansion rates.

2.2.2 Constant Compression Rate Experiments

Surface pressure data can be recorded over a wide range of molecular areas using a constant compression isotherm. During this type of experiment, barriers were compressed at a specific rate as seen in Figure 2.2A when the spread molecules went through phase transitions up and beyond the collapse of the Langmuir film. This type of experiment is commonly used to determine the area a molecule occupies as the film goes through various phase transitions.

2.2.3 Compression and Expansion Isotherms: Hysteresis Loops

One important way of checking a monolayer's stability and reversibility is to perform hysteresis loop experiments. During hysteresis loop experiments, each sample was first compressed at fixed speeds to a designated trough area or surface pressure and then immediately expanded at the same barrier speed back to the initial trough area (Figure 2.2B). For stable monolayers, some hysteresis is normally observed, which is attributed either to a difference in the organization and disorganization of the molecules

or to the failure of domains formed during compression to return to their original state after decompression. For poorly stable monolayers, a continuous decrease of the lift-off area ($A_{lift-off}$) is observed in consecutive isotherms.

2.2.4 Stepwise or “Quasi-static” Compression Experiments

While experimentally similar to a compression isotherm, the stepwise or “quasi-static” isotherm allows time for pressure relaxation after compression of a Langmuir film. After compressing the barriers to a fixed surface area, the barriers were stopped, and Π was allowed to relax to a more "equilibrium" value for a specific time period (typically 5 minutes). After allowing Π to relax, the compression and relaxation process was repeated until the end of the experiment as shown in Figure 2.2C. Stepwise compression is useful for determining film stability both above and below the collapse pressure.

2.2.5 Surface Pressure Relaxation Experiments

For surface pressure relaxation experiments, each sample was first compressed at a constant speed to a specific final surface concentration. Then the barriers were held at that position and the sample was allowed to relax while the surface pressure was recorded as a function of time until a constant value was observed.

2.2.6 Isobaric Area Relaxation Experiments

To explore the 2D→3D nucleation and growth mechanisms of monolayers, the isobaric area relaxation experiments were carried out around the monolayer collapse point. Before an isobaric area relaxation experiment was started, the spread monolayer was continuously compressed at a higher rate to a point near the desired "collapse"

Chapter 2

surface pressure, and then the compression rate was decreased to a small value. Once a constant Π value was attained, the A vs. t curve was recorded as shown in Figure 2.2E.

2.2.7 Successive Addition Experiments

For successive addition experiments, the surface area was held constant (Figure 2.2F) and A was varied by making successive additions of spreading solution to the water surface. After each addition, Π was allowed to relax to a constant value ($\Delta\Pi < 0.1$ mN•m⁻¹ over a 10 minute period). Since compression Π - A isotherms are normally regarded as dynamic measurements, the results from addition experiments can reveal “equilibrium” properties of monolayers.

2.2.8 Brewster Angle Microscopy (BAM)

BAM studies (MiniBAM, NanoFilm Technologie GmbH) were carried out simultaneously during the isotherm measurements and the BAM images were taken by a charge-coupled device (CCD) camera under the "automatic gain control" mode to obtain an optical average brightness rather than absolute intensity values. While this procedure provides the greatest sensitivity for detecting morphological differences, care must be taken in comparing different images as the same feature may appear bright in one image where it has the greatest reflectivity, but grey in another image due to the presence of more strongly reflecting objects.

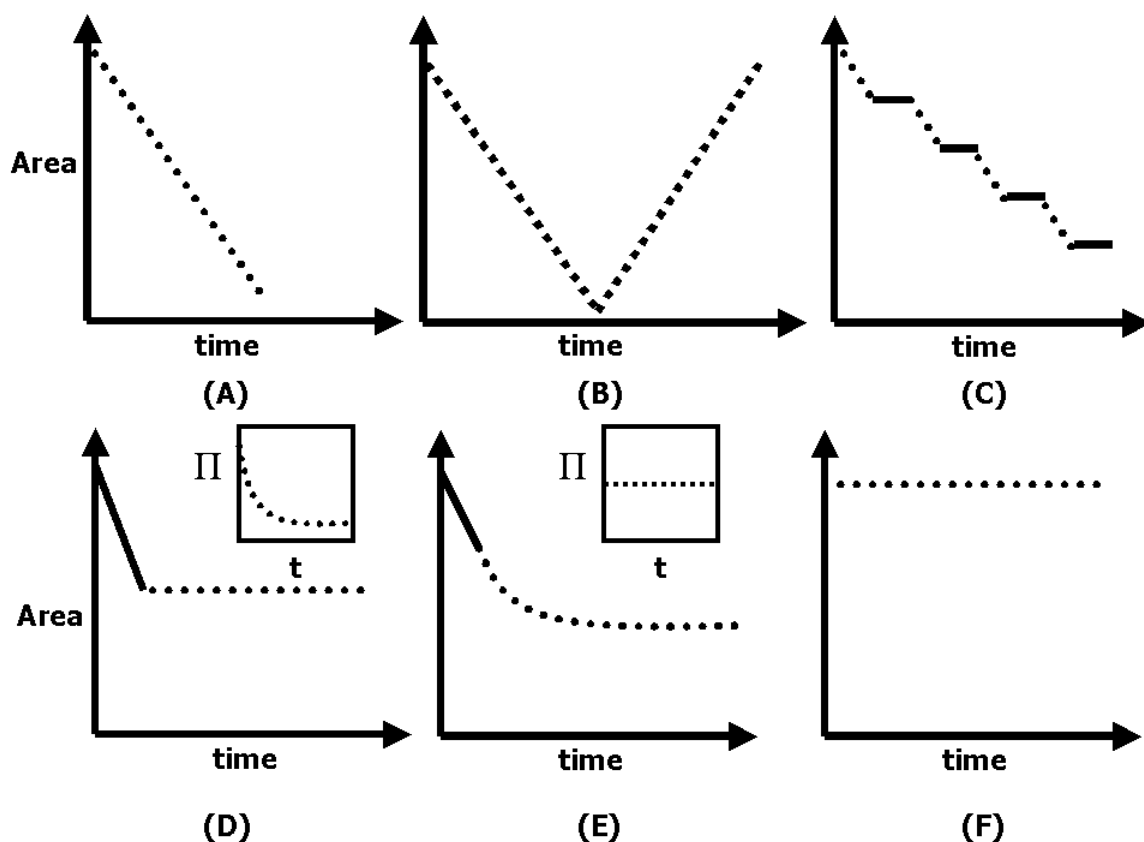


Figure 2.2: Schematic representation of the trough area changing with time in different Langmuir monolayer measurements: (A) A constant rate compression; (B) a hysteresis loop with constant compression and expansion rate; (C) a stepwise or “quasi-static” compression with fixed area decrease and stopping intervals; (D) a surface pressure relaxation experiment at a specific area; (E) an isobaric area relaxation experiment at a constant surface pressure; (F) an addition experiment with a fixed trough area and successive additions of amphiphile solution.

2.2.9 Interfacial Stress Rheometry (ISR)

An interfacial stress rheometer³⁹ developed in Prof. Gerald G. Fuller's group (Department of Chemical Engineering, Stanford University) was used to measure the dynamic interfacial shear rheology of POSS Langmuir thin films. The instrument has a simple design that is based on applying a controlled shear stress via a magnetized probe, a slender PTFE coated needle, at A/W and measuring the resulting deformation (strain). The magnetized probe undergoes oscillatory translational motion at different angular frequencies (ω) along the long axis of an applied sinusoidal magnetic field gradient generated by a pair of AC controlled Helmholtz coils. The amplitude and the phase of the needle's motion relative to the applied force are measured to determine the complex surface shear modulus (G_s^*) comprised of an elastic modulus (G_s') and a loss modulus (G_s''). In addition, a dynamic viscosity, μ_s^* , can be derived from the dynamic surface moduli to describe the general flow behavior of complex materials. Measurements in this study were performed at room temperature. Before doing the frequency sweep (0.9-10 $\text{rad}\cdot\text{s}^{-1}$), the sample is subjected to a strain scan to ensure that the measurements are made in the linear regime. The ISR measurements actually were performed at different Π values on a KSV Langmuir trough (KSV Instruments, Helsinki, Finland) using a platinum Wilhelmy plate to determine Π . For the convenience of comparing ISR and Π - A isotherm data for TCyP, the ISR data obtained at different Π values on the KSV Langmuir trough were plotted against A values based on the isotherm obtained from the Nima Langmuir trough.

CHAPTER 3**Polyhedral Oligomeric Silsesquioxanes: A New Class of Amphiphiles at the Air/Water Interface**

The following chapter appeared as a communication in the Journal of the American Chemical Society, Volume 124, No. 51, (2002) 15194-15195.

3.1 Abstract

Insoluble films of trisilanolisobutyl-POSS and octaisobutyl-POSS at A/W are investigated by means of surface pressure-area per molecule isotherm (Π - A) and Brewster angle microscopy (BAM). Analysis of the experimental results shows the partial cage molecule, trisilanolisobutyl-POSS (TiBuP), is a surface-active molecule that self-assembles into a uniform monolayer upon compression; but the fully condensed cage molecule, octaisobutyl-POSS, is non-amphiphilic.

3.2 Introduction

Over the past decade, polyhedral oligomeric silsesquioxane (POSS) molecules like those shown in Figure 3.1, have attracted considerable interest as "self-healing" high-temperature nanocomposites and space-survivable coatings,^{173,174} low- k dielectric materials,¹³⁷ and as templates for the preparation of nanostructured materials such as liquid crystalline polymers,¹⁶⁰ catalysts,^{119,175} dendrimers,¹⁷⁶ and multi-arm star polymers.¹⁷⁷ POSS molecules represent hybrid organic-inorganic materials with a core-shell structure derived from the controlled hydrolysis of trichloro- or trialkoxysilanes (T units).¹⁷⁸ Synthetic control over the hydrolysis process¹²⁷ leads to an enhancement of cage structures vs. ladder-like or branched structures seen for classical silsesquioxanes.¹⁶³

Chapter 3

The rigid inorganic core provides the strength and oxidative stability of a ceramic, while synthetic control over the organic coronae (R) provides processability and compatibility with other materials. The "self-healing" aspect of POSS-based coatings upon oxidation of the organic coronae occurs when a SiO₂ layer forms thereby preventing further oxidation of the underlying material. While surface and interfacial properties lie at the heart of many potential POSS applications, relatively little is actually known about the surface properties of POSS.¹⁶³⁻¹⁶⁵ Utilizing Brewster angle microscopy (BAM)^{34,35} on Langmuir monolayers, this study demonstrates that the partial cage trisilanolisobutyl-POSS, T₇R₇(OH)₃, forms uniform monolayers like classical surfactants,¹⁷⁹ while the fully condensed octaisobutyl-POSS cages, T₈R₈, are not amphiphilic.

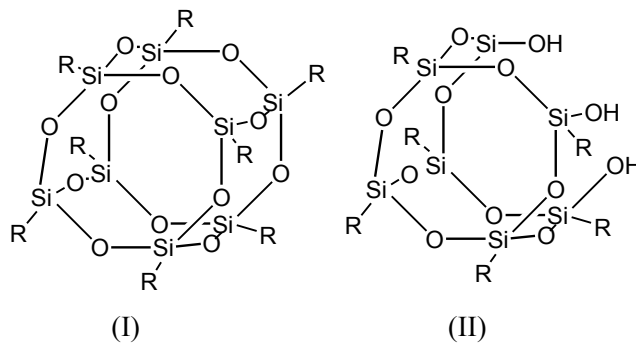


Figure 3.1: Generic structure of closed (T₈R₈) and open cage (T₇R₇(OH)₃) POSS:

(I) T₈R₈, (II) T₇R₇(OH)₃, R = isobutyl

3.3 Experimental

Trisilanolisobutyl-POSS or octaisobutyl-POSS obtained from Hybrid Plastics, Inc. and used without further purification was dissolved in chloroform ($\approx 0.5 \text{ mg}\cdot\text{mg}^{-1}$, HPLC grade) and spread onto the surface of a standard Langmuir trough (500 cm^2 ,

601BAM, Nima Technology) filled with ultra-pure 18.2 M Ω water (Millipore, Milli Q Gradient A-10) maintained at 22.5 °C in a Plexiglas™ box. The surface pressure was measured using a paper Wilhelmy plate to ± 0.1 mN•m⁻¹. Compression rates of 10 to 20 cm²•min⁻¹ were used to vary the surface concentration and BAM studies (MiniBAM, NanoFilm Technologies GmbH) were carried out simultaneously with film compression.

3.4 Results and Discussion

Figure 3.2 shows surface pressure-area per molecule (Π - A) isotherms of trisilanolisobutyl-POSS and octaisobutyl-POSS. With the 20 μ m lateral resolution of the BAM instrument, the coexistence between a liquid and gaseous film (L/G) at $\Pi = 0$ mN•m⁻¹ for trisilanolisobutyl-POSS was unable to be observed. At a surface concentration of $A = 1.95$ nm²•molecule⁻¹, the trisilanolisobutyl-POSS shows a rise in surface pressure corresponding to the formation of a homogeneous (Figure 3.3A) liquid-like monolayer (L). Further compression of the monolayer results in the non-equilibrium formation of a more condensed phase (Figure 3.3B) starting at a surface concentration of 1.35 nm²•molecule⁻¹. Based on the crystal structure for trisilanolcyclohexyl-POSS,¹¹⁹ this area per molecule is consistent with size of a POSS molecule when the three silanol groups anchor the cage to the surface and the isobutyl substituents form a halo parallel to the interface around the inorganic core. Further compression leads to aggregation of the condensed domains (Figure 3.3C). If compression is stopped and the monolayer is allowed to relax (C→D), the pressure falls to an equilibrium value of 12.3 mN•m⁻¹ after 80 min and stable ring-like structures form (Figure 3.3D).

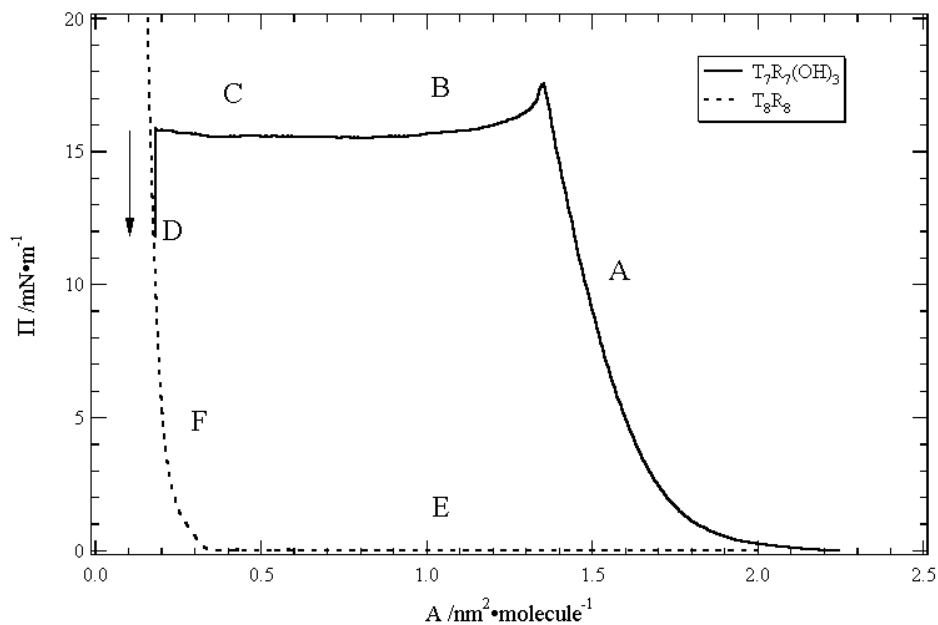


Figure 3.2: Π - A isotherms of T_8R_8 and $T_7R_7(OH)_3$, $R = \text{isobutyl}$. The arrow shows equilibrium relaxation of the surface pressure in the biphasic regime of the $T_7R_7(OH)_3$ film. The letters on the figure correspond to the BAM images in Figure 3.3.

The formation of stable ring-like structures is similar to the formation of equilibrium solid-like domains in lipid systems where the interplay of dipole density and line tension leads to the ring morphology.¹⁸⁰ For the trisilanolisobutyl-POSS systems, both the weak temperature ($\downarrow T$, $\uparrow \Pi_{\text{plateau}}$, $T = 5\text{--}35\text{ }^\circ\text{C}$, $\Delta\Pi < \approx 2\text{ mN}\cdot\text{m}^{-1}$) and compression rate ($\uparrow \text{Rate}$, $\uparrow \Pi_{\text{plateau}}$, $\text{Rate} = 10\text{--}300\text{ cm}^2\cdot\text{min}^{-1}$, $\Delta\Pi < \approx 2\text{ mN}\cdot\text{m}^{-1}$) dependencies for the plateau pressure are consistent with the formation of a solid phase that is quite possibly a collapsed three-dimensional structure as compression of the monolayer does not lead to a further increase in Π .¹⁸¹ In contrast to trisilanolisobutyl-POSS, octaisobutyl-POSS exhibits an isotherm with areas per molecule that are too small

for a physically realistic monolayer state. Figures. 3E and 3F show that the octaisobutyl-POSS film is comparably heterogeneous both at $\Pi = 0$ and $\Pi > 0$ $\text{mN}\cdot\text{m}^{-1}$ which is consistent with three-dimensional aggregates observable at all surface concentrations.

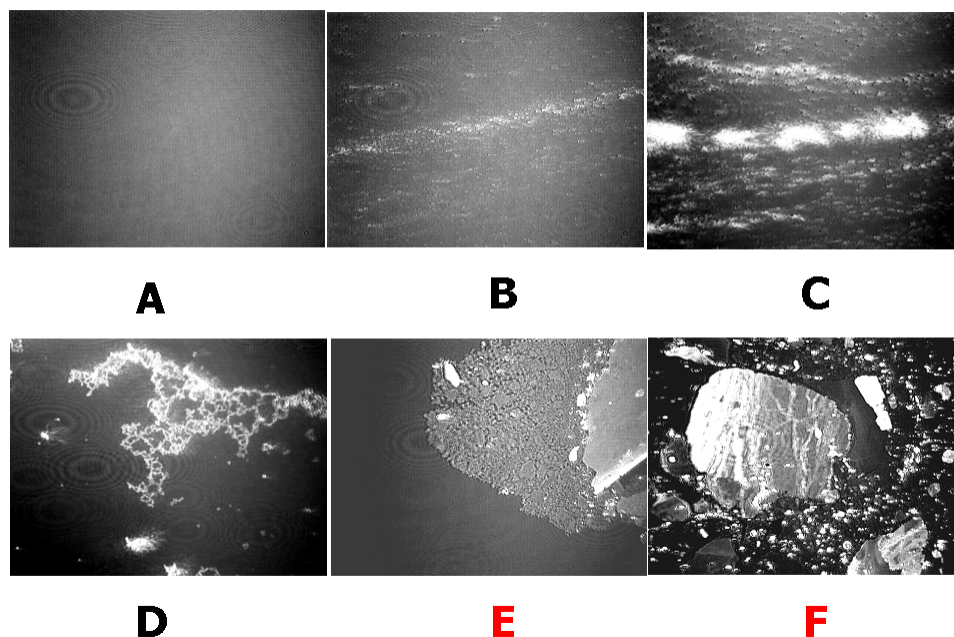


Figure 3.3: BAM images of $T_7R_7(OH)_3$: (A) uniform liquid monolayer, (B) early stages of condensed phase growth, (C) aggregation of the condensed phase domains, and (D) relaxed structure. BAM images for T_8R_8 (E) at $\Pi = 0$ and (F) $\Pi > 0$ $\text{mN}\cdot\text{m}^{-1}$. All images are 4.8×6.4 mm^2 and the letters match the points on the isotherms in Figure 3.2.

3.4 Conclusions

In conclusion, breaking open the POSS-cage converts non-amphiphilic octaisobutyl-POSS into a surface-active molecule that self-assembles into a uniform monolayer at the air/water interface upon compression. Experimental data for trisilanolisobutyl-POSS packing are consistent with expectations from the known crystal

Chapter 3

structure of another trisilanol-POSS derivative.¹¹⁹ Future work will focus on how substituent effects alter the phase behavior of these new amphiphilic materials relative to well-understood lipid systems, the surface viscoelastic properties of these materials as shown in Chapters 4 and 8, and their compatibility with polymeric materials (i.e. non-polar PDMS and polar PDMS) as nanofillers for high temperature coating applications as shown in Chapters 4 through 7.

CHAPTER 4

Isotherm and Brewster Angle Microscopy Studies of Trisilanolisobutyl-POSS at the Air/Water Interface

The following chapter appeared as an article in Langmuir, Volume 20, No. 1, (2004) 109-115.

4.1 Abstract

In Chapter 3, a trisilanol derivative of polyhedral oligomeric silsesquioxanes (POSS), trisilanolisobutyl-POSS (TiBuP), was shown to form a new class of stable Langmuir monolayers at A/W. Moreover, the trisilanolisobutyl-POSS monolayer undergoes a non-equilibrium structural transition (collapse) around a surface pressure of $\Pi \approx 18 \text{ mN}\cdot\text{m}^{-1}$. This chapter explores the mono- and multilayer properties of trisilanolisobutyl-POSS molecules at the air/water interface by the Wilhelmy plate technique and Brewster angle microscopy (BAM). Surface concentrations are controlled by four mechanisms. Results show that both increasing compression rate and decreasing temperature lead to an increase in the surface pressure of the structural transition that is consistent with the formation of solid-like multilayer domains during the collapse process. For compression at a constant rate, small domains initially form and later aggregate to form larger solid masses. Cessation of compression allows these large solid masses to relax into equilibrium ring-like structures with a lower surface pressure, $\Pi \approx 13 \text{ mN}\cdot\text{m}^{-1}$. In contrast, if the film is expanded rapidly, these large solid-like domains relax into "spaghetti" like networks with a residual surface pressure that depends upon the

Chapter 4

initial amount of the solid-like collapsed phase. Finally, successive addition and stepwise compression isotherm experiments lead to different and time-dependent morphologies. Understanding these surface properties of POSS molecules affords an excellent opportunity to design and study POSS/polymer blends for coating applications where POSS molecules with rigid inorganic cores, soft organic coronae, and dimensions comparable to polymeric monolayers can serve as perfectly monodisperse nanofillers as will be shown in Chapter 5 through 7.

4.2 Introduction

Insoluble Langmuir monolayers have attracted considerable attention as model systems for chemistry and physics in confined geometries and as precursors for creating supramolecular architectures through Langmuir-Blodgett films to study biomimetic,¹⁶⁻¹⁹ electronic,^{3,20} and optical^{22,23} processes in ultrathin films. With the advent of microscopic techniques such as fluorescence,¹⁸²⁻¹⁸⁴ Brewster angle,^{34,35} and atomic force microscopy,¹⁸⁵ and x-ray diffraction techniques,^{30,31} it has become possible to classify different phases in monomolecular Langmuir films.

Traditionally, the isotherm of fatty acids can be divided into five regions: a gaseous phase (G); a liquid expanded (LE or L₁) phase corresponding to a liquid-like state that is not observed for all fatty acids; the liquid condensed phases (LC or L₂); a 'solid' phase (S), and a collapse regime. However, recent work has shown that the phase behaviors of long-chain monolayers are more complex than the above classification implies. In addition to regions of coexistent phases,¹⁸⁶ the LC and S phases of fatty acids and molecules of similar structure show multiple phases that reflect different orientations

for closely packed side chains.^{29,78,187-189} Nonetheless, the different fatty acids show degrees of universal behavior.⁷⁹

Phase diagrams for the Langmuir films of fatty acids (C₁₄-C₂₄) at different subphase temperatures ranging from 2 to 45°C have been constructed from the analysis of Π -*A* isotherms in combination with BAM images and show very complicated phase behavior as shown in Figures 1.8 and 1.9.²⁴ The phase diagrams were superimposable with the phase transition temperatures shifted to higher values by 5–10 °C per additional methylene group.²⁴ Other amphiphilic substances, which have different head group structures compared to fatty acids such as alcohols, esters, and acetates, also form stable Langmuir monolayers if they have sufficiently hydrophobic tails with the phase diagrams of alcohols being quite similar to the fatty acids.^{73,81}

The traditional model for amphiphilic molecules, such as fatty acids, can be simplified as rod-like objects due to their large length/diameter ratio. As the length/diameter ratio decreases, the traditional amphiphiles become water-soluble (for fatty acids, C₁₂ is the lower limit) leading to Gibbs monolayers. Hence, different types of molecules are required if one wants to investigate the properties of molecules with small length/diameter ratios.

Over the past decade, polyhedral oligomeric silsesquioxane (POSS) molecules have attracted considerable interest as "self-healing" high-temperature nanocomposites and space-survivable coatings,^{173,174} low-*k* dielectric materials,¹³⁷ templates for the preparation of nanostructured materials such as liquid crystalline polymers,¹⁶⁰ catalysts,^{175,190} dendrimers,¹⁷⁶ and multi-arm star polymers.¹⁷⁷ POSS molecules, which are about 1-2 nm in size, and represent hybrid organic-inorganic materials with a core-

Chapter 4

shell structure, can be thought of as the smallest possible particles of silica.¹⁷⁸ Deng *et al.* demonstrated that the partial cage structure of trisilanolisobutyl-POSS, $T_7R_7(OH)_3$ where $R = \text{isobutyl}$, is a novel amphiphile and can form Langmuir monolayers.¹⁶⁶ In contrast, the fully condensed octaisobutyl-POSS cage, T_8R_8 where $R = \text{isobutyl}$, is not amphiphilic. From POSS' topological features, with small length/diameter ratios and barrel-like shapes, one can imagine trisilanol-POSS will have simpler phase behavior within the experimentally accessible temperature window than fatty acids. Hence, POSS molecules may afford the opportunity to study interactions between polymers and nanofillers in a "two-dimensional" Langmuir monolayer system. This study provides a detailed examination of the monolayer and collapse behavior of trisilanolisobutyl-POSS at the air/water interface. The detailed study of another trisilanol-POSS, trisilanolcyclohexyl-POSS will be discussed in the Chapter 8.

4.3 Experimental

4.3.1 Materials

Trisilanolisobutyl-POSS obtained from Hybrid Plastics, Inc. and used without further purification was dissolved in chloroform ($0.05\text{--}0.5 \text{ mg}\cdot\text{g}^{-1}$, HPLC grade). Due to slow dissolution, the samples were prepared and stored in specially sealed vials to avoid the evaporation of chloroform. Next, the solutions were allowed to dissolve for at least 24 hours at room temperature. Replicates for all the measurements discussed below were done in two or three days to guarantee reproducible results.

4.3.2 Isotherm Studies

The POSS samples were spread onto the surface of a standard Langmuir trough (500 cm², Nima Technology, Ltd., 601BAM) filled with ultra-pure 18.2 MΩ water (Millipore, Milli Q Gradient A-10) maintained at different temperatures in a Plexiglas™ box. The trough temperature was controlled by circulating water from a water bath maintained at 10.0 to 30.0 °C through the trough's base. In order to investigate the thermodynamic properties of trisilanolisobutyl-POSS, four methods were used to vary the surface area or surface concentration: 1) "compression" of the barriers at a constant rate, 2) "stepwise compression" of the barriers, 3) successive "addition" of spreading solution, and 4) "hysteresis" loops (the underlined portions indicate the short form used throughout the chapter). For compression at a constant rate, each sample was compressed at a specific rate (from 10 to 500 cm²•min⁻¹) to a final area per molecule, A , around $A \approx 30 \text{ \AA}^2 \cdot \text{molecule}^{-1}$. For stepwise compression, each sample was initially compressed at a constant rate. After compressing the barriers to a fixed surface area, the barriers were stopped, and the surface pressure, Π , was allowed to relax to a more "equilibrium" value for a specific time period (typically 10 minutes). After allowing Π to relax, the compression and relaxation process was repeated until the end of the experiment. For addition, the surface area was held constant and the surface concentration was varied by making successive additions of spreading solution. After each addition, Π was allowed to relax to a constant minimum value ($\Delta\Pi < 0.1 \text{ mN} \cdot \text{m}^{-1}$ over a 10 minute period). For most surface concentrations, the total relaxation time was on the order of 20-30 min. For hysteresis loops, each sample was compressed at a specific rate (20 cm²•min⁻¹) to a designated area per molecule value and was then immediately expanded back to the

Chapter 4

spread area per molecule (prior to compression) at the same rate. This mechanism was used to test the reversibility of the different structural stages of the film. A minimum of 15 minutes was allocated to ensure the chloroform evaporated before all the isotherm measurements were started. Surface pressure, Π , was recorded simultaneously by the Wilhelmy plate technique during all isotherm measurements. A completely wetted filter paper plate was used as the Wilhelmy plate.

4.3.3 Brewster Angle Microscopy (BAM)

BAM studies (MiniBAM, NanoFilm Technologies GmbH, linear resolution ≤ 20 μm) were carried out simultaneously during the isotherm measurements and the BAM images were taken by a CCD camera. The size of the BAM images presented in this chapter, unless specially noted, was 4.8×6.4 mm^2 . The entire configuration (Langmuir trough, BAM, and Plexiglas™ box) rests on a floating optical table to minimize vibrations.

4.4 Results and Discussion

4.4.1 Π - A Isotherms of Trisilanolisobutyl-POSS

Figure 4.1 shows surface pressure–area per molecule (Π - A) isotherms of trisilanolisobutyl-POSS obtained by three different methods. The addition isotherm is the one representing the thermodynamic "equilibrium" behavior. The stepwise compression isotherm provides an indication of the stability of the film and represents the quasi-static behavior; meanwhile the compression isotherm reveals information about the dynamic behavior of the film under an applied external force (compression). All three isotherms show nearly quantitative agreement up to a surface pressure of $\Pi \approx 2.5$ $\text{mN} \cdot \text{m}^{-1}$ or $A \approx$

$180 \text{ \AA}^2 \cdot \text{molecule}^{-1}$. For the region $A > 230 \text{ \AA}^2 \cdot \text{molecule}^{-1}$ ($\Pi \approx 0 \text{ mN} \cdot \text{m}^{-1}$), there is likely a coexistence between gas-like and liquid-like domains (G/L), prior to the formation of a true gas-like phase (G) at very large A . However, the BAM instrument used in this study has insufficient sensitivity to confirm this conclusion for this system. For the region $180 < A < 230 \text{ \AA}^2 \cdot \text{molecule}^{-1}$, the surface pressure slowly rises as a uniform expanded liquid-like monolayer (LE) forms. In this regime, hysteresis experiments (discussed later, Figure 4.10) show compression of the monolayer is almost perfectly reversible. Further compression of the monolayer, $140 < A < 180 \text{ \AA}^2 \cdot \text{molecule}^{-1}$, corresponds to the formation of a more condensed but still homogeneous liquid-like monolayer (LC).⁷⁷ In each case, the steepest part of the Π - A isotherm extrapolates to nearly identical limiting areas of $A \approx 177 \pm 4 \text{ \AA}^2 \cdot \text{molecule}^{-1}$ for each method. However, the three methods show distinct differences in this regime that reflect the viscoelastic character of the film. The slope $(\partial\Pi/\partial A)_T$ is greatest for constant compression reflecting the elastic response of the film. In contrast, addition which represents the "long-term equilibrium" state has the smallest $(\partial\Pi/\partial A)_T$ value. For stepwise compression, the data lie between these two extremes: There is an initially elastic response by the film during the compression process, followed by a slower relaxation in Π during a viscous response, whereby, the POSS molecules reorient themselves to form a stable film. Hence, the initial compression data during the "stepwise compression" experiments track the pure compression isotherm, while the relaxation data closely follow the addition data.

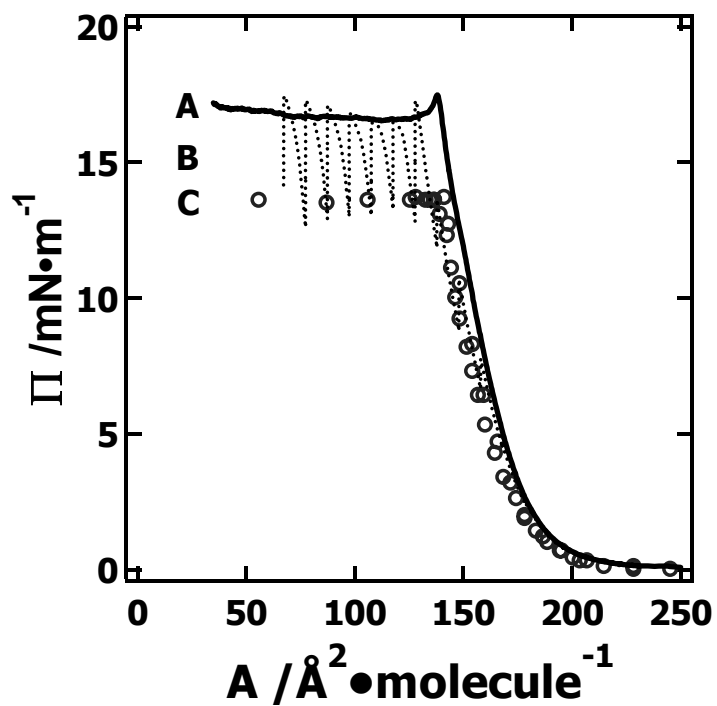


Figure 4.1: Different Π - A isotherms for TiBuP measured at $T = 22.5\text{ }^\circ\text{C}$. The letters on the figure correspond to low speed compression (A – solid line, $10\text{ cm}^2\cdot\text{min}^{-1}$), low speed stepwise compression (B – dotted line, compression rate $10\text{ cm}^2\cdot\text{min}^{-1}$, trough area increment 20 cm^2 , compression interval 300 seconds), and addition (C - circles).

As noted above, the latter region, $140 < A < 180 \text{ \AA}^2 \cdot \text{molecule}^{-1}$, where the monolayer becomes more condensed and its extrapolated cross-sectional area, $A_c \approx 177 \pm 4 \text{ \AA}^2 \cdot \text{molecule}^{-1}$, should represent the amphiphile's molecular size in a closely packed state on the water surface. In order to understand the liquid-like state, trisilanolisobutyl-POSS was modeled to generate the pictures in Figure 4.2. This modeling was done by taking the known crystal structure for another POSS derivative, trisilanolcyclohexyl-POSS,¹¹⁹ to generate the POSS cage, along with the use of CS Chem Draw Pro to substitute isobutyl groups for the cyclohexyl substituents on the cage. The correctly substituted structures were then exported to Chem Draw 3D where MM2 and MOPAC calculations in vacuum were run to minimize the energy state of the structures. Assuming preferential orientation of the hydrophilic trisilanol pocket toward the liquid surface (out of the page in Figure 4.2), it is possible to make some inferences about the two-dimensional packing of the trisilanolisobutyl-POSS. In Figure 4.2A, the dotted circle assumes the POSS behaves like a rigid inorganic core surrounded by a uniform organic corona. For this depiction, MM2 calculations yield a size of $181 \text{ \AA}^2 \cdot \text{molecule}^{-1}$, while MOPAC calculations provide a size of $172 \text{ \AA}^2 \cdot \text{molecule}^{-1}$. Both of these numbers are in excellent agreement with the experimental values summarized in Table 4.1. This agreement suggests two things. First, there is very little lateral interaction between adjacent POSS molecules, Figure 4.2B, suggesting elastic factors will dominate the monolayer's dynamics. Second, the absence of strong lateral packing or interactions mean the film should have size parameters similar to single molecule calculations. Based

on the latter assumption, the maximum possible thickness of the monolayer, Figure 4.2C, can be estimated, as can an effective film thickness, Figure 4.2D.

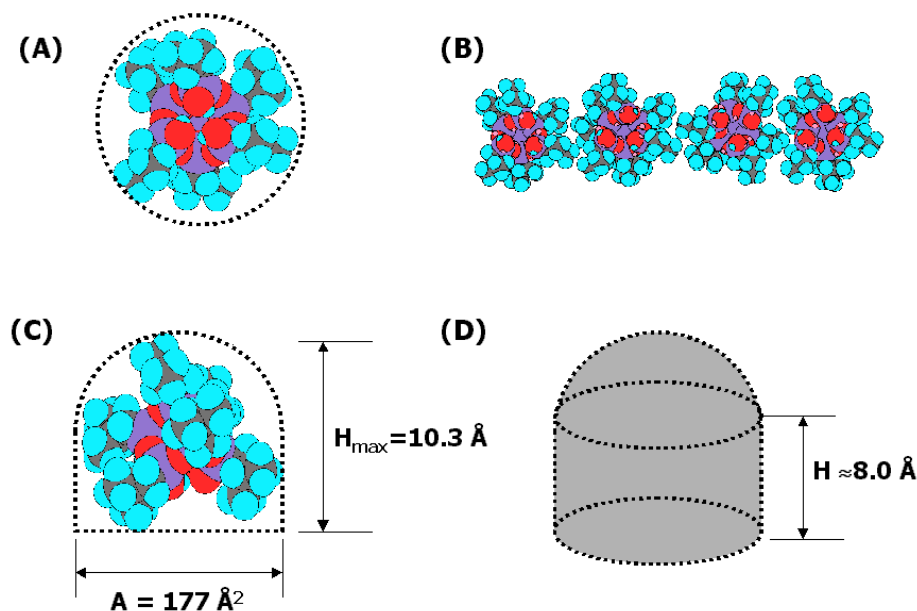


Figure 4.2: Different presentations of molecular models of TiBuP: **(A)** A space-filling model of trisilanolisobutyl-POSS based on the MM2 calculation results. Black atoms are carbon, red atoms are oxygen, purple atoms are silicon, and blue-green atoms are hydrogen. The model represents a configuration where the three silanol groups of POSS are exposed to water (out of the page). The dotted line represents an estimate of the cross-sectional area of a single POSS molecule. **(B)** Four trisilanolisobutyl-POSS molecules "packed" along a line showing the absence of strong lateral interactions. **(C)** Side view of a trisilanolisobutyl-POSS molecule showing the maximum possible thickness at A/W. **(D)** A simple "barrel-like" model of POSS. The hemisphere on top of the barrel provides a reference point for orientation.

For the barrel-like model, the ratio of the maximum height to the cross-sectional diameter (0.68) of trisilanolisobutyl-POSS is much smaller than for traditional lipids, which can be treated as rigid rods with noncircular cross sections, and have the possibility of tilted tails in condensed phases.¹⁹¹ The essential molecular degrees of

freedom for the POSS on the water surface are translation of the entire molecule, the orientation of the hydrophilic head groups (three silanols), and the orientation of the hydrophobic tails (isobutyl groups). With relatively few possible degrees of freedom while anchored to the water surface, the physical picture and the phase behavior for the trisilanolisobutyl-POSS monolayer is fairly clear and simple.

Table 4.1: Experimental and calculated size parameters for TiBuP.

	Diameter (Å)	Cross-Sectional Area (Å ²)	Maximum Height (Å)	Barrel Height (Å)
Addition ^a	N/D	176±2	N/D	N/D
Compression ^a	N/D	179±2	N/D	N/D
MM2 ^b	15.2	181	10.4	8.0
MOPAC ^b	14.8	172	10.2	8.0

N/D = Not Determinable;

(a) experimental value; (b) calculated values from ChemDraw 3D.

Returning to the discussion of the isotherms, the next significant feature is the cusp in the compression isotherm at $A \approx 135 \text{ Å}^2 \cdot \text{molecule}^{-1}$. As this surface concentration is too high to correspond to any reasonable conformation of a single POSS molecule, this non-equilibrium transition corresponds to the collapse of the film into a multilayer structure. The existence of the cusp could represent a yield point between plastic deformation (monolayer compression) and flow (buckling of the monolayer with subsequent transport of the POSS into an upper layer) given the similarity in the isotherm compared with other studies in the literature.³⁸ This feature is absent in the addition isotherm where the material added to the surface can directly enter the upper layers of a multilayer structure. Hence, the key distinction between the compression and addition

methods is the way the multilayer forms. During compression, there is a time-dependent process for the departure of molecules in the rigid monolayer (elastic response) at A/W into an upper multilayer phase, while during addition; only the long-term behavior (viscous response) is observed as the added material directly enters the upper layers. For $A < \approx 135 \text{ \AA}^2 \cdot \text{molecule}^{-1}$, long plateaus are observed by both the compression and addition methods. However, the Π values for the two plateaus are different. The plateau pressure by compression is $\Pi \approx 16 \text{ mN} \cdot \text{m}^{-1}$, while the value for the addition method is $\Pi \approx 13.6 \text{ mN} \cdot \text{m}^{-1}$. The higher pressure for compression reflects the non-equilibrium situation, whereby stepwise compression shows rapid "equilibration" of the surface pressure to the limiting value observed by addition. This feature is consistent with the instability of the compressed film at very high surface concentrations.

4.4.2 Morphology of TiBuP Films by BAM

Figure 4.3 shows BAM images for compression at low speeds ($10 \text{ cm}^2 \cdot \text{min}^{-1}$). As noted above, the BAM instrument used in this study is unable to detect the coexistence of gaseous (G) and "liquid-like" (L) monolayer at $\Pi \approx 0 \text{ mN} \cdot \text{m}^{-1}$ or $A > 230 \text{ \AA}^2 \cdot \text{molecule}^{-1}$. For $180 < A < 230 \text{ \AA}^2 \cdot \text{molecule}^{-1}$, the film appears to be homogeneous and likely corresponds to a liquid-expanded (LE) phase according to the nomenclature outlined in the introduction. For the region $\approx 135 < A < 180 \text{ \AA}^2 \cdot \text{molecule}^{-1}$, the change in slope $(\partial\Pi/\partial A)_T$ suggests the existence of a more condensed liquid-like monolayer as the molecules are packed more tightly together. In this regime, BAM images are still homogeneous, Figure 4.3A. Upon film collapse, $A < \approx 135 \text{ \AA}^2 \cdot \text{molecule}^{-1}$, bright domains of collapsed film start to appear on the background of a tightly packed monolayer, Figure 4.3B. With compression deeper into the collapsed regime, more bright domains start to

form and these domains tend to aggregate into larger structures. The tendency of the multilayer regions of the film to aggregate may be indicative of POSS dimer formation. The crystal structures of trisilanol-POSS derivatives show the unit cell consists of a dimer where the silanol groups form a hydrogen bonded ring.¹¹⁹ Similar aggregation is expected for POSS molecules located in the hydrophobic environment found on top of the underlying POSS monolayer in the collapsed regime. For addition experiments, the BAM images are similar to those seen in Figure 4.3.

4.4.3 Schematic Depiction of the Phase Behavior in a Trisilanolisobutyl-POSS Compression Isotherm

Utilizing the simplified geometry for POSS molecules, Figure 4.2D, a speculative mechanism for film formation of trisilanolisobutyl-POSS at A/W is proposed in Figure 4.4. At first, $180 < A < 230 \text{ \AA}^2 \cdot \text{molecule}^{-1}$, POSS forms a liquid-expanded (LE or L_1) monolayer, Figure 4.4A, where the molecules can move freely around the surface. Upon further compression, $140 < A < 180 \text{ \AA}^2 \cdot \text{molecule}^{-1}$, the molecules are brought into close contact and form a more condensed, strongly elastic, liquid-like monolayer, Figure 4.4B, with dilational deformation of the organic coronae. Around $A \approx 135 \text{ \AA}^2 \cdot \text{molecule}^{-1}$, Figure 4.4C, the strength of the interaction between the hydrophilic silanol groups and the water surface is insufficient to prevent buckling of the monolayer with increasing lateral pressure, resulting in collapse of the film. As noted above, the overshoot in Π is caused by a lag between the viscous response (monolayer collapse) and the rapid elastic stimuli (compression). Based on crystallographic data for a structurally similar POSS derivative, trisilanolcyclohexyl-POSS,¹¹⁹ trisilanolisobutyl-POSS is expected to dimerize in the upper layer whereby hydrogen bonding at the interior of the dimer leads to a

Chapter 4

species completely encapsulated by a hydrophobic shell ($70 < A < 135 \text{ \AA}^2 \cdot \text{molecule}^{-1}$, Figure 4.4D and 4.4E). Multilayer formation, Figure 4.4F, is expected to occur through a similar mechanism as the film is compressed to smaller areas per molecule, $A < 70 \text{ \AA}^2 \cdot \text{molecule}^{-1}$.

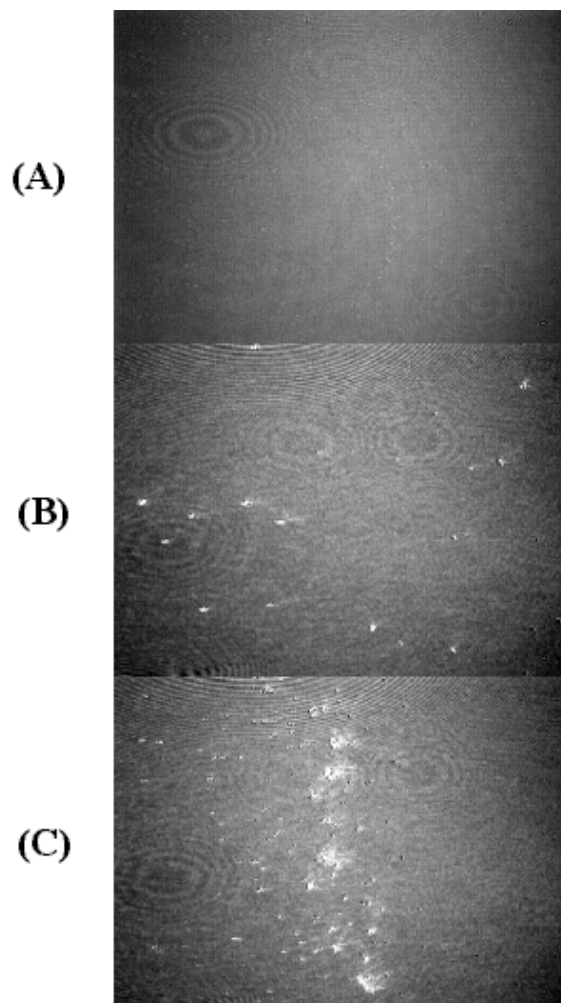


Figure 4.3: Compression BAM images obtained at different A at $10 \text{ cm}^2 \cdot \text{min}^{-1}$: (A) $A = 155 \text{ \AA}^2 \cdot \text{molecule}^{-1}$, (B) $A = 110 \text{ \AA}^2 \cdot \text{molecule}^{-1}$, and (C) $A = 50 \text{ \AA}^2 \cdot \text{molecule}^{-1}$. All images are $4.8 \times 6.4 \text{ mm}^2$.

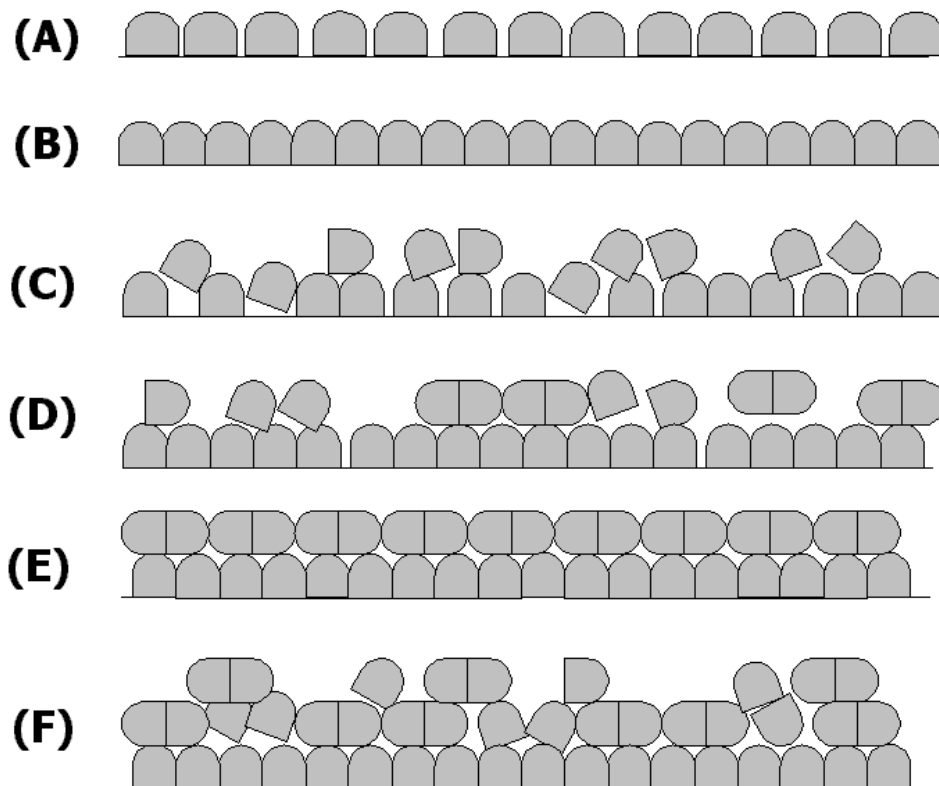


Figure 4.4: Proposed organization of TiBuP films at A/W: **(A)** a liquid-expanded monolayer ($180 < A < 230 \text{ \AA}^2 \cdot \text{molecule}^{-1}$), **(B)** a more condensed densely packed liquid-like monolayer ($\approx 135 < A < 180 \text{ \AA}^2 \cdot \text{molecule}^{-1}$), **(C)** a collapsing monolayer in the region of the "cusp" in the isotherm, **(D)** and **(E)** formation of a bilayer in the collapsing film where the upper layer is comprised of POSS dimers ($70 < A < \approx 135 \text{ \AA}^2 \cdot \text{molecule}^{-1}$), and **(F)** multilayer formation ($A < 70 \text{ \AA}^2 \cdot \text{molecule}^{-1}$).

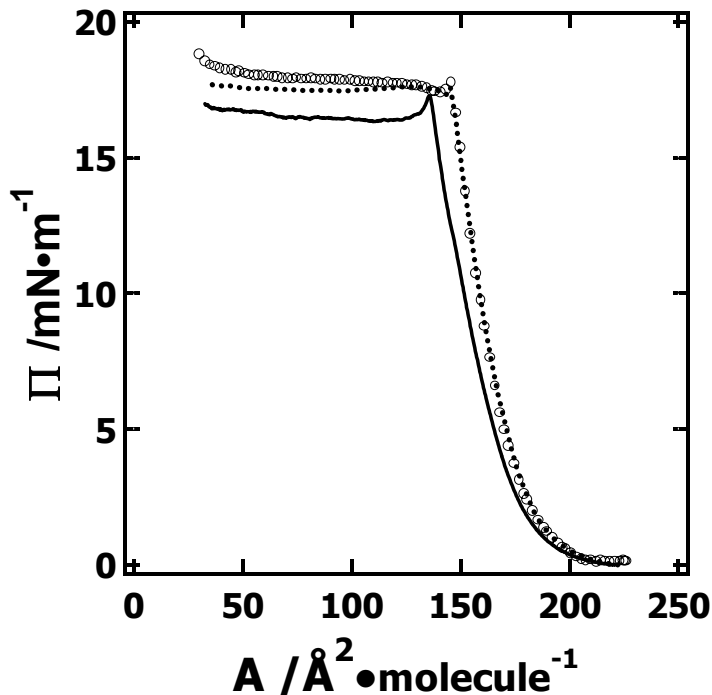


Figure 4.5: The effect of compression rate on isotherms of TiBuP at $T = 22.5$ °C. The compression rates are $10 \text{ cm}^2 \cdot \text{min}^{-1}$ (solid line), $100 \text{ cm}^2 \cdot \text{min}^{-1}$ (dotted line), and $500 \text{ cm}^2 \cdot \text{min}^{-1}$ (circles).

4.4.4 Viscoelastic Effects on Trisilanolisobutyl-POSS Films at A/W

As mentioned above, the cusp in the isotherm observed at the onset of collapse for the trisilanolisobutyl-POSS monolayer is similar to the feature observed with a third-generation poly(benzyl ether) monodendron functionalized at the local point with a single di(ethylene glycol) tail, [G-3]-di(EG), by Kampf *et al.*¹⁹² The presence of the cusp in the POSS isotherm is consistent with a film having an initially strong elastic response that is lagged by a weaker viscous response. Looking at just the maximum static elasticity, $\epsilon_{s,\text{max}} = -A \cdot (\partial \Pi / \partial A)_T \approx 100 \text{ mN} \cdot \text{m}^{-1}$ at $A \approx 150 \text{ \AA}^2 \cdot \text{molecule}^{-1}$ and the shape of the isotherm, trisilanolisobutyl-POSS monolayers may have viscoelastic properties similar to

rigid calixarene monolayers at intermediate pH values.^{193,194} For p-dioctadecanoylcalix[4]arene, the viscoelastic properties of the monolayer state determined by surface light scattering correspond to a film with an infinite lateral modulus. To test this assumption about the viscoelastic behavior and the collapse mechanism, the effects of temperature, compression rate, and reversibility are considered.

Figure 4.5 shows the effect of compression rate on trisilanolisobutyl-POSS monolayers. Three significant features are seen when the compression rate increases: First, the slope of the isotherm in the monolayer state, $(\partial\Pi/\partial A)_T$, increases. Second, the size of the bump that makes up the cusp and signifies the onset of the collapsed regime gets smaller. Finally, the value of the plateau pressure in the collapsed regime ($A < 135 \text{ \AA}^2 \cdot \text{molecule}^{-1}$) increases with compression rate. These features are all consistent with a rigid monolayer having slow structural relaxation processes. In essence, compression of the film occurs at a faster rate than collapse. As a result, there are higher transient surface concentrations and higher surface pressures than one would observe at smaller compression rates, or in the stepwise compression or addition experiments. Another interesting aspect of increased compression rates manifests itself in the morphology of the collapsing film.

Figure 4.6 shows BAM images at $A \approx 70 \text{ \AA}^2 \cdot \text{molecule}^{-1}$ formed at different compression rates (50, 100, and 560 $\text{cm}^2 \cdot \text{min}^{-1}$). At $70 \text{ \AA}^2 \cdot \text{molecule}^{-1}$, the appearance of bright domains was attributed to the formation of a multilayer structure where the POSS molecules are densely packed and may exist as dimers in the upper phase. At the lowest compression rate in Figure 4.6 (A, 50 $\text{cm}^2 \cdot \text{min}^{-1}$), a slightly greater number of aggregates form than at the compression rate of 10 $\text{cm}^2 \cdot \text{min}^{-1}$ shown in Figure 4.2, and some of them

Chapter 4

exhibit an irregular shape. At the higher compression rates, 100 and 560 $\text{cm}^2\cdot\text{min}^{-1}$, rod-like aggregates form, Figure 4.6B and 4.6C, respectively. The heightened order in the rod-like domains would be consistent with the packing of dimeric POSS units along a preferred directional axis. The heightened anisotropy and greater surface fraction of condensed multilayer phase (bright domains) is consistent with the elevated Π value for the collapse transition accompanying a greater compression rate. For these experiments, symmetric compression is used (the two barriers compress from the top and bottom of each picture). As seen in the pictures, the small aspect ratio of the rods do not lead to preferential orientation of the rods with the weak shear gradient induced by compression. Another interesting phenomenon associated with the rod-like aggregation is a difference in the stability of the rod-like structures after the cessation of compression. At the highest compression rate, 560 $\text{cm}^2\cdot\text{min}^{-1}$, and hence the largest applied lateral pressure, the rod-like structures are very stable and maintain an elongated shape for more than 60 minutes. In contrast, the aggregation seen during compression at 100 $\text{cm}^2\cdot\text{min}^{-1}$ is less stable and breaks up into smaller aggregates in less than 30 minutes. Hence, the higher applied lateral pressure appears to produce more robust aggregates with stronger intermolecular interaction and longer lifetimes. At this point, it is necessary to note that the rod-like aggregates are similar but far less extensive and regular than rod-like aggregates for trisilanolcyclohexyl-POSS (TCyP) presented in Chapter 8.

Time-temperature superposition in viscoelastic systems means that changes in process rates can be related to changes in temperature. Hence, cooling down the system in Figure 4.5, should have the same effect as increasing the compression rate, while raising the temperature should be the same effect as slowing down the compression rate.

Figure 4.7 shows Π - A isotherms of trisilanolisobutyl-POSS as a function of temperature at a constant compression rate of $20 \text{ cm}^2 \cdot \text{min}^{-1}$. As expected from Figure 4.5, there is a small increase in the slope, $(\partial\Pi/\partial A)_T$, as a slightly more condensed monolayer forms with decreasing temperature. Similarly, the trends for the collapse behavior also track those expected from Figure 4.5, i.e., the value of the plateau pressure increases with decreasing temperature, whereas the size of the cusp increases with increasing temperature reflecting a quicker relaxation of compressed molecules into a collapsed multilayer. In contrast to the BAM images in Figure 4.6, rod-like aggregates do not form from the low compression rate used within the experimentally accessible temperature window of this study. In all other aspects, except for a slight increase in the surface fraction of multilayer aggregates at lower temperatures, the surface morphology of the collapsed region is consistent with the images seen in Figure 4.3.

4.4.5 Surface Pressure and Morphological Stability and Reversibility of Trisilanolisobutyl-POSS Films at A/W

As noted previously in the discussion of Figure 4.1 for the stepwise compression experiments, Π starts to show signs of instability upon the cessation of compression for $\Pi > 3 \text{ mN} \cdot \text{m}^{-1}$. Within the monolayer state, $\approx 140 < A < 230 \text{ \AA}^2 \cdot \text{molecule}^{-1}$, both the time ($< 5 \text{ min}$) and magnitude ($< \approx 2 \text{ mN} \cdot \text{m}^{-1}$) for Π relaxation once compression is stopped is small. In the collapsed regime, the magnitude of the relaxation in Π is greater. Three examples of this process are shown in Figure 4.8. For the curves in Figure 4.8 (main graph), there is an initially rapid drop in the surface pressure as expected from the stepwise compression experiments. Moreover, the data show, at least for trisilanolisobutyl-POSS, the ten-minute equilibration time used in the stepwise

Chapter 4

compression experiments is a good estimate for the long-term "equilibrium" state as most of the relaxation in Π occurs quickly. After roughly 2-3 hours, complete relaxation occurs and the pressure reaches a stable value that depends on the final area of the compressed film.

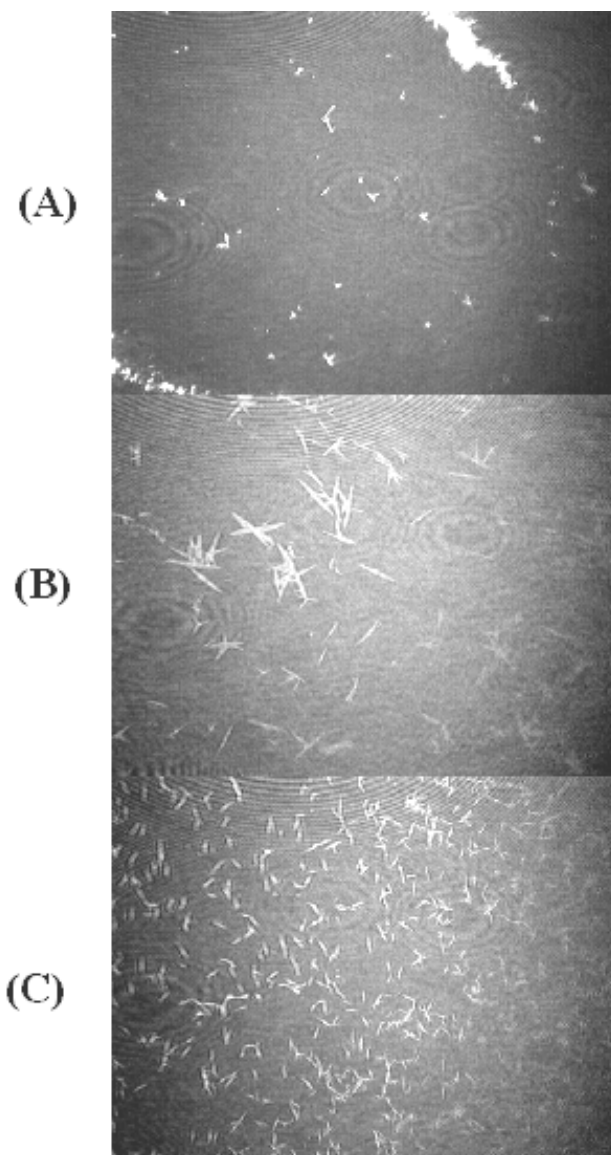


Figure 4.6: BAM images acquired at $A \approx 70 \text{ \AA}^2 \cdot \text{molecule}^{-1}$ and $T = 22.5 \text{ }^\circ\text{C}$ for different compression rates: (A) $50 \text{ cm}^2 \cdot \text{min}^{-1}$, (B) $100 \text{ cm}^2 \cdot \text{min}^{-1}$, and (C) $560 \text{ cm}^2 \cdot \text{min}^{-1}$. All micrographs are $4.8 \times 6.4 \text{ mm}^2$ and the film is symmetrically compressed from the top and bottom of each image.

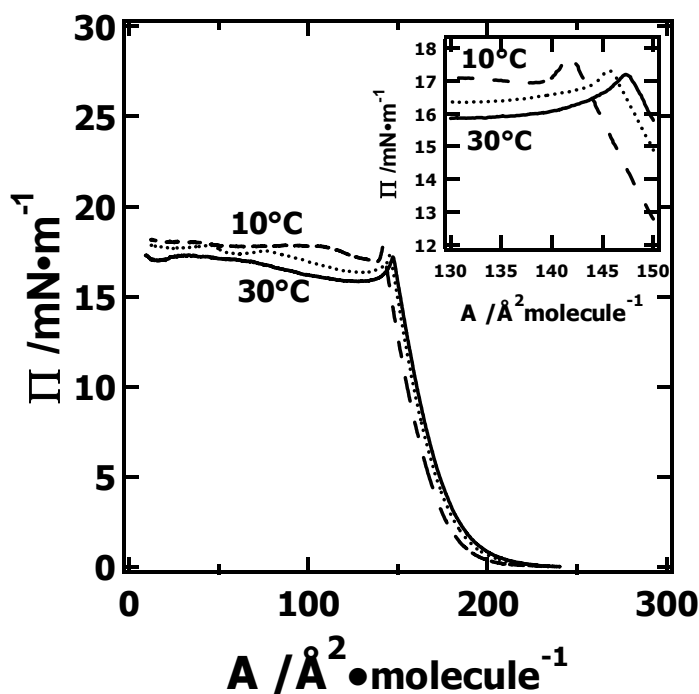


Figure 4.7: Compression Π - A isotherms collected as a function of temperature at a constant compression rate of $20 \text{ cm}^2 \cdot \text{min}^{-1}$. The temperatures correspond to $10.0 \text{ }^\circ\text{C}$ (dashed line), $22.5 \text{ }^\circ\text{C}$ (dotted line), and $30.0 \text{ }^\circ\text{C}$ (solid line). The inset Π - A graph is provided to clarify the differences around the cusp in the isotherm for the three temperatures studied.

During the relaxation process, there is also a change in the morphology of the film. Figure 4.9 shows BAM images for the relaxation process. Aggregation of the multilayer domains (bright patches) leads to ring formation. The resulting morphology is similar to the types of structures seen in the L/G coexistent phases of silicone derivatives¹⁹⁵ and lipid systems.¹⁸⁰ The origin of the ring-like morphologies has been attributed to the interplay between line tension and repulsive dipole-dipole interactions.¹⁸⁰

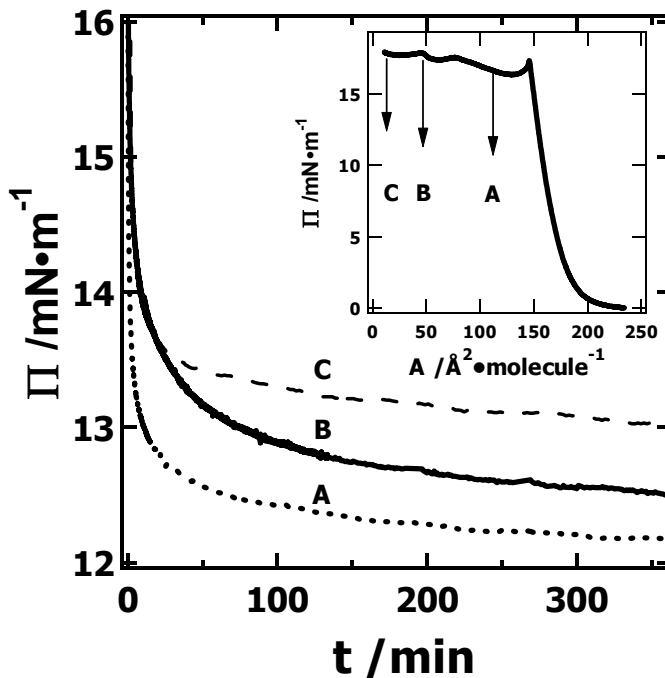


Figure 4.8: Π vs. time (t) curves for three different TiBuP films compressed to different surface concentrations: (A) $80 \text{ \AA}^2 \cdot \text{molecule}^{-1}$, (B) $40 \text{ \AA}^2 \cdot \text{molecule}^{-1}$, and (C) $10 \text{ \AA}^2 \cdot \text{molecule}^{-1}$ at a rate of $20 \text{ cm}^2 \cdot \text{min}^{-1}$ and a temperature of $T = 22.5 \text{ }^\circ\text{C}$. The inset Π - A graph is provided to clarify both the surface concentrations where compression was stopped, and the magnitude of the relaxation in Π (arrows).

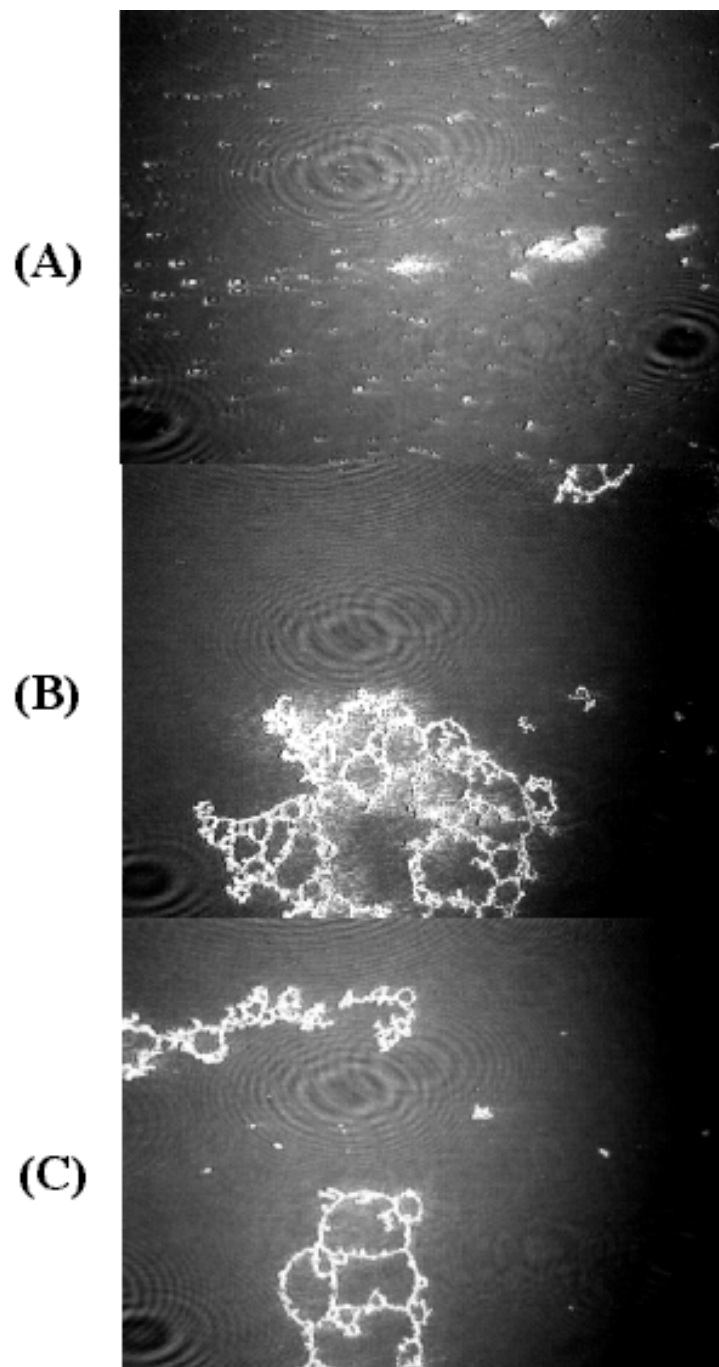


Figure 4.9: Relaxed BAM images obtained at $T = 22.5\text{ }^{\circ}\text{C}$ after compression at $20\text{ cm}^2\cdot\text{min}^{-1}$ to an area of $40\text{ \AA}^2\cdot\text{molecule}^{-1}$: (A) 3.5 min relaxation, (B) 90 min relaxation, and (C) 300 min relaxation. All BAM images are $4.8 \times 6.4\text{ mm}^2$.

As alluded to in the discussion of Figure 4.1, hysteresis experiments are also important for understanding film stability at A/W. Figure 4.10 shows the hysteresis behavior for three different monolayers. One film was compressed to a maximum surface pressure of $\Pi = 4 \text{ mN}\cdot\text{m}^{-1}$ (the imperceptible dashed line in Figure 4.10), and is essentially completely reversible upon expansion of the film. The second monolayer was compressed to a maximum surface pressure of $\Pi = 8 \text{ mN}\cdot\text{m}^{-1}$, the dotted line in Figure 4.10. Expansion of the film from $\Pi = 8 \text{ mN}\cdot\text{m}^{-1}$ reveals some hysteresis that is comparable in magnitude to monolaurin.¹⁹⁶ The final curve in Figure 4.10 shows a hysteresis curve for compression deep into the collapsed regime ($A_{\text{minimum}} = 25 \text{ \AA}^2\cdot\text{molecule}^{-1}$). For this case, there is a large hysteresis loop. The result is expected as POSS aggregates formed upon compression do not completely re-spread as the trough surface area is expanded. In fact, even after complete expansion of the film ($\Pi = 0 \text{ mN}\cdot\text{m}^{-1}$), the aggregates do not completely re-spread even after waiting for several hours. This failure to completely re-spread can be observed by making multiple hysteresis experiments with the same monolayer. For multiple hysteresis loops, the onset of the monolayer state ($\Pi > 0 \text{ mN}\cdot\text{m}^{-1}$) continually shifts to smaller and smaller areas per molecule each time the film is compressed and expanded. This result is consistent with small (smaller than the resolution of our BAM), strongly interacting aggregates, possibly comprised of dimers that remain after expansion of the film. Similar results have been observed for poly (L-glutamic acid) by Reda *et al.*⁷⁴

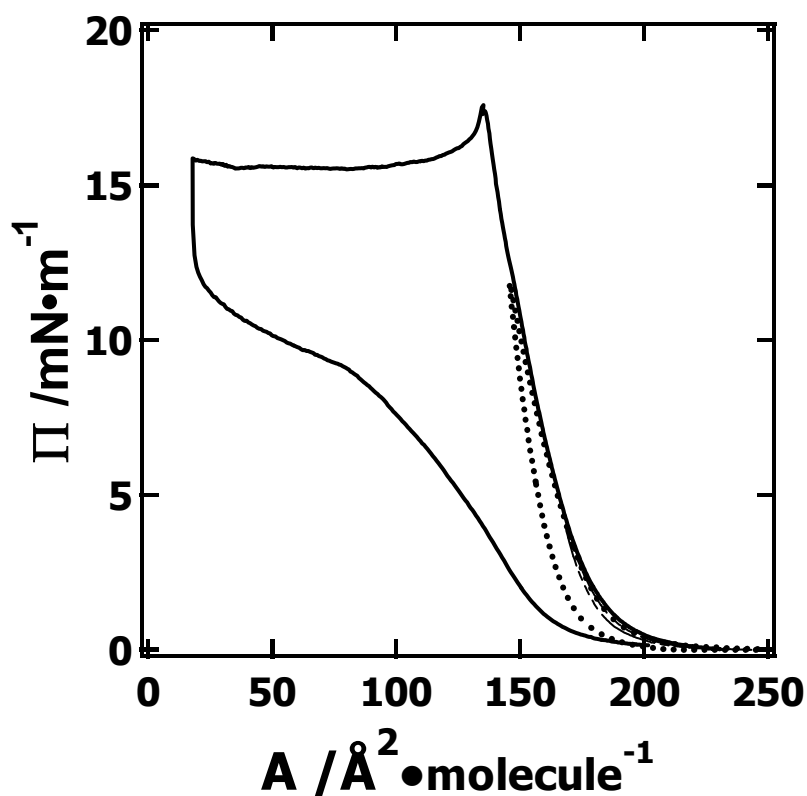


Figure 4.10: Π - A isotherms obtained at $T = 22.5$ °C showing hysteresis behavior for compression and expansion at $20 \text{ cm}^2 \cdot \text{min}^{-1}$. The data correspond to maximum compression to $\Pi = 4 \text{ mN} \cdot \text{m}^{-1}$ (imperceptible dashed line), $\Pi = 8 \text{ mN} \cdot \text{m}^{-1}$ (dotted line), and $A = 25 \text{ \AA}^2 \cdot \text{molecule}^{-1}$ (solid line).

For a more detailed explanation of the shape of the hysteresis isotherm obtained upon compression into the collapsed regime it is helpful to also examine the BAM results. In Figure 4.11, a compression-expansion curve similar to the one in Figure 4.10 is provided along with BAM images at selected points upon the curve. The points A \rightarrow

Chapter 4

D are similar to those features already discussed in Figure 4.3. Upon initial expansion, there is a rapid drop in Π , much like the relaxation experiments (Figures 4.8 and 4.9), leading to the formation of a network-like structure from the dense POSS aggregates, Figure 4.11D. This morphology is similar to the ring-like structures that form in the relaxation experiments, and both the size and density of the network-like domains depend on the degree of aggregation seen at Point D. After this precipitous drop in Π , there is a small plateau that forms. This plateau has a surface pressure that is similar to the "equilibrium" collapse pressure observed in the addition and relaxation experiments, and must reflect some re-spreading for POSS aggregates back to a monolayer state as the barriers are expanded. During this stage, Figure 4.11F and 4.11G, the networks break-up into branched aggregates. Beyond point G in Figure 4.11, Π drops back to zero and the BAM resolvable domains disappear. As noted above, some small domains must remain with very long lifetimes as multiple hysteresis experiments with the same monolayer show a sequential march of the monolayer regime to smaller A values.

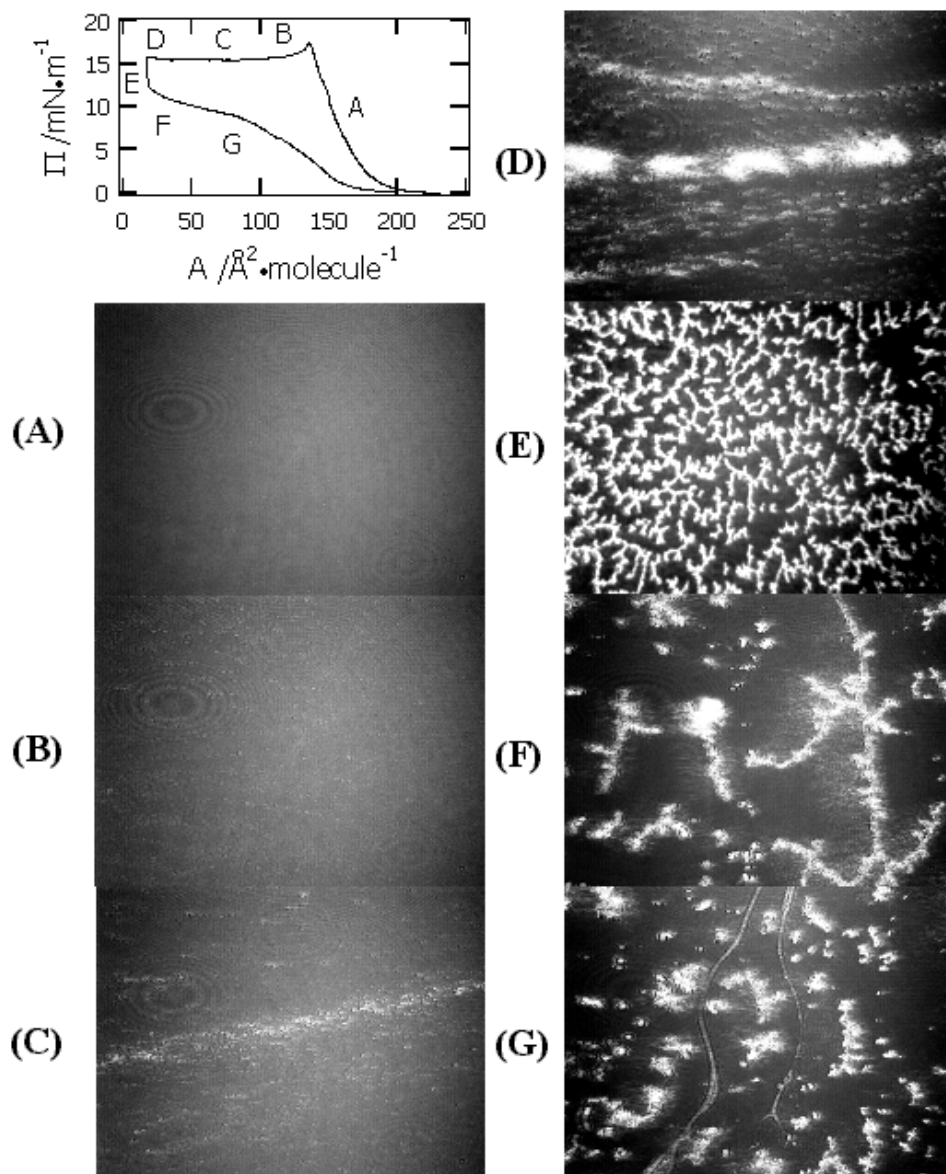


Figure 4.11: BAM images obtained for a compression/expansion loop at $20 \text{ cm}^2 \cdot \text{min}^{-1}$ for $T = 22.5 \text{ }^\circ\text{C}$. The letters on the isotherm correspond to the $4.8 \times 6.4 \text{ mm}^2$ BAM images.

4.5 Conclusion

Trisilanolisobutyl-POSS forms stable Langmuir monolayers at the air/water interface. For $\Pi < \approx 3 \text{ mN}\cdot\text{m}^{-1}$, completely reversible compression isotherms are consistent with a liquid-expanded monolayer. At higher surface pressures, $\Pi > 3 \text{ mN}\cdot\text{m}^{-1}$, the films are more densely packed but still exhibit liquid-like properties prior to collapse. This simple monolayer phase behavior for the "barrel-like" POSS molecules is consistent with expectations from more conventional Langmuir monolayer forming amphiphiles (Figure 1.14). From this point of view, POSS molecules should be excellent model compounds for studying the effects of nanofillers in "2D" confined geometries (Chapters 5 through 7). Moreover, trisilanolisobutyl-POSS exhibits interesting non-equilibrium morphologies during collapse that are similar to morphologies seen in biphasic lipid systems, even though the barrel-like structure inhibits phase transitions within the monolayer state.

CHAPTER 5

Blends of Amphiphilic PDMS and Trisilanolisobutyl-POSS

at the Air/Water Interface

The following chapter appeared as an article in *Macromolecules*, Volume 37, No. 13, (2002) 4900-4908.

5.1 Abstract

In Chapters 3 and 4, trisilanol-POSS derivatives were identified as a new class of Langmuir monolayer forming materials. In order to further explore POSS' nanofiller features and their compatibility with polymeric materials, blends of amphiphilic poly(dimethylsiloxane) (PDMS) and trisilanolisobutyl-POSS with different weight ratio are the subject of this chapter by means of Π - A isotherm and BAM studies. The results show that the PDMS/ trisilanolisobutyl-POSS can form homogeneous monolayers at the air/water interface. At high POSS content (> 80 wt%), a thermodynamic analysis of surface pressure-area per monomer (Π - A) isotherm data suggests possible phase separation prior to collapse of the PDMS component. PDMS-bilayer formation that normally occurs around $\Pi \approx 8 \text{ mN}\cdot\text{m}^{-1}$ shifts to higher surface pressures with increasing trisilanolisobutyl-POSS content indicating compatibility between the two materials in the monolayer state that is analogous to a positive deviation binary liquid mixture. Further compression leads to the collapse of the POSS component into multilayer domains around $\Pi \approx 17.5 \text{ mN}\cdot\text{m}^{-1}$. Brewster angle microscopy shows the amount of PDMS in the blend alters the aggregation state of the non-equilibrium solid-like trisilanolisobutyl-

POSS domains. These results provide insight into POSS aggregation mechanisms that may be present in thicker films and bulk systems.

5.2 Introduction

Over the past decade, polyhedral oligomeric silsesquioxane (POSS) molecules have attracted considerable attention. With rigid inorganic cores and flexible organic coronae of nanometer dimensions,^{127,178} POSS molecules have been used for hybrid organic-inorganic nanocomposites,^{159,197} space-survivable coatings^{173,174} and synthetic templates for nanostructured materials.^{148,160,198-201} The polyhedral silicon-oxygen nanostructured skeleton, from which the name is derived, consists of intermittent siloxanes of the general formula $(\text{SiO}_{3/2})_n$,^{125,154,202,203} which was first reported in 1946.²⁰⁴ By incorporating POSS into polymeric species, improved physical properties such as low- k dielectric constants,^{137,152,156} high glass transition temperatures (T_g),^{130,205} high thermal stability,^{153,206,207} high oxidation resistance,^{173,174} photoresists,²⁰⁸ and unique crystalline materials^{209,210} can be obtained.

POSS molecules, representing hybrid organic-inorganic materials with a core-shell structure, can be thought of as the smallest possible particles of silica.^{127,178} While the interfacial properties are important for future applications of POSS, relatively little is actually known about the surface properties of POSS systems.¹⁶³⁻¹⁶⁵ Recently, Deng *et al.* showed that the partial cage structure of trisilanolisobutyl-POSS, $T_7R_7(\text{OH})_3$ where R = isobutyl, can form stable Langmuir monolayers.^{166,169} In view of POSS' physical structure, with small length/diameter ratios and barrel-like shapes, one can imagine trisilanol-POSS molecules will have simpler monolayer phase behavior than fatty acids

Chapter 5

(Figure 1.14). Hence, POSS molecules may afford the opportunity to study interactions between polymers and nanofillers in a "two-dimensional" Langmuir monolayer system.

This chapter focuses on the compatibility of two amphiphiles, trisilanolisobutyl-POSS and poly(dimethylsiloxane) (PDMS),²¹¹ as blended films at the air/water interface (A/W) by monitoring their interactions with the Wilhelmy plate technique and Brewster angle microscopy (BAM). PDMS was first reported to have surface active properties in 1947.²¹¹ Since then, studies have been performed to show the formation of monolayer and multilayer films at A/W.^{195,212,213} In this study the entire composition range, 0-100 weight percent PDMS, is examined as blends with trisilanolisobutyl-POSS. This study provides a detailed examination of the monolayer and collapse behavior of mixtures of trisilanolisobutyl-POSS with PDMS at A/W.

5.3 Experimental

5.3.1 Materials

Trisilanolisobutyl-POSS (HybridPlastics, Inc.) and PDMS ($M_n = 7.5 \text{ kg}\cdot\text{mol}^{-1}$, $M_w/M_n = 1.09$, Polymer Source, Inc.) were used without further purification. Spreading solutions were made by dissolving the pure components or blends in chloroform ($\approx 0.5 \text{ mg}\cdot\text{g}^{-1}$, HPLC grade). The samples were allowed to dissolve for more than 24 hours.

5.3.2 Isotherm Studies

The blend was spread onto the surface of a standard Langmuir trough (500 cm^2 , Nima Technology, 601BAM) filled with ultra-pure $18.2 \text{ M}\Omega$ water (Millipore, Milli Q Gradient A-10) maintained at $22.5 \text{ }^\circ\text{C}$ in a PlexiglasTM box with a relative humidity of 70 ~ 75%. In order to investigate the thermodynamic properties of the trisilanolisobutyl-

POSS/PDMS mixtures, four methods were used to vary the surface area or surface concentration: (1) "compression" of the barriers at a constant rate, (2) successive "addition" of spreading solution, (3) "hysteresis" loops, and 4) "relaxation" (the portions in quotation marks indicate the short form used throughout the manuscript). For compression at a constant rate, each sample was compressed at $20 \text{ cm}^2 \cdot \text{min}^{-1}$. For hysteresis, each sample was compressed at a speed of $20 \text{ cm}^2 \cdot \text{min}^{-1}$ to a designated average area per monomer value, $\langle A \rangle$, and were immediately expanded at the same speed to a final trough area of 480 cm^2 . This method was used to test the reversibility of the different structural stages of the film. For successive addition, the surface area was held constant and the surface concentration was varied by making successive additions of spreading solution. After each addition, Π was allowed to relax to a constant minimum value ($\Delta\Pi < 0.1 \text{ mN} \cdot \text{m}^{-1}$ over a 10 minute period) after evaporation of the spreading solvent. For low surface pressures, the total relaxation time including solvent evaporation was on the order of 20-30 min, while times on the order of an hour were necessary in the collapsed regime. For relaxation experiments, each sample was compressed at a speed of $20 \text{ cm}^2 \cdot \text{min}^{-1}$ to a final compressed area per POSS molecule, $A_{\text{POSS}} \approx 60 \text{ \AA}^2 \cdot \text{monomer}^{-1}$. The barriers were held at that position and the sample was allowed to relax. The surface pressure was recorded as a function of time until a constant value was observed. For all four methods, a minimum of 15 minutes was allocated after spreading to ensure the chloroform evaporated before all the isotherm measurements were started. Surface pressure, Π , was recorded by the Wilhelmy plate technique during all isotherm measurements. A completely wetted filter paper plate was used as the Wilhelmy plate.

5.3.3 Brewster Angle Microscopy (BAM)

BAM studies (MiniBAM, NanoFilm Technologie GmbH, linear resolution better than or equal to 20 μm) were carried out simultaneously during the isotherm measurements and the BAM images were taken by a CCD camera. The BAM images presented in this chapter are $4.8 \times 6.4 \text{ mm}^2$ unless specifically noted. The entire configuration (Langmuir trough, BAM, and Plexiglas box) rests on a floating optical table to minimize vibrations.

5.4 Results and Discussion

5.4.1 Compression Isotherm Studies of the Pure Components

Figure 5.1 shows a plot of surface pressure, Π , as a function of average area per monomer, $\langle A \rangle$, for different mixtures of PDMS and POSS. At dilute surface concentrations, $\langle A \rangle > 20 \text{ \AA}^2 \cdot \text{monomer}^{-1}$, PDMS is known to form a liquid/gas (L/G) biphasic film.¹⁹⁵ In this regime, all of the Si and O atoms are able to adsorb to the subphase with the hydrophobic methyl substituents oriented into the air reflecting the amphiphilic nature of PDMS. A liquid-like monolayer forms ($14 < \langle A \rangle < 18 \text{ \AA}^2 \cdot \text{monomer}^{-1}$) upon film compression to $\langle A \rangle$ values less than the cross-sectional (limiting) area of a PDMS repeat unit ($\approx 18 \text{ \AA}^2 \cdot \text{monomer}^{-1}$). As Π increases in the monolayer regime, repeating units begin to pull out of the interface and collapse begins (first plateau, $9 < \langle A \rangle < 14 \text{ \AA}^2 \cdot \text{monomer}^{-1}$). At $\langle A \rangle \approx 8 \text{ \AA}^2 \cdot \text{monomer}^{-1}$, there is a smaller rise in Π followed by a second plateau ($\langle A \rangle < 6 \text{ \AA}^2 \cdot \text{monomer}^{-1}$). These transitions were originally described²¹¹ in terms of helix formation; however, more recent studies suggest these are actually multilayer transitions where a "dry" PDMS layer

spreads on top of a hydrated PDMS layer.²¹² As it is not possible for the techniques used in this study to distinguish between the two cases, subsequent discussion will favor the multilayer model.

POSS also exhibits an interesting isotherm.^{166,169} At low surface concentrations ($\langle A \rangle > 220 \text{ \AA}^2 \cdot \text{molecule}^{-1}$, not shown in Figure 5.1), $\Pi \approx 0 \text{ mN} \cdot \text{m}^{-1}$ and the film likely exists in a biphasic L/G coexistent regime³⁵ with increasing compression ($180 < \langle A \rangle < 220 \text{ \AA}^2 \cdot \text{molecule}^{-1}$) the POSS forms a liquid-like monolayer which shows no hysteresis during compression-expansion cycles.³⁵ Further compression in this regime leads to the formation of a less-compressible liquid-like monolayer ($150 < \langle A \rangle < 180 \text{ \AA}^2 \cdot \text{molecule}^{-1}$), where extrapolation back to $\Pi = 0 \text{ mN} \cdot \text{m}^{-1}$ yields a limiting area of $A_o = 175 \text{ \AA}^2 \cdot \text{molecule}^{-1}$ which is in excellent agreement with the known size of a different trisilanol-POSS derivative, trisilanolcyclohexyl-POSS, and molecular modeling of trisilanolisobutyl-POSS.⁴⁰ In this regime, the film only exhibits slight hysteresis during compression-expansion cycles. As the film is compressed further, there is another change in slope ($135 < \langle A \rangle < 150 \text{ \AA}^2 \cdot \text{molecule}^{-1}$). In this regime, the film exists in a truly non-equilibrium state leading to the "cusp" in the isotherm at $\Pi \approx 17.5 \text{ mN} \cdot \text{m}^{-1}$ ($\langle A \rangle \approx 135 \text{ \AA}^2 \cdot \text{molecule}^{-1}$) signifying collapse of the film into multilayer domains. Addition and step-wise compression experiments both show that surface pressure values relax to $\Pi \approx 12.5 \text{ mN} \cdot \text{m}^{-1}$. Moreover, for $\Pi > 17.5 \text{ mN} \cdot \text{m}^{-1}$ the rapid formation of a more condensed phase causes a slight drop in Π until the barriers "catch-up", because the multilayer phase that forms has a smaller area per molecule than in the monolayer state.

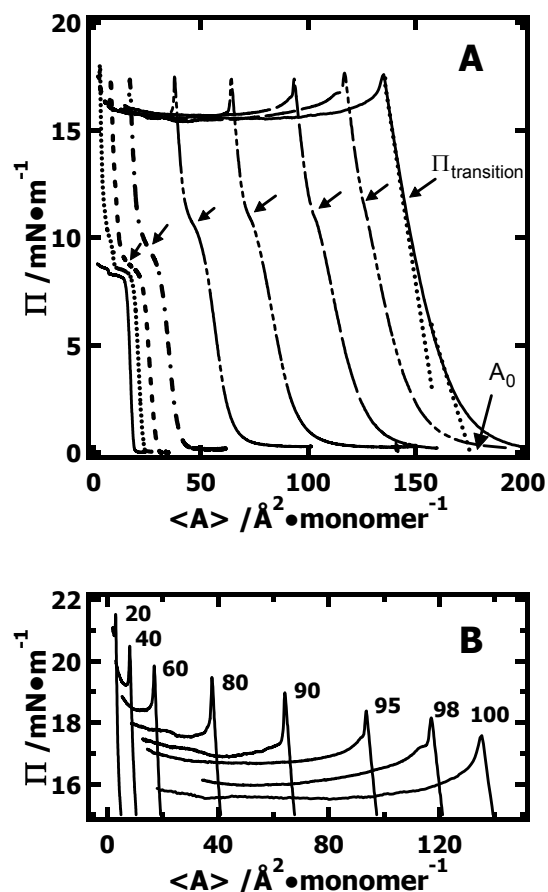


Figure 5.1: Π - $\langle A \rangle$ compression isotherms for TiBuP blends with PDMS: **(A)** Π - $\langle A \rangle$ compression isotherms for trisilanolisobutyl-POSS blends with PDMS. Temperature was constant at 22.5 °C and a compression rate of 20 $\text{cm}^2 \cdot \text{min}^{-1}$ was used. The amount of POSS (wt%) is 0, 20, 40, 60, 80, 90, 95, and 100 from left to right, respectively. The arrows indicate the composition dependent transition surface pressure, $\Pi_{\text{transition}}$, for PDMS multilayer formation. The linear dotted lines are used to show the extrapolation to the cross-sectional area, $A_0 = 175 \text{ \AA}^2 \cdot \text{monomer}^{-1}$, at low Π and the start of the "non-equilibrium" regime at higher Π for the pure trisilanolisobutyl-POSS isotherm. **(B)** The isotherms in Figure 5.1A have been re-plotted whereby each isotherm is off-set from the previous isotherm by an additional $+0.5 \text{ mN}\cdot\text{m}^{-1}$ ($+3.5 \text{ mN}\cdot\text{m}^{-1}$ total off-set for the 20 wt% POSS film from the unaltered 100 wt% POSS film) with decreasing POSS content to highlight the plateau region.

5.4.2 Compression Isotherm Studies of the Blends

Each isotherm, excluding the pure components (left-most curve = PDMS, right-most curve = POSS) represents a mixture with increasing weight percent POSS going from left to right on Figure 5.1. Qualitatively, the mixtures show behavior between the extremes of PDMS and POSS. For $0 < \Pi < 8 \text{ mN}\cdot\text{m}^{-1}$, a liquid-like monolayer is formed for all compositions. In the region $8 < \Pi < 13 \text{ mN}\cdot\text{m}^{-1}$, there is a composition dependent collapse transition, $\Pi_{\text{transition}}$. This transition corresponds to PDMS multilayer formation. Above $\Pi \approx 13 \text{ mN}\cdot\text{m}^{-1}$, all blend isotherms exhibit POSS-like behavior and show an essentially composition independent cusp around $\Pi \approx 17.5 \text{ mN}\cdot\text{m}^{-1}$. The later transition corresponds to the formation of POSS-rich multilayer domains. After the cusp, the mixed isotherms show a long "plateau" as more POSS converts into multilayer domains. These features and their significance are discussed in more detail below.

5.4.3 The Monolayer Regime

Thermodynamic analyses of the isotherms can help understand the mixing behavior at a molecular level. For $\Pi < 8 \text{ mN}\cdot\text{m}^{-1}$, the appropriate expression for ideal mixing is given as:

$$\langle A_{\text{mix,ideal}}(\Pi) \rangle = X_{\text{POSS}} A_{\text{POSS}}(\Pi) + X_{\text{PDMS}} A_{\text{PDMS}}(\Pi) \quad [5.1]$$

where $A_{\text{POSS}}(\Pi)$ and $A_{\text{PDMS}}(\Pi)$ are the values of A at a given Π value for the pure component monolayers and X_{PDMS} and X_{POSS} are the mole fractions. Hence in 2-D, the analogous property to the volume change upon mixing in 3-D, can be defined as:

$$\Delta A_{\text{mix}}(\Pi) = \langle A(\Pi) \rangle - \langle A_{\text{mix,ideal}}(\Pi) \rangle \quad [5.2]$$

Chapter 5

Figure 5.2A shows a plot of $\langle A(\Pi) \rangle$ vs. the mole fraction of POSS in the blend films. Figure 5.2A shows representative data for two different Π values (2 & 7 $\text{mN}\cdot\text{m}^{-1}$) while comparable data for 5 $\text{mN}\cdot\text{m}^{-1}$ was omitted for clarity. Surface pressure values below $\Pi = 8 \text{ mN}\cdot\text{m}^{-1}$ were chosen to avoid pressure induced collapse of the PDMS component. Qualitatively, the data show positive deviation from ideal mixing ($\langle A_{mix,ideal}(\Pi) \rangle$, the dotted lines on the figure). As positive deviation from ideal mixing indicates unfavorable enthalpic interactions, it is also useful to consider the molar Gibbs excess free energy of mixing, ΔG_{excess} , which can also be calculated from the Π - A isotherms of the pure and mixed films:^{1,214}

$$\Delta G_{excess} = \int_0^{\Pi} \Delta A_{mix}(\Pi) d\Pi \quad [5.3]$$

The ΔG_{excess} values for binary mixtures as a function of POSS mole fraction and surface pressure are shown in Figure 5.2B for $\Pi = 2, 5,$ and $7 \text{ mN}\cdot\text{m}^{-1}$. For all the compositions studied, these curves were concave downward, giving positive ΔG_{excess} values, in agreement with unfavorable interactions in binary monolayers.²¹⁴ These values become more positive with increasing surface pressure, indicating that the repulsion between the two components are stronger at larger Π . However, the near-zero values of ΔG_{excess} observed for mixtures containing less than 80 wt% ($\approx 27 \text{ mol}\%$) POSS, are consistent with uniphase mixtures.²¹⁴ In contrast, mixtures containing larger amounts of POSS ($> 80 \text{ wt}\%$, $> 27 \text{ mol}\%$) have large positive ΔG_{excess} values that may be consistent with phase separation.

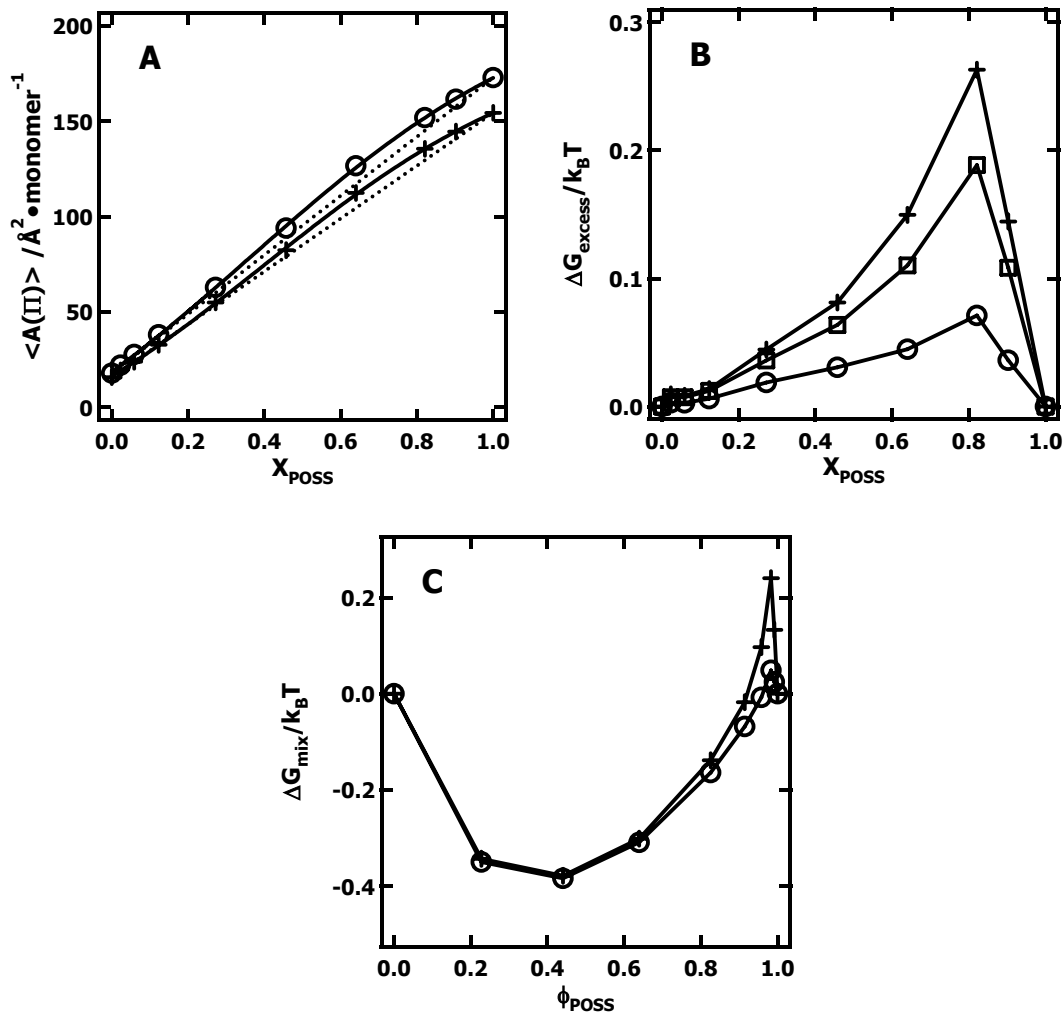


Figure 5.2: $\langle A(\Pi) \rangle$, ΔG_{excess} and ΔG_{mix} as a function of X_{POSS} , or ϕ_{POSS} : (A) Mean surface areas per repeating unit, (B) excess Gibbs free energies of mixing, and (C) estimated Gibbs free energies of mixing calculated from the isotherms at $\Pi = 2$ (\circ), 5 (\square), and $7 \text{ mN}\cdot\text{m}^{-1}$ ($+$) plotted as a function of the POSS mole fraction, X_{POSS} , or volume fraction, ϕ_{POSS} , on a monomer basis. Solid lines are guides for eyes and the dotted lines correspond to the values for ideal mixing. The $\Pi = 5 \text{ mN}\cdot\text{m}^{-1}$ data were omitted from Figure 5.2A and 5.2C for clarity.

Chapter 5

By assuming that the ideal entropy of mixing can be described by Flory-Huggins-type behavior, the Gibbs free energy of mixing, ΔG_{mix} , can be estimated as:

$$\begin{aligned}\Delta G_{mix}(\Pi) &= \Delta G_{excess}(\Pi) + \Delta G_{ideal}(\Pi) \\ &= \Delta G_{excess}(\Pi) + (\phi_{POSS} \ln \phi_{POSS} + \frac{\phi_{PDMS}}{n} \ln \phi_{PDMS})\end{aligned}\quad [5.4]$$

where, ϕ_i is the volume fraction of component i , and n is the number of segments in a polymer chain based on the size of a solvent molecule (here $n = 101/8$).⁴³ These data are shown in Figure 5.2C for $\Pi = 2$ and $7 \text{ mN}\cdot\text{m}^{-1}$ ($5 \text{ mN}\cdot\text{m}^{-1}$ data have been omitted for clarity) indicating that POSS/PDMS phase separation may occur just prior to the collapse transition of the film in POSS/PDMS mixtures containing more than 80 wt% POSS. However, no direct microscopic evidence was seen for this by BAM during compression suggesting POSS and PDMS rich regions may have comparable thicknesses and refractive indices in this regime.

5.4.4 PDMS Collapse

The fact that the films show characteristics of both PDMS and POSS behavior requires a different treatment of the data for $\Pi > 8 \text{ mN}\cdot\text{m}^{-1}$. PDMS undergoes a transition from a monolayer to a multilayer film around $\Pi \approx 8 \text{ mN}\cdot\text{m}^{-1}$.²¹³ Whether this transition occurs through elaborate conformational changes as suggested by Fox *et al.*²¹¹ or a simple spreading of "dry" PDMS on the top of the hydrated PDMS layer^{212,213} is beyond the scope of this chapter as both mechanisms would lead to a film that is roughly two monomer units thick. In this study, the PDMS monolayer \rightarrow multilayer transition manifests itself as a shoulder (shown as arrows in Figure 5.1) in the mixtures. This transition occurs at higher surface pressures in mixtures with increasing trisilanolisobutyl-POSS content. When the pressure is less than $\Pi_{\text{transition}}$, the films are

monolayers and show average characteristics of PDMS and POSS. There is a positive deviation from ideal behavior over the entire composition range (Figure 5.2), ultimately similar with the partial pressure change of two dissimilar liquids.²⁶ The blend films at the water surface below $\Pi_{\text{transition}}$ are thought to be stable monolayers with both components staying at A/W, until the PDMS component is squeezed out of the interface due to a weaker water affinity than the POSS molecules – which is confirmed from the BAM studies and will be discussed later.

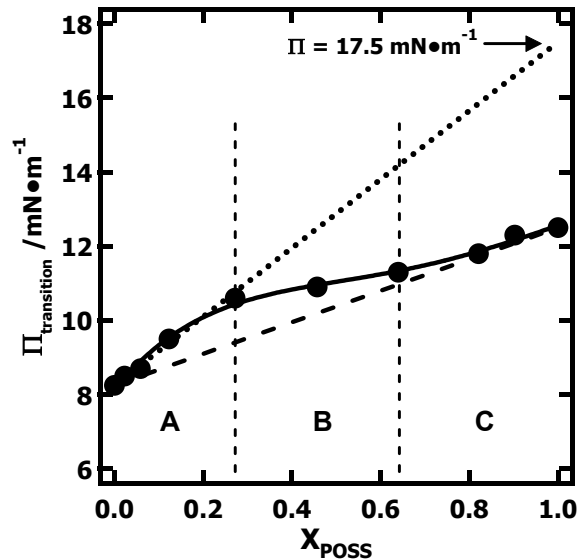


Figure 5.3: $\Pi_{\text{transition}}$ for PDMS multilayer formation as a function of the mole fraction of POSS on a per monomer basis. Filled circles (●) represent experimental data from Figure 5.1, the solid line is provided to highlight the trend, the bold dotted line represents ideal dilute solution behavior (Henry's law), and the dashed line connecting the "equilibrium" transition pressure of the pure components provides ideal solution behavior (Raoult's law). The vertical dashed lines are used to highlight the three distinct regimes (A, B, and C).

Above the shoulder in Figure 5.1, $\Pi_{\text{transition}}$ indicated by arrows, a different analysis is utilized. Figure 5.3 shows $\Pi_{\text{transition}}$ as a function of the mole fraction of POSS, X_{POSS} , calculated on a per monomer basis. The plot in Figure 5.3 can be thought of as a surface analog to a vapor pressure diagram for an ideal-dilute binary mixture of volatile liquids, where the equilibrium collapse pressures of PDMS and POSS represent the vapor pressures of the pure components and the bold dashed line corresponds to the prediction of Raoult's law.²¹⁵ In Figure 5.3, there are three distinct regimes. In region A, ideal-dilute solution behavior is observed with positive deviation from Raoult's law. The dotted line on Figure 5.3 provides the surface analog of a Henry's law regime. By extrapolating the initial slope to pure POSS, one observes a value of $\Pi \approx 17.5 \text{ mN}\cdot\text{m}^{-1}$, or the dynamic collapse value of trisilanolisobutyl-POSS. Hence, one observes a non-ideal enhancement of the pressure dependent stability of PDMS monolayers at low POSS loadings. In region B of Figure 5.3, deviations from Henry's law behavior are observed. By region C on Figure 5.3, Raoult's law behavior is observed with an extrapolation to $\Pi \approx 12.5 \text{ mN}\cdot\text{m}^{-1}$ for pure POSS. This value agrees amazingly well with the "thermodynamically" stable collapse value for trisilanolisobutyl-POSS. Both the transition region, B, and the Raoult's law regime, C, are consistent with unfavorable interactions that may lead to phase separation. Therefore, a suitable interpretation may be that the presence of low viscosity PDMS plasticizes the trisilanolisobutyl-POSS, thereby enhancing the rate at which it collapses leading to a noticeable kink in the isotherm. Hence, region C should be characterized as the preferential collapse of the PDMS component with some collapsing POSS as well. In any event, these transitions

occur in the absence of detectable reflectivity changes as the BAM images are homogeneous over the time scale of the compression.

5.4.5 The Non-equilibrium "Monolayer" Regime

Previous work with trisilanolisobutyl-POSS shows that this POSS derivative forms a non-equilibrium monolayer between $12.5 \text{ mN}\cdot\text{m}^{-1}$ and $17.5 \text{ mN}\cdot\text{m}^{-1}$ upon compression.¹⁶⁹ In this regime, addition, step-wise compression, and compression isotherms yield different results as viscous trisilanolisobutyl-POSS monolayers collapse at a rate which is slower than the compression rate. As a result, continuous compression leads to a rise in Π until ultimate failure occurs with non-equilibrium collapse of the film at $\Pi \approx 17.5 \text{ mN}\cdot\text{m}^{-1}$. As seen in Figure 5.1, this regime shifts to smaller $\langle A \rangle$ as the amount of PDMS increases. Nonetheless, neither increasing PDMS content nor the collapse of the PDMS component has a significant impact on the collapse pressure of the POSS component. Hence, the value of $\Pi \approx 17.5 \text{ mN}\cdot\text{m}^{-1}$ for non-equilibrium POSS collapse is a good measure for the dynamic affinity of trisilanolisobutyl-POSS at the surface for all PDMS compositions.

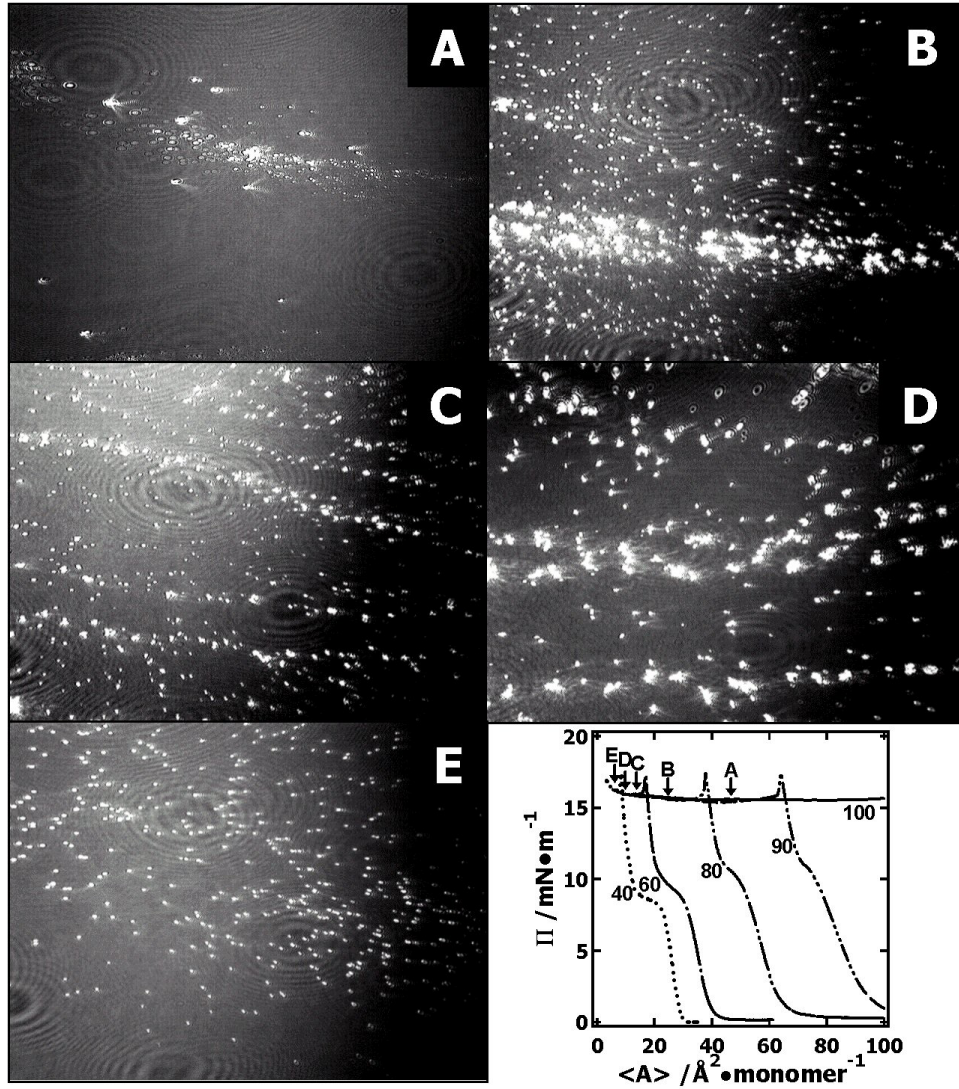


Figure 5.4: BAM images upon compression for different POSS/PDMS blends (wt% POSS, $\langle A \rangle / \text{\AA}^2 \cdot \text{monomer}^{-1}$): **A** (100, 47.4), **B** (90, 25.4), **C** (80, 14.8), **D** (60, 9.5), and **E** (40, 6.4). The $\langle A \rangle$ values all correspond to a POSS concentration of $A_{\text{POSS}} \approx 50 \text{\AA}^2 \cdot \text{molecule}^{-1}$. Solid-like domains appear bright in the images, which are $4.8 \times 6.4 \text{ mm}^2$ in size. The letters on the Π - $\langle A \rangle$ isotherm show the positions where the BAM images were obtained.

5.4.6 Collapse of the POSS Component

Unlike the collapse behavior at the shoulder, which corresponds to the monolayer \rightarrow multilayer transition of PDMS, the surface pressure of the cusp, corresponding to the non-equilibrium formation of more-condensed POSS domains, is unaffected by the amount of PDMS. This transition can be visualized with the aid of BAM as seen in Figure 5.4, where the solid-like domains appear brighter than the rest of the film. The micrographs in Figure 5.4 were chosen to ensure a constant POSS surface concentration of $A_{\text{POSS}} \approx 50 \text{ \AA}^2 \cdot \text{molecule}^{-1}$. This concentration is calculated by assuming the film is only composed of POSS. Pure trisilanolisobutyl-POSS only forms small non-equilibrium solid-like structures when compressed past the collapse pressure. Trisilanolisobutyl-POSS forms more solid-like multilayer domains for small amounts of added PDMS. It is possible that the greater area fraction of solid domain reflects a lower viscosity within the blend. Alternatively, PDMS could serve as a nucleation site for the heterogeneous formation of solid-like domains. These domains tend to aggregate into larger structures (Figure 5.4B). Ultimately, with increasing amounts of PDMS, the formation of solid-like POSS domains apparently becomes more difficult at a specific temperature and Π value as their surface fraction decreases (Figures 5.4D & 5.4E) as one might expect for the addition of a liquid solute. As noted above, there is definitely a larger surface fraction of multilayer domains present in the 90 wt% trisilanolisobutyl-POSS sample. The fact that multilayer domain formation and aggregation occur on a time scale that is initially faster than the rate of compression causes the pressure to drop slightly in the Π - A isotherms at the cusp prior to the formation of a long plateau that is observed upon compression past the cusp.

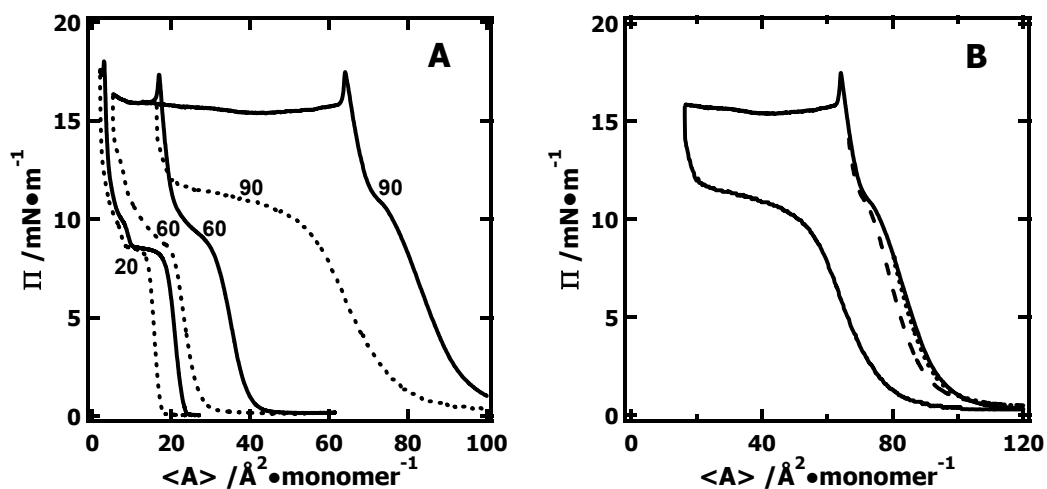


Figure 5.5: Π - $\langle A \rangle$ hysteresis loops for different POSS/PDMS blends. All films were compressed and expanded at $20 \text{ cm}^2 \cdot \text{min}^{-1}$ and a constant temperature of $22.5 \text{ }^\circ\text{C}$. (A) Hysteresis curves for 20, 60, and 90 wt% POSS blends are shown from left to right. Solid curves represent the compression process and the dashed curves represent the expansion process. (B) Hysteresis curves for a single composition, a 90 wt% POSS blend, compressed to $\Pi_{\text{max}} = 8, 12, \text{ and } 16 \text{ mN}\cdot\text{m}^{-1}$ corresponding to dotted, dashed, and solid expansion curves, respectively.

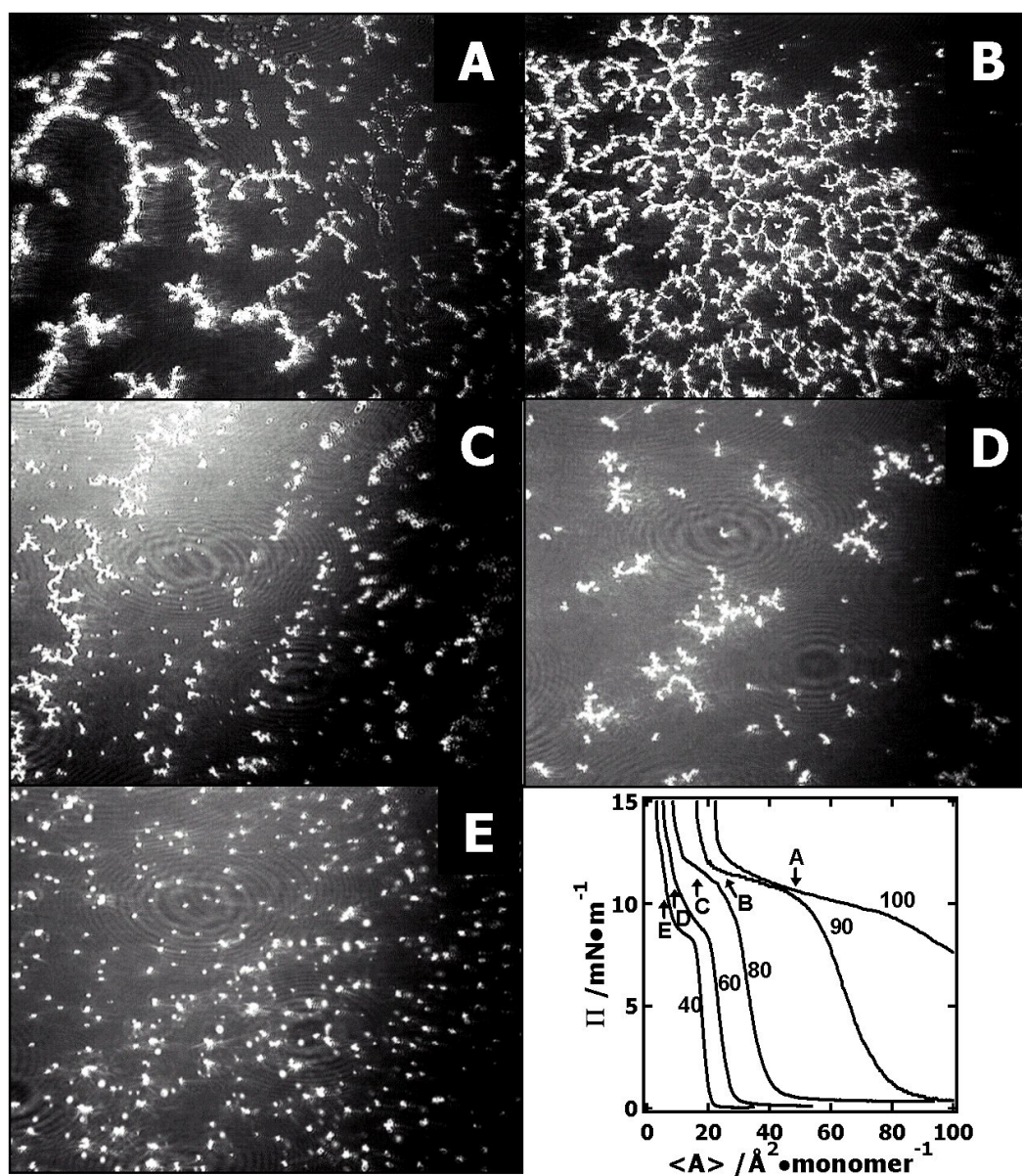


Figure 5.6: BAM images upon expansion for different POSS/PDMS blends (wt% POSS, $\langle A \rangle / \text{\AA}^2 \cdot \text{monomer}^{-1}$): **A** (100, 49.5), **B** (90, 26.0), **C** (80, 14.0), **D** (60, 10.0), and **E** (40, 5.0). The $\langle A \rangle$ values all correspond to a POSS conc. of $A_{\text{POSS}} \approx 50 \text{\AA}^2 \cdot \text{molecule}^{-1}$. Solid-like domains appear bright in the images, which are $4.8 \times 6.4 \text{ mm}^2$ in size. The letters on the Π - $\langle A \rangle$ isotherm show the positions where the BAM images were obtained during the expansion process.

5.4.7 Hysteresis Studies

Once enough PDMS is incorporated into the blended films, the amount of solid present after the cusp decreases and the compression becomes more reversible, as seen in Figure 5.5A. The sudden drop in Π upon expansion does not seem to depend on the amount of PDMS in the blend. Three hysteresis cycles of POSS/PDMS blend films at A/W for fresh monolayers can be seen in Figure 5.5B for the 90wt% POSS blend film. Three general conclusions can be drawn from Figure 5.5B for films at A/W: (1) a very stable reversible monolayer film forms below $\Pi \sim 7 \text{ mN}\cdot\text{m}^{-1}$, i.e., before the PDMS component begins multilayer collapse; (2) irreversible PDMS bilayer formation occurs between $7 \text{ mN}\cdot\text{m}^{-1} < \Pi < 17 \text{ mN}\cdot\text{m}^{-1}$ as the re-spreading of PDMS from the bilayer state is slower than the rate of area expansion; and (3) unstable POSS multilayer domain formation occurs after the cusp resulting in a two step dynamic relaxation process corresponding to the re-spreading of POSS multilayer aggregates and subsequent re-spreading of PDMS. However, this re-spreading is incomplete. If multiple hysteresis loops are performed for the same monolayer, the results are strongly dependent on the maximum surface pressure value, Π_{max} , to which the monolayer is compressed. For $\Pi_{\text{max}} < 7 \text{ mN}\cdot\text{m}^{-1}$, repeated loops are essentially identical. For $7 \text{ mN}\cdot\text{m}^{-1} < \Pi_{\text{max}} < 17 \text{ mN}\cdot\text{m}^{-1}$ there is a small shift in the curves to smaller $\langle A \rangle$ values ($< 5\%$) for the second and later cycles. However, for multiple cycling of films compressed deep into the collapsed regime of the POSS component, like the solid curve in Figure 5.5B, there is a continual shift to smaller $\langle A \rangle$ values for subsequent cycles from the preceding cycle ($> 10\%$ per cycle dependent upon how far the film is compressed into the collapsed regime). This condition suggests that while solid-like POSS domains are no longer visible following the

expansion of the film back to the initial $\langle A \rangle$ value, multilayer domains that are smaller than the resolution of the BAM must exist as subsequent re-compression of the film requires smaller $\langle A \rangle$ values before the surface pressure rises. Moreover, the continual shift in $\langle A \rangle$ with increasing cycle number means that more of the film is converted into a "permanent" multilayer state with each cycle.

When there is a high concentration of trisilanolisobutyl-POSS present and a small amount of PDMS (< 15 wt%), the area fraction of solid domains increases (Figure 5.4B). This feature may occur because the PDMS, when present in small amounts, functions as a nucleation site for the aggregation of trisilanolisobutyl-POSS and is possibly aided by phase separation as noted in the thermodynamic analysis of the monolayer regime. By utilizing BAM, the surface fraction and density of solid-like domains during expansion can be directly observed as seen in Figure 5.6. As more domains form for POSS films with small amounts of PDMS, a "spaghetti-like" network appears. The domains first appear as ring structures as seen in Figure 5.6B. As the trough area expands, these rings break apart into branched "spaghetti-like" strands as seen in Figure 5.6A and to a lesser extent in Figure 5.6C and 5.6D. The nucleation sites that allowed more solid-like domains to form also allow more network-like morphologies to form upon expansion of the barriers (Figure 5.6B). There is, however, a threshold on the amount of solid that will be formed with added PDMS. As can be seen in Figure 5.4C, 5.4D, & 5.4E, as more PDMS is introduced into the system, fewer domain structures form, hence there are also fewer structures upon expansion (Figure 5.6C, 5.6D, & 5.6E). Moreover, when network-like structures fail to form, the predominant morphology is one where most domains exist as small round structures (Figure 5.6E).

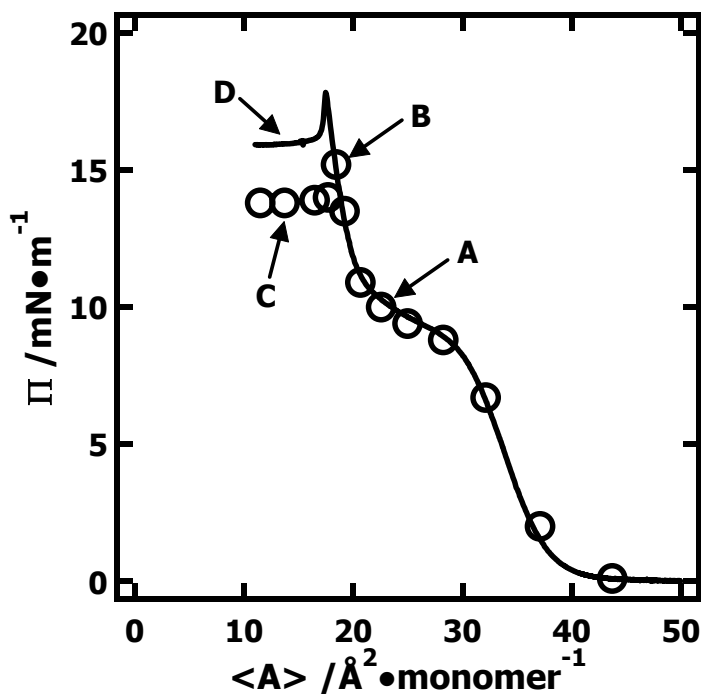


Figure 5.7: A Π - $\langle A \rangle$ isotherm comparison between addition and compression for a 60 wt% TiBuP blend with PDMS. The compression isotherm (solid line) was obtained at $20 \text{ cm}^2 \cdot \text{min}^{-1}$ at a temperature of $22.5 \text{ }^\circ\text{C}$. The circles (\circ) represent "equilibrium" addition data. The letters correspond to the surface concentrations where BAM images shown in Figure 5.8 were obtained.

5.4.8 Addition Experiments

Figure 5.7 contains a representative comparison between compression data and data obtained by making successive additions of spreading solution for the 60 wt% trisilanolisobutyl-POSS blend with PDMS. After spreading, the surface pressure values for all of the addition data were allowed to relax until a stable, "equilibrium" surface

pressure value was obtained. The "equilibrium" condition was arbitrarily chosen to be $\Delta\Pi < 0.1 \text{ mN}\cdot\text{m}^{-1}$ in a 10 min. period. As seen in Figure 5.7, allowing equilibration causes the pressure to stabilize at lower values than under compression conditions. Both isotherms exhibit the same shape and trend, but the plateau pressure of the addition isotherm is lower by about $3 \text{ mN}\cdot\text{m}^{-1}$. Figure 5.8 shows the surface morphologies of the blend film at different surface pressures by addition. The surface blend film was clear before the PDMS transition, and then slightly brighter round liquid domains appeared at surface pressures above about $11 \text{ mN}\cdot\text{m}^{-1}$ (Figure 5.8A) – which is consistent with multilayer formation. Further addition of the mixture onto the surface leads to POSS multilayer domain formation within the upper layer of elongated PDMS bilayer domains (Figure 5.8B and 5.8C). Trisilanol-POSS molecules are believed to form dimers after the cusp,^{167,169} as this would be a more energetically favorable conformation for POSS molecules in the hydrophobic multilayer regime. This hypothesis is supported by the known crystal structure for trisilanolcyclohexyl-POSS, where the unit cell consists of a hydrogen-bonded dimer.¹¹⁹ If dimer does form at the interface, the dimeric-POSS would be non-amphiphilic, as intermolecular hydrogen bonding would replace direct hydrogen bonding between the silanol groups and water. The morphology from the compression method is shown in Figure 5.8D for comparison at the same surface concentration, $\langle A \rangle \sim 16.5 \text{ \AA}^2\cdot\text{monomer}^{-1}$ as Figure 5.8C. The liquid-like multilayer domains of PDMS that appeared in addition are not observed during compression and the condensed POSS multilayer aggregates appear to be smaller in size due to the dynamic nature of the compression process. It is important to note that the absence of liquid-like PDMS multilayer domains in Figure 5.8D obtained by compression does not necessarily mean

Chapter 5

that they do not exist as they could be smaller in size than the resolution of the BAM. Moreover, their presence in the addition experiments in Figure 5.8A-C is consistent with the long equilibration times (at least 30 min. vs. less than 2 min. during continuous compression for comparable Π values) and lower viscosity of the film during evaporation of the spreading solvent that facilitate the formation of large domains.

5.4.9 Relaxation Phenomena

Figures 5.9-5.11 show representative relaxation behavior of POSS/PDMS blends. In Figure 5.9, the surface pressure is plotted as a function of time for representative relaxation curves. Figure 5.9 clearly shows two groups of data. The first group (< 80 wt% POSS) corresponds to those systems that form one phase systems in the monolayer state according to the thermodynamic analysis of the isotherm data. The second group consists of those systems (> 80 wt% POSS) which may form phase separated monolayers just prior to monolayer collapse, and pure trisilanolisobutyl-POSS. The high-POSS content data in Figure 5.9 all relax to the same final surface pressure ($\Pi \approx 12.5 \text{ mN}\cdot\text{m}^{-1}$). As this surface pressure value is comparable to pure trisilanolisobutyl-POSS, one can expect a surface where all of the PDMS is excluded from the water interface and resides on top of the POSS. In contrast, the low-POSS content films relax to a surface pressure value that is actually greater than the value obtained for pure trisilanolisobutyl-POSS. These systems suggest that both the upper and lower levels of the multilayer film contain some PDMS that enhances POSS-water interactions thereby supporting a film with a higher surface pressure. While the molecular basis for this behavior is speculative, it is supported by BAM. Figure 5.10 shows representative morphological data for the relaxation of a 90:10 POSS:PDMS blend by weight following the cessation of

compression. The initial pressure at the cessation of compression, Π_0 , of each blend film is stated in Table 5.1, where both the collapse surface pressures from addition and compression are also included. As seen in Figure 5.9 and Table 5.2 for trisilanolisobutyl-POSS, there is a rapid initial relaxation in Π upon the cessation of compression and then a slower decrease in surface pressure until a stable value of $\Pi = 12.5 \text{ mN}\cdot\text{m}^{-1}$ is obtained. During the early stages of Π relaxation, the solid-like POSS domains aggregate into ring-like structures to minimize the contributions of line tension and dipole density to the total energy of the non-equilibrium system.¹⁸⁰ Representative BAM micrographs in Figure 5.5.10 for the relaxation process of a 90 wt% POSS blend show that the relaxation in Π is accompanied by the aggregation of more condensed domains to form ring-like structures at intermediate Π , before breaking up into smaller aggregates at the lower equilibrium Π . In this respect, the behavior is the same as pure trisilanolisobutyl-POSS.¹⁶⁹ The ring-like structures that form during the Π relaxation process are consistent with the non-equilibrium formation of solid-like domains in a liquid-like monolayer matrix.¹⁸⁰

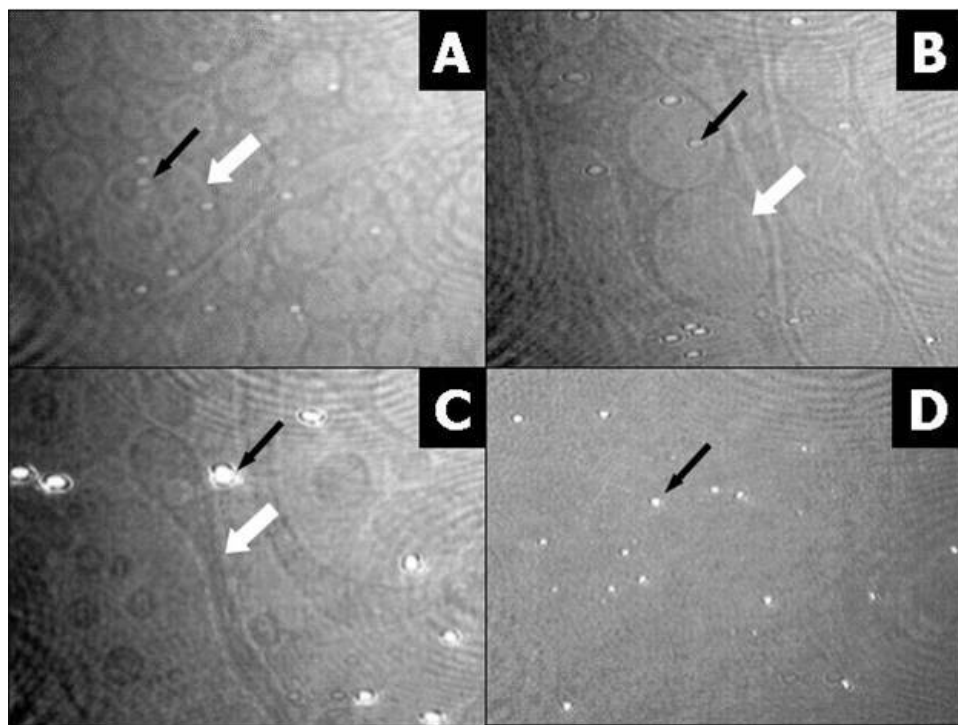


Figure 5.8: BAM morphologies obtained by addition and compression of a 60 wt% TiBuP blend with PDMS ($\Pi / \text{mN} \cdot \text{m}^{-1}$, $\langle A \rangle / \text{\AA}^2 \cdot \text{monomer}^{-1}$): **A** (10.9, 21), **B** (15.2, 18), and **C** (14, 16.5) all by addition versus **D** (16.5, 16.5) by compression. Solid-like domains appear bright in the images, while coexistent liquid-like phases, BAM images **A** \rightarrow **C**, have much lower contrast. In order to highlight these features, white arrows have been added to highlight examples of thicker PDMS domains (medium brightness) on the monolayer background (darkest features), and dark arrows are used to highlight POSS aggregates (brightest, small circular domains) which tend to initially form in the thicker PDMS domains. All images are $2.4 \times 3.2 \text{ mm}^2$ in size.

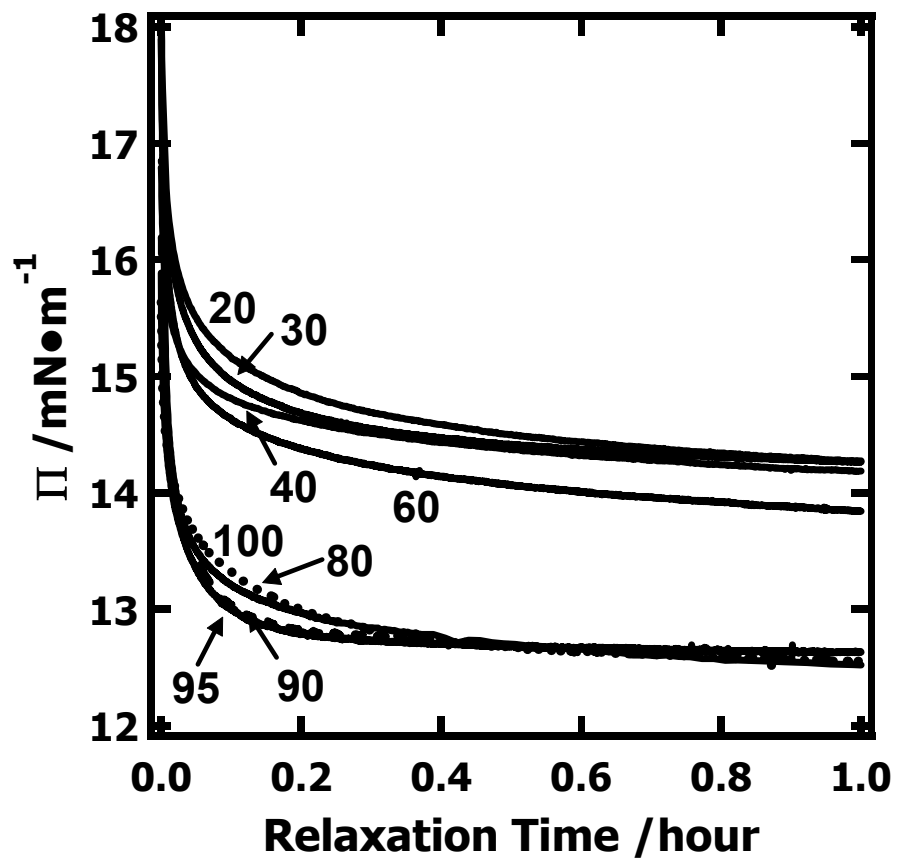


Figure 5.9: Relaxation, Π vs. t , curves for blends of TiBuP with PDMS. Compression ceased at the Π_0 values given in Table 5.1 for each composition ratio.

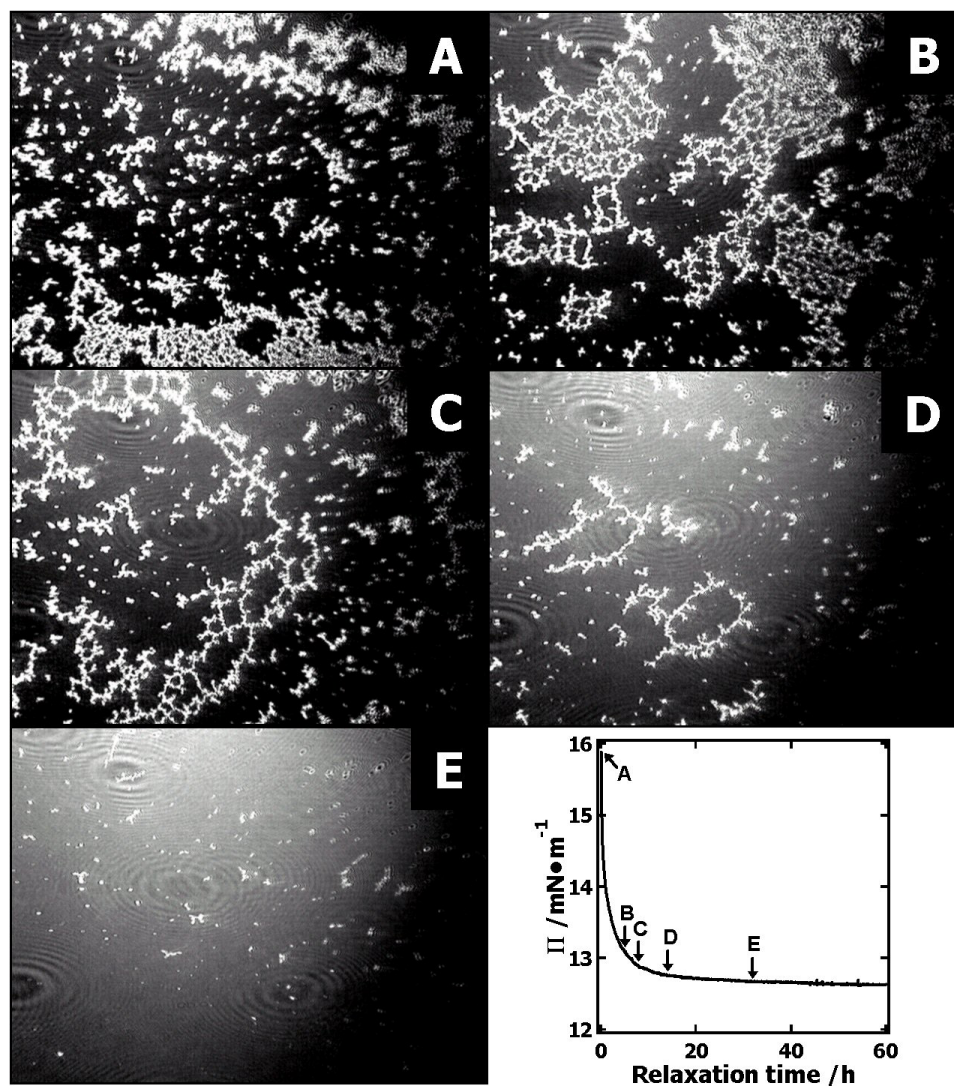


Figure 5.10: Morphologies obtained from a relaxation experiment for 90 wt% TiBuP blend with PDMS at a constant area, $\langle A \rangle = 28.5 \text{ \AA}^2 \cdot \text{monomer}^{-1}$. The BAM images (A \rightarrow E) correspond to the labeled points on the Π vs. t relaxation curve. Solid-like domains appear bright in the images, which are $4.8 \times 6.4 \text{ mm}^2$ in size.

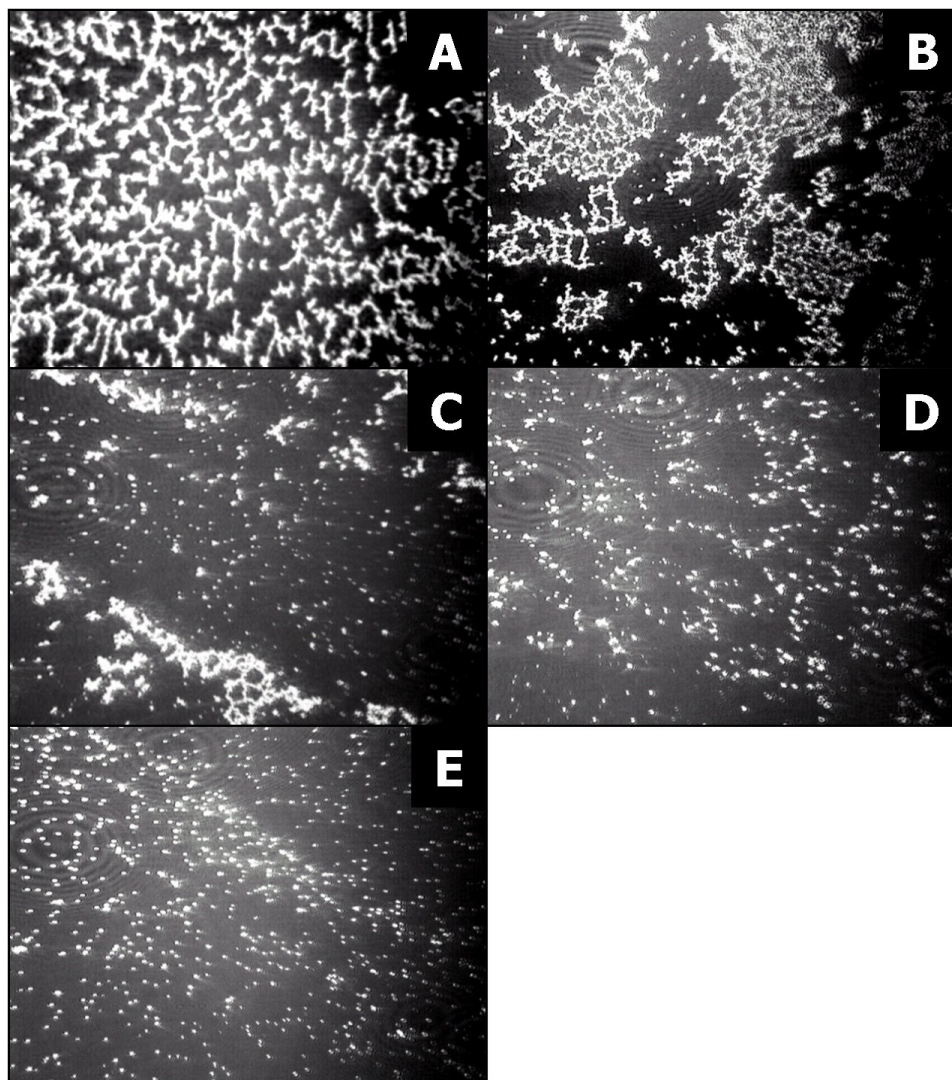


Figure 5.11: Film morphologies after 5 minutes of relaxation for different TiBuP/PDMS blends (wt% POSS, $\langle A \rangle / \text{\AA}^2 \cdot \text{monomer}^{-1}$): **A** (100, 60), **B** (90, 28.5), **C** (80, 17.6), **D** (60, 11.4), and **E** (40, 6.7). The $\langle A \rangle$ values all correspond to a POSS concentration of $A_{\text{POSS}} \approx 60 \text{\AA}^2 \cdot \text{molecule}^{-1}$. Solid-like domains appear bright in the images, which are $4.8 \times 6.4 \text{ mm}^2$ in size.

Table 5.1: Important Π values for TiBuP/PDMS blends at A/W*

wt% POSS	mol% POSS ^a	Collapse Pressure (mN•m ⁻¹) ^b	Collapse Pressure (mN•m ⁻¹) ^c	Initial Relaxation Pressure (mN•m ⁻¹) ^d	Final Relaxation Pressure (mN•m ⁻¹) ^e
0	0	8.5	8.5	8.5	8.5
20	2	18.0	13.7	17.7	14.1
30	4	17.9	-----	17.8	14.1
40	6	17.5	13.8	16.8	14.0
60	12	17.3	13.8	15.9	12.9
80	27	17.5	12.6	15.6	12.4
90	46	17.5	12.8	15.6	12.6
95	64	17.4	-	16.2	12.4
100	100	17.6	12.5	15.7	12.3

* Π values are accurate within ± 0.2 ; ^a mol% derived on a the monomer basis, where POSS is treated as a single monomer; ^b for compression at $20 \text{ cm}^2 \cdot \text{min}^{-1}$; ^c for addition; ^d Initial Π_0 values for Figure 5.9; ^e Final Π values for Figure 5.9

Figure 5.11 shows BAM micrographs for the early stages of Π relaxation for blends of variable POSS content. Interestingly, the images on Figure 5.11 are nearly identical to the result seen for hysteresis experiments in Figure 5.6. With decreasing POSS content within the films, solid-like domains formed at A/W fail to aggregate into connected ring structures and instead form islands. This observation is further evidence for PDMS multilayer formation on top of the POSS/PDMS blend at A/W, where the water surface is not completely covered by POSS molecules upon compression. Under these conditions, PDMS molecules still could interact with POSS molecules laterally and enhance film stability as evidenced by the higher final Π values.

Returning to Figure 5.9, the Π - t decay curves are not single exponentials, suggesting that a complex collapse mechanism exists. The decay process is dominated by a fast relaxation process that rapidly decreases the pressure to a value near the plateau ("equilibrium") value. This fast process was assigned to a reorganization of the blend film (following its non-equilibrium compression) because the magnitude ($\Delta\Pi$) increases with both the compression rate and the target surface pressure (result not shown). This reorganization may be due to an adjustment in the distribution of dipole moments and mean distances. A process that slowly decreases Π to the plateau pressure is observed at longer times. This process was interpreted as a loss of material from the interface (or multilayer formation) and could result from a nucleation and growth process resulting in three-dimensional (3-D) aggregates.

Table 5.2: Parameters used to fit the relaxation of TiBuP/PDMS blends

wt% POSS	a_1^a	a_2^a	τ_1 /sec ^a	τ_2 /min ^a	τ_3 /h ^a
20	0.1473 ± 0.0005	0.0445 ± 0.0005	30.6 ± 0.4	9.8 ± 0.2	128 ± 2
30	0.1194 ± 0.0003	0.0707 ± 0.0003	28.8 ± 0.2	7.0 ± 0.1	68 ± 1
40	0.0966 ± 0.0003	0.0481 ± 0.0003	28.2 ± 0.4	12.7 ± 0.2	79 ± 1
60	0.0975 ± 0.0004	0.0666 ± 0.0004	19.8 ± 0.3	9.4 ± 0.2	57 ± 1
80	0.0947 ± 0.0003	0.0934 ± 0.0003	18.6 ± 0.2	7.7 ± 0.1	96 ± 1
90	0.1015 ± 0.0002	0.0969 ± 0.0002	14.4 ± 0.1	3.5 ± 0.1	136 ± 1
95	0.0983 ± 0.0004	0.1098 ± 0.0004	10.2 ± 0.1	3.0 ± 0.1	54 ± 1
100	0.1691 ± 0.0007	0.0758 ± 0.0007	14.4 ± 0.2	6.8 ± 0.1	112 ± 3

^a \pm one standard deviation

Chapter 5

Qualitatively, the relaxation behavior seen in Figure 5.9 must consist of at least a fast and a slow mode. Quantitatively, a triple exponential function:

$$\Pi/\Pi_0 = a_1 \exp(-t/\tau_1) + a_2 \exp(-t/\tau_2) + (1 - a_1 - a_2) \exp(-t/\tau_3) \quad [5.5]$$

where a_1 and a_2 are exponential pre-factors, and τ_1 , τ_2 , and τ_3 provide different relaxation times, was found to adequately describe the data in Figure 5.9. Results for the fitting parameters for different trisilanolisobutyl-POSS/PDMS blends are summarized in Table 5.2. The first term in eq. 5.5, $a_1 \exp(-t/\tau_1)$, describes the initial drop in Π upon the cessation of compression. The first reorganization time, τ_1 , is on the order of less than one minute, and is similar for all blend compositions (Table 5.2). This behavior reflects a stronger influence by the elastic rather than viscous properties of the monolayer. Hence, the first term has been attributed to local, short-range, re-organization of the functional groups of the molecules within the monolayer.

The second term in eq. 5.5, yields a relaxation time on the order of a few minutes. In this step, there is a continuation of dipolar and chain segment relaxation along with long-range adjustment of symmetry, mean distances between domains, and the dissipation of surface pressure gradients to produce the network structures seen in Figures 5.10 and 5.11, as well as their ultimate break-up. As the pre-factor, a_2 , is much smaller than a_1 , these processes are less significant for this system than the molecular scale re-arrangements.

The final term in eq. 5.5, $(1 - a_1 - a_2) \exp(-t/\tau_3)$, has relaxation times on the order of $\tau_3 \sim 100$ h. This term accounts for multilayer aggregation but is much longer than the experimental observation window. Hence, the pre-factor defines the final plateau Π

value as the experimental time scale $\ll \tau_3$. In terms of Π/Π_0 (Table 5.1), the percentage change in Π during relaxation increases with increasing POSS content in the film. This observation suggests that lower film viscosities accompanying the addition of PDMS minimize the importance of relaxation processes during film compression. This result is also consistent with the observed hysteresis behavior in Figure 5.5A.

5.5 Conclusions

One of the key remaining challenges for POSS nanotechnology is the successful blending of POSS based materials with polymers for transparent hybrid organic-inorganic nanocomposites. In this chapter, uniform blend monolayers of trisilanolisobutyl-POSS and PDMS could be formed up to 80 wt% POSS in the presence of an attractive surface (water). With increasing surface concentration, there is an initial departure from the monolayer state through PDMS desorption into a multilayer structure. Further compression leads to desorption of trisilanolisobutyl-POSS and the formation of more condensed solid-like POSS aggregates in a PDMS fluid where one can reasonably expect POSS molecules to hydrogen bond with one another and form dimer structures as they do in bulk crystal structures.¹¹⁹ Hence this study provides insight into aggregation mechanisms that may also be important in POSS/polymer blends and coatings.

In Chapter 6, the ability to alter this aggregation behavior through polar substituents on the PDMS chains is examined.

CHAPTER 6**Blends of Amphiphilic Trisilanolisobutyl-POSS and Phosphine Oxide****Substituted Poly(dimethylsiloxane) at the Air/Water Interface**

The following chapter appeared as an article in Langmuir, Volume 21, No. 5, (2005) 1908-1916.

6.1 Abstract

In Chapter 5, blends of trisilanolisobutyl-POSS and a non-polar “regular” PDMS have been investigated. In this chapter, blends of trisilanolisobutyl-POSS and a polar PDMS derivative, poly(dimethyl-co-methylvinyl-co-methyl, 2-diphenyl phosphine oxide ethyl) siloxane (PDMS-PO), spread as Langmuir monolayers at the air/water interface are used to examine the surface phase behavior and aggregation of trisilanolisobutyl-POSS as a function of silicone composition. Analyses of the surface pressure-area per monomer (Π - A) isotherms in terms of the collapse pressures and excess Gibbs free energies of mixing indicate the monolayers form slightly negative deviation mixtures. Direct observations of surface morphology with Brewster angle microscopy in the collapsed regime reveal that the governing factor for aggregation is the collapse Π of the component with a stronger affinity for water. In trisilanolisobutyl-POSS/PDMS-PO blends, POSS aggregates as discrete domains and does not coalesce into larger aggregates or network-like structures for < 80 wt% POSS, a feature that is vastly different from a previous study of POSS blended with regular poly(dimethylsiloxane).

6.2 Introduction

Polymer monolayers spread at the air/water interface have attracted the attention of many scientists for orientational control at the molecular level²¹⁶⁻²²⁰ and potential technological applications in optical devices,^{22,23} biomimetic surfaces,^{18,19} and electronic^{3,20} processes. For these applications, Langmuir-Blodgett (LB) films offer well-defined and oriented supramolecular architectures. At a more fundamental level, these same features can be captured to aid in the understanding of physical properties at surfaces and interfaces.

Since poly(dimethylsiloxane) (PDMS) was first reported to have surface active properties in 1947,²¹¹ studies have focused on and revealed the formation of monolayer and multilayer films at the air/water interface.^{212,213} In addition to interesting surface properties, silicones also have a variety of desirable bulk properties. Polysiloxanes have low glass transition temperatures and are thermally stable at higher temperatures relative to most organic polymers.²²¹ Silicones also offer versatility for electrical components because of their small thermal expansion coefficients. The incorporation of phosphorus into the polymer backbone or as a pendant group is one approach to forming flame retardant materials.²²² Furthermore, incorporating phosphine oxide moieties can significantly increase adhesive strength to a variety of metal and inorganic oxide surfaces. This effect is analogous to polar nitrile containing polysiloxanes, which exhibit adhesive peel strengths twice those of nonpolar PDMS on aluminum adherents.²²² In an approach that is consistent with the propensity of polar silicones for hydrogen bonding, this study utilizes these physical interactions between polar functional groups on polysiloxanes and hydroxyl groups on silica “surfaces” as depicted in Figure 6.1. This

approach is similar to one commonly utilized in housing materials for microelectronics where synthetically tailored silicones containing thermally conductive fillers afford the necessary adhesive properties, electrical insulation, and thermal dissipation of heat from the transistors. In this chapter, these same types of interactions will be used to control the dispersion of model polyhedral oligomeric silsesquioxane (POSS) nanofillers.

POSS molecules have attracted scientific attention^{124,127,223} because of their organic/inorganic hybrid molecular structure. By incorporating POSS into polymers, physical properties such as low dielectric constants (k),^{137,152,156,224} thermal properties including increased glass transition temperatures (T_g)^{130,149,150,205,225} and thermal stability,^{153,206,207} and improved oxidation resistance^{173,174} can be obtained. While surface and interfacial properties may play a key role in many potential POSS applications, the surface properties of POSS are relatively unknown.¹⁶³⁻¹⁶⁵ Recently, investigations of the surface properties of POSS molecules at the air/water interface have been reported.^{166,167,169} These studies showed that trisilanol-POSS derivatives are surface active, and self-assemble into uniform monolayers upon compression; but fully condensed POSS cages like octaisobutyl-POSS are nonamphiphilic.

In this study, interactions between amphiphilic molecules of trisilanolisobutyl-POSS and phosphine oxide substituted PDMS (PDMS-PO) are presented for studies conducted at the air/water interface (A/W) utilizing Brewster angle microscopy (BAM) on Langmuir monolayers. Here, POSS serves as the model silica “surface,” and this report shows that PDMS-PO can be used to prevent POSS aggregation into multilayer “networks” seen in pure trisilanolisobutyl-POSS^{166,169} and blends of trisilanolisobutyl-POSS with regular PDMS.¹⁶⁸

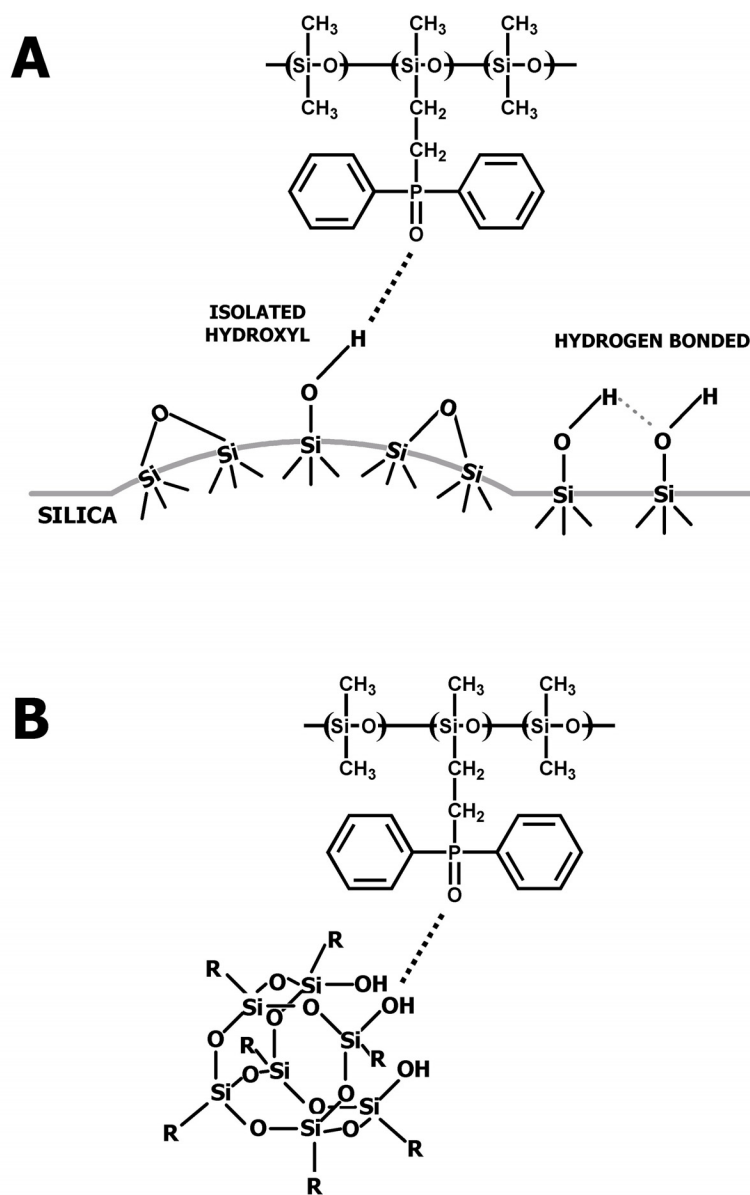


Figure 6.1: A model of hydrogen bonding between the phosphine oxide moiety and (A) a silica surface of a semiconductor,²²² and (B) a model silica nanoparticle of TiBuP.

6.3 Experimental

6.3.1 Materials

Trisilanolisobutyl-POSS was obtained from Hybrid Plastics, Inc. and served as the nanofiller. The polymer shown in Figure 6.2,²²⁶ poly(dimethyl-co-methylvinyl-co-methyl, 2-diphenyl phosphine oxide ethyl) siloxane (PDMS-PO) containing about 15 mol% of the phosphine oxide repeating unit ($M_n = 3.7 \text{ kg}\cdot\text{mol}^{-1}$ by NMR, $T_g = -48 \text{ }^\circ\text{C}$) was used as the polar silicone. *sec*-Butylsilyl- and trimethylsilyl-terminated PDMS ($M_n = 7.5 \text{ kg}\cdot\text{mol}^{-1}$, $M_w/M_n = 1.09$, Polymer Source, Inc.) was used as a non-polar "regular" silicone for comparisons. HPLC grade chloroform (J. T. Baker) was used without further purification to prepare spreading solutions with concentrations around $0.5 \text{ mg}\cdot\text{ml}^{-1}$. All of the samples were allowed to dissolve for at least 24 hours prior to use.

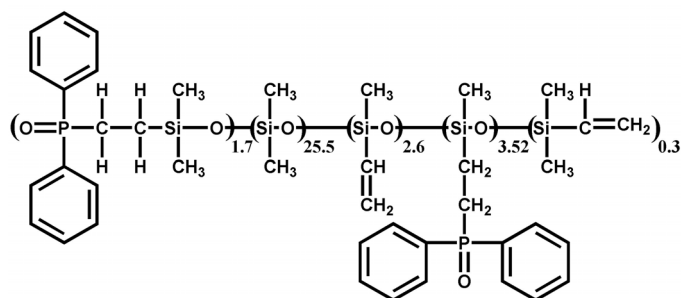


Figure 6.2: The molecular structure of PDMS-PO.

6.3.2 Isotherm and Brewster Angle Microscopy (BAM) Studies

Monolayers were spread onto the surface of a Langmuir trough (500 cm^2 , 601BAM, Nima Technology) filled with ultra-pure water ($18.2 \text{ M}\Omega$, MilliQ Gradient A-10, Millipore) maintained at $22.5 \text{ }^\circ\text{C}$ in a PlexiglasTM box with a relative humidity of

Chapter 6

70~75%. The surface of the water was further cleaned by suctioning off potential impurities from the interface. Polymer solutions were spread onto the water surface using a Hamilton gas-tight syringe and the spreading solvent was allowed to evaporate by waiting a suitable amount of time (~ 20 min). In order to investigate the thermodynamic properties of the trisilanolisobutyl-POSS/PDMS-PO mixtures, four methods were used to vary the surface area or surface concentration: (1) "compression" of the barriers at a constant rate, (2) successive "addition" of spreading solution, (3) "hysteresis" loops, and 4) "stepwise compression" (the portions in quotation marks indicate the short form used throughout the manuscript). For compression at a constant rate, each sample was compressed at $15 \text{ cm}^2 \cdot \text{min}^{-1}$. For hysteresis, each sample was compressed at a speed of $15 \text{ cm}^2 \cdot \text{min}^{-1}$ to a designated average area per monomer value, $\langle A \rangle$, and were immediately expanded at the same speed to a final trough area of 480 cm^2 . This method was used to test the reversibility of the different structural stages of the film. For successive addition, the surface area was held constant and the surface concentration was varied by making successive additions of spreading solution. After each addition, Π was allowed to relax to a constant minimum value ($\Delta\Pi < 0.1 \text{ mN} \cdot \text{m}^{-1}$ over a 10 minute period) after evaporation of spreading solvent. For most surface concentrations, the relaxation time was on the order of 20-30 min. For stepwise compression, each sample was initially compressed at a constant rate. After compressing the barriers to a fixed surface area, the barriers were stopped, and the surface pressure, Π , was allowed to relax to a more "equilibrium" value for a specific time period (typically 5 min). After allowing Π to relax, the compression and relaxation process was repeated until the end of the experiment. The surface pressure was measured using a paper Wilhelmy plate to ± 0.1

$\text{mN}\cdot\text{m}^{-1}$ and the surface micrographs were captured using BAM (BAM-601, NanoFilm Technologie GmbH) during compression of the film. All BAM micrographs are 4.8×6.4 mm^2 and have at least $20\ \mu\text{m}$ lateral resolution.

6.4 Results and Discussion

6.4.1 Isotherms of the Single Component Silicone Films

The surface pressure–area per monomer (Π - A) isotherm of PDMS-PO is compared to non-polar PDMS in Figure 6.3. The shape of the isotherm is related to the relative hydrophilicity and hydrophobicity of the respective substances, and the limiting area, A_o , can be determined by an extrapolation of the steepest portion of the Π - A isotherm curve back to zero surface pressure. The isotherm for PDMS is consistent with literature results.²¹¹⁻²¹³ The lift-off concentration ($\Pi > 0\ \text{mN}\cdot\text{m}^{-1}$) for PDMS-PO is shifted to higher A values by about $5\ \text{\AA}^2\cdot\text{monomer}^{-1}$ relative to "regular" PDMS because of the larger size of the phosphine oxide containing repeat units. In spite of this difference, the limiting areas per monomer for PDMS-PO by compression, $A_{o,PDMS-PO} = 17\ \text{\AA}^2\cdot\text{monomer}^{-1}$ as indicated by the dashed line on Figure 6.3, is quite similar to the value of $18\ \text{\AA}^2\cdot\text{monomer}^{-1}$ for PDMS. In fact, doing the extrapolation to $\Pi = 0$ with the addition data ($A_{o,PDMS-PO} = 20\ \text{\AA}^2\cdot\text{monomer}^{-1}$) in Figure 6.1 (open circles), and then averaging the compression and addition results yields nearly identical A_o values for PDMS ($18\ \text{\AA}^2\cdot\text{monomer}^{-1}$) and PDMS-PO ($18.5\ \text{\AA}^2\cdot\text{monomer}^{-1}$). Unlike non-polar or regular PDMS, PDMS-PO does not show a second transition. For regular PDMS, a plateau at $\Pi = 8.5\ \text{mN}\cdot\text{m}^{-1}$ and a rise in Π at $A = 8\ \text{\AA}^2\cdot\text{monomer}^{-1}$ correspond to the formation of a thicker PDMS layer through an elaborate conformational change,²¹¹ or

Chapter 6

more likely through standard multilayer formation.¹⁴ In this study, the multilayer explanation is favored for the subsequent discussion. As the phosphine oxide functional group is strongly polar, it anchors PDMS to A/W and supports a monolayer up to $\Pi_{\text{collapse,PDMS-PO}} \approx 38 \text{ mN}\cdot\text{m}^{-1}$, and $A_{\text{collapse,PDMS-PO}} = 8 \text{ \AA}^2\cdot\text{monomer}^{-1}$ where multilayer collapse begins. The effect of the PO substituents on the collapse pressure is similar to the effect telechelic-polar groups have on PDMS isotherms.²²⁷ Another important feature of Figure 6.1 is the excellent agreement (quantitative up to $\Pi = 30 \text{ mN}\cdot\text{m}^{-1}$) between compression and addition data for PDMS-PO. Beyond $\Pi = 30 \text{ mN}\cdot\text{m}^{-1}$, the addition data is slightly lower than the compression data suggesting non-polar PDMS segments may collapse out of the interface before the polar functionalized repeat units. This behavior along with hysteresis experiments (not shown) reveal complete reversibility up to $\Pi_{\text{collapse,PDMS-PO}}$, a feature that is similar to the well-known behavior of regular PDMS. Hence, even if there is localized collapse of the non-polar PDMS segments during compression prior to the collapse of the polar functional "anchors", the process is reversible just like "regular" PDMS. As expected, compression past the collapse point leads to large hysteresis loops, whose areas grow with deeper compression into the collapsed regime. Hence, PDMS-PO has ideal monolayer properties for studying how polar substituents alter the aggregation of POSS nanofillers in Langmuir monolayers.

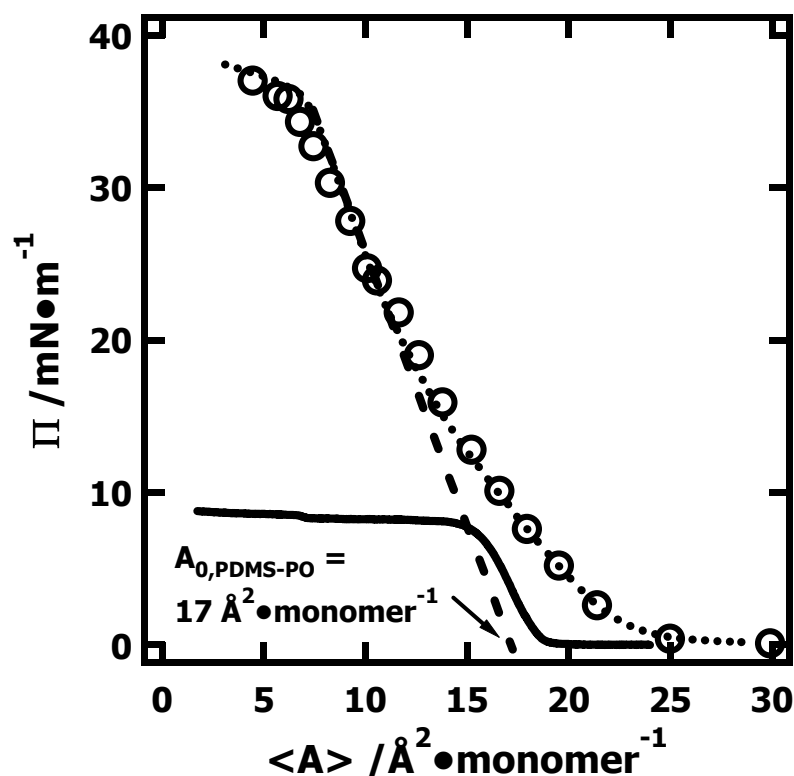


Figure 6.3: Π - A isotherms of PDMS (—) and PDMS-PO (·····) obtained by compression and PDMS-PO by addition (○) at A/W and 22.5 °C. The dashed line shows the extrapolation to $\Pi = 0 \text{ mN}\cdot\text{m}^{-1}$ used to obtain the limiting area per monomer, $A_0 = 17 \text{ \AA}^2\cdot\text{monomer}^{-1}$, of PDMS-PO from the compression experiment. The same extrapolation using the addition data yields a slightly larger value, $A_0 = 20 \text{ \AA}^2\cdot\text{monomer}^{-1}$. The average value for the two methods is in excellent agreement with "regular" PDMS.

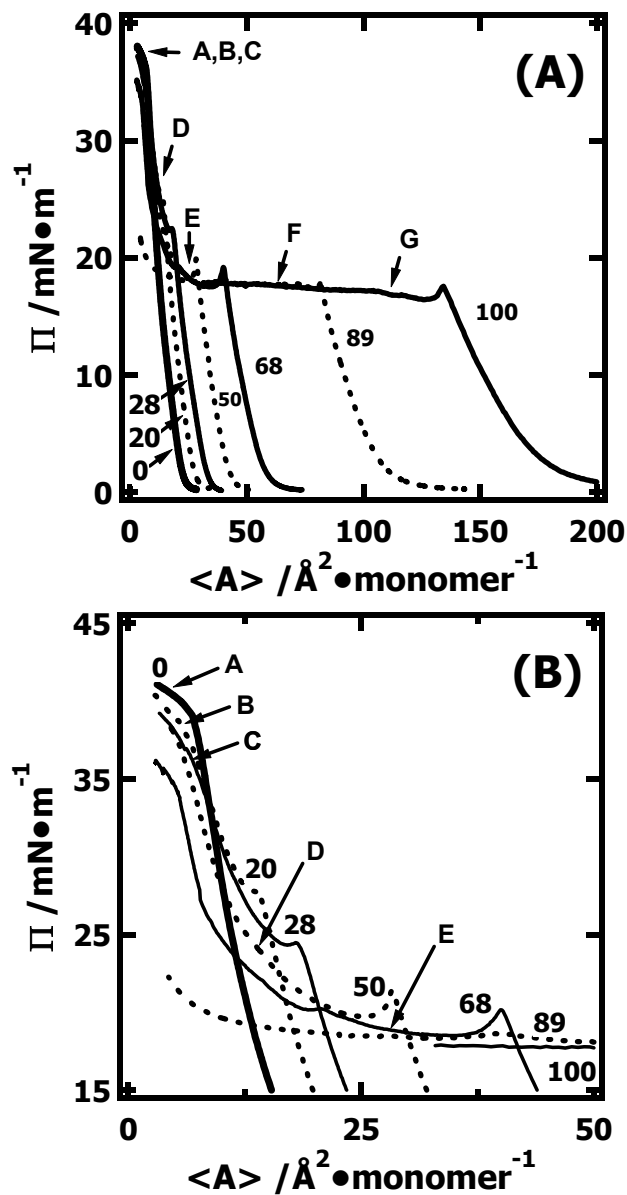


Figure 6.4: Π - A isotherms of PDMS-PO/TiBuP blends at 22.5 °C: (A) Π - A isotherms of PDMS-PO/trisilanolisobutyl-POSS mixed thin films spread at A/W and 22.5 °C. The numbers inside the figure denote the wt% POSS in the blends. The letters with arrows on the figure indicate A values where the BAM images in Figure 6.5 were obtained. (B) The isotherms in (A) have been replotted to expand the collapsed regime.

6.4.2 Compression Isotherms of PDMS-PO/Trisilanolisobutyl-POSS Mixed Films

Figure 6.4A shows isotherms of PDMS-PO/trisilanolisobutyl-POSS blends. Focusing on the pure POSS isotherm (right-most curve), the POSS molecules change their state from a liquid expanded (LE) type film to a more condensed liquid-like film as compression proceeds. Prior to the dynamic collapse pressure of the single-component trisilanolisobutyl-POSS film, BAM images show the monolayer is homogeneous. This feature is also true for all mixtures of trisilanolisobutyl-POSS with PDMS-PO. At about $145 \text{ \AA}^2 \cdot \text{molecule}^{-1}$, there is sufficient lateral pressure ($\Pi_{\text{collapse,POSS}} \approx 17.5 \text{ mN} \cdot \text{m}^{-1}$) to squeeze POSS molecules in the single component film out of the air/water interface to form multilayer POSS domains.^{166,169} In this process, the trisilanolisobutyl-POSS molecules may form non-amphiphilic dimers due to their hydrophobic surroundings similar to the conformation of trisilanolcyclohexyl-POSS in the crystalline state.^{119,169} Upon further compression inside the long plateau region that follows the collapse transition of POSS, POSS molecules continuously form multilayer domains. BAM images show that the multilayer POSS aggregates continue to grow in area fraction after the collapse point with small domains coalescing into larger aggregates (Figure 6.5H). The anisotropic nature of the aggregation in Figure 6.5H arises because of shear flow during symmetric compression from the top and the bottom of the image. These mechanical factors produce an alignment of the large aggregates in Figure 6.5H parallel to the compression barriers. In contrast, the single component isotherm of PDMS-PO, the left-most curve in Figure 6.4, is relatively simple with $\Pi_{\text{collapse,PDMS-PO}} \approx 38 \text{ mN} \cdot \text{m}^{-1}$ as discussed in the preceding section.

Chapter 6

All the isotherms of the binary blend films lie between the isotherms of the pure components in the monolayer state. The collapse transition pressure for the POSS component, $\Pi_{\text{collapse,POSS}}$, systematically increases as the amount of POSS decreases except for the blend with 89 wt% POSS. The increase in $\Pi_{\text{collapse,POSS}}$ with increasing PDMS-PO content is consistent with PDMS-PO/trisilanolisobutyl-POSS compatibility as favorable interactions stabilize the POSS component and keep it in the monolayer state to higher Π values. One possible source of these favorable interactions is hydrogen bonding between the silanol moieties of POSS and the P=O group on the PDMS which can compete with POSS dimer formation which is believed to occur in the multilayer state. Ultimately, the second rise in Π observed at the end of the plateau corresponding to the collapse of the POSS component achieves a value of $\Pi = 38 \text{ mN}\cdot\text{m}^{-1}$ (not shown) before forming a second plateau that corresponds to $\Pi_{\text{collapse,PDMS-PO}}$. This latter feature is not explicitly shown for all blends as it is not possible to obtain the entire isotherm, large and small A , in a single experiment for POSS compositions $> 50 \text{ wt}\%$ with the compression ratio of our instrument.

In Figure 6.5, BAM micrographs of the blends are shown at a specific area per POSS molecule of 120 \AA^2 , i.e., after the collapse transition pressure of pure trisilanolisobutyl-POSS. Each image is taken at that area except for the 20 and 28 wt% blends due to geometrical limitations. These constraints arise from the need to spread at large enough A to start at $\Pi = 0$ and the size of the BAM instrument which limits the observable range of the full compression ratio of the trough. These two factors limit the minimum observable A_{POSS} value. Hence, Figure 6.4B and 6.4C represent the minimum observable A_{POSS} values for 20 and 28 wt% POSS, respectively. The reasons for

choosing $A_{POSS} \approx 120 \text{ \AA}^2 \cdot \text{monomer}^{-1}$ are as follows: (1) All BAM images in the monolayer state for all compositions are uniphaseic; (2) $\Pi_{\text{collapse,POSS}}$ is a function of blend composition indicating that PDMS-PO inhibits the collapse of the POSS component. Hence, comparisons between isotherms and BAM images for different mixtures at constant Π values are only valid in the monolayer state, as comparisons at constant Π values above the $\Pi_{\text{collapse,POSS}}$ value of pure films for the mixtures can lead to invalid comparisons between vastly different phases; and 3) By choosing a value of $A_{POSS} = 120 \text{ \AA}^2 \cdot \text{molecule}^{-1}$, all blends have collapsed, and the apparent surface density of POSS is constant between samples. In this comparison, increasing the PDMS-PO content of the film is equivalent to diluting the system perpendicular to the interface by increasing the overall film thickness. As shown in Figure 6.5, the number of aggregates decreases and the size of the aggregates increase as the amount of POSS increases for blends with PDMS-PO. While this result may seem contradictory to the conclusion drawn from the isotherms, it is important to note that this is not true for two reasons. First, the aggregation in Figure 6.5B through 5D occurs at substantially higher Π values than for pure trisilanolisobutyl-POSS films. In fact BAM images for high PDMS-PO content (> 50 wt%) at $\Pi < 20 \text{ mN} \cdot \text{m}^{-1}$ are homogeneous as these films still reside in the monolayer state. Second, aggregation behavior in the monolayer and multilayer states can be quite different. In the monolayer both PDMS-PO and POSS are hydrated. After the collapse of the POSS component, most of the POSS will reside in a "dry state" above the hydrated monolayer. Hence the presence of a surface that is attractive to both components (in this case through hydrogen bonding) can inhibit aggregation that would otherwise occur in bulk systems.

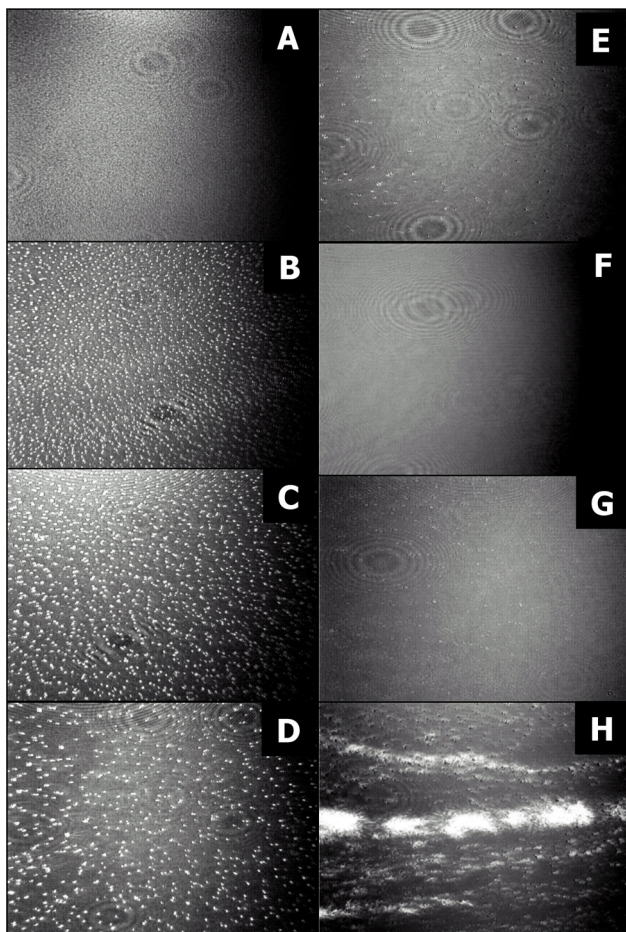


Figure 6.5: BAM images for different blends of TiBuP and PDMS-PO at $A_{POSS} = 40 \text{ \AA}^2 \cdot \text{monomer}^{-1}$: A = 0 (pure PDMS-PO), B = 20, C = 28, D = 50, E = 68, F = 89, G = 100 and H = 100 wt% POSS. The images correspond to the points indicated by letters and arrows on Figure 6.4 and were taken at $T = 22.5 \text{ }^\circ\text{C}$ and a compression rate of $15 \text{ cm}^2 \cdot \text{min}^{-1}$ (compressed symmetrically from the top and bottom of each image). Solid-like domains appear bright in the images, which are $4.8 \times 6.4 \text{ mm}^2$ in size. Image A shows pure PDMS-PO is homogeneous up to $\Pi_{\text{collapse, PDMS-PO}}$. Images D-G correspond to a constant $A_{POSS} \approx 120 \text{ \AA}^2 \cdot \text{monomer}^{-1}$. Due to compression ratio limits discussed in the text, images B and C correspond to $A_{POSS} = 180$ and $140 \text{ \AA}^2 \cdot \text{monomer}^{-1}$ for 20 and 28 wt% POSS, respectively. Image H shows representative POSS aggregation upon further compression of a pure trisilanolisobutyl-POSS film to $A_{POSS} = 40 \text{ \AA}^2 \cdot \text{monomer}^{-1}$. Specific values of $\langle A \rangle$, A_{POSS} , and Π for each image are (identifying letter, $\langle A \rangle / \text{\AA}^2 \cdot \text{monomer}^{-1}$, $A_{POSS} / \text{\AA}^2 \cdot \text{molecule}^{-1}$, $\Pi / \text{mN} \cdot \text{m}^{-1}$): (A, 4.5, n/a, 37.5), (B, 6, 180, 35.5), (C, 7, 140, 34.1), (D, 14.5, 116, 22.1), (E, 28, 124, 17.3), (F, 63, 118, 17.7), (G, 120, 120, 16.6), and (H, 40, 40, 17.8).³⁹

Another interesting feature of Figure 6.5 is the uniformity of the size and shape of the aggregates in the blend films. Further compression of the blends leads to a higher density of the aggregates, but does not significantly alter either their size or shape as long as the POSS content is < 80 wt%. This feature is markedly different from pure trisilanolisobutyl-POSS films (Figure 6.5H),^{166,169} or the reported behavior for trisilanolisobutyl-POSS blends with normal PDMS, which show similar morphologies to pure trisilanolisobutyl-POSS films for small amounts of PDMS (< 40 wt%).¹⁶⁸

6.4.3 Hysteresis and Dynamic Behavior of PDMS-PO/Trisilanolisobutyl-POSS Mixed Films

Figure 6.6 shows Π - A isotherms for a 76 wt% trisilanolisobutyl-POSS blend with PDMS-PO by all four methods used to control surface concentration. The qualitative behavior depicted in Figure 6.6 is representative of all blend compositions. The solid compression line along with the dashed expansion line in Figure 6.6 correspond to a single hysteresis loop for a 76 wt% trisilanolisobutyl-POSS blend with PDMS-PO for compression deep into the multilayer regime. Much like PDMS-PO and trisilanolisobutyl-POSS, the blend is almost completely reversible up to $\Pi_{\text{collapse,POSS}}$. As expected, the degree of hysteresis is a function of how far one compresses the film into the multilayer regime. Additionally, multiple hysteresis cycles show a progressive shift to smaller A values suggesting that not all of the POSS-rich aggregates completely dissolve back to the monolayer state upon complete expansion of the film. This behavior is similar to the behavior seen in trisilanolisobutyl-POSS films and its blends with regular PDMS. Another important feature from Figure 6.6 is the agreement between the addition isotherm (open circles) and the compression curve (solid line) in the monolayer state

reflecting the reversibility observed during hysteresis experiments within this regime. For the addition experiment, the $\Pi_{\text{collapse,POSS}}$ and plateau Π value obtained after the POSS component begins to collapse are different than the values observed for compression at a fixed rate. These features are similar to the behavior observed in pure trisilanolisobutyl-POSS films, and its blend films with regular PDMS. Unlike trisilanolisobutyl-POSS blends with regular PDMS, both the $\Pi_{\text{collapse,POSS}}$ and plateau Π values in trisilanolisobutyl-POSS blends with PDMS-PO are dependent on the blend composition. This feature will be subsequently discussed in the section on thermodynamic analyses of the isotherms. Finally, step-wise compression data in Figure 6.6 (dotted lines) rectify the difference between the dynamic (compression) isotherm and the more "equilibrium" addition isotherm. By allowing Π to relax at each A value in the step-wise compression isotherm, the instability of the plateau region during compression experiments is clearly revealed. While Π was only allowed to relax for 5 minutes in the step-wise experiments of Figure 6.6, this period of time is almost long enough to achieve the "equilibrium" plateau Π values seen in the addition experiments. This fast Π relaxation is similar to the behavior reported for trisilanolisobutyl-POSS blends with regular PDMS.

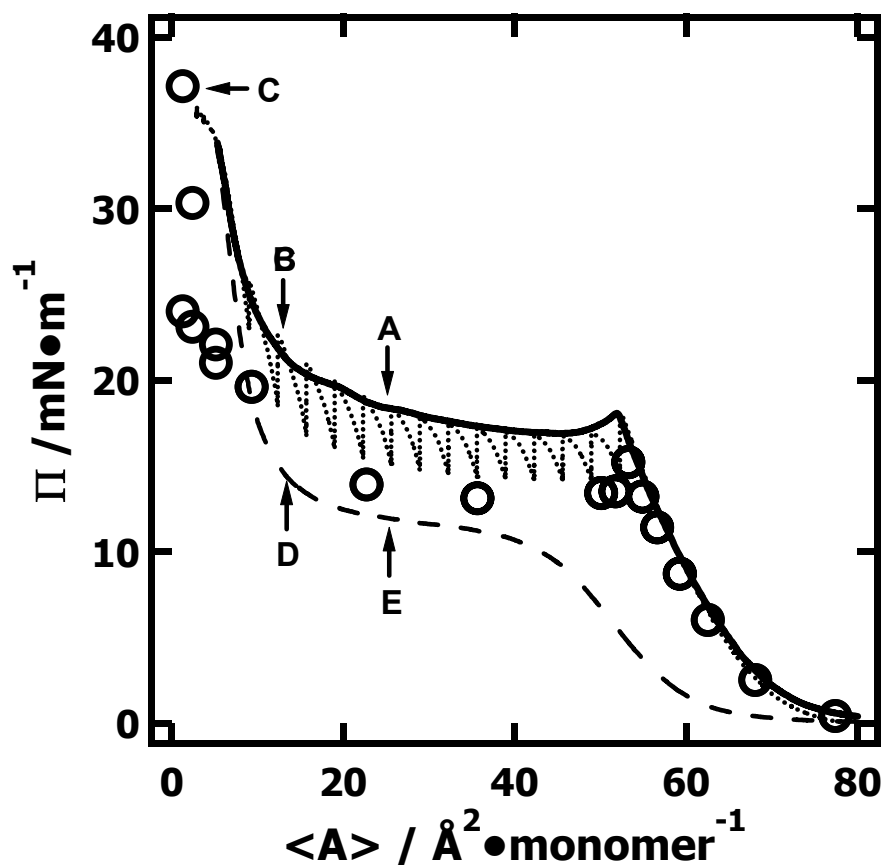


Figure 6.6: Π - A isotherms for a 76 wt% trisilanolisobutyl-POSS blend with PDMS-PO at A/W and 22.5 °C. The solid curve represents compression at a fixed rate of 15 $\text{cm}^2 \cdot \text{min}^{-1}$, while the dashed line represents expansion at the same rate to complete a hysteresis loop. The dotted curve signifies step-wise compression experiments, while the open circles (\circ) correspond to addition data. Letters and arrows on the isotherm indicate the $\langle A \rangle$ values in Figure 6.7 where the BAM images were taken.

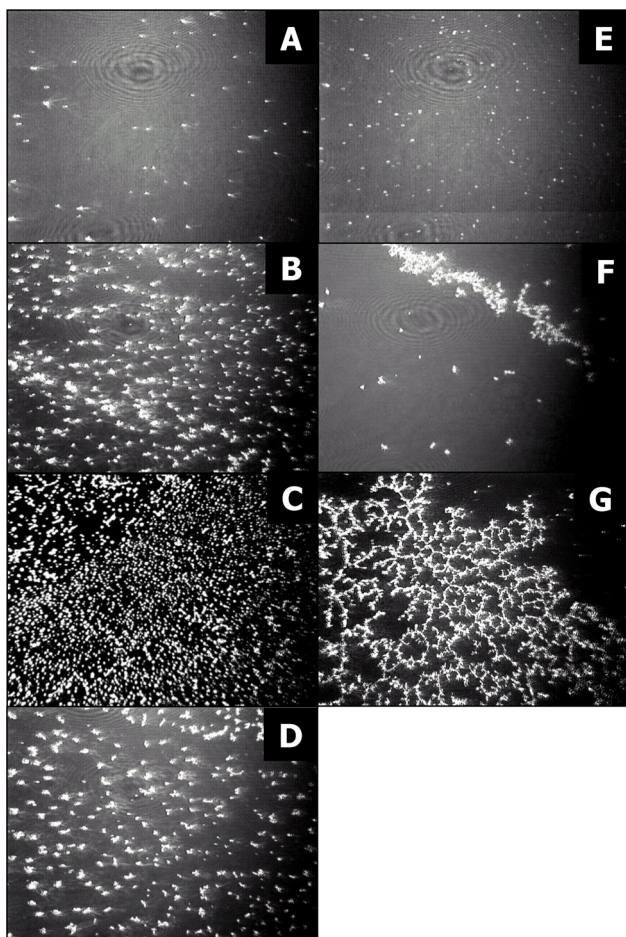


Figure 6.7: BAM images obtained from a 76 wt% TiBuP blend with PDMS-PO at 22.5 °C by different methods for controlling the surface concentration. Images A through E correspond to the letters and arrows on Figure 6.6. Image A and B (compression) and D and E (expansion) correspond to the hysteresis loop in Figure 6.6. Figure C shows addition data at the highest achievable Π value. Specific values of $\langle A \rangle$, A_{POSS} , and Π from images A through E are summarized as (identifying letter, $\langle A \rangle / \text{\AA}^2 \cdot \text{monomer}^{-1}$, $A_{POSS} / \text{\AA}^2 \cdot \text{molecule}^{-1}$, $\Pi / \text{mN} \cdot \text{m}^{-1}$): (A, 24.5, 77.4, 18.4), (B, 13.1, 41.4, 21.4), (C, 1.4, 4.4, 37.1), (D, 13.0, 41.0, 14.6), and (E, 26.0, 82.0, 11.9). For comparison at an equivalent A_{POSS} to image B, image F (obtained upon compression) shows an 89 wt% trisilanolisobutyl-POSS blend with PDMS-PO (F, 21.5, 40.3, 18.1). For comparison at an approximately equivalent A_{POSS} to image D, image G (obtained upon expansion) shows a 90 wt% trisilanolisobutyl-POSS blend with regular PDMS (G, 26, 50, 11.2),⁴². Images F and G clearly show the type of aggregation that is completely suppressed by PDMS-PO for < 80 wt% POSS.

BAM images were also obtained for the isotherms presented in Figure 6.6. Below $\Pi_{\text{collapse,POSS}}$ ($= 18 \text{ mN}\cdot\text{m}^{-1}$ for 76 wt% trisilanolisobutyl-POSS), all BAM images are homogeneous, hence they are not shown in Figure 6.7. As seen in Figure 6.7A and 6.7B, compression to $\langle A \rangle$ values as small as $13 \text{ \AA}^2\cdot\text{monomer}^{-1}$ ($A_{\text{POSS}} = 41 \text{ \AA}^2\cdot\text{molecule}^{-1}$) does not lead to a significant change in the size or shape of the POSS aggregates for a 76 wt% trisilanolisobutyl-POSS blend with PDMS-PO. These features are common to all PDMS-PO blends with a trisilanolisobutyl-POSS content $< 80\text{wt}\%$. As the trisilanolisobutyl-POSS composition increases above $80\text{wt}\%$, the aggregates in blends with PDMS-PO start to grow, and a signature for sub-network structure starts to appear in $89\text{wt}\%$ trisilanolisobutyl-POSS blend film with PDMS-PO (Figure 6.7F). As noted earlier in the discussion of Figure 6.5H, the anisotropic nature of Figure 6.7F also arises from weak shear alignment of the larger aggregates parallel to the compression barriers. Network-like structures arising from the aggregation of multilayer POSS-rich aggregates like that seen in Figures 6.5H and 6.7F are usually seen in pure trisilanolisobutyl-POSS films and its blends with regular PDMS at $> \approx 60 \text{ wt}\%$ POSS.¹⁶⁸ One example of the network-like structures that can form during expansion or Π relaxation of a highly compressed blend of regular PDMS with trisilanolisobutyl-POSS is shown in Figure 6.7G (for $90 \text{ wt}\%$ POSS).¹⁶⁸ Here, PDMS-PO clearly delays the onset and the extent of the aggregation relative to regular PDMS in blends with trisilanolisobutyl-POSS. Furthermore, even the aggregation seen in Figure 6.7F for the $89\text{wt}\%$ trisilanolisobutyl-POSS blend with PDMS-PO fails to produce extensive network-like structures upon expansion reinforcing this conclusion. Figure 6.7C shows another interesting facet of the PDMS-PO blends with trisilanolisobutyl-POSS and corresponds to addition data at $\Pi = 37.1 \text{ mN}\cdot\text{m}^{-1}$ or

Chapter 6

$\langle A \rangle = 1.4 \text{ \AA}^2 \cdot \text{monomer}^{-1}$ ($A_{POSS} = 4.4 \text{ \AA}^2 \cdot \text{monomer}^{-1}$). Unlike blends of trisilanolisobutyl-POSS with regular PDMS,¹⁶⁸ the morphology obtained by addition, Figure 6.7C, is essentially identical to the result obtained by compression even past the collapse transition of PDMS-PO. As addition experiments are expected to interfere with the formation of larger aggregates,¹⁶⁸ it is not surprising that there is no significant difference for the non-aggregating systems of PDMS-PO blends with trisilanolisobutyl-POSS at < 80 wt% POSS. Another important feature of Figure 6.7 is the reversibility of the morphology during hysteresis experiments: Figure 6.7A vs. Figure 6.7D and Figure 6.7B vs. Figure 6.7D; even though there is a relatively large hysteresis loop in Figure 6.6 upon expansion of the film and the fact that multilayer domains remain even after complete expansion of the film. This behavior is very different from pure trisilanolisobutyl-POSS monolayers (Chapters 3 and 4),^{166,169} and blends of trisilanolisobutyl-POSS with regular PDMS (Chapter 5).¹⁶⁸ In trisilanolisobutyl-POSS/PDMS blends with sufficient POSS (> 60 wt%), “network-like” POSS aggregates, or residual elements of broken network-like structures are observed upon the expansion of films compressed deep into the collapsed regime (Figure 6.7G).⁴² The fact that small trisilanolisobutyl-POSS aggregates require greater Π values to form and fail to aggregate into extensive network-like structures suggests that strongly favorable interactions are present between trisilanolisobutyl-POSS and PDMS-PO.

At this stage, three general conclusions can be drawn from the aforementioned experiments on Langmuir films of PDMS-PO blended with trisilanolisobutyl-POSS at A/W: (1) A very stable reversible and homogeneous monolayer film forms for $\Pi < \Pi_{\text{collapse,POSS}}$ (equilibrium), i.e., before the POSS component begins multilayer collapse;

(2) Composition dependent, irreversible, and unstable POSS multilayer formation occurs upon compression past the cusp in the isotherms, i.e. in the plateau regime, resulting in a two-step dynamic relaxation process upon expansion from a highly compressed blend corresponding to the re-spreading of POSS multilayer aggregates; and (3) Strongly polar substituents on PDMS-PO seem to promote the formation of multilayer domains that are uniform in terms of their size and dispersion. The remainder of this chapter focuses on thermodynamic aspects of the first two conclusions and their impact on a potential model for explaining the last conclusion.

6.4.4 Thermodynamic Analyses of the Isotherm Studies

Thermodynamic information about interactions in multicomponent monolayers can be inferred from isotherm studies. For an ideally mixed binary blend, the collapse pressure must vary with composition between the values for the pure component monolayers:²²⁸

$$\Pi_{\text{collapse, mix}} = X_1 \Pi_{\text{collapse, 1}} + X_2 \Pi_{\text{collapse, 2}} + \dots + X_k \Pi_{\text{collapse, k}} \quad [6.1]$$

where, $\Pi_{\text{collapse, } i}$ and X_i represent the surface pressure at collapse and the mole fraction on a per molecule basis of the i^{th} component in a k component film, respectively. On the other hand, if both components are completely incompatible two different phases are then present at collapse and Π_{collapse} becomes independent of composition and equal to the smaller pure component value as the less stable monolayer species preferentially collapses. Intermediate behavior occurs for films with partial miscibility.

A recent study showed trisilanolisobutyl-POSS has limited compatibility with regular PDMS (Chapter 5).¹⁶⁸ In that work, $\Pi_{\text{collapse, PDMS}}$, the component with the lower collapse pressure, initially followed eq. 6.1 during compression experiments. However,

Chapter 6

with increasing POSS content, the dynamic $\Pi_{\text{collapse,PDMS}}$ values obtained for mixtures by compression of the film flattened out at a value near $\Pi_{\text{collapse,PDMS}} = 12.5 \text{ mN}\cdot\text{m}^{-1}$, or the "equilibrium" $\Pi_{\text{collapse,POSS}}$ value. The overall behavior was better described by Henry's Law behavior.^{26,168} The presence of PDMS had no effect on the dynamic $\Pi_{\text{collapse,POSS}} = 17.5 \text{ mN}\cdot\text{m}^{-1}$ observed during compression experiments. As $\Pi_{\text{collapse,POSS}}$ is the significant transition for the formation of POSS multilayer aggregates, these values are plotted in Figure 6.8 for blends of PDMS-PO with trisilanolisobutyl-POSS. In the present study, $\Pi_{\text{collapse,POSS}} < \Pi_{\text{collapse,PDMS-PO}}$. As noted in Figure 6.8, there is a nearly continuous transition in the dynamic collapse pressure from pure trisilanolisobutyl-POSS to pure PDMS-PO with a slightly negative deviation from ideal behavior (eq. 1 and the dashed line in Figure 6.8). This observation is consistent with compatibility between the PDMS-PO and trisilanolisobutyl-POSS components. Enhanced compatibility between blends of trisilanolisobutyl-POSS with PDMS-PO compared to blends with PDMS may arise from the ability of PDMS-PO to hydrogen bond with the silanol groups of the incomplete POSS cage, which could keep POSS molecules from desorbing from the interface until a higher lateral pressure is applied. Interestingly, a straight line extrapolation of the initial negative deviation from ideal behavior for the dynamic (compression) data as trisilanolisobutyl-POSS is added to PDMS-PO (dotted line on Figure 6.8) intersects the right-hand axis ($X_{\text{POSS}} = 1$) at $12.5 \text{ mN}\cdot\text{m}^{-1}$, the "equilibrium" $\Pi_{\text{collapse,POSS}}$ value. Hence, the dynamic $\Pi_{\text{collapse,POSS}}$ value can be thought of as a "two-dimensional" Henry's Law constant for the negative deviation mixtures observed during compression experiments. This behavior is further clarified by a set of addition experiments. The open symbols (\circ) in Figure 6.8 represent the plateau surface pressures

or the "equilibrium" $\Pi_{\text{collapse,POSS}}$ values ($12.5 \text{ mN}\cdot\text{m}^{-1}$ for pure trisilanolisobutyl-POSS)¹⁶⁹ of the blend films obtained by addition experiments at different blend compositions. "Equilibrium" $\Pi_{\text{collapse,POSS}}$ values increase in a nearly linear fashion as the trisilanolisobutyl-POSS content decreases. Here, the dotted line in Figure 6.8 that served as a Henry's Law comparison for the dynamic $\Pi_{\text{collapse,POSS}}$ values obtained in compression experiments, serves as an ideal mixing prediction (eq. 1) for "equilibrium" $\Pi_{\text{collapse,POSS}}$ values obtained in addition experiments. As revealed in Figure 6.8, the "equilibrium" $\Pi_{\text{collapse,POSS}}$ values show essentially ideal to slightly negative deviation behavior for the entire composition range. As reported previously⁴² and shown as open triangles in Figure 6.8, the presence of "regular" PDMS (no polar functional groups) in blends with trisilanolisobutyl-POSS does not affect the dynamic $\Pi_{\text{collapse,POSS}}$ values. Taken collectively, these observations are consistent with hydrogen bonding between phosphine oxide substituents on PDMS and silanol groups on the POSS cage that can stabilize POSS in the monolayer to higher Π values.

As discussed previously, analysis of the collapse pressures suggests compatibility between PDMS-PO and trisilanolisobutyl-POSS. Another mechanism for attaining thermodynamic information about the interactions between PDMS-PO and trisilanolisobutyl-POSS is to determine the "two-dimensional" analogs to three-dimensional mixing properties from the isotherms in the monolayer state. The excess areas of mixing, $\Delta A_{\text{mix}}(\Pi)$, the two-dimensional analogs to the volume changes upon mixing in bulk systems, provide a measure of nonideality and can be calculated as a function of surface pressure and mixture composition using the additivity rule.^{1,229} The

relationship between $\Delta A_{mix}(\Pi)$ and the molar ratios of component 1 (x_1) and component 2 (x_2) in a binary mixture on a per monomer basis is expressed as eq. 6.2 and 6.3.

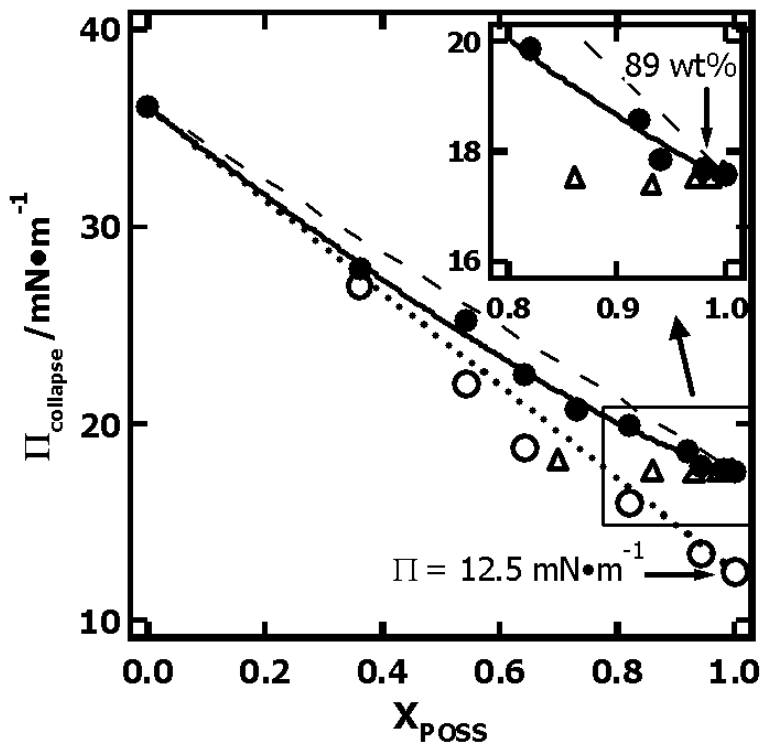


Figure 6.8: Composition dependence of $\Pi_{collapse,POSS}$ for TiBuP blends with PDMS-PO obtained by compression (\bullet , dynamic) and addition (\circ , "equilibrium") at A/W and 22.5 °C. The solid line is provided to highlight the trend, the bold dotted line represents ideal dilute solution behavior (Henry's law), and the dashed line corresponds to the values for ideal mixing for the compression (dynamic) data. The corresponding composition independent dynamic $\Pi_{collapse,POSS}$ values obtained by compression for trisilanolisobutyl-POSS blends with regular PDMS (\triangle) are provided for comparison.¹⁶⁸ Mole fractions are calculated on a per molecule basis.

$$\langle A_{mix,ideal}(\Pi) \rangle = x_1 A_1(\Pi) + x_2 A_2(\Pi) \quad [6.2]$$

$$\Delta A_{mix}(\Pi) = \langle A(\Pi) \rangle - \langle A_{mix,ideal}(\Pi) \rangle \quad [6.3]$$

where $\langle A(\Pi) \rangle$ is the actual experimental average area per monomer of the mixed monolayer, and $\langle A_{mix,ideal}(\Pi) \rangle$ is the calculated average area per monomer of the mixture based on the experimental areas per monomer of each pure component at a specific Π value, $A_1(\Pi)$ and $A_2(\Pi)$, for component 1 and 2, respectively. In these binary mixtures of PDMS-PO and trisilanolisobutyl-POSS, surface thermodynamic analyses reveal nearly ideal mixing, which is most likely due to the compensating effects of the polymer-polymer interactions, as might be found under θ conditions for polymer solutions, and specific interactions between the two species. Deviations from the additivity rule indicate miscibility and interactions between the two components, with positive excess areas of mixing meaning greater cohesion between molecules of the same chemical species rather than between the unlike components. In contrast, negative excess areas of mixing are indicative of greater cohesive forces between unlike molecules than between two identical molecules as might be expected in a mixture of oppositely charged species or a system with intermolecular hydrogen bonding. This thermodynamic analysis was carried out for the mixtures at three different Π values. In Figure 6.9A, $\langle A(\Pi) \rangle$ at $\Pi = 4$, 8, and 16 $\text{mN}\cdot\text{m}^{-1}$ are plotted against the monomer mole fraction of trisilanolisobutyl-POSS (symbols) and are compared with the predicted values ($\langle A_{mix,ideal}(\Pi) \rangle$, dashed lines) based on the additivity rule (eq. 6.2) for compression (dynamic) experiments.

Chapter 6

Within experimental error, $\langle A(\Pi) \rangle$ values closely follow the calculated values obtained from the additivity rule and may show slightly negative deviation. The near additivity of the mean areas and the variation in $\Pi_{\text{collapse,POSS}}$ with the molar ratio demonstrate that the two components are essentially ideally miscible at A/W in the monolayer state. This behavior is clearly different from regular PDMS blends with trisilanolisobutyl-POSS, which showed strongly positive deviation from area additivity.¹⁶⁸

The molar Gibbs excess free energy of mixing, ΔG_{excess} , can also be calculated from the Π - A isotherms of the pure and mixed films:^{1,214}

$$\Delta G_{\text{excess}} = \int_0^{\Pi} \Delta A_{\text{mix}}(\Pi) d\Pi \quad [6.4]$$

The ΔG_{excess} values (multiplied by 10 for better y-axis scaling) for binary mixtures as a function of POSS mole fraction and surface pressure are shown in Figure 6.9B. For all Π values, these curves are concave upward, giving slightly negative ΔG_{excess} values, a result that is in agreement with the thermodynamic conditions for miscibility and favorable interactions in binary monolayers.¹ At most compositions, these values become more negative with increasing Π , indicating that the interactions between the two components are stronger at larger Π . The near-zero values of ΔG_{excess} observed for mixtures, mean that the films exhibit near ideal mixtures with values of the same magnitude as those reported in the literature for compatible mixtures of fatty acid compounds, $\Delta G_{\text{excess}} \sim 0.5 k_B T$.^{1,230-233} Moreover, the thermodynamic analysis for the PDMS-PO blends with trisilanolisobutyl-POSS are in complete agreement with BAM studies as all BAM images are homogeneous in the monolayer state.

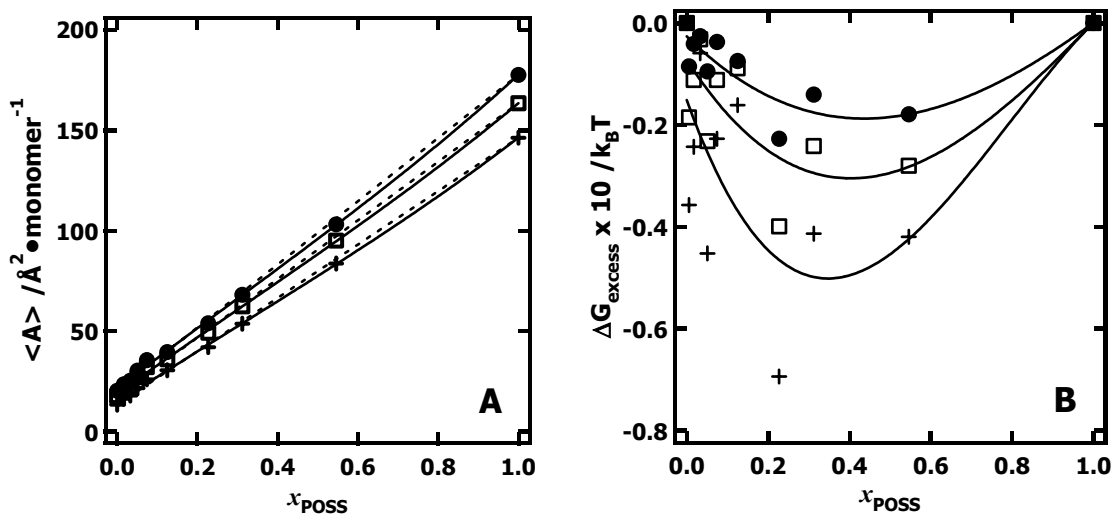


Figure 6.9: $\langle A(\Pi) \rangle$ and ΔG_{excess} of trisilanolisobutyl-POSS/PDMS-PO blends: (A) Mean surface areas and (B) excess Gibbs free energies of mixing calculated from the isotherms ($T = 22.5 \text{ }^\circ\text{C}$) of trisilanolisobutyl-POSS and PDMS-PO at $\Pi = 4$ (\bullet), 8 (\square), and 16 ($\+$) $\text{mN}\cdot\text{m}^{-1}$. Solid lines are guides for the eye and the dashed lines correspond to the values for ideal mixing. Note that the ΔG_{excess} values in (B) have been multiplied by 10 for better y-axis scaling.

6.4.5 A Model for Aggregation in PDMS-PO/Trisilanolisobutyl-POSS Blends

Based on the thermodynamic analyses of the preceding section, Figure 6.10 is offered as a cartoon model for the observed aggregation behavior in the BAM studies. As trisilanolisobutyl-POSS (black circles) has a lower collapse pressure than PDMS-PO (black lines with small open circles) in the monolayer state, it is the POSS component that will be preferentially ejected into the upper layers of a multilayer structure upon compression. For trisilanolisobutyl-POSS in the upper layer, two fates can be expected: (1) monomeric POSS (light gray half ovals) will hydrogen bond with PDMS-PO, or (2)

Chapter 6

dimeric POSS (light gray ovals) will form, whereby two trisilanolisobutyl-POSS molecules will form a set of intermolecular hydrogen bonds similar to what is found for the crystal structure of trisilanolisocyclohexyl-POSS.¹¹⁹ If dimeric POSS forms, the only interactions it can have with the underlying monolayer are relatively weak van der Waals interactions. As a consequence trisilanolisobutyl-POSS molecules in the upper layer of the single component film^{166,169} or blend systems with regular PDMS¹⁶⁸ tend to form small POSS-rich aggregates that ultimately aggregate into ever larger structures (like Figure 6.5H) and lead to network-like structures upon expansion (Figure 6.7G). During the initial stages of trisilanolisobutyl-POSS collapse in blends with PDMS-PO, somewhat similar behavior is expected. The POSS component is squeezed out of the interface and forms POSS-rich domains. In contrast to the trisilanolisobutyl-POSS/regular PDMS blends, the POSS component of the upper domain is likely to exist in both monomeric and dimeric forms, with the monomeric POSS stabilized by hydrogen bonding with PDMS-PO. As a consequence, there will be stronger adhesion between the POSS-rich multilayer domains in blends with PDMS-PO versus blends with regular PDMS. Moreover, the PDMS-PO appears to act as a stabilizer of the POSS-rich multilayer domains resulting in uniform sized aggregates that may correspond to surface micelles (Figure 6.5B to 6.5D for example),^{116,219,220,234} which never coalesce or grow into larger aggregates (Figure 6.7A-6.7E) as long as the POSS content remains below 80 wt%. These features suggest that PDMS-PO forms a physisorbed coating on the POSS-rich domains and provides a “two-dimensional” steric stabilizing layer that is analogous to the use of polymeric surfactants to stabilize colloidal silica.²³⁵ These features are depicted in Figure 6.10 and show that the main effect of increasing the amount of PDMS-PO is an

increase in the surface pressure where POSS-rich domains form leading to a higher surface density of aggregates rather than dramatic changes in particle size or size distribution. Future work will require more detailed studies by techniques such as atomic force microscopy on Langmuir-Blodgett films to discern between uniform sized aggregates of smaller particles and surface micelles.

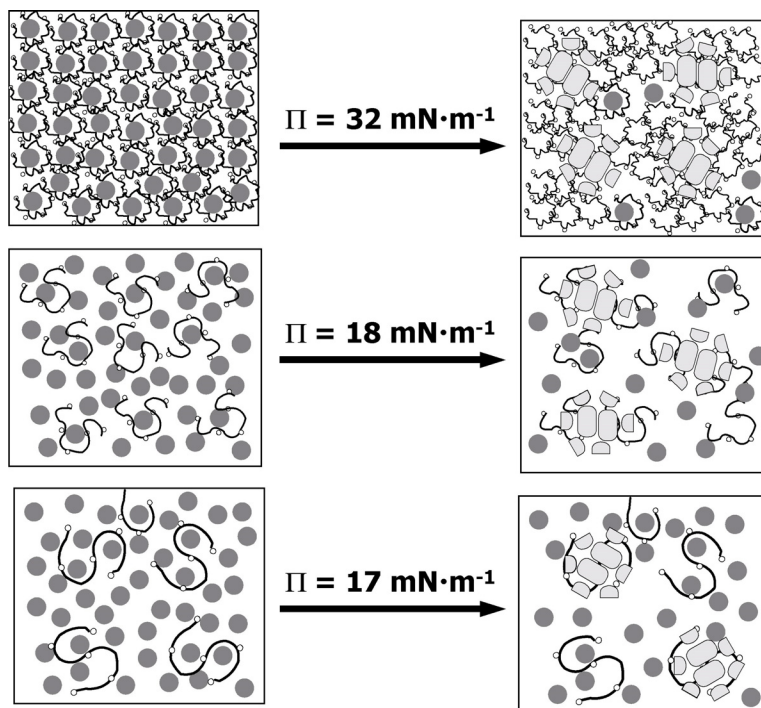


Figure 6.10: A proposed aggregation mechanism of mixed thin films of PDMS-PO:trisilanolisobutyl-POSS at A/W for $A_{POSS} = 120 \text{ \AA}^2 \cdot \text{monomer}^{-1}$ (top view): (a) 1:1 mol ratio ($\sim 20 \text{ wt\% POSS}$, $\Pi = 32 \text{ mN} \cdot \text{m}^{-1}$), (b) 1:5 mol ratio ($\sim 28 \text{ wt\% POSS}$, $\Pi = 18 \text{ mN} \cdot \text{m}^{-1}$), and (c) 1:10 mol ratio ($\sim 68 \text{ wt\% POSS}$, $\Pi = 17 \text{ mN} \cdot \text{m}^{-1}$). Mole ratio is calculated on a per molecule basis. The left side of the figure represents the film state prior to collapse. The dark grey circles correspond to trisilanolisobutyl-POSS in the monolayer, the light-grey half-ovals correspond to monomeric trisilanolisobutyl-POSS in the multilayer, light grey ovals correspond to dimeric trisilanolisobutyl-POSS in the multilayer, and black chains correspond to PDMS-PO with small open white circles depicting PO functional groups.

6.5 Conclusions

Trisilanolisobutyl-POSS blends with PDMS made polar through the use of pendent phosphine oxide groups (PDMS-PO) exhibit dramatically different surface morphologies upon collapse of the POSS component in Langmuir films than the corresponding blends with regular PDMS.¹⁶⁸ Whereas PDMS/trisilanolisobutyl-POSS blends form irregular aggregates of multilayer POSS-rich domains upon compression and network-like structures upon expansion at high POSS weight fractions, PDMS-PO/trisilanolisobutyl-POSS blends form uniform aggregates which never coalesce into larger aggregates over the accessible surface concentration range, and remain dispersed upon expansion for <80 wt% POSS. This difference in aggregation is attributed to the formation of surface micelles in the PDMS-PO/trisilanolisobutyl-POSS system, where hydrogen bonding between the POSS-rich aggregates and PDMS-PO lead to steric stabilization of the POSS-rich multilayer aggregates. Assuming the proposed mechanism is correct, it provides tremendous insight into enhancing POSS/polymer compatibility through the use of trisilanol-POSS derivatives and appropriate polar functional comonomers for producing better POSS/polymer nanocomposites.

In Chapter 7, the blending behavior of one closed-cage non-amphiphilic POSS derivative (octaisobuylyl-POSS, Chapter 3) with amphiphilic PDMS is investigated. For this study, we hope to reveal the aggregation mechanism for this “real” nanofiller in polymeric matrix. Due to its non-amphiphilicity, the thermodynamics analysis methods adopted in Chapter 5 and 6 will be not appropriate and new analyses routes are required.

CHAPTER 7

Blends of Amphiphilic Poly(dimethylsiloxane) and Non-Amphiphilic Octaisobutyl-POSS at the Air/Water Interface

The following chapter appeared as an article in Langmuir, Volume 21, No. 6, (2005) 2250-2259.

7.1 Abstract

In Chapters 5 and 6, the detailed results from different blends of PDMS and a polar derivative with amphiphilic trisilanolisobutyl-POSS were discussed. In this chapter, we will explore the interfacial behavior of PDMS blends with a closed cage non-amphiphilic POSS, octaisobutyl-POSS. The results obtained from Brewster angle microscopy (BAM) and surface pressure – area per monomer (Π - A) isotherm studies in Chapter 3 shows that non-amphiphilic polyhedral oligomeric silsesquioxane (POSS) nanofiller, octaisobutyl-POSS, forms aggregates at all surface concentrations at the air/water interface. When amphiphilic poly(dimethylsiloxane) (PDMS) is blended with octaisobutyl-POSS (> 10 wt% PDMS) the degree of POSS aggregation dramatically decreases. Thermodynamic analyses and morphology studies through Π - A isotherm data and BAM, respectively, exhibit three distinct composition regimes: (1) Blends with > 70 wt% POSS have unstable isotherms whose shapes deviate from PDMS and form large rigid domains comparable to, but smaller than pure, octaisobutyl-POSS films; (2) At compositions between \approx 40 and 70 wt% POSS, the isotherms' features are qualitatively similar to pure PDMS, and extensive nanofiller "networks" are observed by BAM; and

(3) For compositions $\leq \approx 30$ wt% POSS, the isotherms are essentially those of pure PDMS with small POSS domains dispersed in the PDMS matrix. These results provide further insight into nanofiller aggregation mechanisms and dispersion that may be present in thicker films and bulk systems.

7.2 Introduction

Polyhedral oligomeric silsesquioxane (POSS) molecules have attracted increasing attention over the past two decades. Arising from silsesquioxane chemistry, $(\text{SiO}_{3/2})_n$, first reported in 1946,²⁰⁴ POSS molecules consist of rigid polyhedral inorganic nanostructured skeletons with flexible organic coronae.^{125,127,154,178,202,203} The unique hybrid organic-inorganic structure and size (≈ 1.5 nm diameters and molecular weights $\approx 1 \text{ kg}\cdot\text{mol}^{-1}$) make POSS the smallest possible particles of silica with applications in shape memory materials,²²³ semi-conducting polymers,²³⁶ self-healing and space-survivable coatings,^{173,174} as well as synthetic templates for nanostructured materials.^{148,160,198-201,237} The incorporation of POSS into polymeric systems has led to materials with improved physical properties such as low- k dielectric constants,^{137,152,156,224} elevated glass transition temperatures (T_g),^{130,205} increased thermal decomposition temperatures and reduced flammability.¹⁴³

POSS' interfacial properties are important for future applications in nanotechnology; however, relatively little is known about the surface properties of POSS systems.¹⁶³⁻¹⁶⁵ Recently, a number of studies have shown that trisilanol-POSS derivatives form stable Langmuir monolayers,^{166,167,169} while completely condensed POSS cages do not.¹⁶⁶ This feature has led to the study of POSS as a model "two-dimensional" (2D)

nanofiller. Hottle, et al. reported Langmuir film studies that showed monolayer blends of amphiphilic trisilanolisobutyl-POSS and amphiphilic poly(dimethylsiloxane) (PDMS) form positive deviation mixtures in the presence of an attractive surface (water) (Chapter 5).¹⁶⁸ Additionally, they showed that in the multilayer regime trisilanolisobutyl-POSS blends with PDMS form network-like aggregates of filler particles. In a follow-up study, Kim et al. showed these network-like aggregates could be converted to uniform dispersions of homogeneous "particle" aggregates by using a PDMS derivative that was modified by polar phosphine oxide substituents (Chapter 6).¹⁷⁰

Previous studies have shown that PDMS is surface-active and forms monolayer and multilayer films at A/W.^{168,170,195,211-213} This chapter focuses on the compatibility of non-amphiphilic octaisobutyl-POSS¹⁶⁶ and amphiphilic PDMS²¹¹ as blend films at the air/water interface (A/W) by monitoring their interactions with the Wilhelmy plate technique and Brewster angle microscopy (BAM). This system has been chosen as a model for a traditional filler system in quasi-2D. For the sake of this chapter, a traditional filler is defined as a physical dispersion of filler particles (octaisobutyl-POSS) within a polymer matrix (PDMS) yielding similar or improved properties (in this case interfacial tension) relative to the pure system with substantially smaller amounts of polymer. Given the structural similarity between the PDMS matrix and the octaisobutyl-POSS molecule (a model filler of nanometer dimensions), this system should represent an ideal case for studying nanofiller dispersion in "2D" films in the absence of strongly favorable enthalpic filler-matrix interactions. In this study, the entire composition range, 0–100 wt% PDMS, is probed and an in-depth examination of the dispersion of

Chapter 7

octaisobutyl-POSS in PDMS with comparisons to the trisilanolisobutyl-POSS/PDMS blend system¹⁶⁸ is presented.

7.3 Experimental

7.3.1 Materials

Octaisobutyl-POSS (HybridPlastics, Inc.) and PDMS ($M_n = 7.5 \text{ kg}\cdot\text{mol}^{-1}$, $M_w/M_n = 1.09$, Polymer Source, Inc.) were used without further purification. Spreading solutions were made by dissolving the pure components in chloroform ($\approx 0.5 \text{ mg}\cdot\text{g}^{-1}$, HPLC grade). The samples were allowed to dissolve for at least 24 h.

7.3.2 Isotherm Studies

The blend was spread onto the surface of a standard Langmuir trough (500 cm^2 , Nima Technology, 601BAM) filled with ultrapure $18.2 \text{ M}\Omega$ water (Millipore, Milli-Q Gradient A-10) maintained at $22.5 \text{ }^\circ\text{C}$ in a PlexiglasTM box with a relative humidity of 70 – 75%. The surface pressure, Π , was determined by the Wilhelmy plate method using a paper plate. In order to investigate the thermodynamic properties of the octaisobutyl-POSS/PDMS blends, four methods were utilized to vary the surface concentration: (1) "compression" of the barriers at a constant rate, (2) "hysteresis" loops, (3) "relaxation" experiments, and (4) successive "addition" of spreading solution at a fixed surface area (the portions in quotation marks indicate the short form used throughout the paper). For compression experiments and hysteresis loops, the sample was compressed at a rate of $15 \text{ cm}^2\cdot\text{min}^{-1}$ to an arbitrary average area per monomer value, $\langle A \rangle$, and were immediately expanded at the same rate back to the initial trough area of 480 cm^2 . The hysteresis method was used to test the reversibility of the different structural stages of the film. For

relaxation experiments, each sample was compressed at a speed of $15 \text{ cm}^2 \cdot \text{min}^{-1}$ to a final compressed area per PDMS monomer of, $A_{PDMS} \approx 5 \text{ \AA}^2 \cdot \text{monomer}^{-1}$ unless otherwise noted. The barriers were held at that position, and the sample was allowed to relax to a constant Π value (defined as $\Delta\Pi < 0.1 \text{ mN} \cdot \text{m}^{-1}$ over a one hour time frame) at a constant surface concentration. For successive addition experiments, the surface area was held constant and successive additions of spreading solution were made to vary the surface concentration. After each addition, Π was allowed to relax to a constant minimum value $\Delta\Pi < 0.1 \text{ mN} \cdot \text{m}^{-1}$ over a 15 min time frame after allowing at least 15 minutes for the spreading solvent to evaporate. For low surface pressures, the total relaxation time including solvent evaporation was on the order of 30 min, while times on the order of 1 h were necessary in the collapsed regimes.

7.3.3 Brewster Angle Microscopy (BAM)

BAM studies (MiniBAM, NanoFilm Technologie GmbH, with linear resolution of at least $20 \text{ }\mu\text{m}$) were carried out simultaneously during the isotherm measurements, and the BAM images were taken with a CCD camera. The BAM images presented in this chapter are $4.8 \times 6.4 \text{ mm}^2$ unless specifically noted. In order to minimize vibrations, the entire configuration (Langmuir trough, BAM, and Plexiglas™ box) rests on a floating optical table.

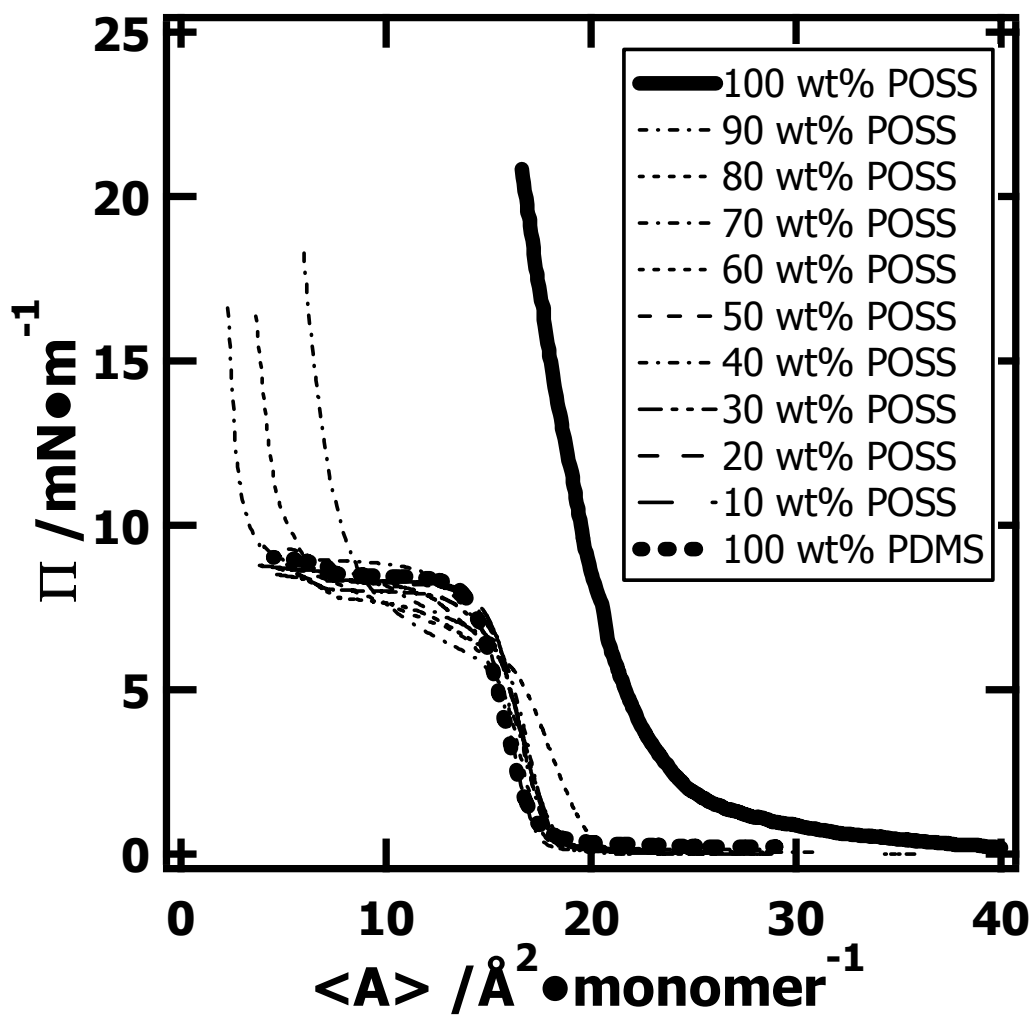


Figure 7.1: Π - $\langle A \rangle$ compression isotherms for octaisobutyl-POSS blends with PDMS at 22.5 °C and a compression rate of 15 cm²·min⁻¹. Specific details for individual blends are more clearly revealed in Figure 7.3.

7.4 Results and Discussion

7.4.1 Compression Isotherm Studies of the Blends

Figure 7.1 shows a plot of surface pressure, Π , as a function of the average area per monomer, $\langle A \rangle$, for each blend of octaisobutyl-POSS with PDMS. The isotherm for pure octaisobutyl-POSS is consistent with a non-amphiphilic material. Extrapolation of the steepest portion of the isotherm back to the x-axis yields a limiting area per molecule, $A_o \approx 18 \text{ \AA}^2 \cdot \text{monomer}^{-1}$. Given the fact that there is no significant size difference between octaisobutyl-POSS and trisilanolisobutyl-POSS, which has a limiting area of $A_o \approx 175 \text{ \AA}^2 \cdot \text{monomer}^{-1}$,^{166,169} means that octaisobutyl-POSS must exist in a multilayer state at all A in this study. This feature is illustrated in Figure 7.2 for BAM images taken during the compression of pure octaisobutyl-POSS films, where POSS aggregates immediately upon spreading and remains aggregated for all Π at A/W. Returning to Figure 7.1, PDMS lies at the other extreme of composition. The PDMS isotherm is in good agreement with previous studies.^{168,195,211-213} PDMS forms a liquid-like monolayer with $A_o \approx 18 \text{ \AA}^2 \cdot \text{monomer}^{-1}$ and exhibits an initial collapse transition at $\Pi_C \approx 8 \text{ mN} \cdot \text{m}^{-1}$. At $A \approx 7.5 \text{ \AA}^2 \cdot \text{monomer}^{-1}$, there is a second transition to a plateau of $\Pi \approx 9 \text{ mN} \cdot \text{m}^{-1}$. The second plateau led Fox et al. to propose a helical model for PDMS conformations at A/W,²¹¹ although more recent studies favor a multilayer model which will be assumed here.^{195,212,213} Unlike the multilayers of octaisobutyl-POSS, the narrow molecular weight distribution PDMS used here exhibits homogeneous BAM images at all A , as reported elsewhere.¹⁹⁵

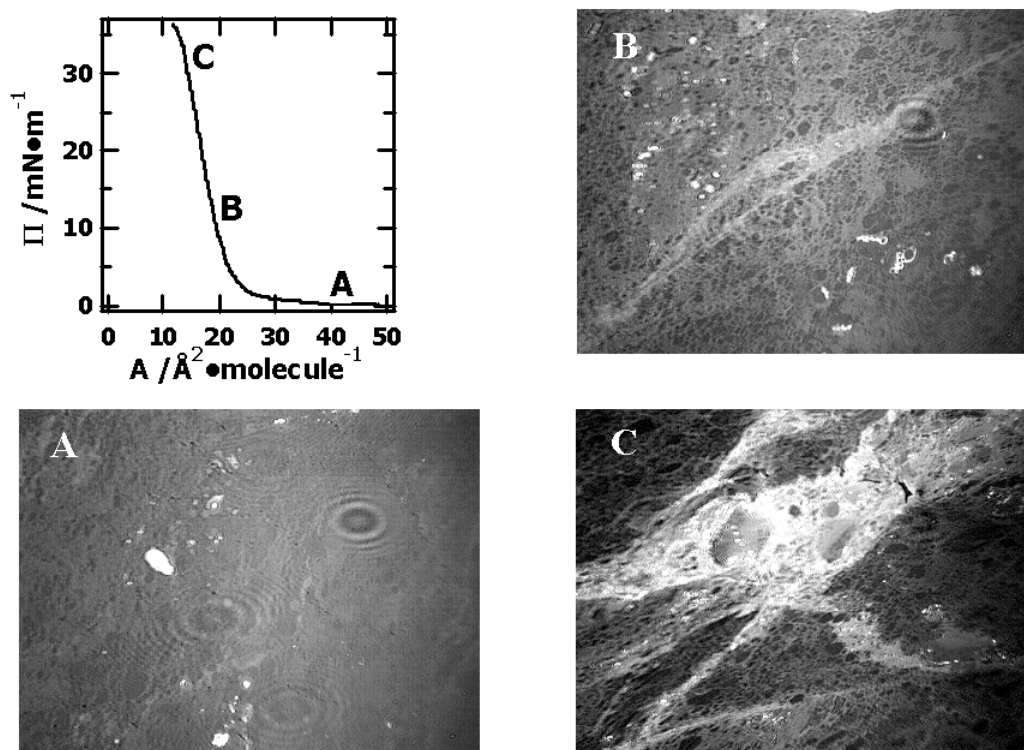


Figure 7.2: BAM images upon compression of an pure octaisobutyl-POSS Langmuir film at 22.5 °C and a compression rate of $15 \text{ cm}^2 \cdot \text{min}^{-1}$. The letters on the Π - A isotherm show the positions where the BAM images were obtained. Solid-like domains appear bright in the $4.8 \times 6.4 \text{ mm}^2$ BAM images.

The other remarkable feature of Figure 7.1 is the fact that all the mixed isotherms show approximately the same $\langle A_o \rangle$ values and isotherm shapes as pure PDMS. These

features mean that octaisobutyl-POSS has a traditional filler effect for $\Pi < \approx 6 \text{ mN}\cdot\text{m}^{-1}$. Under these conditions, octaisobutyl-POSS resides at the surface, but the surface tension properties are similar to what one would get for pure PDMS films. As seen in Figure 7.3, for $\Pi > \approx 6 \text{ mN}\cdot\text{m}^{-1}$, there is significant deviation from the Π - A isotherm of PDMS with increasing wt% POSS. The deviation is further highlighted in Figure 7.4 which shows a plot of the onset pressure for collapse, Π_C , as a function of the wt% POSS, as well as the plateau pressure value, Π_{plateau} , for the mixture's analog to the first plateau of the pure PDMS isotherm. As seen in Figure 7.4, all of the blend films show deviation from the pure PDMS isotherm around $\Pi_C \approx 6 \text{ mN}\cdot\text{m}^{-1}$, and exhibit composition dependent Π_{plateau} values. The presence of octaisobutyl-POSS can also affect the second transition of PDMS at $A \approx 8 \text{ \AA}^2\cdot\text{monomer}^{-1}$. For 70 to 90 wt% octaisobutyl-POSS, there is not a distinct plateau corresponding to the first plateau of the PDMS isotherm. Instead, there is a change in slope as the octaisobutyl-POSS collapses out of the PDMS with Π eventually rising to the Π_{plateau} value for PDMS near the end of the plateau for the pure PDMS isotherm. Subsequently, there is a sharp rise in Π similar to pure octaisobutyl-POSS at an $\langle A \rangle$ value where pure PDMS would show its transition to a second plateau. Similarly, for $40 < \text{wt\% octaisobutyl-POSS} < 70$, the first plateau is not as long as the one observed for pure PDMS films, and the transition to a second plateau like pure PDMS is not nearly as sharp. Finally, for $< \approx 40 \text{ wt\% octaisobutyl-POSS}$, the plateau behavior of the isotherms is qualitatively similar to pure PDMS. While the preceding discussion has treated octaisobutyl-POSS as a filler, and considered how POSS affects the properties of PDMS, it is also useful to consider things from the perspective of octaisobutyl-POSS.

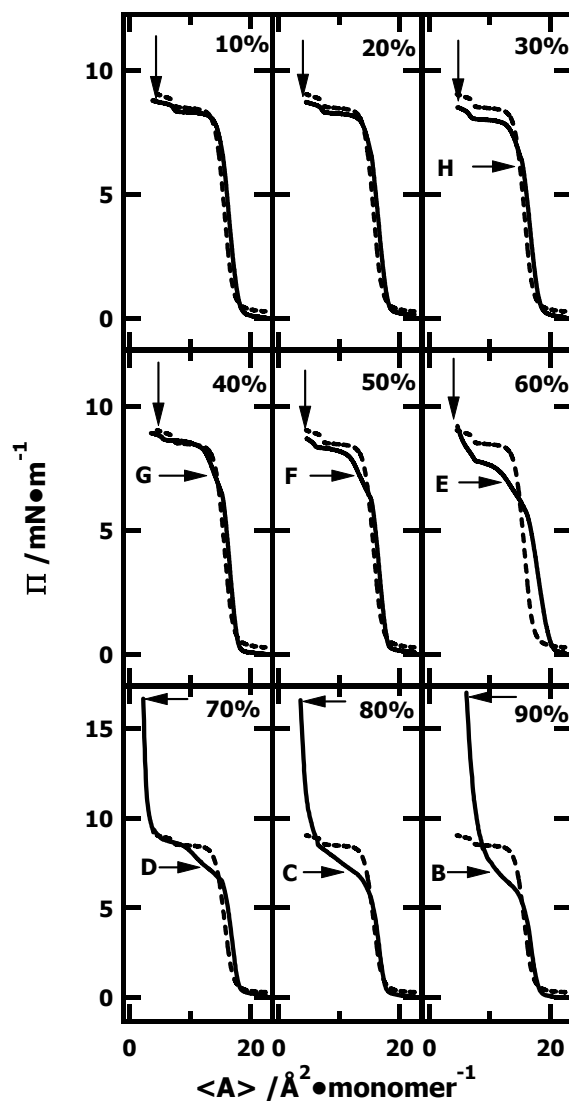


Figure 7.3: Separated replots of each isotherm in Figure 7.1. In order to more clearly see the effect of octaisobutyl-POSS on the transitions of PDMS, each Π - A isotherm in Figure 7.1 is plotted separately along with the pure PDMS isotherm. The percentage in the upper right-hand corner of each plot represents the wt% POSS present in the blend. The solid line (—) corresponds to the blend isotherm and the dashed line (---) represents the pure PDMS isotherm. The arrows without letters indicate the points where expansion of the film started for the hysteresis experiments in Figures 7.7-7.11. The horizontal arrows that point to the right labeled with letters indicate the points where the corresponding BAM images presented in Figure 7.6 were taken.

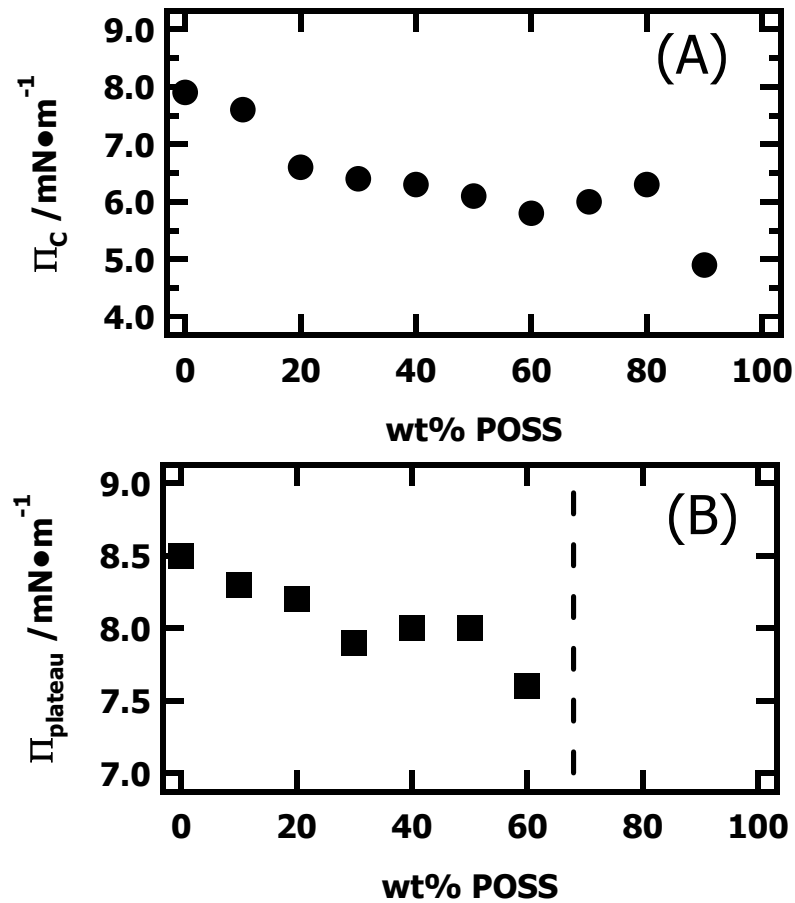


Figure 7.4: Π_C and 1st "PDMS" Π_{plateau} value as a function of wt% POSS: From the Π - $\langle A \rangle$ isotherms presented in Figures 7.1 and 7.3, (A) shows Π_C of the isotherms plotted as a function of wt% POSS, and (B) provides a plot of the first "PDMS" Π_{plateau} value as a function of wt% POSS. As seen in Figure 7.3, no distinct plateau corresponding to PDMS collapse is observed in the blends for ≥ 70 wt% octaisobutyl-POSS (right of dashed line on (B)).

As seen in Figure 7.1, the addition of as little as 10wt% PDMS causes the octaisobutyl-POSS isotherm to shift dramatically. In fact, Π - $\langle A \rangle$ isotherms for the

Chapter 7

mixtures of octaisobutyl-POSS with PDMS all exhibit the same lift-off area per monomer ($\langle A \rangle$ value where Π rises from zero) within experimental error. Unfortunately, unlike blends of PDMS and trisilanolisobutyl-POSS (an open cage form of octaisobutyl-POSS),¹⁶⁸ the octaisobutyl-POSS blends with PDMS do not have a gradual transition from the pure POSS isotherm to the pure PDMS isotherm due to the non-amphiphilic nature of octaisobutyl-POSS, thereby complicating thermodynamic analyses of the mixing behavior. Because octaisobutyl-POSS fails to form a true monolayer, traditional treatments of mixing in terms of differences in experimental A vs. expected values from ideal mixing, and determinations of the excess Gibbs free energy of mixing become meaningless. Hence a different approach is required.

Considering the fact that all of the blend isotherms in Figures 7.1 and 7.3 have an appearance that is more like PDMS than octaisobutyl-POSS, the surface behavior of the blends will be considered in terms of the PDMS component. Figure 7.5A shows the same data in Figure 7.1 plotted as a function of the area per PDMS repeating unit, A_{PDMS} , which is calculated solely on the basis of the amount of PDMS spread on the surface and the trough area. This calculation is equivalent to assuming that no octaisobutyl-POSS was spread. As expected, there is a shift to larger A_{PDMS} with increasing wt% POSS without a dramatic change in the shape of the isotherm for $\Pi < \approx 6 \text{ mN}\cdot\text{m}^{-1}$. A working hypothesis for explaining this behavior is that non-amphiphilic POSS acts like a "true" filler in the sense that it occupies trough area and excludes PDMS, thereby confining PDMS to a smaller surface area and causing larger apparent A_{PDMS} values for the same Π values. Given the fact that the shapes of the curves are similar, it appears that

octaisobutyl-POSS' only contribution to the surface tension change is making the effective surface area smaller.

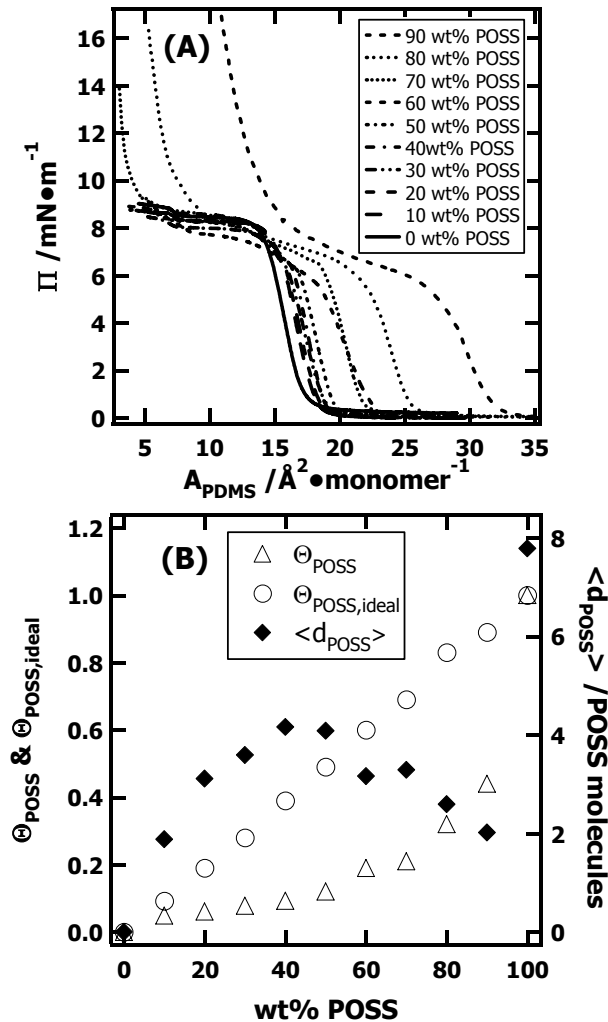


Figure 7.5: (A) Π - A_{PDMS} compression isotherms for octaisobutyl-POSS blends with PDMS at 22.5 °C and a compression rate of $15 \text{ cm}^2\cdot\text{min}^{-1}$. This plot was obtained by converting the $\langle A \rangle$ values from Figure 7.1 to A_{PDMS} values for each blend isotherm. (B) Plots of Θ_{POSS} and $\Theta_{POSS,ideal}$ (left axis) and $\langle d_{POSS} \rangle$ (right axis) as a function of wt% POSS at $\Pi = 5 \text{ mN}\cdot\text{m}^{-1}$. The values on the right hand axis represent the average POSS domain thickness in terms of the number of POSS molecules.

Chapter 7

Assuming this hypothesis is correct, it is then possible to estimate the fraction of the surface that is occupied by octaisobutyl-POSS as well as the average thickness of the POSS-rich domains. If one assumes a perfectly immiscible system where the octaisobutyl-POSS is not surface active but excludes POSS from part of the surface, the area fraction of the surface covered by PDMS at a given Π value is defined as:

$$\Theta_{PDMS}(\Pi) = \frac{A_{PDMS,pure}(\Pi)}{A_{PDMS,mix}(\Pi)} \quad [7.1]$$

Values of the octaisobutyl-POSS area fraction in the binary system,

$$\Theta_{POSS}(\Pi) = 1 - \Theta_{PDMS}(\Pi) \quad [7.2]$$

can then be compared to expectations based on ideal mixing where all octaisobutyl-POSS exists on the surface as a film of unimolecular thickness. For ideal mixing the average area per repeating unit is defined as:

$$\langle A_{ideal} \rangle = X_{PDMS} A_{PDMS,pure}(\Pi) + X_{POSS} A_{POSS,pure}(\Pi) \quad [7.3]$$

where X_{PDMS} and X_{POSS} , and $A_{PDMS,pure}(\Pi)$ and $A_{POSS,pure}(\Pi)$ correspond to the mole fractions of PDMS or octaisobutyl-POSS, and the molecular areas of a PDMS repeat unit and an octaisobutyl-POSS molecule in a pure monolayer, respectively. Based on eq. 7.3, the ideal area fraction of octaisobutyl-POSS is simply given as:

$$\Theta_{POSS,ideal}(\Pi) = \frac{X_{POSS} A_{POSS,pure}(\Pi)}{X_{PDMS} A_{PDMS,pure}(\Pi) + X_{POSS} A_{POSS,pure}(\Pi)} \quad [7.4]$$

Table 7.1: Area fractions and average thicknesses of octaisobutyl-POSS blends with PDMS at $\Pi = 5 \text{ mN}\cdot\text{m}^{-1}$.

$wt\% \text{ POSS}$	X_{POSS}	$A_{\text{PDMS,mix}}(\Pi)$	$\Theta_{\text{POSS}}^{\text{b}}$	$\Theta_{\text{POSS,ideal}}^{\text{c}}$	$\langle d_{\text{POSS}} \rangle^{\text{d}}$
0	0	15.4 ^a	0	0	0
10	0.0092	16.2	0.049	0.092	1.9
20	0.021	16.4	0.061	0.19	3.1
30	0.035	16.7	0.078	0.28	3.6
40	0.055	17.0	0.093	0.39	4.2
50	0.080	17.5	0.12	0.49	4.1
60	0.12	19.0	0.19	0.60	3.2
70	0.17	19.6	0.21	0.69	3.3
80	0.31	22.6	0.32	0.83	2.6
90	0.43	27.5	0.44	0.89	2.0
100	1	N/A	1	1	7.8 ^e

^a $A_{\text{PDMS,pure}}(\Pi)$, ^bFrom eq.7.2,

^cFrom Eq. 7.4 using $A_{\text{POSS,pure}}(5 \text{ mN}\cdot\text{m}^{-1}) = 168 \text{ \AA}^2\cdot\text{molecule}^{-1}$, ^dFrom eq. 7.5,

^eCalculated from $A_{\text{Trisilanolisobutyl-POSS}}(5 \text{ mN}\cdot\text{m}^{-1})/A_{\text{Octaisobutyl-POSS}}(5 \text{ mN}\cdot\text{m}^{-1})$.

To apply eq. 7.4, reasonable estimates of $A_{\text{POSS,pure}}(\Pi)$ for octaisobutyl-POSS in a monolayer state are required. As octaisobutyl-POSS is non-amphiphilic, values for trisilanolisobutyl-POSS are used as their sizes are expected to be similar. Table 7.1 summarizes experimental and calculated parameters for the octaisobutyl-POSS blend with PDMS at $\Pi = 5 \text{ mN}\cdot\text{m}^{-1}$, assuming $A_{\text{POSS,pure}}(\Pi) = 168 \text{ \AA}^2\cdot\text{molecule}^{-1}$ and using $A_{\text{PDMS,pure}}(\Pi) = 15.4 \text{ \AA}^2\cdot\text{molecule}^{-1}$. As seen in Table 7.1, $\Theta_{\text{POSS}}(\Pi)$ obtained according to eq. 7.2 differs from $\Theta_{\text{POSS,ideal}}(\Pi)$ obtained from eq. 7.4. Interestingly, this difference systematically decreases with decreasing wt% POSS in the blend as seen in Figure 7.5B. Another important point is that $\Theta_{\text{POSS,ideal}}(\Pi)$ is always larger than the corresponding $\Theta_{\text{POSS}}(\Pi)$ values obtained through eq. 7.2. This feature is expected for a perfectly immiscible system, where the non-amphiphilic octaisobutyl-POSS is known to form

Chapter 7

inhomogeneous three dimensional (3D) aggregates at all surface concentrations (Figure 7.2). Using an equation similar to eq. 7.1, the average thickness of POSS domains in the blend is given by:

$$\langle d_{POSS} \rangle = \frac{\Theta_{POSS,ideal}(\Pi)}{\Theta_{POSS}(\Pi)} \quad [7.5]$$

The $\langle d_{POSS} \rangle$ values obtained from eq. 7.5 represent the average thickness in terms of the number of POSS molecules for the multilayer 3D aggregates. These values are also summarized in Table 7.1 and on Figure 7.5B (plotted on the right-hand axis). Interestingly, this analysis of the isotherm data suggests that PDMS is capable of physically disrupting octaisobutyl-POSS aggregation at the surface. As all favorable thermodynamic interactions have been eliminated (the assumption of a perfectly immiscible system), this model is the surface analog to the physical mixing of filler particles in bulk systems. Another key feature is that if one takes a ratio of pure component molecular areas at $5 \text{ mN}\cdot\text{m}^{-1}$, $A_{Trisilanolisobutyl-POSS}(5 \text{ mN}\cdot\text{m}^{-1})/A_{Octaisobutyl-POSS}(5 \text{ mN}\cdot\text{m}^{-1})$, the approximate average film thickness in pure octaisobutyl-POSS films (Figure 7.2) is ≈ 8 POSS molecules. This value is at least 2X larger than all of the blend films indicating that PDMS dramatically improves the dispersion of non-amphiphilic octaisobutyl-POSS at A/W below Π_C . In the next section, the validity of the hypothesis that PDMS physically disperses POSS is examined by BAM.

7.4.2 BAM Image Analyses for Compression Isotherms

In the preceding discussion, the addition of as little as 10 wt% PDMS to octaisobutyl-POSS induced dramatic changes in the Π - A isotherms (Figures 7.1 – 7.3). The subsequent analysis of the isotherms suggests that there must be a dramatic change in the degree of octaisobutyl-POSS aggregation within the blend films through physical

dispersion of the POSS component. In order to test this hypothesis, BAM was used to track changes in surface morphology with changes in blend composition. Figure 7.6 shows representative BAM micrographs obtained during compression for different blend compositions. In order to make an initial comparison, A_{PDMS} is fixed at $A_{PDMS} = 15 \text{ \AA}^2 \cdot \text{monomer}^{-1}$, a value that corresponds to $\Pi \approx 6 \text{ mN} \cdot \text{m}^{-1}$ on the pure PDMS isotherm. At this point, all of the blend isotherms except for 90 wt% octaisobutyl-POSS exhibit something that resembles an isobestic point in spectroscopy ($\Pi \approx 7 \text{ mN} \cdot \text{m}^{-1}$, Figure 7.5A). In contrast the 90 wt% octaisobutyl-POSS ($\Pi \approx 8.5 \text{ mN} \cdot \text{m}^{-1}$) and the pure octaisobutyl-POSS films ($\Pi \approx 30 \text{ mN} \cdot \text{m}^{-1}$) have significantly greater Π values. At $A_{PDMS} = 15 \text{ \AA}^2 \cdot \text{monomer}^{-1}$, as well as $\Pi < 8 \text{ mN} \cdot \text{m}^{-1}$, the PDMS homopolymer forms a homogeneous monolayer,^{195,212,213} while octaisobutyl-POSS at $A_{POSS} = 15 \text{ \AA}^2 \cdot \text{monomer}^{-1}$, as well as $\Pi = 7 \text{ mN} \cdot \text{m}^{-1}$, forms an extremely heterogeneous multilayer film (Figure 7.2C or 7.6A).¹⁶⁷ The features of the mixed isotherms at $A_{PDMS} = 15 \text{ \AA}^2 \cdot \text{monomer}^{-1}$ are not surprising as all the films have sufficient PDMS present to form a nearly complete monolayer independent of any octaisobutyl-POSS that is present. Hence, between Π_C and the isobestic point, octaisobutyl-POSS must be squeezed out of the interface with essentially all of the PDMS remaining at A/W. As seen in Figure 7.6, there appear to be three distinct regimes corresponding to the multilayer state formed as octaisobutyl-POSS is squeezed out of the interface: (I) $\Pi > \approx 70 \text{ wt\%}$ octaisobutyl-POSS, where "sheet-like" morphologies are similar to pure octaisobutyl-POSS films; (II) $\approx 40 \leq \Pi \leq \approx 70 \text{ wt\%}$ octaisobutyl-POSS where ring- or network-like aggregates form; and (III) $\Pi \leq \approx 30 \text{ wt\%}$ octaisobutyl-POSS where only small aggregates form. It should be noted that BAM

images for both the 40 and 50 wt% octaisobutyl-POSS films in Figure 7.6 show behavior that is qualitatively closer to Regime III behavior than Regime II behavior as any ring-like structures are small and difficult to see in BAM images during compression experiments. However, their behavior during hysteresis, relaxation, and addition experiments clearly places them into Regime II. In order to better understand the aggregation behavior of octaisobutyl-POSS in PDMS blends, hysteresis experiments were also performed in each regime.

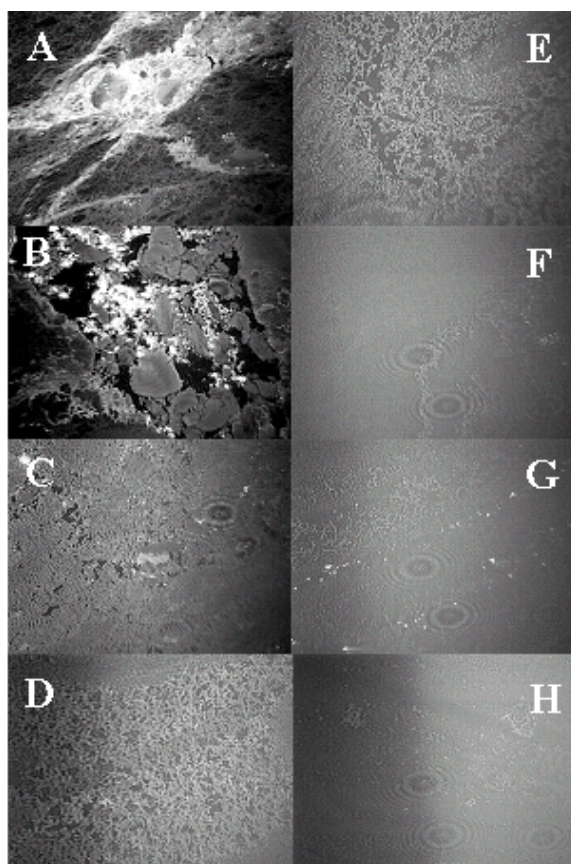


Figure 7.6: BAM images upon compression for different octaisobutyl-POSS/PDMS blends (wt % POSS, $\langle A \rangle / \text{\AA}^2 \cdot \text{monomer}^{-1}$, $\Pi / \text{mN} \cdot \text{m}^{-1}$): A (100, 16.0, 23.3), B (90, 10.9, 7.3), C (80, 12.0, 6.8), D (70, 12.4, 7.0), E (60, 13.1, 6.9), F (50, 13.3, 7.3), G (40, 14.6, 7.5) and H (30, 15.5, 6.1). The $\langle A \rangle$ value for image A corresponds to $A_{POSS} = 16.0 \text{ \AA}^2 \cdot \text{molecule}^{-1}$ and the $\langle A \rangle$ values B – H correspond to a PDMS concentration of $A_{PDMS} \approx 15.0 \text{ \AA}^2 \cdot \text{molecule}^{-1}$. The points where the BAM images for the blends were taken are indicated by horizontal arrows that point to the right and the corresponding letters on Figure 7.3. Solid-like domains appear bright in the $4.8 \times 6.4 \text{ mm}^2$ images.

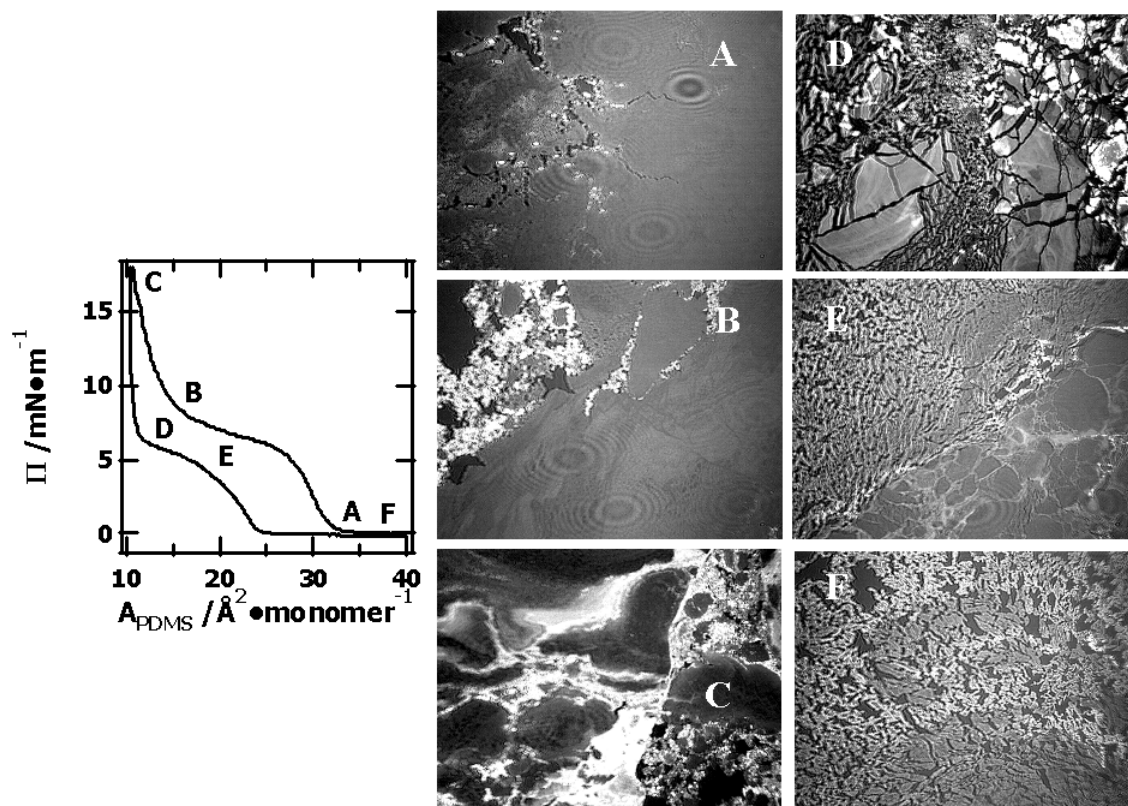


Figure 7.7: BAM images obtained during a hysteresis experiment at 22.5 °C and a compression rate of 15 cm²·min⁻¹ for a 90 wt% octaisobutyl-POSS blend with PDMS. The letters on the Π - A_{PDMS} isotherm indicate where individual BAM images were taken. The points also correspond to (Image, $\langle A \rangle / \text{\AA}^2 \cdot \text{monomer}^{-1}$, $\Pi / \text{mN} \cdot \text{m}^{-1}$): (A, 24.0, 0), (B, 13.1, 6.4), (C, 6.5, 14.8), (D, 8.0, 5.6), (E, 11.5, 3.2), and (F, 32.1, 0). Solid-like domains appear bright in the 4.8 × 6.4 mm² images.

7.4.3 Hysteresis Experiments

BAM images from compression experiments (Figure 7.6) that identified three morphological regimes based on blend composition have prompted hysteresis experiments to further explore the aggregation process. Figure 7.7 shows a hysteresis loop, representative of Regime I ($> \approx 70$ wt% octaisobutyl-POSS), for compression deep into the collapsed multilayer region for a 90 wt% octaisobutyl-POSS blend with PDMS. Much like the compression data for octaisobutyl-POSS, compression to $\Pi > 9 \text{ mN}\cdot\text{m}^{-1}$ leads to large thick aggregates (brightest structures in Figure 7.7C). Upon expansion, these large domains "shatter" much like a glass (Figure 7.7D) before forming dense ring-like structures at $\Pi = 0 \text{ mN}\cdot\text{m}^{-1}$ (Figure 7.7F). In this region (Figure 7.7F), the morphology is qualitatively similar to what one might expect for coexisting gas and liquid domains in a PDMS film.¹⁹⁵ These ring-like structures arise because of the competing effects of line tension and dipole density.²³⁸ Normally, the L/G coexistence regime can not be seen for narrow polydispersity PDMS samples like the one used in this study.¹⁹⁵ Here, the octaisobutyl-POSS appears to reside within and above the liquid-like PDMS portion of the film, essentially serving as a marker to enhance optical contrast in BAM between the L and G phases.

As an example of representative behavior for Regime II (≈ 40 to 70 wt% octaisobutyl-POSS), Figure 7.8 shows a hysteresis loop and BAM images for a 70 wt% octaisobutyl-POSS blend with PDMS. Drawing on Figure 7.8, this regime is characterized by several features. Starting at $\Pi = 0$, ring-like morphologies corresponding to L/G coexistence where octaisobutyl-POSS is located in the liquid-like PDMS phase (Figure 7.8A and 7.8F) are observed. Compressing the film at (A) leads to

the formation of a liquid-like "monolayer" (Figure 7.8B, $0 < \Pi < 6 \text{ mN}\cdot\text{m}^{-1}$) that can best be described as "homogeneously heterogeneous". At this point, the large irregular POSS domains in Figure 7.2 (pure octaisobutyl-POSS) have been broken up into much smaller domains that appear to be significantly more uniform in size and shape. Compression into the region corresponding to the second plateau of PDMS does not dramatically alter this morphology (Figure 7.8C), but does cause some thickening of the multilayer domains. While we could not easily observe the regime where Π increases again at the end of the 70 wt% octaisobutyl-POSS blend (Figure 7.3 and the isotherm in Figure 7.8) due to the finite compression ratio of the Langmuir trough, it is reasonable to assume that larger POSS aggregates are forming like those seen in Figure 7.2C for pure octaisobutyl-POSS and in Figure 7.7C for a 90 wt% blend of octaisobutyl-POSS with PDMS. Upon expansion of the film in Figure 7.8, one sees that the morphology is qualitatively reversible, a feature that is distinctly different from the behavior seen in Regime I (shown in Figure 7.7 for a 90 wt% blend of octaisobutyl-POSS with PDMS).

Turning to Regime III ($\leq \approx 30 \text{ wt}\%$ octaisobutyl-POSS blended with PDMS), Figure 7.9 shows hysteresis behavior for a 30 wt% blend of octaisobutyl-POSS with PDMS. The first point to show significant structure does not occur until the first plateau during compression (A on Figure 7.9). In the plateau regions, the multilayer films appear to be "homogeneously heterogeneous" (Figure 7.9A through 7.9C). Upon expansion, Figure 7.9D is similar to Figures 7.9A through 7.9C; however, Figure 7.9E shows weak and broken ring-like morphology that suggests two coexisting liquid phases (one POSS-rich and one POSS-poor) that has similarities with the G/L coexistence regime in Figure 7.9F except that the ring-like structures have broken up. Here, it is clear that with

decreasing wt% POSS, the ability of the POSS aggregates to chain into network-like structures is significantly retarded by the PDMS component. For even smaller POSS contents (< 30 wt%) there is essentially no large-scale aggregation.

As seen in the three representative hysteresis loops, there are composition dependent changes during expansion. In order to better see this, Figures 7.10 and 7.11 show representative BAM images during expansion at $\Pi = 4 \text{ mN}\cdot\text{m}^{-1}$ representing a liquid like film, and at $\Pi = 0 \text{ mN}\cdot\text{m}^{-1}$ representing G/L coexistence for films that were initially compressed to the arrows in Figure 7.3, respectively. For Figure 7.11, BAM images were taken at an A_{PDMS} value that was $5 \text{ \AA}^2\cdot\text{monomer}^{-1}$ larger than the point where Π returned to zero upon expansion. The exception to this is pure octaisobutyl-POSS which does not return to $\Pi = 0$ during a hysteresis experiment. Hence a comparable A_{POSS} value was chosen and Π was noted accordingly in the legend of Figure 7.11. As seen in Figure 7.10, there is a progressive change from sheet-like structures (pure octaisobutyl-POSS) to broken sheet structures (Regime I), to ring-like structures (Regime II) and broken rings (Regime III). The formation of the ring-like structures in the liquid-like film is most probably a reflection of a non-equilibrium coexistence of a liquid-like PDMS-rich film with a liquid-like phase rich in solid-like POSS aggregates. This feature is qualitatively similar to the behavior seen in blends of amphiphilic trisilanolisobutyl-POSS.¹⁶⁸ In that study, the authors implied that hydrophobic dimers formed through strong intermolecular hydrogen-bonding similar to the unit cell of trisilanol-POSS crystal structures.¹¹⁹ The similarity in morphology seen here for non-amphiphilic octaisobutyl-POSS supports the interpretation for the trisilanolisobutyl-POSS/PDMS system. Upon expansion into the G/L coexistence region, these POSS

aggregates existing as ring- or network-like structures persist, but occupy a smaller area fraction than at $\Pi = 4 \text{ mN}\cdot\text{m}^{-1}$ (Figure 7.11). Another important feature of Figure 7.11 is that the qualitative appearance of the features still follows the composition regimes previously identified, i.e. denser aggregates at $> 70 \text{ wt}\%$ POSS, definite ring-like structures at intermediate compositions, and the breakdown of the ring-like structures for $\leq \approx 30 \text{ wt}\%$ POSS.

One final facet for the hysteresis experiments is the reversibility of the isotherms. Figures 7.7–7.11 all represented compression deep into the region of the isotherm that had $\langle A \rangle$ corresponding to the multilayer state of PDMS (second plateau). In this respect, the qualitative sizes and shapes of the hysteresis loops are comparable to PDMS, which is known to be almost perfectly reversible prior to the first plateau ($\Pi < 8 \text{ mN}\cdot\text{m}^{-1}$), with a bit greater hysteresis upon compression into the first plateau. Representative hysteresis loops are shown in Figure 7.12 for compression up to Π_C for each composition regime (top graphs), and for compression to an A_{PDMS} value ($\approx 10 \text{ \AA}^2\cdot\text{monomer}^{-1}$) that is sufficiently small to ensure the PDMS component has started to collapse into the multilayer state (bottom graphs). As seen in Figure 7.12, there is a slight composition dependence with larger hysteresis loops for greater wt% POSS, but otherwise, the isotherm and morphological features are consistent with expectations from PDMS homopolymer monolayers and Figures 7.7–7.11.

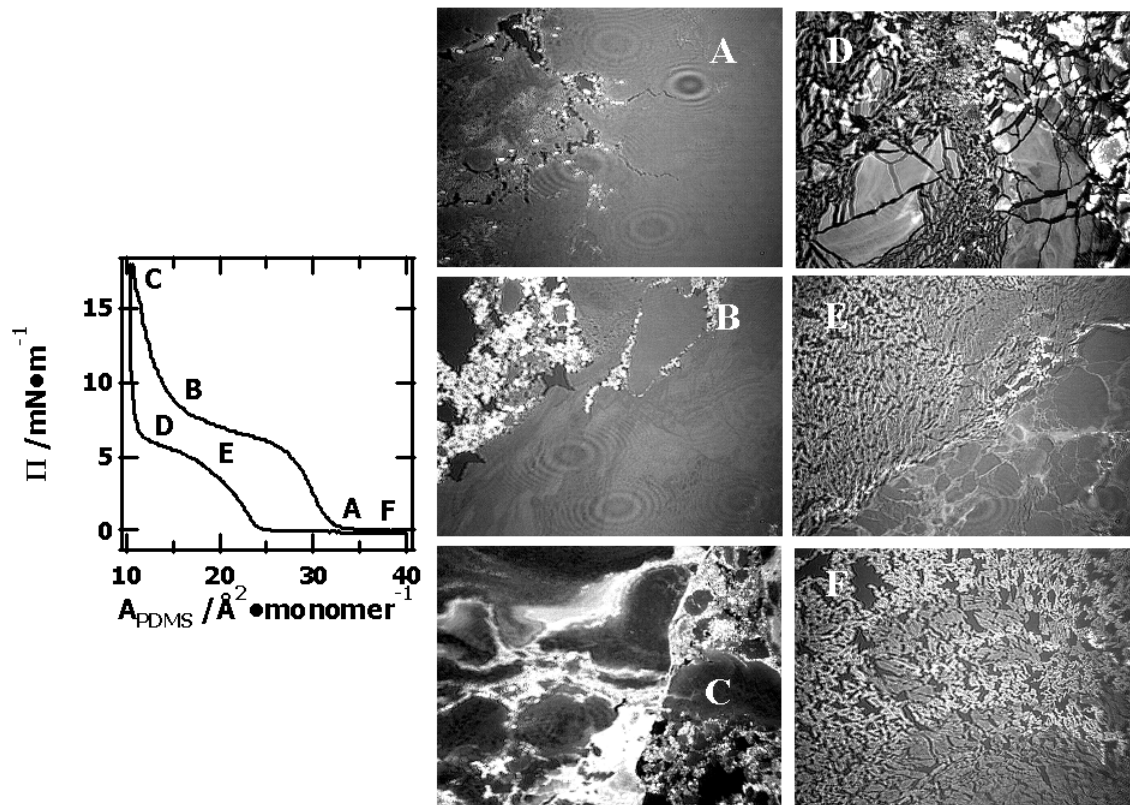


Figure 7.8: BAM images obtained during a hysteresis experiment at 22.5 °C and a compression rate of 15 cm²·min⁻¹ for a 70wt% octaisobutyl-POSS blend with PDMS. The letters on the Π - A_{PDMS} isotherm indicate where individual BAM images were taken. The points also correspond to (Image, $\langle A \rangle / \text{\AA}^2 \cdot \text{monomer}^{-1}$, $\Pi / \text{mN} \cdot \text{m}^{-1}$): (A, 21.1, 0), (B, 12.4, 7.3), (C, 5.8, 8.8), (D, 7.6, 8.4), (E, 14.0, 0.3), and (F, 28.1, 0). Solid-like domains appear bright in the 4.8×6.4 mm² images.

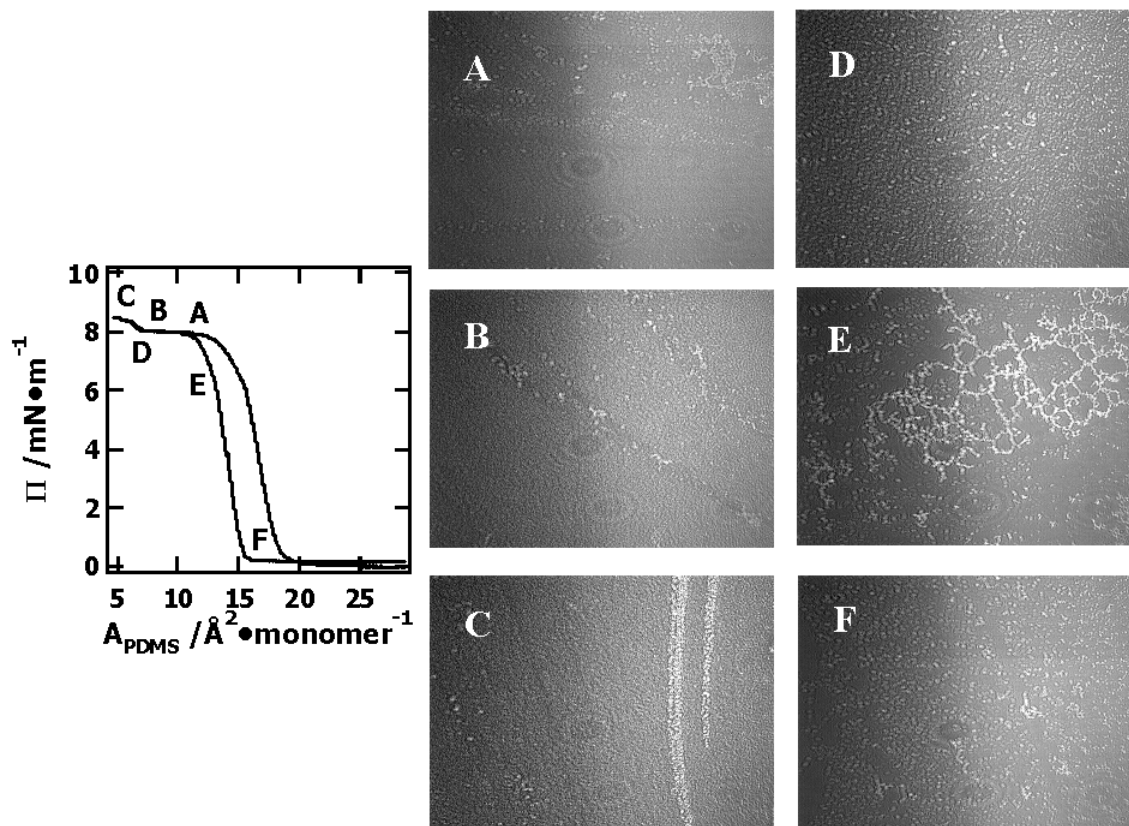


Figure 7.9: BAM images obtained during a hysteresis experiment at 22.5 °C and a compression rate of 15 cm²·min⁻¹ for a 30wt% octaisobutyl-POSS blend with PDMS. The letters on the Π - A_{PDMS} diagram indicate where individual BAM images were taken. The points also correspond to (Image, $\langle A \rangle / \text{\AA}^2 \cdot \text{monomer}^{-1}$, $\Pi / \text{mN} \cdot \text{m}^{-1}$): (A, 12.3, 7.9), (B, 6.7, 8.2), (C, 4.9, 8.5), (D, 8.6, 8.0), (E, 12.5, 6.9), and (F, 17.7, 0). Solid-like domains appear bright in the 4.8 × 6.4 mm² images.

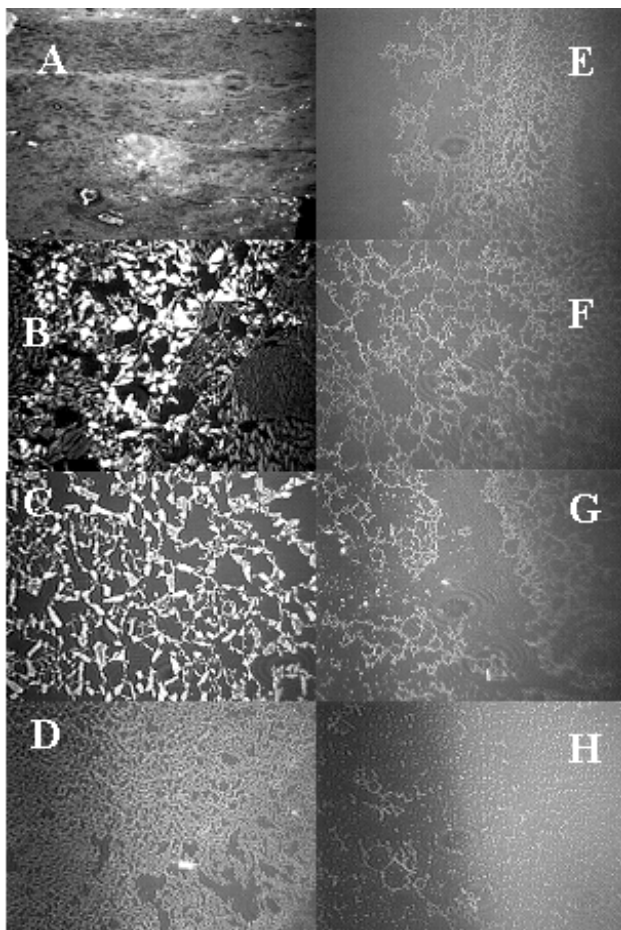


Figure 7.10: BAM images upon expansion for different octaisobutyl-POSS/PDMS blends with PDMS at $\Pi = 4 \text{ mN}\cdot\text{m}^{-1}$ (wt % POSS, $\langle A \rangle / \text{\AA}^2\cdot\text{monomer}^{-1}$, $A_{PDMS} / \text{\AA}^2\cdot\text{monomer}^{-1}$): A (100, 23.3, N/A), B (90, 10.0, 17.7), C (80, 11.8, 17.0), D (70, 12.6, 15.2), E (60, 14.7, 16.6), F (50, 14.5, 15.8), G (40, 16.2, 17.0) and H (30, 14.0, 14.5). Solid-like domains appear bright in the $4.8 \times 6.4 \text{ mm}^2$ images.

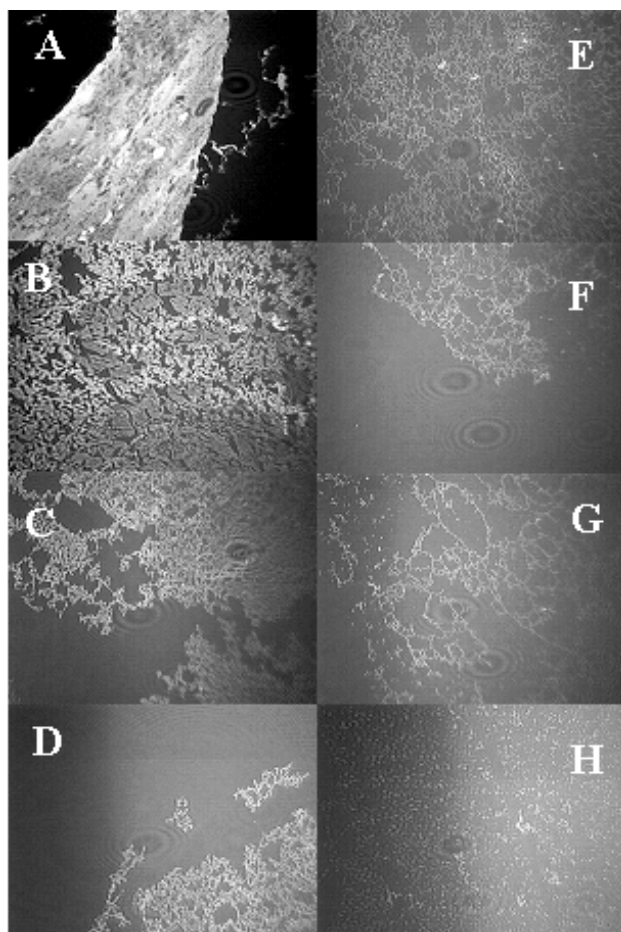


Figure 7.11: BAM images upon expansion for different octaisobutyl-POSS/PDMS blends with PDMS at $\Pi = 0 \text{ mN}\cdot\text{m}^{-1}$ (wt % POSS, $\langle A \rangle / \text{\AA}^2\cdot\text{monomer}^{-1}$, $A_{PDMS} / \text{\AA}^2\cdot\text{monomer}^{-1}$): A (100, 30.5, N/A), B (90, 32.1, 56.7), C (80, 26.4, 38.1), D (70, 20.8, 25.0), E (60, 20.5, 23.2), F (50, 19.5, 21.3), G (40, 19.0, 20.1) and H (30, 17.7, 18.3). For the pure octaisobutyl-POSS film (A), the image was taken at $\Pi = 3.0 \text{ mN}\cdot\text{m}^{-1}$. Solid-like domains appear bright in the $4.8 \times 6.4 \text{ mm}^2$ images.

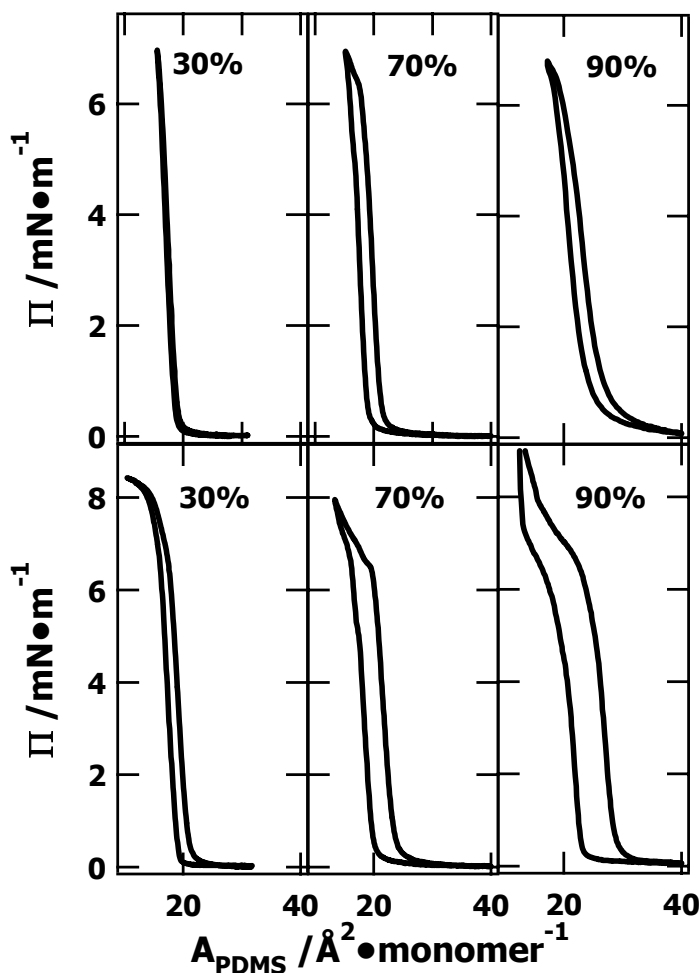


Figure 7.12: Representative $\Pi - A_{PDMS}$ hysteresis loops for octaisobutyl-POSS blends with PDMS for compression up to Π_C ($\approx 7 \text{ mN}\cdot\text{m}^{-1}$, upper 3 graphs) and for compression into the collapsed regime of the PDMS component ($A_{PDMS} \approx 10 \text{ \AA}^2\cdot\text{monomer}^{-1}$, lower 3 graphs). The percentage in the corner of each plot represents the wt% octaisobutyl-POSS present in the blend. Temperature was held constant at $22.5 \text{ }^\circ\text{C}$ with a compression/expansion rate of $15 \text{ cm}^2\cdot\text{min}^{-1}$.

7.4.4 Relaxation Experiments

Another mechanism for probing the stability of different morphologies and isotherm features is to compress the films to a fixed area value and observe changes in Π and morphology with time ("relaxation" experiments). For these experiments several types of behavior were seen: (1) Pure octaisobutyl-POSS films relax to a final $\Pi = 0$ value for all initial Π values if the system is given enough time; (2) Films containing ≥ 70 wt% octaisobutyl-POSS blended with PDMS that have been compressed to Π values greater than the second plateau of PDMS ($\Pi > \approx 9 \text{ mN}\cdot\text{m}^{-1}$) relax to a value of $\Pi \approx 8 - 9 \text{ mN}\cdot\text{m}^{-1}$; and (3) All mixtures compressed to Π values on the order of the plateau pressure for PDMS relax to a Π value that is also on the order of $\Pi \approx 8 - 9 \text{ mN}\cdot\text{m}^{-1}$. The second and third cases are identical to pure PDMS and show that PDMS stabilizes the mixed monolayer. These features are illustrated for octaisobutyl-POSS (two different initial Π values) and 90, 70, and 30wt% blends of octaisobutyl-POSS with PDMS in Figure 7.13. These differences also manifest themselves in the morphologies observed by BAM. For the case of octaisobutyl-POSS, there are no significant morphological changes from Figure 7.2. Large irregularly shaped aggregates remain at all times. In contrast, the morphology of the blends is composition and time dependent. Figure 7.14 shows one early, and one late stage BAM micrograph for each of the blend relaxation curves shown in Figure 7.13. As seen in Figure 7.14A & 7.14B, the 90 wt% octaisobutyl-POSS blend eventually forms the same kind of "shattered-glass" morphology seen in Figure 7.7D for hysteresis experiments. Similarly, both the 70wt% (Figure 7.14C & 7.14D) and 30wt% (Figure 7.14E & 7.14F) give rise to ring-like structures that are similar to hysteresis experiments in Figures 7.8 and 7.9, respectively.

Chapter 7

For the ring-forming compositions, the average "cell" size grows with decreasing POSS content. As Π is on the order of $8.5 \text{ mN}\cdot\text{m}^{-1}$, the system must represent the coexistence of a liquid-like PDMS monolayer with another liquid-like phase rich in solid-like POSS aggregates. Presumably, differences in line tensions and dipole densities between the two phases leads to network-like structures that are similar to the behavior seen in monolayers for lipid systems with coexisting liquid expanded (LE) and liquid condensed (LC) phases.¹⁸⁰ More importantly for POSS based systems, the "relaxation" behavior of the octaisobutyl-POSS/PDMS blends is very similar to blends of trisilanolisobutyl-POSS with PDMS,¹⁶⁸ even though octaisobutyl-POSS is non-amphiphilic. This feature reinforces the somewhat speculative conclusion that trisilanol-POSS derivatives tend to aggregate into hydrogen bonded dimers with essentially totally hydrophobic exteriors (like an octaisobutyl-POSS molecule) that aggregate at A/W upon film collapse.¹⁶⁷⁻¹⁶⁹ The dimeric structure is also consistent with the bulk crystal structure of trisilanolcyclohexyl-POSS.¹¹⁹ For compositions below 30 wt% POSS, rings fail to form and branched structures or small aggregates exist instead. This feature is also similar to the behavior observed in blends of trisilanolisobutyl-POSS with PDMS.¹⁶⁸

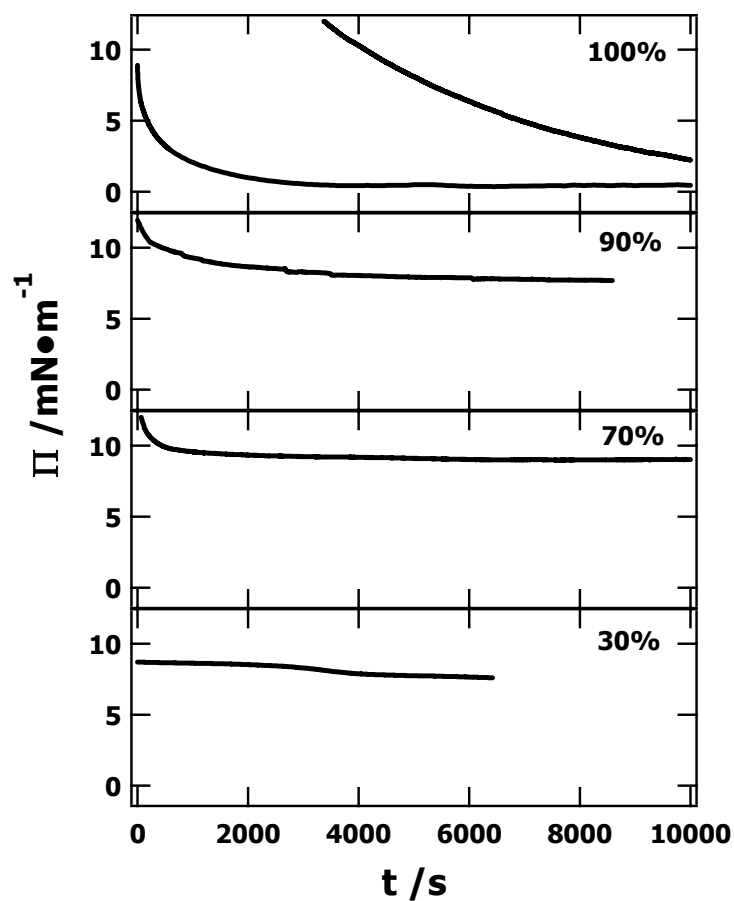


Figure 7.13: Relaxation, Π vs. t , curves for blends of octaisobutyl-POSS with PDMS at 22.5 °C. The percentage in the corner of each plot represents the wt% POSS present in the blend. 100 wt % POSS is shown twice, for relaxation from $\Pi = 9 \text{ mN}\cdot\text{m}^{-1}$ (left curve) and $\Pi = 40 \text{ mN}\cdot\text{m}^{-1}$ (right curve).

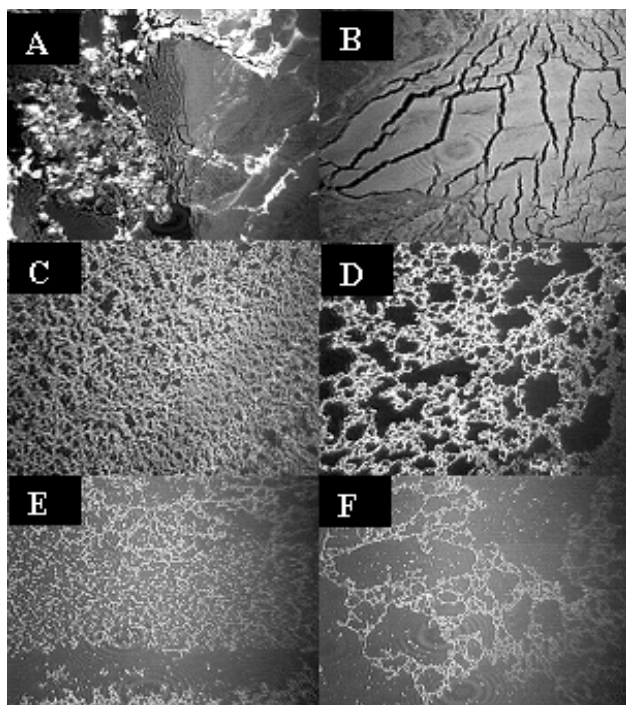


Figure 7.14: BAM images during relaxation for different octaisobutyl-POSS/PDMS blends (wt % POSS, t /s): A (90, 1500), B (90, 47000), C (70, 1500), D (70, 40000), E (30, 1500), F (30, 5300) at 22.5 °C. A and B were compressed to an area per PDMS molecule of $A_{PDMS} = 17 \text{ \AA}^2 \cdot \text{monomer}^{-1}$ and C – F were compressed to an area per PDMS molecule of $A_{PDMS} \approx 5 \text{ \AA}^2 \cdot \text{monomer}^{-1}$. Solid-like domains appear bright in the images, which are $4.8 \times 6.4 \text{ mm}^2$ in size.

7.4.5 Addition Experiments

Figure 7.15 shows how data obtained by making successive additions of spreading solution compare to compression data for octaisobutyl-POSS blends with PDMS at A/W. After spreading and allowing time for solvent evaporation, Π was allowed to relax to an "equilibrium" pressure, defined as $\Delta\Pi < 0.1 \text{ mN} \cdot \text{m}^{-1}$ for 15

minutes. For 90wt% octaisobutyl-POSS, it is observed that the extremely high Π values achievable during compression experiments are not easily attained during successive additions of spreading solution. This behavior is consistent with Figure 7.13, which shows the high Π films of the 90wt% octaisobutyl-POSS blend are unstable and will ultimately relax to smaller Π values if given sufficient time. The instability of Π is also the cause of the lower area per PDMS molecule at which Π rises. The addition isotherm does not start to increase until an A_{PDMS} value closer to the value for the pure PDMS isotherm (dashed line in Figure 7.15). This behavior is reasonable if one assumes that only PDMS contributes to the "equilibrium" Π value, and addition experiments come the closest of all the techniques used to control the surface concentration to approaching equilibrium conditions. Hence, during "addition" sufficient time exists for POSS to aggregate until enough PDMS is spread to fill the surface, whereby a degree of aggregation comparable to pure octaisobutyl-POSS is expected in the 90wt% POSS blend. For films with less octaisobutyl-POSS (Figure 7.15B and 15C), there is better agreement with the compression data suggesting the degree of aggregation should be more similar to the compression and hysteresis experiments.

Figure 7.16 presents BAM images taken during addition experiments. Each image represents the morphology that is observed at a surface concentration value that would fall on the first plateau of a pure PDMS isotherm. The morphologies are similar to those observed during hysteresis experiments. The "sheet" of POSS that forms during compression experiments for ≥ 80 wt% octaisobutyl-POSS is still formed during successive additions, but breaks up during the subsequent relaxation period to yield a morphology (Figure 7.16A) that is more similar to pure octaisobutyl-POSS than the

cracked patterns seen during relaxation for 90wt% octaisobutyl-POSS blends with PDMS (Figure 7.14B). Ring formation is observed during both the 70 and 30 wt% octaisobutyl-POSS successive addition experiments; however, for 30 wt% POSS most of the rings break apart once a stable Π value is obtained (Figure 7.16B & 16C). These latter features are similar to what is observed by the other methods for controlling surface concentration.

The main results from addition experiments can be summarized as follows: (1) Regime I (> 70 wt% POSS): Addition Π - A isotherms show long relaxation times that are consistent with Figure 7.13 and are shifted to smaller A_{PDMS} values relative to compression experiments because of enhanced aggregation of the POSS component. (2) Regime II ($40 \leq$ wt% POSS ≤ 70): Addition and compression Π - A isotherms show excellent agreement. The relaxation in Π is similar to Figure 7.13; however, the use of additional spreading solvent appears to yield ring-like morphologies that are more similar to Figure 7.14F than Figure 7.14D. (3) Regime III (≤ 30 wt% POSS): Addition and compression Π - A isotherms also show excellent agreement and Π relaxation is fast just like in Figure 7.13. However, the resulting morphologies observed by BAM show fragments of ring-like structures rather than true ring-like structures like those shown in Figure 7.14F. The subtle differences in morphology between addition and relaxation experiments appear to arise from the fact that non-equilibrium morphologies formed during film compression in relaxation experiments are subject to slower dynamics than addition experiments where faster relaxation processes occur through the addition and evaporation of a low viscosity diluent (additional spreading solvent).

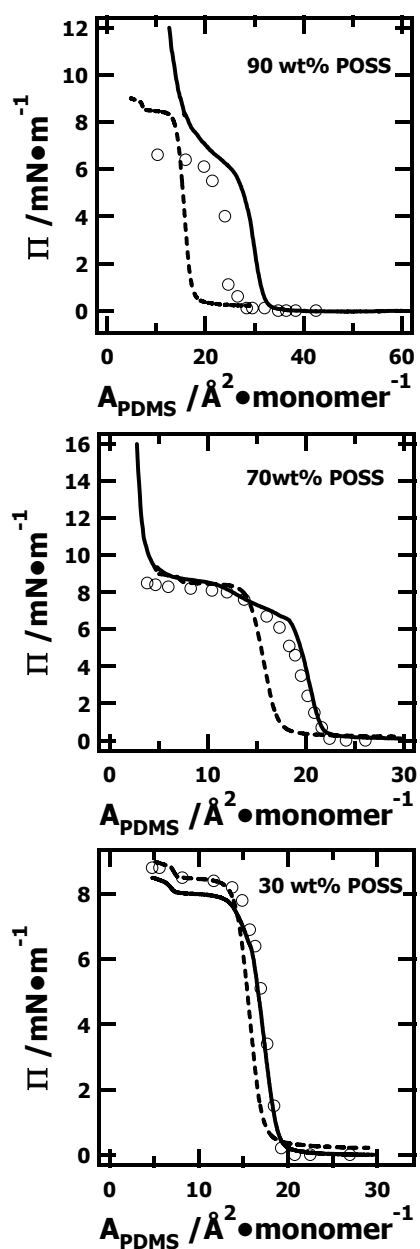


Figure 7.15: Π - A_{PDMS} addition isotherms for octaisobutyl-POSS blend with PDMS at 22.5 °C. The (o) markers represent the addition isotherm data, the (—) line represents the compression isotherm for the specified wt% POSS, and the (---) line represents the compression isotherm for pure PDMS as a comparison.

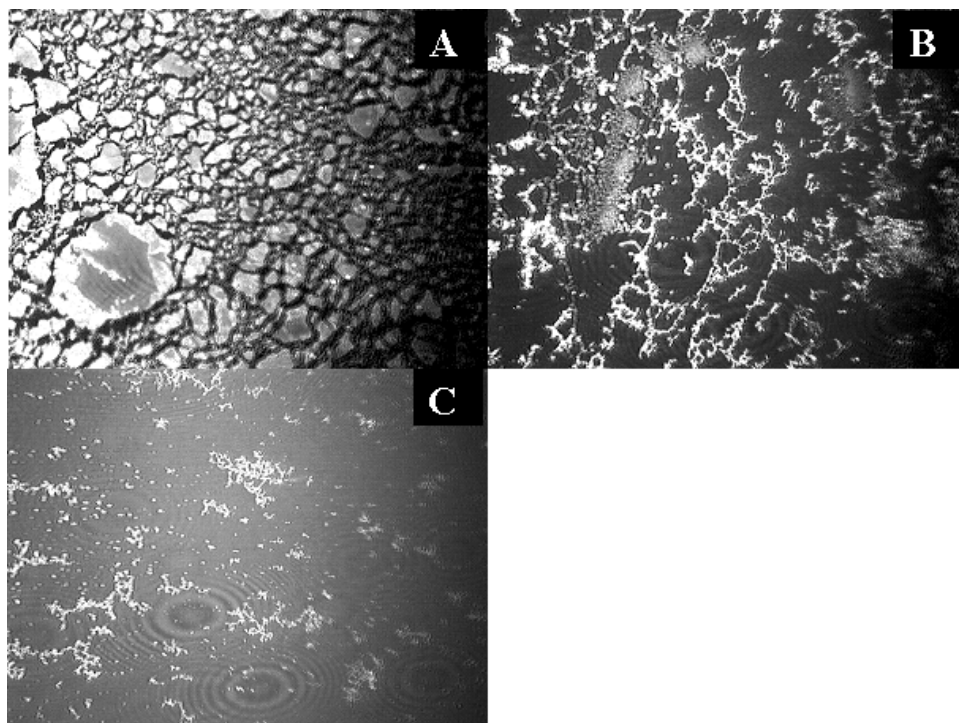


Figure 7.16: BAM images obtained upon successive addition of spreading solution for octaisobutyl-POSS blends with PDMS (wt% POSS, $\langle A \rangle / \text{\AA}^2 \cdot \text{monomer}^{-1}$, t / min): A (90, 6.8, 40), B (70, 10.0, 32), and C (30, 11.3, 20) at 22.5 °C. All images correspond to an area per PDMS molecule of $A_{PDMS} \approx 12 \text{\AA}^2 \cdot \text{monomer}^{-1}$. Solid-like domains appear bright in the images, which are $4.8 \times 6.4 \text{ mm}^2$ in size.

7.5 Conclusions

This study demonstrates interesting morphological regimes in blends of PDMS and octaisobutyl-POSS as Langmuir monolayers at A/W. In these systems, octaisobutyl-POSS appears to act as a true aggregating nanofiller in the sense that it confines PDMS to a smaller effective trough area causing Π to increase at larger A_{PDMS} values. Even though pure octaisobutyl-POSS is non-amphiphilic and exists in a multilayer state at all A in the pure state, its blends with PDMS exhibit a number of morphologies that are similar with blends of trisilanolisobutyl-POSS with PDMS.¹⁶⁸ The similarity in morphology suggests the proposed hydrogen-bonded dimer model leading to POSS multilayer-aggregates in trisilanol-POSS derivatives is reasonable.¹⁶⁷⁻¹⁶⁹ The fact that such well-ordered multilayer systems arise from a non-amphiphilic filler material suggest that a wide variety of non-amphiphilic nanofillers could be used to explore fundamental filler effects on the mechanical and transport properties of confined systems within well-defined Langmuir monolayers. Moreover, the ring or network-like morphologies are highly reminiscent of proposed bridging structures leading to mechanical improvements in filled polymers for bulk systems.²³⁹

CHAPTER 8

Phase Behavior, Morphologies, and Viscoelastic Properties of Trisilanolcyclohexyl-POSS at the Air/Water Interface

The following chapter appeared as the combination of a communication in Langmuir, Volume 20, No. 7, (2004) 2527-2530 and an article in Langmuir Volume 21, No. 6, (2005) 2375-2385.

8.1 Abstract

In the previous chapters, trisilanolisobutyl-POSS (TiBuP) has been reported to form stable monolayers and its blends with PDMS and PDMS-PO to form homogenous monolayers and multiphase multilayers at the air/water (A/W) interface. This chapter explores the mono- and multilayer properties of another POSS derivative, trisilanolcyclohexyl-POSS, by means of surface pressure–area per molecule (Π - A) isotherms, Brewster angle microscopy (BAM), and interfacial stress rheometry (ISR) measurements. With the average thickness varying from traditional Langmuir monolayers (1 POSS molecule thick) to trilayers (3 POSS molecules thick), the morphology studies by BAM reveal that the TCyP monolayer can collapse into different 3D structures by homogeneous or heterogeneous nucleation mechanisms. For homogeneous nucleation, analysis by Vollhardt et al.’s nucleation and growth model reveals that TCyP monolayers collapse via instantaneous nucleation with hemispherical edge growth into trilayer at $\Pi = 3.7 \text{ mN}\cdot\text{m}^{-1}$. Both surface storage (G_s') and loss (G_s'') moduli obtained by ISR reveal three different non-Newtonian flow regimes that correlate with phase transitions in the Π - A isotherms: (A) A viscous liquid-like “monolayer”; (B)

A "biphasic regime" between a liquid-like viscous monolayer and a more rigid trilayer; and (C) An elastic solid-like "trilayer". These observations provide interesting insights into collapse mechanisms and structures in Langmuir films. For symmetric compression past the trilayer state, TCyP thin films at A/W undergo a series of phase transitions from trilayers (3 POSS molecule thick) to unique stable rod-like hydrophobic aggregates in multilayer films (≈ 8 POSS molecules thick) that are dramatically different from "collapsed" morphologies seen in other systems. Stable and hydrophobic rod-like structure formation on water is presumably due to trisilanocyclohexyl-POSS' unique molecular structure and strong tendency to form intermolecular hydrogen bonds in the solid state. These results are consistent with existing POSS/polymer composite research, which shows POSS molecules tend to aggregate and crystallize into lamellar nanocrystals.

8.2 Introduction

Monolayers of insoluble amphiphiles at the air/water interface (Langmuir monolayers) serve as important model systems for understanding two-dimensional (2D) ordering, phase transitions, wetting, and interfacial rheology²⁴ and as interesting models for biological membranes.²⁵ Furthermore, Langmuir monolayers have attracted considerable attention over the past two decades as important precursors for creating supramolecular architectures through the Langmuir-Blodgett technique to study biomimetic,¹⁶⁻¹⁹ electronic,^{4,20,21} and optical^{22,23} processes in ultra thin films.

Langmuir films have traditionally been composed of either low molecular weight amphiphiles with polar heads and long hydrophobic tails, such as fatty acids and

Chapter 8

phospholipids, or amphiphilic polymers.^{1,3,5} With the introduction of new techniques such as fluorescence microscopy (FM),^{182,184} Brewster angle microscopy (BAM),^{34,35} atomic force microscopy (AFM),^{185,240} and grazing incidence X-ray diffraction (GIXD),^{30,31} numerous thermodynamic and structural studies have been carried out on low molecular weight Langmuir monolayers of lipids that reveal the existence of at least 10 different "2D" monolayer phases with surface analogs to gas, liquid, smectic liquid-crystalline, and crystalline phases in bulk.^{24,78,188,241} While most work has focused on lipid systems in monolayer states, some efforts have been made to study monolayer collapse or multilayer regimes in small molecule amphiphiles.²⁴²⁻²⁴⁹ When Langmuir monolayers are compressed beyond their equilibrium "collapse pressure", Π_{collapse} , the surface pressure-area per molecule (Π - A) isotherm exhibits a maximum value followed by either a sharp Π drop, or a plateau.¹ With the aid of TEM,^{242,243,245} BAM,^{246,248} GIXD,^{249,250} and AFM,^{246,248,250} either direct one-step transitions from monolayers to three-dimensional (3D) bulk phases or progressive layer-by-layer transitions are observed for collapsing lipid systems. After Smith et al.²⁴⁴ found that the "slow" collapse of several lipid systems above the equilibrium spreading pressure (ESP) was consistent with a model of homogeneous nucleation and subsequent growth of 3D fragments, Vollhardt et al.²⁵¹⁻²⁵⁵ developed a simple theoretical model to describe the nucleation and growth kinetics for 2D \rightarrow 3D collapse processes. Under the assumption of ideal *homogeneous* nucleation, the decrease in A with time, t , during isobaric area relaxation experiments can be fit to different nucleation and growth models by treating the total collapse rate as the convolution of the nucleation and growth rates and by considering overlapping effects on the growing centers.²⁵¹⁻²⁵³ Gourier et al.²⁴⁹ and Ybert et al.²⁵⁶ subsequently proposed

three different collapse mechanisms for lipid systems by also considering the influence of Π_{collapse} and compression rate.

With much longer backbones containing both hydrophilic and hydrophobic components, the Π - A isotherm for amphiphilic macromolecules are somewhat simpler than lipid systems with a molecular weight dependent gas-like regime, a molecular weight independent semi-dilute fluid-like monolayer regime, and a collapsed regime.^{1,257,258} One interesting case is polysiloxanes,^{181,258,259} which have shown more than seven stepwise transitions during multilayer formation. While the evidence for layer-by-layer transitions is clear, questions about packing or ordering of polymeric species at the air/water interface remain unanswered due to the complex conformations of the polymer backbone and side groups. In contrast to simple lipid amphiphiles, which can be treated as rod-like objects due to their large length/diameter ratio and exhibit rich monolayer phase transitions and ordering, amphiphilic flexible-coil polymers should lie flat on the water surface and exhibit simpler layer-by-layer multilayer formation. Hence, different types of molecular models are required if one wants to explore how structural differences between traditional amphiphiles and macromolecules affect transitions between monomolecular and multilayer regimes. One route for exploring these differences is amphiphilic oligomers with molecular weights around $1 \text{ kg}\cdot\text{mol}^{-1}$.²⁶⁰

Over the last two decades one class of oligomers, polyhedral oligomeric silsesquioxane (POSS) molecules (as shown by Figure 8.1),^{166,169} have attracted considerable attention. With rigid inorganic cores and flexible organic coronae of nanometer dimensions,¹¹⁹ POSS molecules can serve as “nanofillers” in polymeric materials. With these features, POSS/polymer nanocomposites exhibit improved

Chapter 8

oxidative and thermal stability (inorganic behavior), while retaining the processability of the matrix because of the compatibility of the organic exterior of the POSS molecules with the matrix polymer. Thus far, POSS molecules have been utilized in various applications such as protective materials and coatings in extreme environments,^{173,174} biomedical materials,^{161,162} and as synthetic templates for nanostructured materials.^{148,157,160,198,200,201,237} Given POSS' small molecular size (1-1.5 nm), the surface and interfacial properties become very important for future applications in nanotechnology and other fields; however, limited information exists about the surface properties of POSS.^{163,164} Recently Deng et al.^{166,169} demonstrated that trisilanolisobutyl-POSS (TiBuP) is a novel amphiphile that forms stable Langmuir monolayers at A/W (Chapters 3 and 4). Moreover, TiBuP has been used as a model nanofiller to study interactions between polymers and nanofillers in Langmuir monolayer systems (Chapter 5 and 6).^{168,170} From POSS' topological features, with small length/diameter ratios and bulky shapes, it is not surprising that trisilanol-POSS derivatives have much simpler monolayer phase transitions than lipid systems. However, even though TiBuP and TCyP have similar molecular shapes and sizes, TiBuP exhibits a very long "collapsed" plateau in its Π - A isotherm, even at very high surface concentrations, while TCyP shows a step-by-step series of ordered multilayer transitions like polysiloxanes.^{181,258,259} In order to better understand these differences, it is necessary to explore the details of the 2D \rightarrow 3D transformation for TCyP Langmuir films.

One of the main focuses of this chapter will be on the phase transitions in TCyP Langmuir films from the monolayer regime to the trilayer (based on the average surface concentration) regime. The first step will be a quantitative comparison of the Π - A

isotherms between TiBuP and TCyP, noting the similarities and differences in the phase transition behavior between these two trisilanol-POSS derivatives. Next, differences in the morphological patterns acquired by BAM during the monolayer collapse process of TCyP films for homogeneous and heterogeneous nucleation conditions will be presented. These studies ensure that isobaric area relaxation experiments used to study the nucleation and growth of a multilayer structure occur under homogeneous nucleation conditions. Finally the correlation between the observed morphologies and the rheological properties of the Langmuir films obtained by interfacial stress rheometry (ISR),^{39,103} will reveal dramatic changes (more than 6 orders of magnitude) in the surface shear modulus between the monolayer and multilayer regimes.

Another focus of this chapter will be to demonstrate that trisilanolcyclohexyl-POSS molecules have very strong intermolecular interactions, which cause POSS molecules to self-assemble into highly ordered, stable, and hydrophobic solid thin films with a unique rod-like morphology at the air/water interface when surface concentration increasing more than trilayer. This part of study provides insight into the following two questions: (1) "How strongly do POSS molecules interact with each other?" and, (2) "Can POSS molecules aggregate into "supramolecular" assemblies?" Both questions should be relevant to understanding POSS aggregation as it pertains to enhancements in T_g and modulus in hybrid nanocomposites.

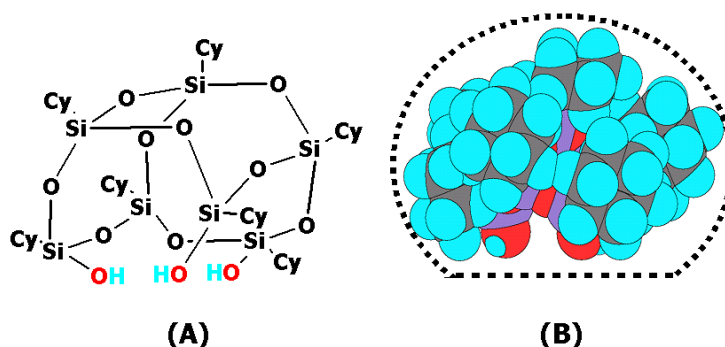


Figure 8.1: Generic structure and space-filling model of TCyP at A/W: (A) Generic structure of the trisilanocyclohexyl-POSS molecule (Cy = cyclohexyl). (B) A space-filling model of trisilanocyclohexyl-POSS based on X-ray diffraction data.¹¹⁹ Gray atoms are carbon, red atoms are oxygen, purple atoms are silicon, and green atoms are hydrogen. The model represents a configuration where the three-silanol groups of POSS are exposed to water. The dotted line represents a simple idealized side-view projection of trisilanocyclohexyl-POSS with an estimate of the cross-sectional area of $A_c \approx 1.78 \text{ nm}^2 \cdot \text{molecule}^{-1}$ and the maximum height as $H \approx 0.92 \text{ nm}$. The simplified model will be used in Figure 8.15.

8.3 Experimental

8.3.1 Materials

Both trisilanolisobutyl-POSS (TiBuP) and trisilanocyclohexyl-POSS (TCyP) obtained from Hybrid Plastics, Inc. and dried in a vacuum oven for 3 days at 40 °C were dissolved in chloroform ($\sim 0.02 \text{ mg} \cdot \text{g}^{-1}$, HPLC grade). Due to slow POSS dissolution, the samples were sealed in special glass vials and sonicated (Fisher Scientific FS140H)

for more than 1 hour. Next, the solutions were allowed to dissolve for at least 36 hours at room temperature. Replicates for all the measurements discussed below were done in two or three days to guarantee reproducible results.

8.3.2 Surface Pressure Measurements

Prior to starting experiments, the trough was repeatedly cleaned with chloroform and rinsed with at least a 20 fold excess of ultrapure 18.2 M Ω water (Millipore, Milli Q Gradient A-10). In general, TCyP samples were initially spread onto the surface of a standard Langmuir trough (500 cm², Nima Technology, Ltd., 601BAM) filled with ultrapure water in a PlexiglasTM box. Three different methods for spreading TCyP were employed in this chapter: (1) "*Normal Spreading*" Conditions – TCyP solutions were spread onto a "cold" water surface (T = 22.5 °C). The chloroform is allowed to evaporate for a minimum of 15 min before compression of the film begins. (2) "*Homogeneous Spreading*" Conditions – TCyP solutions were spread onto "hot" water (T ~ 45 °C). After spreading on "hot" water, sufficient time (\approx 2 hours) was allocated for the subphase to reach room temperature as defined by a constant surface tension value ($\Delta\gamma \leq 0.1$ mN \cdot m⁻¹ over a 30 min period). The reason for spreading on "hot" water is to break up potential TCyP aggregates in the submonolayer regime given TCyP's strong tendency to form dimers in bulk.¹¹⁹ While the Π -A isotherms are essentially identical to those obtained by "normal spreading", the morphology of the films can be dramatically different due to different nucleation mechanisms (a principle feature of this chapter). (3) "*Heterogeneous Spreading*" Conditions – The procedure is the same as for "homogeneous" spreading. However, once the spreading solvent has evaporated and the temperature of the film has reached the desired experimental temperature (T = 22.5 °C), the film is compressed and

Chapter 8

expanded in three continuous hysteresis loops between $0 \leq \Pi \leq 2 \text{ mN}\cdot\text{m}^{-1}$ in order to reintroduce a limited number of three dimensional nuclei.

Subsequently, the trough temperature was controlled by circulating water from a water bath maintained at the appropriate experimental temperature, $22.5 \pm 0.2 \text{ }^\circ\text{C}$. The relative humidity for the system was 70–75 %. The surface pressure, Π , was recorded by the Wilhelmy plate technique during all isotherm measurements. A completely wetted filter paper plate was used as the Wilhelmy plate.

In order to investigate the thermodynamic properties and characterize 2D→3D nucleation and growth mechanisms of TCyP, four methods were used to vary the surface area or surface concentration (A): (1) symmetric "compression" of the confined monolayers with two barriers at various constant rates, (2) "quasi-static compression" of the barriers; (3) successive "addition" of spreading solution, and (4) "isobaric" area relaxation experiments (the underlined portions indicate the short form used throughout the manuscript). For compression at a constant rate, each sample was compressed at a specific rate ($20 \text{ cm}^2\cdot\text{min}^{-1}$) to a final A around $0.2 \text{ nm}^2\cdot\text{molecule}^{-1}$. For quasi-static compression, each sample was initially compressed at $20 \text{ cm}^2\cdot\text{min}^{-1}$. After compressing the barriers to a fixed surface area, the barriers were stopped, and Π was allowed to relax to a more "equilibrium" value for a specific time period (typically 5 minutes). After allowing Π to relax, the compression and relaxation process was repeated until the end of the experiment. For successive addition experiments, the surface area was held constant and A was varied by making successive additions of spreading solution to the water surface. After each addition, Π was allowed to relax to a constant value ($\Delta\Pi < 0.1 \text{ mN}\cdot\text{m}^{-1}$ over a 10 minute period). In order to explore the 2D→3D nucleation and growth

mechanisms of TCyP, the isobaric area relaxation experiments were carried out around the monolayer collapse point. Before an isobaric area relaxation experiment was started, the spread monolayer was continuously compressed at a higher rate, $40 \text{ cm}^2 \cdot \text{min}^{-1}$, to a point near the desired "collapse" surface pressure, and then the compression rate was decreased to $20 \text{ cm}^2 \cdot \text{min}^{-1}$. Once a constant Π value was attained, the A vs. t curve was recorded.

8.3.3 Brewster Angle Microscopy (BAM)

BAM studies (MiniBAM, NanoFilm Technologie GmbH) were carried out simultaneously during the isotherm measurements and the BAM images were taken by a charge-coupled device (CCD) camera under the "automatic gain control" mode to obtain an optical average brightness rather than absolute intensity values. While this procedure provides the greatest sensitivity for detecting morphological differences, care must be taken in comparing different images as the same feature may appear bright in one image where it has the greatest reflectivity, but grey in another image due to the presence of more strongly reflecting objects. The BAM images shown in this chapter have a linear resolution of at least $20 \mu\text{m}$. Image processing, such as the surface plot in Figure 8.8I, was done with the aid of an image processing macro in Igor Pro 4.03 (WaveMetrics Inc.). The entire set-up (Langmuir trough, BAM, and Plexiglas box) rests on a floating optical table to minimize vibrations.

8.3.4 Interfacial Stress Rheometry (ISR)

An interfacial stress rheometer³⁹ was used to measure the dynamic interfacial shear rheology of TCyP. The instrument has a simple design that is based on applying a controlled shear stress via a magnetized probe, a slender PTFE coated needle, at the

Chapter 8

air/water interface (A/W) and measuring the resulting deformation (strain). The magnetized probe undergoes oscillatory translational motion at different angular frequencies (ω) along the long axis of an applied sinusoidal magnetic field gradient generated by a pair of AC controlled Helmholtz coils. The amplitude and the phase of the needle's motion relative to the applied force are measured to determine the complex surface shear modulus (G_s^*) comprised of an elastic modulus (G_s') and a loss modulus (G_s''). In addition, a dynamic viscosity, μ_s^* , can be derived from the dynamic surface moduli to describe the general flow behavior of complex materials. Measurements in this study were performed at room temperature. Before doing the frequency sweep (0.9-10 $\text{rad}\cdot\text{s}^{-1}$), the sample is subjected to a strain scan to ensure that the measurements are made in the linear regime. The ISR measurements actually were performed at different Π values on a KSV Langmuir trough (KSV Instruments, Helsinki, Finland) using a platinum Wilhelmy plate to determine Π . For the convenience of comparing ISR and Π - A isotherm data for TCyP, the ISR data obtained at different Π values on the KSV Langmuir trough were plotted against A values based on the isotherm obtained from the Nima Langmuir trough. The ISR instrument is described in more detail elsewhere.^{39,103}

8.4 Results and Discussion

8.4.1 Comparison between TCyP and TiBuP

Figure 8.1A shows the molecular structure of trisilanocyclohexyl-POSS (TCyP) with an orientation that is similar to the space-filling model given in Figure 8.1B. In both cases, the models depict the molecule in a configuration where the hydrophilic trisilanol pocket is oriented as if it were sitting on the water surface. Figure 8.1 is generated by the

Phase Behavior, Morphologies, and Viscoelastic Properties of TCyP at A/W

CS ChemOffice package based on X-ray diffraction (XRD) data from Feher et al.¹¹⁹ The dotted hemisphere-like trace provides a side-view projection of an ideal TCyP molecule with an estimated cross-sectional area of $A_c \approx 1.78 \text{ nm}^2 \cdot \text{molecule}^{-1}$ and a maximum height of $H \approx 0.92 \text{ nm}$. From this simplified hemisphere-like model, the ratio of the non-polar "chain length", L_{tail} to A_c for TCyP can be estimated as $L_{\text{tail}}/A_c \approx 0.5 \text{ nm}^{-1}$, which is similar to TiBuP^{166,169} and approximately 5-10% of the value for traditional lipids such as stearic acid.²⁴ Like TiBuP, the essential molecular degrees of freedom for TCyP on the water surface are limited, which means that the monolayer's physical structure and phase behavior at A/W should be relatively simple.

Figure 8.2 shows Π - A isotherms of TiBuP and TCyP, obtained at room temperature, $T = 22.5 \text{ }^\circ\text{C}$, with a constant compression rate of $20 \text{ cm}^2 \cdot \text{min}^{-1}$. From the isotherms, TiBuP and TCyP have very similar limiting area values of $A_o \approx 1.77$ and $1.81 \text{ nm}^2 \cdot \text{molecule}^{-1}$, respectively. Traditionally, A_o values represent the average size of closely packed molecules existing in the monolayer-state, where the amphiphilic molecules take on an orientation with hydrophobic tails oriented toward air and the hydrophilic head groups anchored to the water subphase. Due to the bulky molecular shapes and the small ratio between tail length and cross-sectional area, Figure 8.1, these two trisilanol-POSS molecules have A_o values that are in excellent agreement with A_c values obtained from models based on crystallographic data and previous studies.^{119,169} Hence, unlike traditional lipid amphiphiles, the short side groups on the POSS cage do not exhibit significant extension away from the interface. While these two derivatives have similar molecular size and monolayer behavior prior to their apparent dynamic collapse molecular areas ($A_{\text{collapse}} \sim 1.36$ and $1.64 \text{ nm}^2 \cdot \text{molecule}^{-1}$ for TiBuP and TCyP,

respectively), their Π - A isotherms reveal vastly different behavior in the collapsed regime (small A) and exhibit very different 2D \rightarrow 3D phase transitions and higher order multilayer phases.

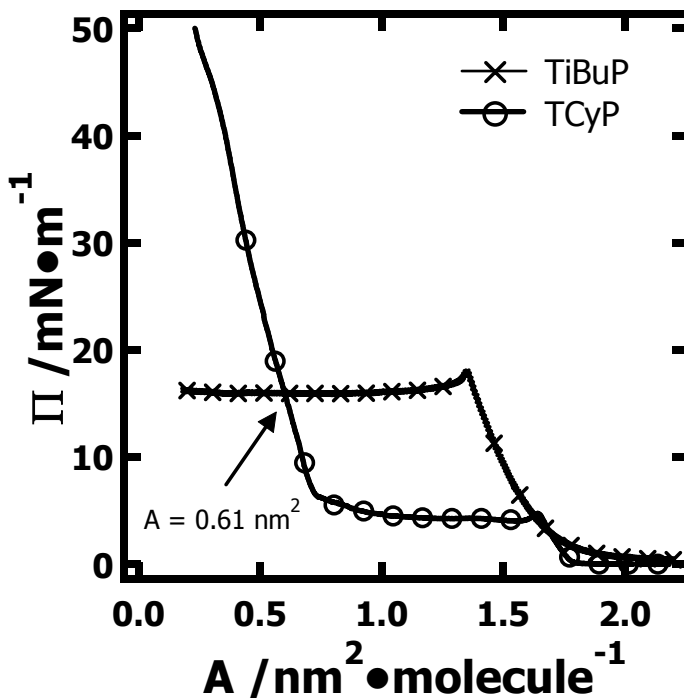


Figure 8.2: Π - A isotherms comparison between trisilanolisobutyl-POSS (TiBuP) and trisilanolcyclohexyl-POSS (TCyP) measured at room temperature, $T = 22.5\text{ }^\circ\text{C}$, with a constant compression rate of $20\text{ cm}^2\cdot\text{min}^{-1}$. Every 15th data point is labeled (cross, TiBuP; circle, TCyP) to avoid obscuring the isotherms' features. The arrow in the lower left corner indicates the second crossover point of the two isotherms, $A = 0.61\text{ nm}^2\cdot\text{molecule}^{-1}$.

Phase Behavior, Morphologies, and Viscoelastic Properties of TCyP at A/W

When proceeding with a point-by-point comparison, there are several important points for comparison needed to be highlighted:

(1). TiBuP has a higher dynamic collapse surface pressure ($\Pi_{\text{collapse}} \sim 18 \text{ mN}\cdot\text{m}^{-1}$) at a smaller $A_{\text{collapse}} \sim 1.36 \text{ nm}^2\cdot\text{molecule}^{-1}$ than TCyP ($\Pi_{\text{collapse}} \sim 4.7 \text{ mN}\cdot\text{m}^{-1}$ and $A_{\text{collapse}} \sim 1.64 \text{ nm}^2\cdot\text{molecule}^{-1}$).

(2). After the dynamic collapse point, TiBuP exhibits a long plateau with $\Pi_{\text{plateau}} \sim 16 \text{ mN}\cdot\text{m}^{-1}$, whereas the corresponding Π_{plateau} value for TCyP is approximately one-fourth as large, $\Pi_{\text{plateau}} \sim 4.3 \text{ mN}\cdot\text{m}^{-1}$. In the TCyP system, Π_{plateau} is not reflecting the inherent hydrophilic character of a silanol functional group, which should be the same for both TCyP and TiBuP. Rather for TCyP, molecular models (Figure 8.1B) show that the cyclohexyl groups wrap back around the Si-O cage, partially covering the trisilanol pocket. In contrast, the smaller isobutyl groups in TiBuP do not impinge upon the trisilanol pocket nearly as much as the cyclohexyl groups in TCyP. As a result, stronger hydrogen bonding between water and TiBuP is observed relative to water and TCyP. Therefore, higher Π values are required to remove TiBuP from A/W than TCyP.

(3). For TiBuP, Π remains flat at Π_{plateau} to $A \leq 0.2 \text{ nm}^2\cdot\text{molecule}^{-1}$; however, TCyP's plateau ends around $A \approx 0.91 \text{ nm}^2\cdot\text{molecule}^{-1}$. In the region $0.73 \leq A \leq 0.91 (\approx A_c/2) \text{ nm}^2\cdot\text{molecule}^{-1}$, Π slowly rises by about $1.4 \text{ mN}\cdot\text{m}^{-1}$.

(4). With further compression of the film, $0.61 (\approx A_c/3) \leq A \leq 0.73 \text{ nm}^2\cdot\text{molecule}^{-1}$, Π rises more sharply with a slope, $(\partial\Pi/\partial A)_T$, that is comparable to the value seen for TiBuP in the range of $1.36 \leq A \leq 1.64 \text{ nm}^2\cdot\text{molecule}^{-1}$ as shown in Figure 8.3. Because of compression at a faster rate than structural relaxation phenomena in an LB-film, 2D \rightarrow 3D collapse can actually start before an obvious signature is readily apparent in the

Chapter 8

Π - A isotherm of a liquid condensed (LC) monolayer. Given the shape of the isotherms, it is believed that TCyP and TiBuP both form LC monolayers. Hence, even though TCyP already collapses with a small "cusp" at a very small $\Pi_{collapse} \sim 4.7 \text{ mN}\cdot\text{m}^{-1}$ as shown in Figure 8.2, departure from a "2D" monolayer may already start at smaller Π values. In order to explore this further, Figure 8.3A provides the static dilational elasticity, $\epsilon_s = -A \cdot (\partial\Pi/\partial A)_T$, of the monolayers for TCyP and TiBuP prior to their apparent collapse points in the Π - A isotherms ($A_{collapse} \sim 1.36$ and $1.64 \text{ nm}^2\cdot\text{molecule}^{-1}$ for TiBuP and TCyP, respectively). Looking at ϵ_s - A in Figure 8.3A, both trisilanol-POSS derivatives exhibit continuously increasing ϵ_s right up to the collapse point in the isotherms. At the collapse points, the maximum static elasticity values are comparable, $\epsilon_{s, \max} \approx 70 \pm 10$ and $90 \pm 10 \text{ mN}\cdot\text{m}^{-1}$ for TCyP and TiBuP, respectively. However, the shapes of the two curves in Figure 8.3A are quite different: for TCyP, ϵ_s rises to $\epsilon_{s, \max}$ over an A range of $0.15 \text{ nm}^2\cdot\text{molecule}^{-1}$; however, for TiBuP, ϵ_s rises to $\epsilon_{s, \max}$ over an A range of $0.65 \text{ nm}^2\cdot\text{molecule}^{-1}$. Hence, even though the two molecules are essentially the same size, according to the A_c values from molecular modeling, the isobutyl substituents appear to have greater flexibility and compressibility than the cyclohexyl groups. The fact that the cyclohexyl groups are relatively incompressible and rigid in tightly packed structures compared to TiBuP would favor more stable dimer formation in TCyP than TiBuP. The fact that both TCyP and TiBuP show cusps in the isotherm means that ϵ_s drops to zero (mathematically negative) at the collapse point. In Figure 8.3B, ϵ_s shows additional transitions after the initial collapse process. As ϵ_s is related to the derivative of the Π - A isotherm, these features highlight small kinks in the Π - A isotherm that accompany the

multilayer transitions leading to stable rod-like aggregates in the region $A < A_c/3$. Interestingly, $A = 1.64 \text{ nm}^2 \cdot \text{molecule}^{-1}$ corresponds to the first crossover point for TiBuP and TCyP and the collapse point of TCyP. While the slopes are similar for $4 < \Pi < 17 \text{ mN} \cdot \text{m}^{-1}$, the static dilational elasticity, $\epsilon_s = -A \cdot (\partial \Pi / \partial A)_T$, for TCyP is necessarily $< 1/2$ the value of TiBuP at these Π values because of the smaller A values for TCyP in this region.

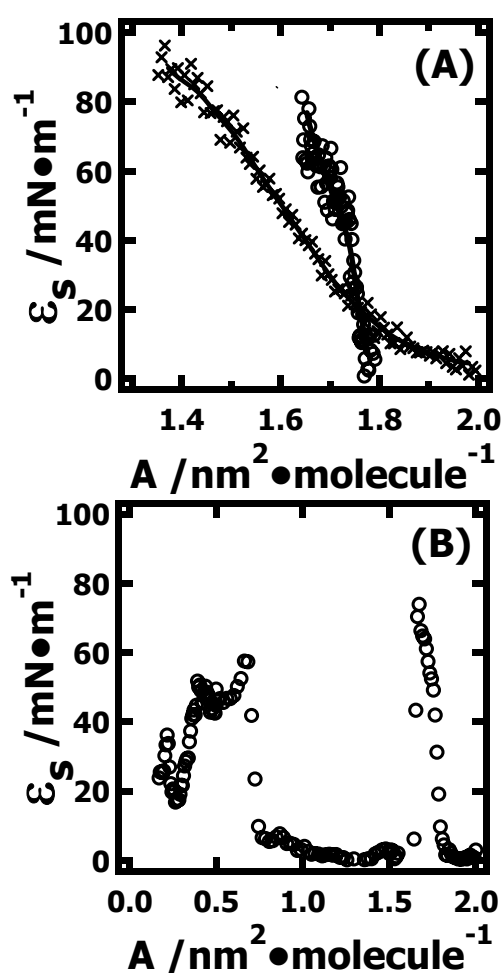


Figure 8.3: ϵ_s - A for TiBuP (crosses, (A)) and TCyP (circles, (A) and (B)) at $T = 22.5 \text{ }^\circ\text{C}$ with a constant compression rate of $20 \text{ cm}^2 \cdot \text{min}^{-1}$ up to the collapse point (A) and for the entire A range of TCyP (B). Solid trend lines on (A) are used to guide the eyes. The scatter in the data on (A) reflects the error associated with the numerical differentiation of the Π - A isotherm and is directly attributed to the finite Π resolution ($\pm 0.1 \text{ mN} \cdot \text{m}^{-1}$) of the surface pressure sensor.

Chapter 8

(5). TCyP and TiBuP exhibit a second crossover point at $A \approx 0.61 \text{ nm}^2 \cdot \text{molecule}^{-1}$ or $\Pi \sim 16 \text{ mN} \cdot \text{m}^{-1}$. Based on the surface concentration, at $A \approx 0.61 \text{ nm}^2 \cdot \text{molecule}^{-1}$ ($\approx A_c/3$), POSS films could exist as trilayers (average thickness), i.e. a "vertically oriented" POSS dimer on top of a hydrated monolayer.

(6). Finally, after the second crossover point, $A < 0.61 \text{ nm}^2 \cdot \text{molecule}^{-1}$, TCyP films undergo a series of multilayer phase transitions with different kinks occurring from $\Pi = 16 \text{ mN} \cdot \text{m}^{-1}$ ($A \approx 0.61 \text{ nm}^2 \cdot \text{molecule}^{-1}$) to $60 \text{ mN} \cdot \text{m}^{-1}$ ($A \approx 0.16 \text{ nm}^2 \cdot \text{molecule}^{-1}$); however, no such transitions are observed in TiBuP as Π still remains constant at $\Pi_{\text{plateau}} \sim 16 \text{ mN} \cdot \text{m}^{-1}$ over this range of surface concentrations.

Since it is reasonable to regard these two trisilanol-POSS molecules as similar-sized amphiphiles with $A_c \approx 1.80 \text{ nm}^2 \cdot \text{molecule}^{-1}$, and given the inherent error in A ($\approx 3\text{-}5\%$) for the experimental results of TiBuP and TCyP, an unavoidable question arises: With similar molecular structures and sizes, why does TCyP behave so differently from TiBuP at A/W after the monolayer starts to collapse? The answer appears to rest with the ability of some trisilanol-POSS derivatives to form stable dimers.

As observed by Feher et al.,¹¹⁹ TCyP, with cyclohexyl rings that pack tightly around the inorganic Si-O core, forms strong hydrogen bonded dimers in the crystalline state. The hydrogen bonding in the dimer occurs in an inherently symmetric fashion between adjacent atoms of the hydroxyl groups with very close intermolecular O-O distances of about 0.26 nm. The highly symmetrical nature of the intermolecular hydrogen bonding interactions allows TCyP molecules to readily form stable dimers. In contrast, dimer formation in TiBuP, with less symmetric and more flexible isobutyl side groups, is apparently a higher energy state; in other words, if TiBuP forms dimers, they

are not as regular or as stable as TCyP dimers. In fact, the proposed organization for TiBuP Langmuir films at A/W provided by Deng et al.¹⁶⁹ for the entire compression process of TiBuP is based on the belief that a monolayer always exists at the bottom of the film, while the upper layers in TiBuP multilayer films consist of mixtures of monomeric TiBuP and unstable dimers. Expansion of highly compressed TiBuP monolayers show that TiBuP films exhibit significant respreading that would be consistent with easily broken dimers if they form as shown in Figure 8.4.

Figure 8.4 shows representative hysteresis loops for TCyP and TiBuP compressed to different final A values. For compression to $A \approx 1.50 \text{ nm}^2 \cdot \text{molecule}^{-1}$, TiBuP has not quite reached the dynamic Π_{collapse} and shows reasonable hysteresis for a LC monolayer. In contrast, TCyP has collapsed but shows reasonable respreading after a sharp drop in Π to a value of $2 \text{ mN} \cdot \text{m}^{-1}$ after the barriers are opened. This value is 20% below $\Pi_{\text{collapse}} = 2.6 \text{ mN} \cdot \text{m}^{-1}$ obtained for addition experiments. For compression to $A \approx 0.65 \text{ nm}^2 \cdot \text{molecule}^{-1}$, both TiBuP (C) and TCyP (D) have collapsed. In both cases, the average surface concentration suggests a trilayer structure. For TiBuP there is a sharp drop in Π to $\Pi = 12 \text{ mN} \cdot \text{m}^{-1}$ (4% below $\Pi_{\text{collapse}} = 12.5 \text{ mN} \cdot \text{m}^{-1}$ observed during addition experiments), followed by a more gentle drop in Π back to zero. The difference between the lift-off A value during compression (where Π becomes > 0) and the A value where $\Pi = 0$ upon expansion, is $\Delta A \approx 0.1 \text{ nm}^2 \cdot \text{molecule}^{-1}$. In contrast, TCyP undergoing the same degree of compression (D), shows much larger ΔA values ($\approx 0.3 \text{ nm}^2 \cdot \text{molecule}^{-1}$). These observations indicate significantly greater respreading of TiBuP compared to TCyP even at intermediate compression. For compression deep into their multilayer regimes ($A \approx 0.15 \text{ nm}^2 \cdot \text{molecule}^{-1}$), TiBuP and TCyP show the largest relative deviation in respreading

Chapter 8

behavior. Qualitatively the curve for TiBuP (E) is similar to compression to $A \approx 0.65 \text{ nm}^2 \cdot \text{molecule}^{-1}$ (C), with a slightly larger ΔA value ($\approx 0.25 \text{ nm}^2 \cdot \text{molecule}^{-1}$). In contrast, TCyP is very different, Π falls to zero upon expansion by $A \approx 0.25 \text{ nm}^2 \cdot \text{molecule}^{-1}$ yielding a ΔA value of $\approx 1.6 \text{ nm}^2 \cdot \text{molecule}^{-1}$. This behavior is attributed to stable dimers that yield unique rod-like hydrophobic aggregates that have been described elsewhere.⁴⁴ In fact, if multiple hysteresis loops are run for the compression ratios corresponding to (E) and (F), TCyP curves shift strongly to the left with each cycle, while TiBuP curves shift more slowly. This difference is attributed to weaker dimers in TiBuP films upon collapse in TCyP films.

Hence, one might conclude that the long plateau existing in the Π - A isotherm of TiBuP actually represents an equilibrium processes between unstable dimers breaking into single amphiphiles and unstable dimers reforming from single POSS molecules. For TCyP, with a similar molecular size and structure, the fact that its Π - A isotherm has little qualitative difference with the behavior of TiBuP up to the collapse points is not surprising. However, TCyP behaves quite differently in its collapsed and multilayer regimes. Hysteresis experiments for TCyP show significantly less respreading as shown in Figure 8.4. In fact compression to $\Pi \approx 60 \text{ mN} \cdot \text{m}^{-1}$ causes stable-hydrophobic rod-like aggregates to form. These aggregates do not instantaneously respread upon expansion of the film as shown in Figure 8.4. This behavior is attributed to stable dimer formation. Apparently, when the monolayer is compressed past its collapse point, stronger van der Waals (VDW) interactions between the cyclohexyl substituents of TCyP vs. the smaller isobutyl groups of TiBuP may help to stabilize TCyP dimers and cause them to respread more slowly during a hysteresis experiment.

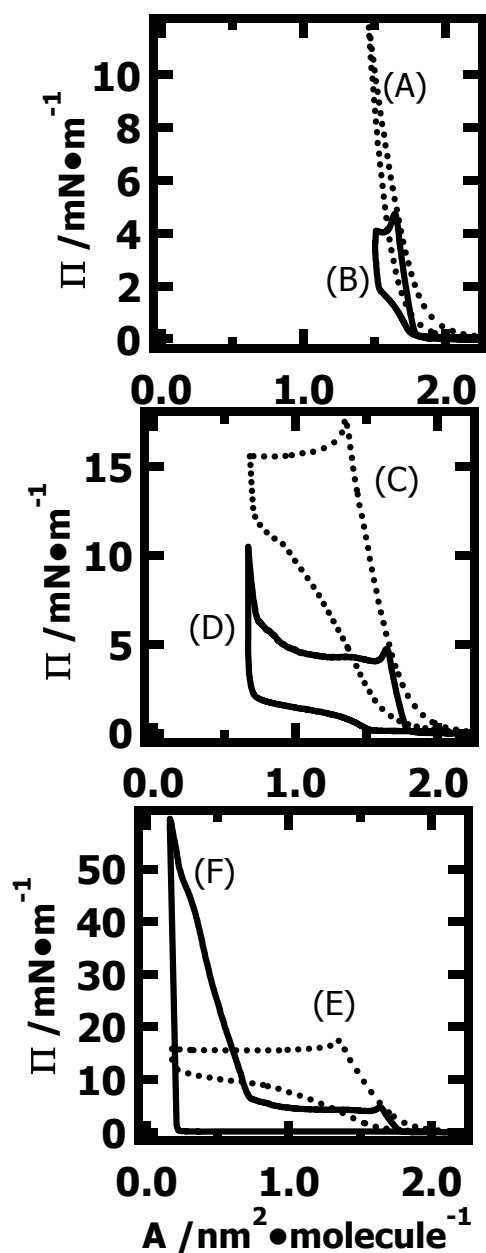


Figure 8.4. Comparison of hysteresis curves of TiBuP and TCyP: Hysteresis curves for TiBuP compressed to different final A values: (A), (C), and (E). Hysteresis curves for TCyP compressed to the same final A values as TiBuP: (B), (D), and (E). All experiments were performed at $T = 22.5\text{ }^{\circ}\text{C}$ and a compression rate of $20\text{ cm}^2\cdot\text{min}^{-1}$.

The collapse parameters actually reflect dynamic compression experiments at a fixed rate of $20 \text{ cm}^2 \cdot \text{min}^{-1}$ as shown in Figure 8.5A. Significantly, different results are not observed at experimentally accessible slower compression rates (down to $\sim 10 \text{ cm}^2 \cdot \text{min}^{-1}$). However, previous studies have shown that TiBuP exhibits $\Pi_{\text{plateau}} = \Pi_{\text{collapse}} \sim 12.5 \text{ mN} \cdot \text{m}^{-1}$ for "addition" experiments and higher Π_{plateau} and Π_{collapse} values at higher compression rates.¹⁶⁹ Similar results are seen for TCyP. In particular, addition experiments show $\Pi_{\text{plateau}} = \Pi_{\text{collapse}} \sim 2.6 \text{ mN} \cdot \text{m}^{-1}$ as shown in Figure 8.5C.

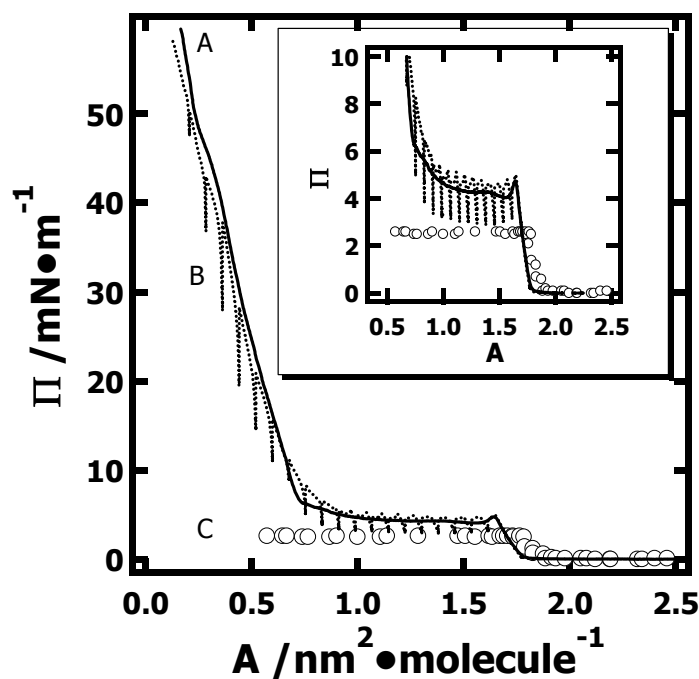


Figure 8.5: Different Π - A isotherms for TCyP at $T = 22.5 \text{ }^\circ\text{C}$. The letters on the figure correspond to low speed compression (A – solid line, $20 \text{ cm}^2 \cdot \text{min}^{-1}$), low speed quasi-static compression (B – dotted line, compression rate $20 \text{ cm}^2 \cdot \text{min}^{-1}$, trough area increment 20 cm^2 , 300 second interval between compression steps), and addition (C – circles). The inset shows an enlargement of the same isotherms for $\Pi \leq 10 \text{ mN} \cdot \text{m}^{-1}$.

As addition experiments are done at an effective compression rate approaching zero, addition experiments can be thought of as "equilibrium" experiments and show that the transition from the liquid-like monolayer to the multilayer regime is really a discontinuous collapse transition. The cusps seen in the dynamic compression experiments arise from slow dynamics for the transition from a two-dimension (2D) monolayer to a three-dimensional (3D) state in rigid liquid condensed (LC) POSS monolayers. In this respect, $\Pi_{\text{collapse}}(\text{addition}) < \Pi < \Pi_{\text{collapse}}(\text{compression})$ leads to a non-equilibrium monolayer that resides in a state analogous to a supercooled liquid. This feature will be important for the selection of appropriate Π values for performing isobaric area relaxation experiments for exploring 2D→3D nucleation and growth mechanisms through the theory of Vollhardt, et al.²⁵¹⁻²⁵³ An alternative approach for obtaining information about dynamic behavior is through "quasi-static compression" experiments (Figure 8.5B). "Quasi-static compression" experiments show that about 5 min is required for TCyP films to "relax" to a near equilibrium state in the monolayer and plateau regions with longer relaxation times for $\Pi > 6 \text{ mN}\cdot\text{m}^{-1}$ as shown in Figure 8.5B. The longer relaxation times at higher Π suggest a more viscoelastic film. ISR results showing enhanced viscoelastic moduli in this regime will be discussed later.

8.4.2 Nucleation and Growth of 3D Domains from TCyP Monolayer Films During Isothermal Compression Experiments

Here the main focus of the morphology studies of TCyP is to understand the nucleation and growth process for 2D→3D transitions at $A < A_{\text{collapse}}$ rather than the high ordered rod-like structures being presented in section 8.4.6. Under "normal spreading" conditions, heterogeneous nucleation of 3D domains in a highly compressed monolayer

Chapter 8

can occur if a material fails to spread completely prior to compression, thereby leaving preformed nuclei. This situation tends to be the case for TCyP Langmuir films (an example is available as Figure 8.6).

Figure 8.6 shows two BAM images, $A = 1.05$ and $0.81 \text{ nm}^2 \cdot \text{molecule}^{-1}$, Figure 8.6A and 8.6B, respectively, acquired under "normal spreading" conditions, i.e. the TCyP monolayer was formed by spreading a chloroform solution on the water surface at room temperature, $T = 22.5 \text{ }^\circ\text{C}$, and compressing at a rate of $20 \text{ cm}^2 \cdot \text{min}^{-1}$. Within the monolayer background (darkest regions), Figures 8.6A and 8.6B exhibit two different 3D aggregation patterns: Small dots (bright white structures) and oil-like platelets that can contain bright dots inside. From the principle of Brewster angle microscopy,^{34,35} one observes structures in BAM images that arise from differences in the intensity of reflected p -polarized light. From eq. 1.13 the reflected intensity, I_r , at Brewster's angle is proportional to the square of film thickness, h^2 . Given the simplicity and symmetry of POSS molecules, the assumption that the monolayer and dimer (if it forms) should have similar n values should be reasonable. Hence, the heterogeneity observed from TCyP's BAM images during the 2D→3D processes should arise from h variation. Based on this conclusion and returning to Figure 8.6, some of the dots dispersed in the monolayer have similar brightness (thickness) to the larger platelets, while the dots trapped inside the oil-like aggregates are brighter suggesting they possess much greater thickness. This complexity of the layer structure implies that different types of aggregates exist and may likely arise from the coexistence of homogeneous and heterogeneous nucleation.

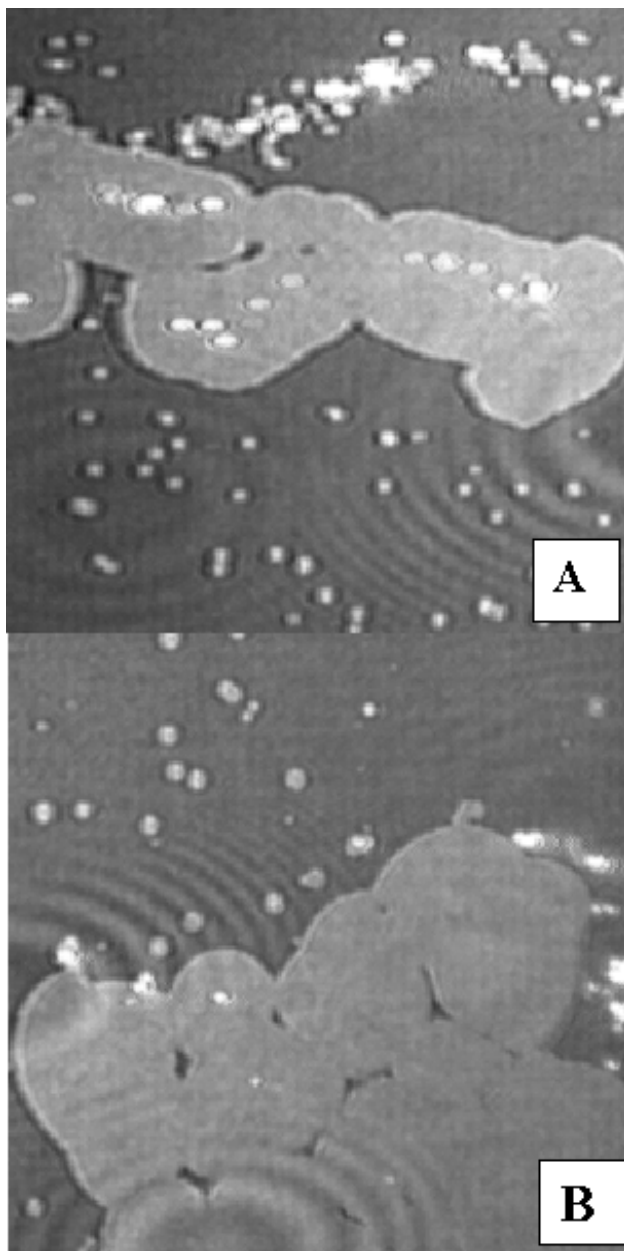


Figure 8.6: Typical BAM images obtained for TCyP at $T = 22.5$ °C with a compression rate of $20 \text{ cm}^2 \cdot \text{min}^{-1}$ after spreading the film at room temperature. Image A and B, with dimensions of $2.4 \times 2.4 \text{ mm}^2$, are acquired at $A = 1.05$ and $0.81 \text{ nm}^2 \cdot \text{molecule}^{-1}$, respectively.

Chapter 8

In general, theoretical descriptions of 2D→3D nucleation and growth processes in Langmuir films assume homogeneous nucleation. Following an Avrami approach used in polymer crystallization studies,²⁶¹⁻²⁶³⁶ work by Vollhardt et al.²⁵¹⁻²⁵³ provided a simple theoretical model for a nucleation and growth mechanism to describe 2D→3D collapse processes in metastable Langmuir monolayers under the assumption of ideal *homogeneous* nucleation. In this model, the total collapse rate is described by the convolution of the nucleation rate and the growth rate, and also considers the effect of overlapping domains during the growth stage.²⁵¹⁻²⁵³ The model considers two typical homogeneous nucleation modes, instantaneous nucleation with monodisperse centers and progressive nucleation with polydisperse centers. This model leads to an expression of the overall nucleation and growth rate for different geometrical growth centers. The generalized expression²⁵¹⁻²⁵³ of the nucleation and growth model allowing for overlapping domains is:

$$z = \frac{A_i - A(t)}{A_i - A_\infty} = 1 - \exp\left[-K_x(t - t_i)^x\right] \quad [8.1]$$

where z is the real normalized volume of the monolayer, $A(t)$ is the area per molecule of the monolayer at time, t , based on the surface concentration, A_i is the area per molecule of the monolayer at the start of the isobaric Π relaxation experiment, A_∞ is the area per molecule of the monolayer for $t \rightarrow \infty$, K_x is a model specific constant for different nucleation and growth models, the exponent x is a characteristic quantity obtainable from isobaric experiments for a specific nucleation model, and t_i is the induction time for nucleation. In order to apply eq. 8.1 to the nucleation and growth of 3D domains in TCyP films, efforts were undertaken to ensure "homogenous spreading" conditions and

verify that they were significantly different from "heterogeneous spreading" conditions (Figures 8.7 and 8.8).

Although the isotherms obtained by "homogeneous spreading" and "heterogeneous spreading" conditions exhibited excellent agreement to those prepared by "normal spreading" conditions, the BAM images exhibit very different features (Figures 8.7 and 8.8). As seen in Figure 8.7, "homogeneous spreading" conditions allow one to observe classical gas bubbles in the LC/G coexistence region (Figure 8.7A and 8.7B). Within the LC monolayer region, ($A_{collapse} \leq A \leq A_c$, Figure 8.7C), the film is uniform until $A_{collapse}$ is approached and some small oval dots begin to appear (not really shown in Figure 8.7). For compression past the uniform LC regime, Figure 8.7C, where the film collapses, most of the image area (Figure 8.7D through 8.7I) shows two level gray scaling, unlike the relatively larger number of small bright (thick) aggregates in Figure 8.8. As the intensity of reflected p -polarized light in BAM is proportional to the film thickness squared as shown in 8.6,^{34,35} the uniform gray scale suggests multilayer regimes of uniform thickness on a monolayer background. As A decreases further, the number density of dots increases; however, at least initially, individual dots are widely dispersed (Figure 8.7D) until $A \approx 0.91 (A_c/2) \text{ nm}^2 \cdot \text{molecule}^{-1}$ (Figure 8.7E), where some small dots appear to aggregate with more ill-defined boundaries. For $A < A_c/2$, small dots combine into ever larger platelets with an increased contrast relative to the monolayer background as shown in Figure 8.7F. Even the 3D aggregates appear to retain a more uniform distribution as the size of the platelets increase from Figure 8.7G to 8.7H until Figure 8.7I, where the boundaries of the platelets more or less disappear and lead to the final

Chapter 8

formation of a nearly "uniform" trilayer film. We should note that some heterogeneous nucleation still appears as the brightest dots in Figure 8.7F through 8.7H.

Figure 8.8 shows BAM images obtained under "heterogeneous spreading" conditions. As $\Pi = 2 \text{ mN}\cdot\text{m}^{-1}$ is close to Π_{collapse} in the addition isotherm, the goal was to try to perturb the homogeneous monolayer's equilibrium state and initiate the formation of some aggregates to act as heterogeneous nucleation centers. Evidence that this process was successful could be observed in the Π - A isotherms, which shifted to smaller A values in Figure 8.8 relative to the "homogeneous spreading" case (solid curve). As shown in Figure 8.8, platelet patterns dominate the BAM images for all Π ; meanwhile only a few small oval dots (like those seen in Figure 8.7) appear. Most platelets in Figure 8.8 have an extremely bright dot in their center. The structures in Figure 8.8 are similar to the "fish-eye" pattern observed in dewetting thin liquid films that arise from a nucleation and growth mechanism where dust or dirt in the system serve as nucleation centers.²⁶⁴ As A decreases, the platelets' sizes increase while the average number density of platelets remains relatively constant, these features are consistent with a heterogeneous nucleation processes. As shown in Figure 8.8A, heterogeneous nuclei already exist at the onset of the monolayer regime and the platelets begin to grow from these nuclei (Figures 8.8B→8.8E) until they reach a limiting size ($R \approx 350 \text{ }\mu\text{m}$) where they start to overlap, Figure 8.8F. After overlapping, the platelets combine together (Figure 8.8G) and finally form a nearly "uniform" trilayer around $A \approx 0.6 (A_c/3) \text{ nm}^2\cdot\text{molecule}^{-1}$, Figure 8.8H. To further explore the structural character of the platelets formed by heterogeneous nucleation, a simple 3D surface plot of the reflected intensity from the BAM image for a selected platelet ($0.8 \times 0.8 \text{ mm}^2$, dashed rectangular frame in Figure 8.8E) without a

background subtraction is presented in Figure 8.8I. Figure 8.8I clearly shows that the platelet has a very thick heterogeneous nucleus with a saturated intensity. Outside the heterogeneous nuclei there is a flat circular region (as noted by the Greek letter α in Figure 8.8I) with relatively uniform intensity. This plateau region is ascribed to a multilayer structure. At the edge of region α , a circular ridge is observed and corresponds to the edge of the platelet. Outside the platelet, there is another flat region (denoted by the Greek letter β in Figure 8.8I) with a somewhat less uniform intensity. The β region should be representative of a monolayer. The two ridges can be attributed to the intermediate structures where TCyP multilayers grow up from the monolayer. Not all of the platelets in Figure 8.8 form at the same time (size heterogeneity) or have a bright spot in the middle suggesting some homogeneous nucleation is also occurring. Based on Figures 8.7 and 8.8, it appears that it is possible to decouple homogeneous nucleation from heterogeneous nucleation for TCyP at A/W.

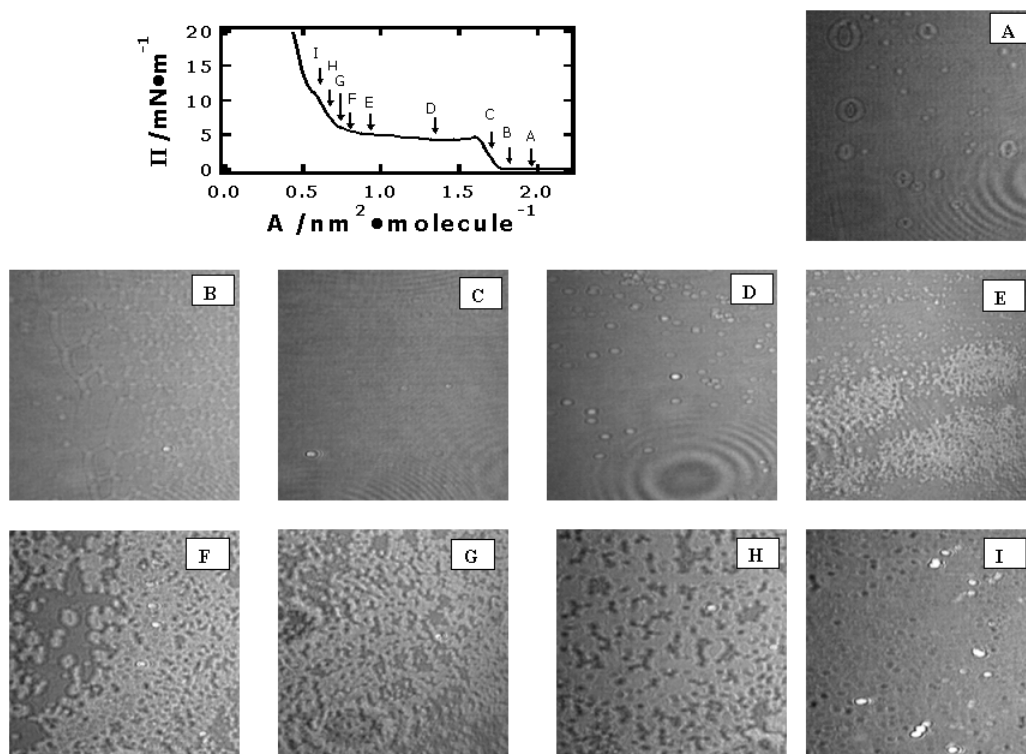


Figure 8.7: BAM images for different A for a TCyP film prepared by "homogeneous" spreading conditions at $T = 22.5$ °C with a compression rate of $20 \text{ cm}^2\cdot\text{min}^{-1}$. The letters on the Π - A isotherm correspond to the A values where the $2.4 \times 2.4 \text{ mm}^2$ BAM images were obtained.

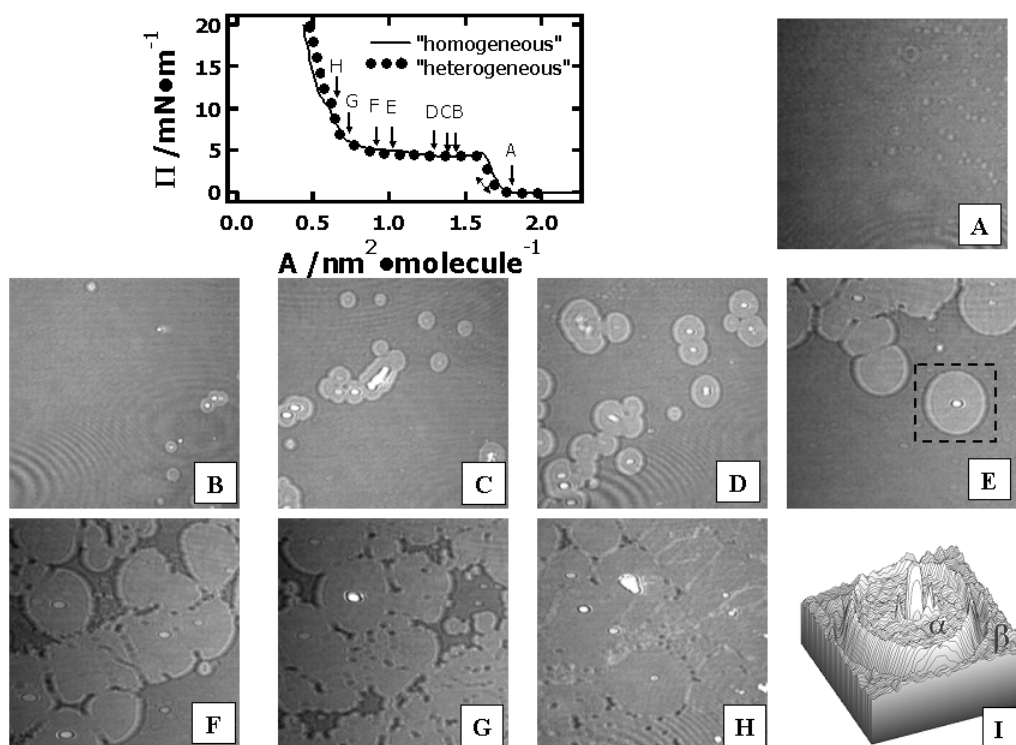


Figure 8.8: BAM images for different A for a TCyP film prepared by "heterogeneous" experimental conditions at $T = 22.5 \text{ }^\circ\text{C}$ with a compression rate of $20 \text{ cm}^2 \cdot \text{min}^{-1}$. The letters on the "heterogeneous" Π - A isotherm (dotted curve) correspond to the A values where the $2.4 \times 2.4 \text{ mm}^2$ BAM images were obtained. The dashed rectangular frame ($0.8 \times 0.8 \text{ mm}^2$) in image 8E represents the region used for creating $0.8 \times 0.8 \text{ mm}^2$ surface plot (I).

8.4.3 Nucleation and Growth of 3D Domains from TCyP Monolayer Films During Isobaric Area Relaxation Experiments

The morphology studies on TCyP films in Figure 8.7 and 8.8 show that by careful sample preparation, TCyP can form multilayers by homogeneous nucleation. Moreover, dynamic studies shown in Figure 8.5 suggest that the window, $2.6 < \Pi < 4.7 \text{ mN}\cdot\text{m}^{-1}$, may be suitable for isobaric area relaxation experiments to study nucleation and growth mechanisms in TCyP Langmuir films. Several isobaric experiments at different Π values were examined revealing a more restricted Π window over which eq. 8.1 does a good job of describing the experimental data. For example, when the isobaric area relaxation is performed at $\Pi < 3.7 \text{ mN}\cdot\text{m}^{-1}$, there is no significant movement of the barriers indicating a very long induction time and insufficient surface energy to overcome the energy barrier for nucleation. Data from a typical isobaric area relaxation experiment for TCyP at $\Pi = 3.7 \text{ mN}\cdot\text{m}^{-1}$ are shown in Figure 8.9. The graph shows an initially concave-downward shape before turning upward at intermediate times and approaching a limiting value (A_∞) at late times. By using the different nucleation and growth models for collapsing monolayers provided by Vollhardt et al. and following the same fitting procedure,²⁵¹⁻²⁵³ different nucleation mechanisms with different x exponents have been evaluated by converting eq. 8.1 into a linear relationship and fitting the experimental data:

$$\left[\ln \frac{1}{1-z} \right]^{1/x} = K_x^{1/x} (t - t_i) \quad [8.2]$$

The best fitting model corresponds to instantaneous nucleation with hemispherical edge growth ($x = 1.5$), while the other models,²⁵¹⁻²⁵³ i.e. $x = 2.5$, progressive nucleation with hemispherical edge growth, and $x = 4$, progressive nucleation with hemispherical growth

from basal areas, deviate substantially from the experimental data. The fitting parameters with one standard deviation errors bars for the best fit according to a model for instantaneous nucleation with hemispherical edge growth are: $K_x = 0.178 \pm 0.007 \text{ h}^{-1.5}$, $A_i = 1.72 \pm 0.01 \text{ nm}^2 \cdot \text{molecule}^{-1}$, $A_\infty = 0.65 \pm 0.01 \text{ nm}^2 \cdot \text{molecule}^{-1}$, and $t_i = 0.36 \pm 0.06 \text{ h}$. Both A_i and A_∞ are in excellent agreement with the onset and end, respectively, of the biphasic LC monolayer/multilayer regime. At $A_\infty = 0.65 \pm 0.01 \text{ nm}^2 \cdot \text{molecule}^{-1}$, the surface concentration is consistent with the existence of a vertically oriented trilayer. At higher Π values ($\Pi > 3.7 \text{ mN} \cdot \text{m}^{-1}$), the nucleation and growth rates become too fast, and the shape of the curve is no longer described by eq. 8.1. This situation represents a case where the nucleation rate has become so large that the samples have large negative induction times. In essence, the nuclei are forming even before the isobaric Π value is obtained. This situation is similar to the behavior observed in isothermal polymer crystallization by differential scanning calorimetry, where Avrami analyses are typically limited to a portion of the crystallization window where the degree of undercooling (supercooling) is small enough to avoid nucleation prior to reaching the desired crystallization temperature.²⁶¹⁻²⁶³

For instantaneous nucleation, monodisperse 3D centers appear simultaneously and the number of nuclei rapidly reaches a maximum value that remains constant during the growth stage. In contrast, progressive nucleation leads to polydisperse nuclei with various sizes. From BAM images (Figure 8.10, 0.53 h) for an isobaric experiment ($\Pi = 3.7 \text{ mN} \cdot \text{m}^{-1}$, $22.5 \text{ }^\circ\text{C}$), some small dots (3D nuclei) appear with similar shapes in the monolayer background and are initially widely separated from each other. Hence the BAM image in Figure 8.10 at 0.53 h is consistent with the early stages of instantaneous

Chapter 8

nucleation and is similar to what is observed during isothermal compression between $A_c/2$ and $A_{collapse}$ (Figure 8.7D). As the nucleation and growth process progresses further, additional nucleation centers have grown to a detectable size in BAM images (Figure 8.10, 1.57 h), and soon the number density of nuclei appears to reach a constant maximum value (Figure 8.10, 1.92 h). While the resolution of the MiniBAM instrument (at least 20 μm) and the automatic gain mode may make it difficult to detect nuclei that form at later times because of their small size and thickness, all detectable nuclei have similar sizes and shapes. Based on the nucleation and growth model that best fits the experimental data, as soon as the nuclei are formed, the sizes of the aggregates grow from the edge (Figure 8.10, 1.92 h \rightarrow 4.47 h) as shown in the schematic diagram in the lower left-hand corner of Figure 8.9. As the domains grow, the aggregates start to overlap (Figure 8.10, 1.92 h \rightarrow 6.63 h); however, due to resolution limits of the BAM instrument, additional efforts will be required in the future to obtain higher resolution images as domains start to overlap.

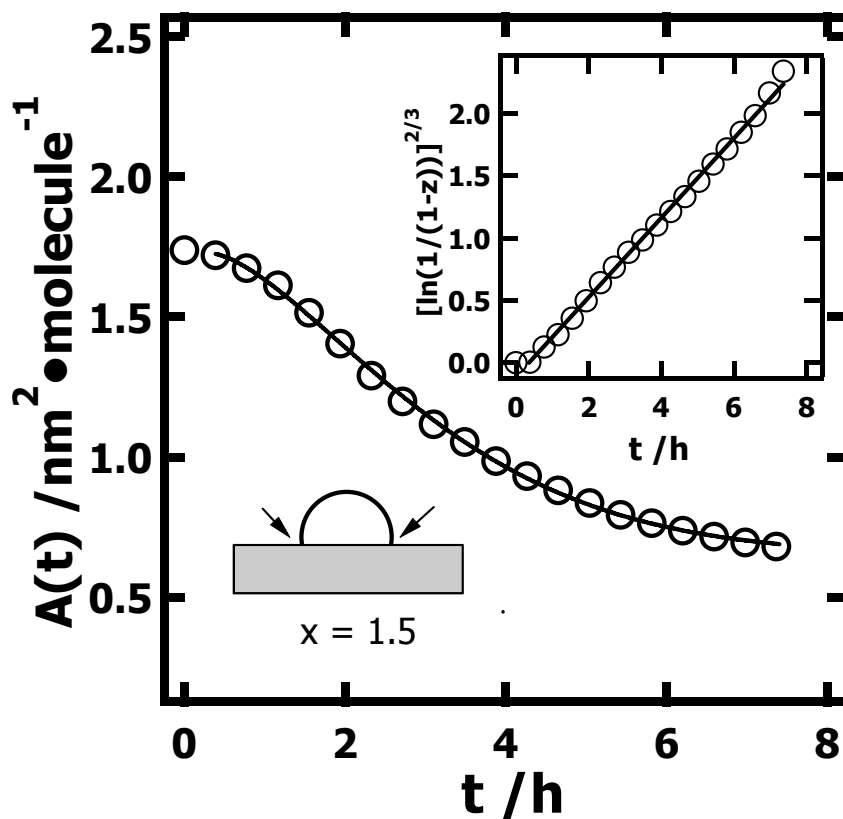


Figure 8.9: $A(t)$ versus t for TCyP during isobaric area relaxation experiments at $\Pi = 3.7$ $\text{mN}\cdot\text{m}^{-1}$ (circles) along with the fitting result for instantaneous nucleation with hemispherical edge growth ($x = 1.5$ in eq. 8.1, solid line) at 22.5°C . A simple schematic model of nucleation with hemispherical edge growth is shown in the lower left-hand corner of the figure. The solid line in the inset represents the evaluation of the best fitting result according to eq. 8.2.

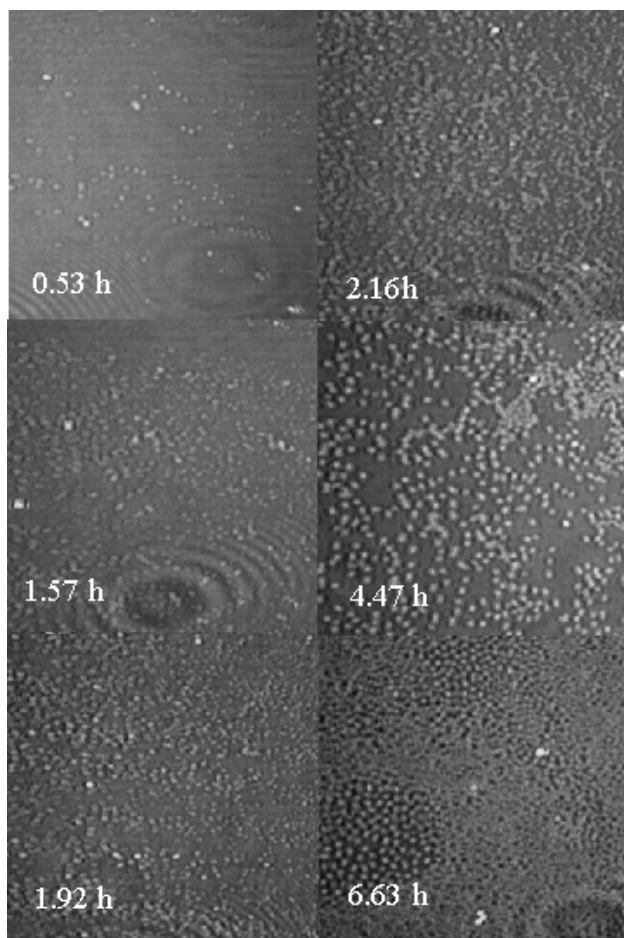


Figure 8.10: BAM images of TCyP acquired at $\Pi = 3.7 \text{ mN}\cdot\text{m}^{-1}$ and $T = 22.5 \text{ }^\circ\text{C}$ for the isobaric area relaxation experiment in Figure 8.9. The time at which each image was obtained is indicated in the lower left-hand corner of each image. During the induction period, $t_i = 0.36 \pm 0.06 \text{ h}$, little aggregates (dots) can be observed. All images are $2.4 \times 2.4 \text{ mm}^2$.

8.4.4 Surface Rheology of TCyP Films at A/W

The structural features of TCyP films can be related to the rheological properties by utilizing interfacial stress rheometry (ISR),³⁹ which allows for the simultaneous measurement of both storage (G_s') and loss (G_s'') moduli at a high sensitivity (approximately 10 times greater than conventional disk devices) as eq. 1.14.³⁹ While G_s' is a measure of the elastic or solid-like character of a surface, G_s'' is a measure of the viscous or fluid-like character. If G_s'' is greater than G_s' , the tangent of the loss angle, $\tan\delta = G_s''/G_s' > 1$, demonstrating that the film's viscous or fluid-like character is stronger. Conversely, $G_s' > G_s''$ is indicative of an elastic object with $\tan\delta < 1$. To describe the overall flow behavior of complex materials, a dynamic viscosity, $\mu_s^*(\omega)$, is commonly used as shown by eq. 1.15. In Figure 8.11, G_s' and G_s'' for TCyP films at a low frequency ($\omega = 0.92 \text{ rad}\cdot\text{s}^{-1}$) are plotted together with the corresponding Π - A isotherm (right-hand axis) as a function of A . These data can be used to compute $\tan\delta = G_s''/G_s'$. A plot of these values is provided as Figure 8.12 at $\omega = 0.92 \text{ rad}\cdot\text{s}^{-1}$. Based on Figure 8.11, three clear regimes are observed: (1) the monolayer and monolayer-rich biphasic regime, (2) the multilayer rich biphasic regime, and (3) the multilayer regime where average film thicknesses based on surface concentration would be consistent with a trilayer structure.

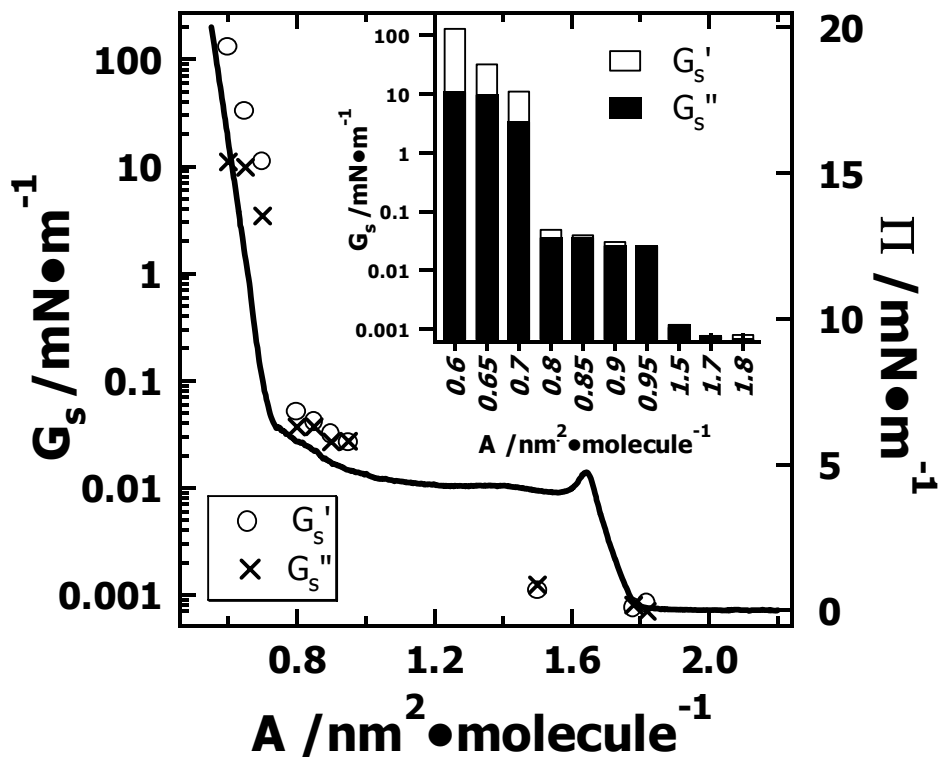


Figure 8.11: G_s' (\circ) and G_s'' (\times) measured at a low frequency ($\omega = 0.92 \text{ rad}\cdot\text{s}^{-1}$, $T = 22.5$ °C) for TCyP as a function of A . By using the right-hand axis, the Π - A isotherm is plotted together with the ISR data for comparison. The bar graph in the upper right corner of the figure is provided to more clearly show which modulus is larger at a given A value. One standard deviation error bars on G_s' and G_s'' are smaller than the size of the symbols.

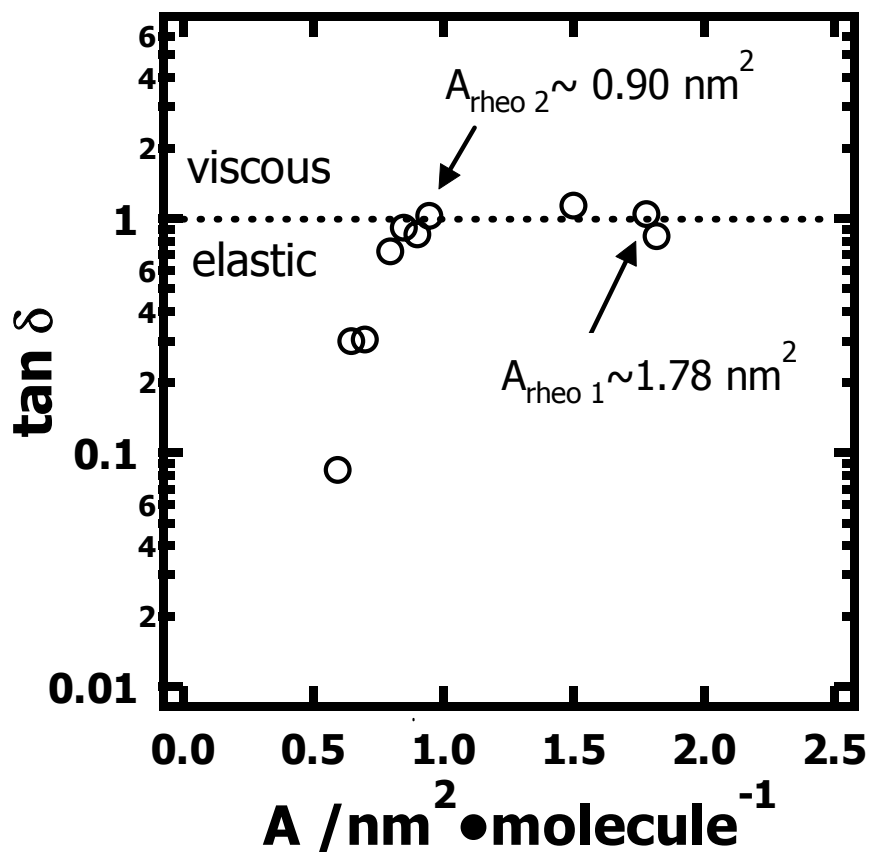


Figure 8.12: $\tan \delta$ vs. A for TCyP ($T = 22.5 \text{ }^\circ\text{C}$, $\omega = 0.92 \text{ rad}\cdot\text{s}^{-1}$). The dotted line ($\tan \delta = 1$) is used to define regimes where viscous and elastic responses are larger. Two crossover points occurring around $A = 1.78$ and $0.90 \text{ nm}^2 \cdot \text{molecule}^{-1}$, are very close to A_c and $A_c/2$ on the Π - A isotherm. One standard deviation error bars on $\tan \delta$ are smaller than the size of the symbols.

Chapter 8

Within the monolayer region ($A_{collapse} < A < A_c$), both G_s' and G_s'' have magnitudes that are comparable and close to zero. Based on $\tan\delta$ values that are slightly greater than 1, the monolayer regime appears to form a slightly viscous film in contrast to the slightly elastic response observed on the pure water surface. This rheological transition occurs around $A_{rheo\ 1} \sim 1.78 \text{ nm}^2 \cdot \text{molecule}^{-1}$, which corresponds to TCyP's cross-sectional area (A_c). In this regime, standard ISR analysis reveals a film with an anomalous frequency dependence as $\tan\delta$ increases with increasing frequency (Figure 8.13). At present, the true significance of this behavior is not known. Due to the small magnitude of the moduli, G_s' values become vanishingly small and even negative after applying a hydrodynamic correction for the viscous drag on the floating needle that arises from the bulk subphase. For this reason, the data for the frequency sweeps in the monolayer and monolayer-rich biphasic region have fewer points than the data sets from the multilayer-rich regimes. Future work focusing on improvements to the hydrodynamic correction for low modulus films will be necessary for studies in the monolayer regime.

For $A < A_{collapse}$, there is an initially monolayer-rich biphasic region near the collapse point where the magnitude of the moduli at $\omega = 0.92 \text{ rad} \cdot \text{s}^{-1}$ begin to increase to slightly higher values relative to the monolayer regime. In this region, $\tan\delta$ still shows the same anomalous frequency dependence as the monolayer. Further compression into the biphasic regime yields an ISR "dead-zone" ($0.95 < A < 1.50 \text{ nm}^2 \cdot \text{molecule}^{-1}$). Because of the heterogeneity of the biphasic region (monolayer + multilayer) and the large difference in mechanical properties between the monolayer and multilayer, the initial orientation of the magnetized needle could not be suitably positioned by the magnetic field of the rheometer's DC controlled Helmholtz coils. For example, if the

initial alignment is done in a predominately multilayer-rich region of the film, the needle needs a stronger magnetic force to fix its original position. However, during the subsequent application of a time-dependent magnetic field gradient by the AC controlled Helmholtz coils, the needle probe can be dragged out of detector window (an inverted microscope) if it encounters a predominately monolayer-rich region of the film. As a consequence, ISR yields wildly irreproducible results in the "dead-zone".

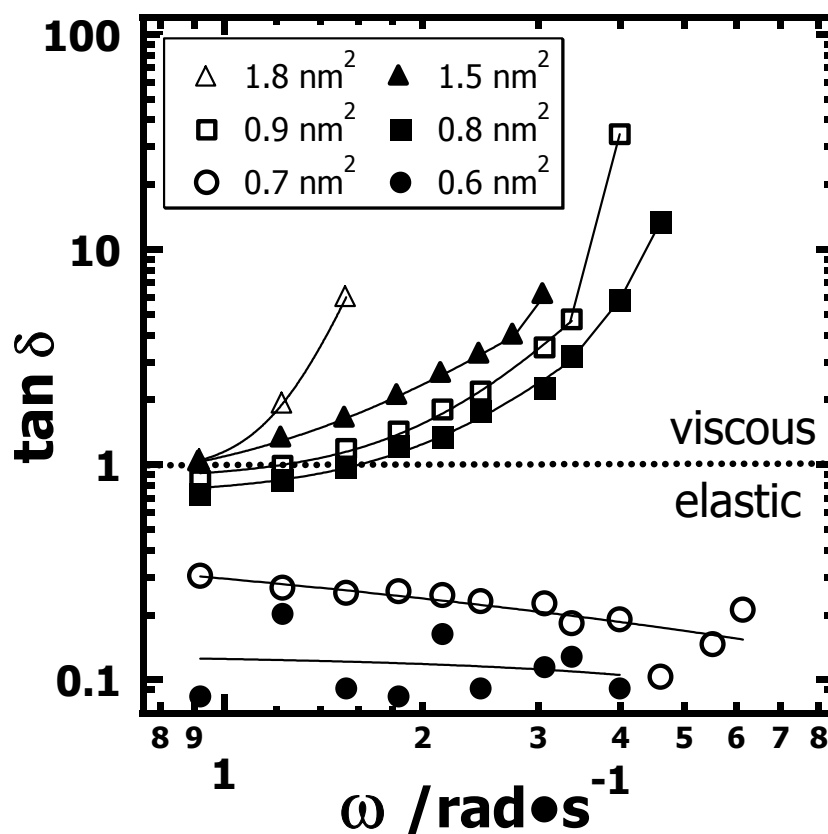


Figure 8.13: $\tan\delta$ as a function of ω for TCyP at the different A (indicated in the legend for the different symbols) at $T = 22.5^\circ\text{C}$.

Chapter 8

For the monolayer and monolayer-rich biphasic region, both moduli are small and of a comparable magnitude, $G_s' \approx G_s''$ (Figures 8.11). At the other end of the regime, the formation of a multilayer-rich biphasic film, $A \leq 0.95 \text{ nm}^2 \cdot \text{molecule}^{-1}$, leads to a situation where ISR is again a suitable technique for probing the rheological properties of the film. As shown in Figure 8.11, there is a two order of magnitude increase in the moduli values from the monolayer-rich end of the biphasic regime to the multilayer-rich end. As the surface concentration keeps increasing, another rheological transition at $\omega = 0.92 \text{ rad} \cdot \text{s}^{-1}$ is observed for TCyP in Figure 8.13 as $\tan \delta$ drops back below 1 at $A_{rheo 2} \sim 0.90 \text{ nm}^2 \cdot \text{molecule}^{-1}$. As seen in Figure 8.13, this is only true at the lowest frequencies, because $\tan \delta$ still shows the same anomalous frequency behavior as in the monolayer regime. The existence of this transition is more clearly seen in the complex viscosity shown in Figure 8.14. $|\mu_s^*|$ shows a non-Newtonian increase in value with increasing frequency ($|\mu_s^*(\omega)| \sim \omega^{0.5 \pm 0.2}$, one standard deviation error bars for 3 different A values) for the monolayer and monolayer-rich biphasic regimes. In contrast, at $A_{rheo 2} \sim 0.90 \text{ nm}^2 \cdot \text{molecule}^{-1}$, $|\mu_s^*|$ shows a non-Newtonian decrease in value with increasing frequency ($|\mu_s^*(\omega)| \sim \omega^{-1.5 \pm 0.2}$, one standard deviation error bars for 4 different A values) which is consistent with a more strongly elastic system. While $A = A_c/2$ at $A_{rheo 2} \sim 0.90 \text{ nm}^2 \cdot \text{molecule}^{-1}$, BAM images in Figures 8.7 and 8.8 are not consistent with the existence of a true bilayer as they show domains of roughly uniform thickness (multilayer) that start to interact with each other at this surface concentration independent of the spreading method and nucleation mechanism of multilayer structures. As a consequence, Π rises, as do G_s' , G_s'' and $|\mu_s^*|$.

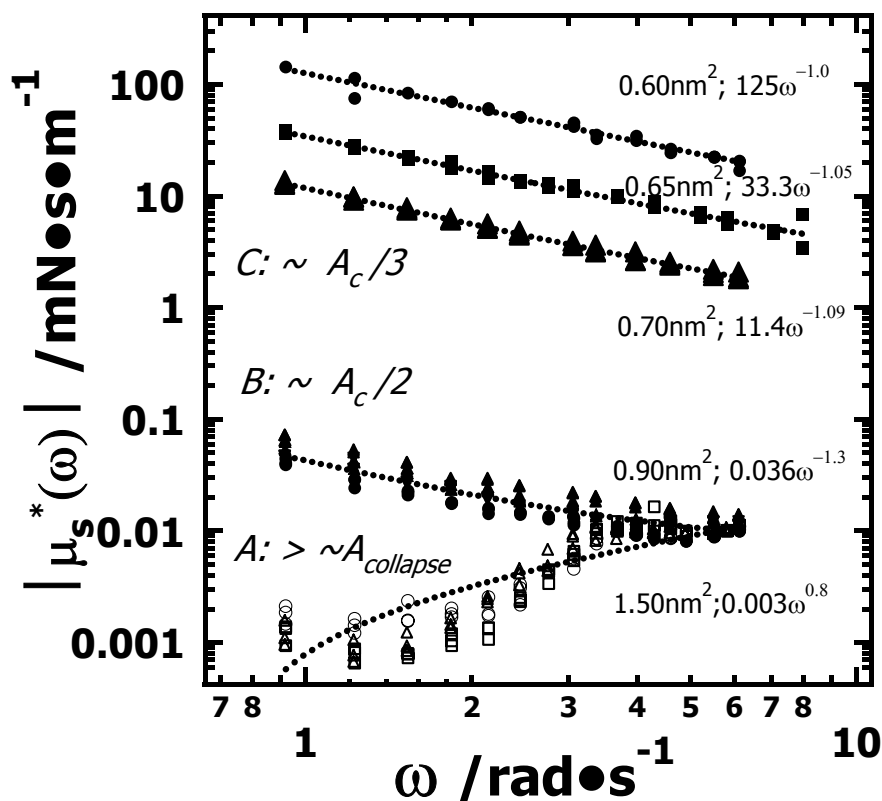


Figure 8.14: $|\mu_s^*(\omega)|$ at different A values. From the shapes and trends three distinct rheological regimes can be determined: (A) monolayer films and monolayer-rich films in the coexisting monolayer/multilayer regime near $A_{collapse}$; (B) multilayer-rich films in the coexisting monolayer/multilayer regime near $A_c/2$; and (C) the ordered and rigid trilayer regime around $A_c/3$. The dotted lines represent power law fits to the data, $|\mu_s^*(\omega)| = C\omega^D$ where C and D are fitting parameters at the indicated areas per molecule. For Regimes A and B, different symbols correspond to different surface concentrations, and the dotted lines correspond to two representative fits: 1.50 and $0.90 \text{ nm}^2 \cdot \text{molecule}^{-1}$, respectively.

Chapter 8

Further compression of the film past the end of the plateau region, $0.61 < A < 0.74$ $\text{nm}^2 \cdot \text{molecule}^{-1}$, causes substantial changes in the viscoelastic behavior. As seen in Figures 8.11 and 8.13, $G_s' > G_s''$ and $\tan \delta$ decreases slightly with increasing frequency. This behavior is similar to the behavior one would expect for any viscoelastic object. The BAM images in Figures 8.7 and 8.8, show that in this regime, multilayer domains come together to form an almost uniformly covered multilayer surface. The magnitudes of G_s' and G_s'' reach the maximum values, which ISR can measure (on the order of 200 $\text{mN} \cdot \text{m}^{-1}$). These values are at least four orders of magnitude greater than the values observed in the multilayer rich biphasic region. As seen in Figure 8.14, $|\mu_s^*|$ also shows the expected three to four order of magnitude increase over the values at $A_c/2$ based on Figure 8.11. However, the non-Newtonian frequency dependence ($|\mu_s^*(\omega)| \sim \omega^{-1.05 \pm 0.04}$, one standard deviation error bars for 3 different A values) is qualitatively similar to the multilayer rich biphasic region. Based purely on surface concentration, $0.6 \text{ nm}^2 \cdot \text{molecule}^{-1} \approx A_c/3$, which would be consistent with a trilayer structure and the A_∞ value obtained from isobaric area relaxation experiments. This feature suggests that the hydrated monolayer is responsible for the viscous response, but the dry ordered (presumably composed of dimers) upper layer leads to much stronger elastic responses. These responses overwhelm the contribution from the underlying hydrated monolayer such that the overall response of the film to shear is elastic.

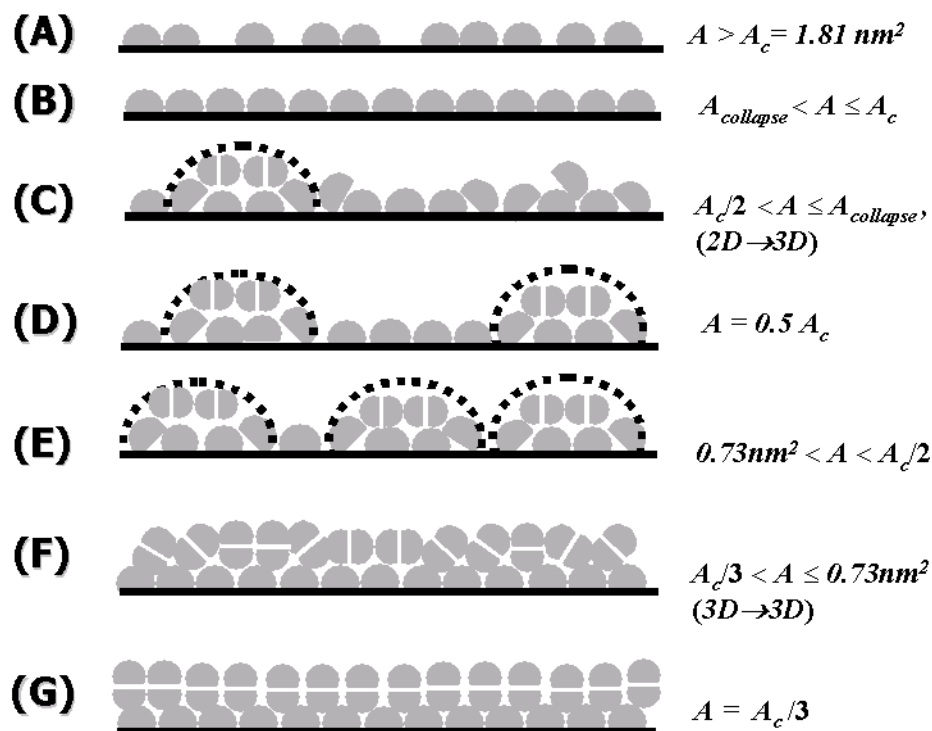


Figure 8.15: Proposed organization of trisilanolcyclohexyl-POSS films going from 2D to 3D films at A/W during symmetric compression: (A) a dilute LC/G regime, $1.81 (A_c) < A < 2.3 \text{ nm}^2 \cdot \text{molecule}^{-1}$, (B) a LC monolayer, $\approx 1.6 (A_{collapse}) < A \leq 1.8 (A_c) \text{ nm}^2 \cdot \text{molecule}^{-1}$, (C) 2D \rightarrow 3D collapse through dimerization via instantaneous nucleation with hemispherical edge growth (indicated by the dotted hemisphere), $0.91 (A_c/2) < A \leq 1.6 (A_{collapse}) \text{ nm}^2 \cdot \text{molecule}^{-1}$, (D) an intermediate state depicting isolated multilayer domains on top of a TCyP monolayer, (E) overlapping hemispherical domains on top of the underlying TCyP monolayer, $0.73 < A < 0.91 (A_c/2) \text{ nm}^2 \cdot \text{molecule}^{-1}$, (F) a 3D \rightarrow 3D transition to more vertically oriented dimers on top of a monolayer, $0.61(A_c/3) < A \leq 0.73 \text{ nm}^2 \cdot \text{molecule}^{-1}$, and (G) an ideal trilayer (3 POSS molecules thick) structure formed by a vertically oriented condensed dimer layer residing on top of a monolayer.

8.4.5 Schematic Depiction of the Phase Behavior from a Monolayer to a Trilayer in a TCyP Film During a Compression Experiment

Based on the comparison between TCyP and TiBuP isotherms, and by utilizing the simplified model for TCyP molecules described in Figure 8.1B, a mechanism for film formation of TCyP from monolayers (1 POSS molecule thick) to trilayers (a POSS monolayer hydrogen bonded to water with vertically orientated POSS dimers on top) at A/W is proposed in Figure 8.15. All of the POSS conformations implied by this diagram should be regarded as local structural elements arranged in idealized macroscopic structures based on BAM studies in Figures 8.7, 8.8, and 8.10. At $A > A_c = 1.81 \text{ nm}^2 \cdot \text{molecule}^{-1}$ or $\Pi \approx 0 \text{ mN} \cdot \text{m}^{-1}$, TCyP forms a biphasic liquid-condensed/gas (LC/G) film, Figure 8.15A. This feature is consistent with BAM studies under homogeneous spreading conditions (Figure 8.7A and 8.7B). In principle, isolated molecules could exist at much larger A values than those examined in this study. After compression to $A < A_c$ and prior to the collapse point $A_{collapse}$, $1.6 \leq A \leq 1.81 \text{ nm}^2 \cdot \text{molecule}^{-1}$, a LC film forms upon close-packing of the TCyP molecules, Figure 8.15B. For $A < A_{collapse}$, the strength of the interaction between the hydrophilic silanol groups and the water subphase is not strong enough to keep all TCyP molecules at the air/water interface, leading to the formation of three-dimensional structures. Within the low Π collapsed regime, $0.91 (\approx A_c/2) \leq A \leq 1.61 \text{ nm}^2 \cdot \text{molecule}^{-1}$ (or $\Pi \approx 4.3 \text{ mN} \cdot \text{m}^{-1}$) the bottom monolayer likely persists; however, intermolecular hydrogen bonding would favor the formation of dimer aggregates for TCyP molecules ejected from A/W during compression as depicted in Figure 8.15C. This feature is consistent with the uniform domain thicknesses seen in Figures 8.7, 8.8, and 8.10, and the conclusion from the isobaric area relaxation

experiments at $\Pi = 3.7 \text{ mN}\cdot\text{m}^{-1}$ that the 2D \rightarrow 3D nucleation and growth process occurs through instantaneous nucleation with hemispherical edge growth. These features are also consistent with ISR results showing the dynamics of the monolayer rich biphasic regime are similar to the monolayer, and the rheological "dead-zone" that arises from the biphasic nature of the plateau region. As the molecular area reaches $A_c/2$, Figure 8.15D, surface concentration would suggest a structure approaching a uniform bilayer should form. However, BAM results show that initially isolated (Figure 8.15D) dimer rich aggregates start to interact with each other (Figures 8.7 and 8.8) as the amount of monolayer present in the biphasic monolayer/multilayer regime starts to decrease. The onset of overlapping domains is depicted in Figure 8.15E. This behavior is consistent with the small rise in Π ($\approx 1.4 \text{ mN}\cdot\text{m}^{-1}$) in the region $0.73 \leq A \leq 0.91$ ($\approx A_c/2$) $\text{nm}^2\cdot\text{molecule}^{-1}$ (Figure 8.2), as well as the end of the rheological "dead-zone" as ISR reveals higher moduli. Upon further compression 0.61 ($\approx A_c/3$) $\leq A \leq 0.73 \text{ nm}^2\cdot\text{molecule}^{-1}$ a 3D \rightarrow 3D transition to vertically oriented dimers (Figure 8.15F) leads to a sharper increase in Π and G_s^* until a complete and rigid trilayer (average thickness based on surface concentration) is formed (Figure 8.15G). As shown in the next section, the compression of TCyP films to $A < 0.61$ ($\approx A_c/3$) $\text{nm}^2\cdot\text{molecule}^{-1}$ ultimately leads to stable rod-like multilayer structures.

8.4.6 Unique Rod-like Surface Morphologies in Highly Ordered TCyP Multilayers

When a uniform hydrophobic POSS trilayer film finally forms (for $A < 0.61$ ($\approx A_c/3$) $\text{nm}^2\cdot\text{molecule}^{-1}$), the trilayer is still compressible and Π rises again. BAM images taken in this regime (Figure 8.16A & B, $A = 0.40$ & $0.35 \text{ nm}^2\cdot\text{molecule}^{-1}$, respectively) show the coexistence of at least two different phases – the thicker domains (brighter

Chapter 8

structures) existing within a thinner film (dark background). Below $A = 0.61 \text{ nm}^2 \cdot \text{molecule}^{-1}$ the top dimer film further collapses into dimer multilayers until the one apparent kink, $A \approx 1/2$ of $A_c/3$, is observed in the Π - A isotherm, which indicates the trisilanolcyclohexyl-POSS dimers undergo a series of continuous transformations from a trilayer film (3 POSS molecules thick) to a thicker film (6 POSS molecules thick). For A values below $A = 0.33 \text{ nm}^2 \cdot \text{molecule}^{-1}$, the "hexalayer" (6 POSS molecules) enter a regime ($0.24 < A < 0.33 \text{ nm}^2 \cdot \text{molecule}^{-1}$) where Π increases more slowly upon compression, which suggests a less rigid multilayer phase, or a phase transition toward a more condensed structure such as one might see during crystallization or the formation of liquid-condensed monolayer in the LC-LE coexistence region of phospholipid monolayers for continuous compression experiments.²⁶⁵ As seen in Figure 8.16C ($A = 0.3 \text{ nm}^2 \cdot \text{molecule}^{-1}$), this regime is uniformly heterogeneous and the cessation of compression still causes Π relaxation to a value around $1 \text{ mN} \cdot \text{m}^{-1}$ after 30 minutes (data not shown in the figures), which means the water subphase is still powerful enough to break up dimers and form a partial monolayer of monomeric POSS in a mechanism similar to the case discussed above.

Further compression to A values below another kink ($A < 0.24 \text{ nm}^2 \cdot \text{molecule}^{-1}$, $\sim 1/8$ of A_c) induces the liquid-like dimer film to self-assemble into very unique rod-like aggregates as shown in Figure 8.16D ($A = 0.2 \text{ nm}^2 \cdot \text{molecule}^{-1}$) which are less compressible given the increase in slope and align as expected parallel to the compressing barriers.²⁶⁶⁻²⁶⁸ Even with the naked eye one can see a thin solid film forms on the water surface. The rigid rods are very stable and maintain their morphology on the water surface for more than 36 hours when A is held constant, even though the cessation

of compression causes an immediate relaxation in Π down to a value of zero (data shown in the Figure 8.6). This observation is consistent with the formation of a totally hydrophobic film with persistent dimer-dimer interactions that are stronger than water-dimer interactions. Considering the POSS structure (Figure 8.1), one can imagine that exposure of the trisilanol pocket to air would be a high energy state that favors POSS aggregation into hydrogen bonded dimers, thereby forming a completely hydrophobic exterior. When POSS films reach a critical thickness, ≈ 8 POSS molecules, intermolecular hydrogen bonding between POSS molecules appears to be favored over POSS-water interactions, and the stable rod-like hydrophobic aggregates form. Thus far, no additional experimental proof, such as electron and X-ray diffraction methods, exists to identify whether or not these rod-like aggregates are crystalline, but due to their stability and tremendous length scales from BAM images (mm dimensions) future work will investigate the crystallinity of these films. In order to obtain better contrast in the BAM images and to clarify the morphology of the rods, the barriers are expanded to form a non-equilibrium gas-solid coexistent film, whereby the loose structure of the rods against a water background lead to high contrast images like those shown in Figure 8.16E - G. Without the confinement of the barriers, the rod-like aggregates can rotate into "random" orientations relative to the barriers in Figures 8.16E - G. When POSS aggregates are exposed to large open areas of water, the rod-like structures ultimately peel off the rod-rich domains and relax into "dragon-like" shapes due to the interplay of dipole density and line tension¹⁸⁰ as seen in Figure 8.16G.

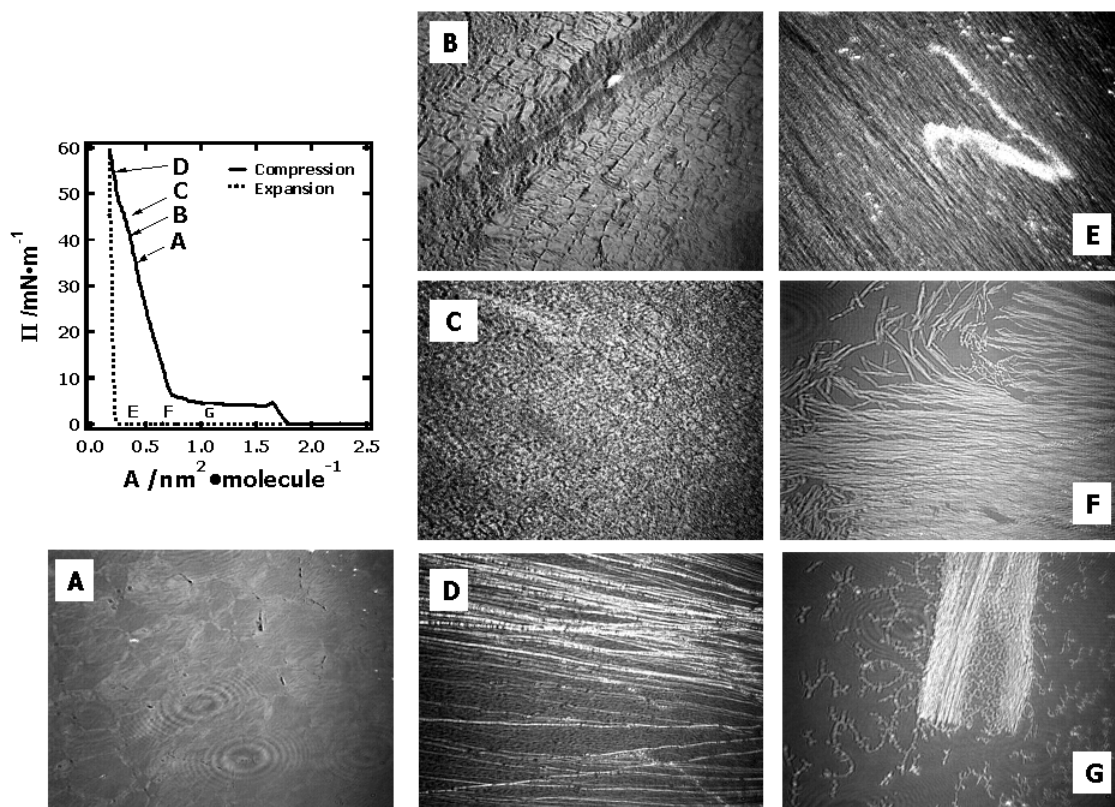


Figure 8.16: BAM images for TiBuP at different areas per molecule smaller than $A_c/3$ for the compression/expansion rate of $20 \text{ cm}^2 \cdot \text{min}^{-1}$ and $T = 22.5 \text{ }^\circ\text{C}$. The letters correspond to the points on the hysteresis loop. All BAM images are $4.8 \times 6.4 \text{ mm}^2$ and the film is symmetrically compressed from the top and bottom of each image. Due to the automatic gain feature of the BAM instrument noted in the experimental section, each BAM image has an independent grey scale.

8.5 Conclusions

Π - A isotherm, BAM, and ISR studies reveal important equilibrium and non-equilibrium phase transitions for trisilanocyclohexyl-POSS (TCyP) Langmuir films ranging from the limiting area $A_o \approx A_c = 1.78 \text{ nm}^2 \cdot \text{molecule}^{-1}$ to a surface concentration that is consistent with a trilayer structure ($A_c/3$). These results reveal four important regimes: (1) $A_{collapse} < A < A_c$ where the LC monolayer exhibits rheological properties consistent with $G_s' < G_s''$. Around $A_{collapse}$, the results show that the TCyP monolayer can undergo collapse through either a heterogeneous mechanism, or a homogeneous mechanism with instantaneous nucleation and hemispherical edge growth. Based on the A_∞ values from isobaric compression experiments, the preferred aggregate thickness should be on the order of 3 POSS molecules thick. During the early stages of collapse, the monolayer-rich biphasic film demonstrates rheological properties similar to the LC monolayer. (2) $A_c/2 < A < A_{collapse}$, the low Π phase coexistence regime between monolayer and multilayer structures. In this regime, ISR is not a suitable technique for determining the films viscoelastic properties, yielding a rheological "dead-zone". At the end of the rheological "dead zone", the amount of monolayer phase is sufficiently small to start detecting significantly larger moduli (≈ 2 orders of magnitude greater than the monolayer). (3) In the regime, $0.73 \text{ nm}^2 \cdot \text{molecule}^{-1} < A < A_c/2$, Π , G_s' and G_s'' start to gently increase; however, G_s' grows faster leading to $\tan \delta < 1$. This behavior is attributed to the interactions between TCyP dimer domains on top of a hydrated TCyP monolayer. (4) In the final regime, corresponding to $A_c/3 < A < 0.73 \text{ nm}^2 \cdot \text{molecule}^{-1}$, TCyP appears to form a well-ordered rigid trilayer, as Π , G_s' , and G_s'' all rise sharply. For the case of G_s' the values are nearly three orders of magnitude greater than those observed at $A_c/2$. In

Chapter 8

this respect, G_s' grows much faster than G_s'' with decreasing A leading to a sharp drop in $\tan\delta$ for the strongly elastic film. In summary, this experimental study provides important insight into the aggregation mechanism and rheological properties of trisilanol-POSS derivatives, an interesting class of molecules that have been identified as ideal nanofillers for studying confinement effects on filled polymer systems as Langmuir monolayers.^{168,170}

With continuously increasing surface concentration via compression, trisilanolcyclohexyl-POSS amphiphiles at A/W systematically shows transitions from traditional Langmuir monolayers (1 POSS molecule) to unique rod-like hydrophobic aggregates in multilayer films (≈ 8 POSS molecules, or ≈ 8 nm thick) that are dramatically different from "collapsed" morphologies seen in other systems.^{181,269-271} This tendency to form stable and hydrophobic rod-like structures on water is presumably due to their unique molecular structure and strong tendency to form intermolecular hydrogen bonds in the solid state.¹¹⁹ This result is consistent with existing POSS polymer composite research, which shows POSS molecules have a strong tendency to aggregate and crystallize into lamellar (2-dimensional) nanocrystals.^{147,158} Future research will focus on more detailed characterization of the rod-like structure with techniques such as X-ray diffraction and atomic force microscopy.

CHAPTER 9

Conclusions and Suggestions for Future Work

9.1 Overall Conclusions

9.1.1 POSS at A/W

In conclusion, breaking the POSS-cage converts non-amphiphilic octasubstituted-POSS molecules into surface-active trisilanol-POSS molecules that self-assemble into uniform and stable monolayers at the air/water interface (A/W) upon compression. With small length/diameter ratios and bulky shapes, the monolayer phase behavior and packing states of different POSS are much simpler than the traditional rod-like lipids as shown in Figures 1.14 and 9.1. In general, the monolayer phases of POSS can be described as two simple regions: a gas phase (G) at very large molecular areas and a liquid phase (L) before 3D structures form during collapse of the monolayers. Due to the intrinsic orientational constraints of different R groups, different trisilanol-POSS derivatives remain in a monolayer state for different degrees of compression. For example, trisilanolcyclohexyl-POSS (TCyP), which has very crowded cyclohexyl substituents in either a “boat” or “chair” conformation, has the shortest monolayer region and begins to collapse into multilayers around $5 \text{ mN}\cdot\text{m}^{-1}$. In contrast, trisilanoethyl-POSS (TEtP) can remain in a monolayer state until $\Pi = 32 \text{ mN}\cdot\text{m}^{-1}$. As shown in Figure 9.2, most of the experimental limiting area (A_o) for different trisilanol-POSS derivatives are consistent with the expected cross-sectional area (A_c) either from the molecular modeling or from the solid-state crystal structure. As seen in Figure 9.2, only the isotherms of trisilanolphenyl-POSS (TPP) deviate from the expected result with a much small experimental limiting area ($A_o = 152 \pm 8 \text{ \AA}^2$) than its cross-sectional area ($A_c \approx 210 \text{ \AA}^2$),

which could originate from “interdigitation” or “interlocking” phenomena of phenyl groups that will be discussed later in this chapter. The interdigitation of phenyl groups in a TPP monolayer is believed to facilitate the formation of ultrathin TPP films on solid substrates by the Langmuir-Blodgett (LB) technique.

With the different R groups as coronae, trisilanol-POSS derivatives can have very different collapse behavior showing strong substituent effects even though they have similar molecular sizes as shown in Figures 9.1 and 9.2. While trisilanolcyclopentyl-POSS (TCpP), trisilanolcyclohexyl-POSS (TCyP), and trisilanolisobutyl-POSS (TiBuP) isotherms have cusps that indicate the starting point of 2D→3D collapse processes, TEtP and TPP show smooth transitions from monolayers to multilayers without cusps. Moreover, the morphology studies of TiBuP, TCpP, and TCyP show rich heterogeneity of various 3D structures after their monolayers collapse while TPP and TEtP exhibit nearly “homogeneous” 2D→3D transitions. Both the disappearance of the cusp and the near “homogeneity” for 2D→3D process for TEtP and TPP reveal they must have different 2D→3D transition mechanisms from TiBuP, TCpP, and TCyP.

Due to the strong tendency for dimer formation, TCyP and TCpP multilayers follow a layer-by-layer formation mechanism and the surface pressure rises again after the plateau for 2D→3D transition before ultimately reaching very high surface pressure values that induce the formation of highly ordered hydrophobic solid-like multilayers. Unlike TCyP and TCpP, TiBuP has a very flexible isobutyl corona, which may inhibit dimer formation. TiBuP exhibits a very long after-collapse plateau and does not rise again. In fact, TiBuP films only form disordered 3D aggregates. The formation of ordered aggregates of TCpP and TCyP may also serve to explain why researchers who

are looking for improvements in mechanical properties in POSS nanocomposites, focus on Cy and Cp substituted POSS as their nanofiller candidates.

9.1.2 POSS/Polymer Blends at A/W

While trisilanol-POSS derivatives can be regarded as novel Langmuir monolayer forming materials with rich 2D→3D phase transitions, the results from the POSS/polymer blends at A/W provide a good opportunity to study the interactions between polymers and POSS molecules acting as nanofillers.

Uniform blends TiBuP and PDMS as Langmuir films can be formed at all compositions at A/W. With increasing surface concentration, there is an initial departure from the monolayer state through PDMS desorption into a multilayer structure. Further compression leads to the desorption of TiBuP and the formation of more condensed solid-like POSS aggregates in a PDMS fluid. Meanwhile, TiBuP blends with polar PDMS-PO exhibit dramatically different surface morphologies upon collapse of the POSS component relative to the corresponding blends with regular PDMS. Contrary to the formation of irregular aggregates of multilayer POSS-rich domains upon film compression and network-like structures upon film expansion at high POSS weight fractions in PDMS/TiBuP blends, PDMS-PO/TiBuP blends form uniform aggregates which never coalesce into larger aggregates over the accessible surface concentration range, and remain dispersed upon expansion for <80 wt% POSS. This difference in aggregation is attributed to the formation of surface micelles in the PDMS-PO/TiBuP system, where hydrogen bonding between the POSS-rich aggregates and PDMS-PO lead to steric stabilization of the POSS-rich multilayer aggregates.

The study of PDMS/octaisobutyl-POSS blends as Langmuir monolayers at A/W demonstrates interesting morphological regimes. In these systems, octaisobutyl-POSS appears to act as a true aggregating nanofiller. Even though pure octaisobutyl-POSS is non-amphiphilic and exists in a multilayer state at all A in the pure state, its blends with PDMS exhibit a number of morphologies that are similar with blends of TiBuP with PDMS. The fact that the well-ordered multilayer systems arise from a non-amphiphilic filler material suggest that a wide variety of non-amphiphilic nanofillers could be used to explore fundamental filler effects on the mechanical and transport properties of confined systems within well-defined Langmuir monolayers.

From the above points of view, POSS molecules should be excellent model compounds for studying the effects of nanofillers in "2D" confined geometries.

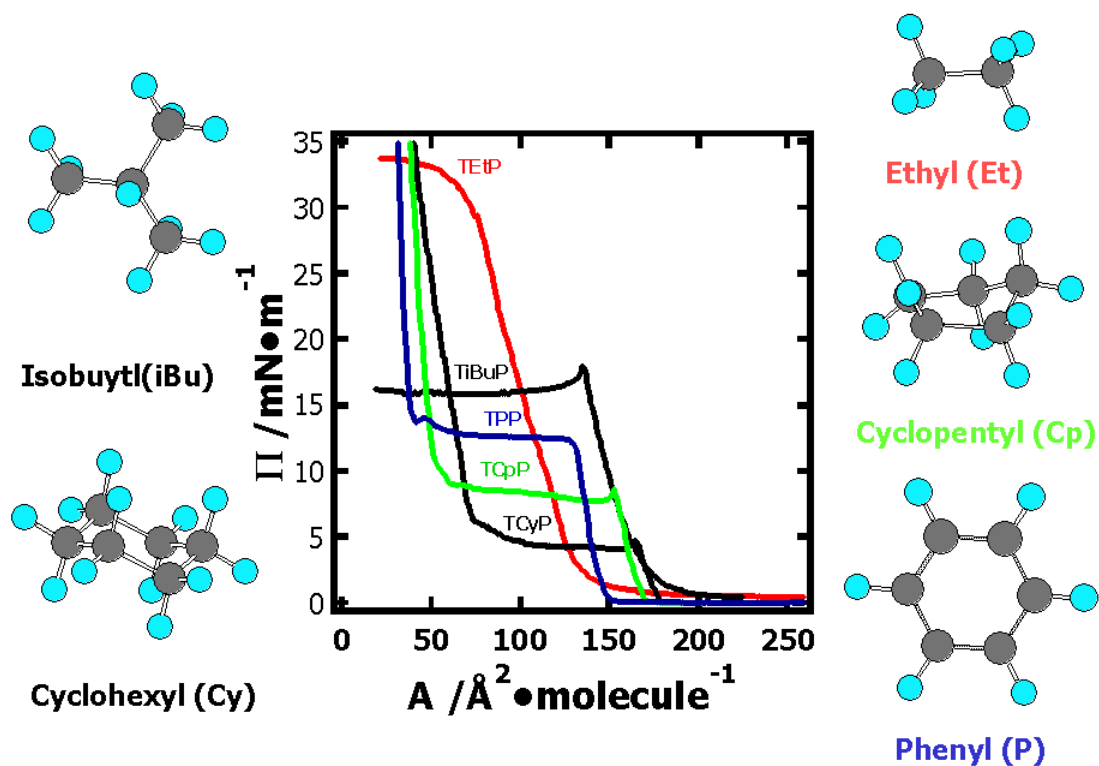


Figure 9.1: Summary of compression Π - A isotherms of different trisilanol-POSS molecules at room temperature, $T = 22.5\text{ }^\circ\text{C}$, with compression rates of $20\text{ cm}^2\cdot\text{min}^{-1}$. Two black solid curves represent the well-investigated isotherms of trisilanolisobutyl- and trisilanolcyclohexyl-POSS, respectively. Each POSS derivatives' R group is represented by a ball and stick model to provide insight into size differences between substituents. In these models, black atoms are carbon and green atoms are hydrogen.

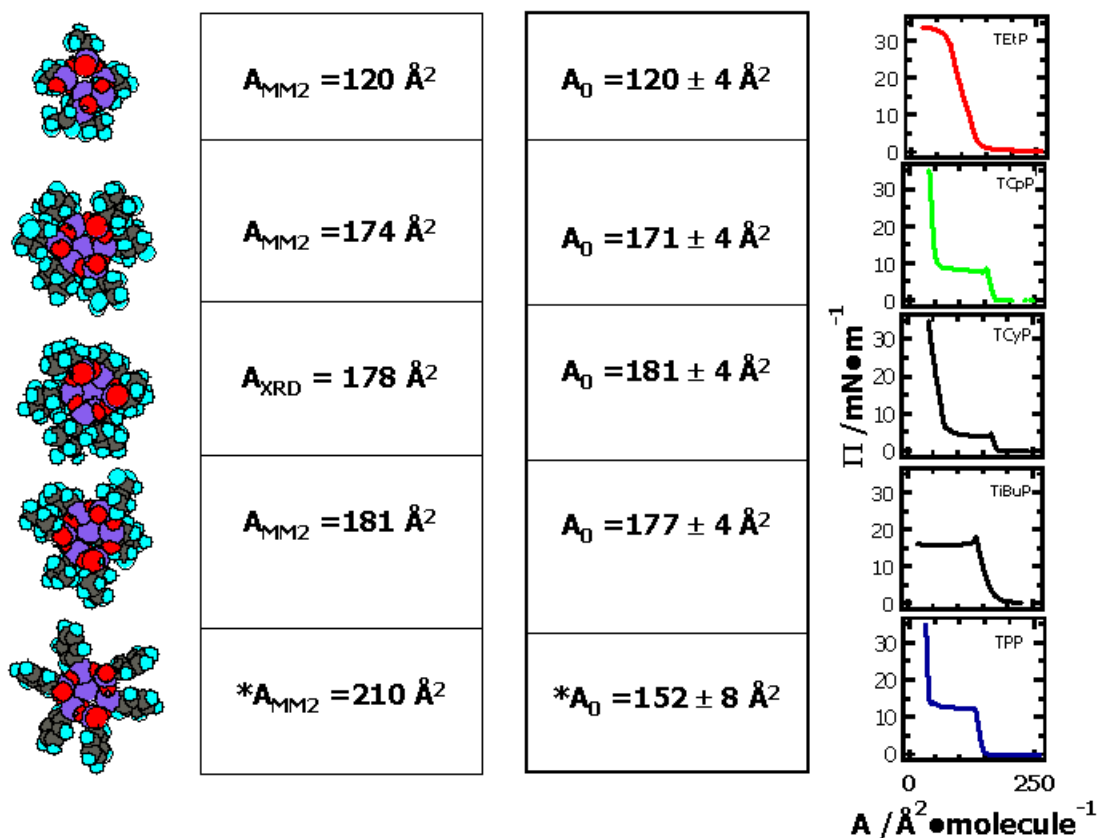


Figure 9.2: A comparison of cross-sectional areas from modeling results (A_{MM2}) or XRD data (A_{XRD}) and limiting area (A_0) obtained from compression Π - A isotherms. The space-filling models of trisilanol-POSS are based on the MM2 calculation results from Chem3D. Black atoms are carbon, red atoms are oxygen, purple atoms are silicon, and blue-green atoms are hydrogen. The model represents a configuration where the three silanol groups of POSS are exposed to water (out of the page).

9.2 Suggestions for Future Work

Most of efforts of this dissertation have been applied to the characterization of two trisilanol-POSS species (TiBuP and TCyP) and their interfacial properties are now well understood. While we can say that they are two typical examples and have provided us with basic knowledge for POSS systems, explaining the behavior of other POSS molecules at A/W still exists as a major challenge. From this point of view, this dissertation only serves as a starting point for the future exploration of POSS. In this section I will provide some suggestions for future work based on my preliminary results. One interesting case is trisilanolphenyl-POSS (TPP) that recently has been reported to form Langmuir-Blodgett (LB) multilayer films by Y-type deposition with quantitative (100%) transfer ratios.^{272,273} Meanwhile, another intriguing case is a fluorinated disilanol-POSS derivative, fluoro(13)disilanolcyclopentyl-POSS or F(13)DCpP, which has gradually obtained attention due to its unusual distorted square- or rhombus-shaped 2D crystal formation at A/W. On the basis of existing knowledge and experience acquired from our previous results, I will briefly point out the challenges and present possible explanations for some of the key features of the monolayer phase transitions, 2D→3D processes, and 3D aggregation mechanisms in TPP and F(13)DCpP Langmuir monolayer systems.

9.2.1 Trisilanolphenyl-POSS (TPP) at A/W

Thus far, TPP is the only trisilanol-POSS derivative that can undergo LB-multilayer transfer with quantitative transfer ratios. As a consequence, POSS LB-films on solid substrates can be utilized to explore many interesting research topics concerning POSS materials, such as optical properties in POSS materials, pH stability of POSS

materials, POSS-metal ion complexes, interfaces in POSS/polymer bilayers, and complexes between POSS and organophosphonates, which are important for developing transparent nanocomposite coatings, sensors for chemical warfare agents, and catalytic surfaces. For these reasons, the research on TPP as Langmuir films at A/W lags behind studies on transferred LB-films on solid substrates. While the difference in A_o between TPP and other trisilanol-POSS derivatives is essentially the basis of its LB-transfer properties, more effort should be applied to study TPP as a Langmuir monolayer.

Even though the phenyl (P) group is a C_6 group as are cyclohexyl (Cy) substituents, TPP has very different surface properties at A/W from TCyP. If we go through TPP's compression isotherm and corresponding BAM images at different surface concentrations (Figure 9.3), we do not observe any apparent aggregate formation even at the end of the compression process. The TPP films seem to be very uniform and look like gels or liquid crystals rather than the rigid and crystal-like films observed for TCyP (Figure 8.16). Can all TPP films exist in a monolayer state for this wide surface concentration range ($250 \rightarrow 30 \text{ \AA}^2 \cdot \text{molecule}^{-1}$)? The question is easily answered by the morphology changes in the following expansion process. As soon as a highly compressed TPP film (final $A \approx 30 \text{ \AA}^2 \cdot \text{molecule}^{-1}$) is expanded, cracks form. The cracks represent the exposure of water substrate or thin TPP monolayers (slender black cracks) in thick TPP multilayer films (big bright domains). While the very small molecular area values tell us that the film cannot exist as a monolayer at such high surface concentrations, we hereby face a challenge: to explain the mechanism of relatively "uniform" multilayer formation, especially for the 2D \rightarrow 3D plateau ($47 < A < 130 \text{ \AA}^2 \cdot \text{molecule}^{-1}$) where other trisilanol-POSS derivatives like TCyP exhibit large

Chapter 9

heterogeneous 3D domains. Moreover, unlike other trisilanol-POSS derivatives, TPP does not show a cusp at the start of its long plateau (signifying collapse) and its calculated cross-sectional area from molecular models ($A_{MM2} = 210 \text{ \AA}^2 \cdot \text{molecule}^{-1}$) shows a large deviation from the experimental limiting area ($A_o = 152 \pm 8 \text{ \AA}^2 \cdot \text{molecule}^{-1}$, Figure 9.2). In order to better solve the aforementioned problems, molecular modeling is pursued to explore potential differences in molecular packing of TPP compared to TCyP at A/W in Figure 9.4.

Unlike TCyP, where the Cy groups fill the space around the inorganic cage, “free-space” remains around the inorganic cage of TPP molecules because the phenyl substituents are rigid. In order to fill this space, the phenyl groups may “interdigitate” or “interlock” during the formation of a more condensed monolayer. Based on that assumption, we then measured the cross-sectional area of TPP after their interdigitation (Figure 9.4) and found that the value ($A_{MM2} \approx 158 \text{ \AA}^2 \cdot \text{molecule}^{-1}$) is close to our experimental results ($A_o = 152 \pm 8 \text{ \AA}^2 \cdot \text{molecule}^{-1}$, Figure 9.2). Actually the studies of one typical liquid-crystal amphiphile, 4'-n-octyl-4-cyanobiphenyl (8CB), at A/W revealed a similar “interdigitation” effect of phenyl groups²⁷⁴ and can be used as a guide for future research into phenyl ring interdigitation in TPP. Meanwhile, the increased TPP monolayer density and viscosity coming from interlocking phenyl side groups may be used to explain why condensed TPP monolayers (around $\Pi = 10 \text{ mN} \cdot \text{m}^{-1}$) can be transferred via the LB-technique while other trisilanol-POSS derivatives cannot. We also believe that the replacement of the expected cusp with a smooth collapse transition in the Π - A isotherm for TPP's 2D→3D process ($A \approx 130 \text{ \AA}^2 \cdot \text{molecule}^{-1}$) is closely related to the proposed model of interdigitation.

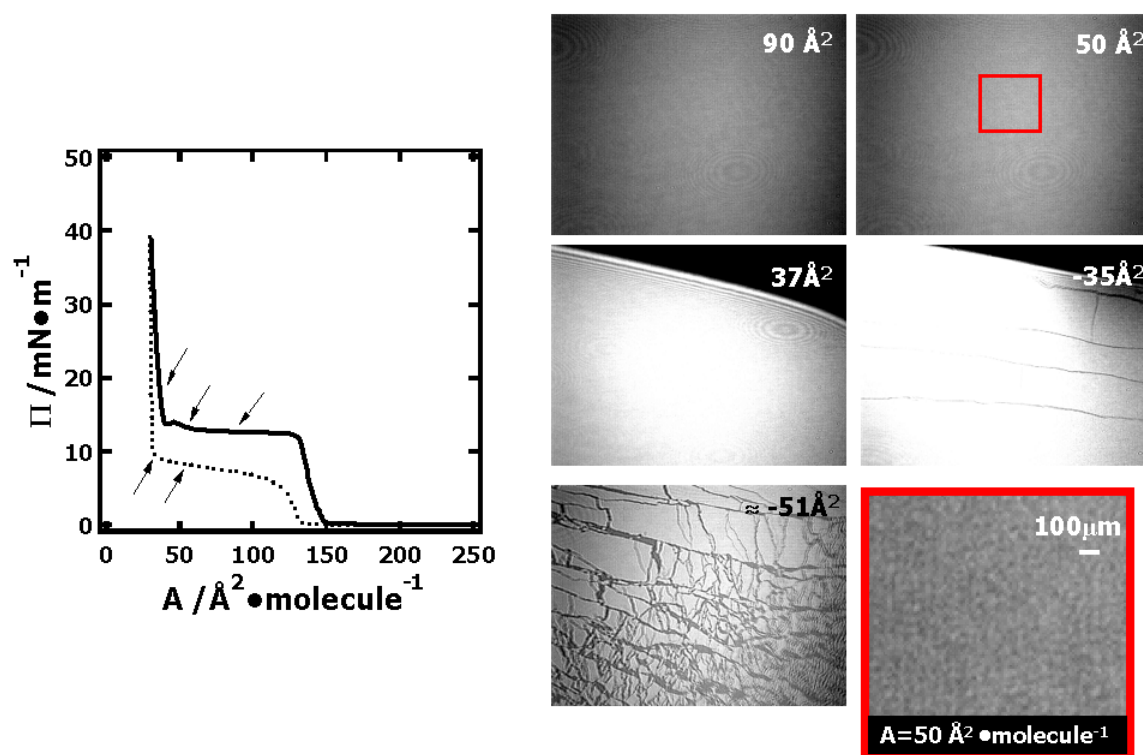


Figure 9.3: BAM images obtained from a hysteresis loop at different A for a TPP film with a constant compression/expansion rate of $20 \text{ cm}^2 \cdot \text{min}^{-1}$ at $T = 22.5 \text{ }^\circ\text{C}$. The arrows on the Π - A isotherm (solid curve for compression and dotted curve for expansion) correspond to the A values where the $6.4 \times 4.8 \text{ mm}^2$ BAM images were acquired. The red rectangular frame ($1.2 \times 1.2 \text{ mm}^2$) in the image taken at $A = 50 \text{ \AA}^2 \cdot \text{molecule}^{-1}$ represents the region used for creating an enlarged BAM image shown in the lower right-hand corner. The enlarged image shows the coexistence of 3D structures (gray domains) and monolayer (darker domains) with weak brightness contrast. The weak contrast is consistent with the proposed organization of damp 3D aggregates laying above the monolayer in Figure 9.5.

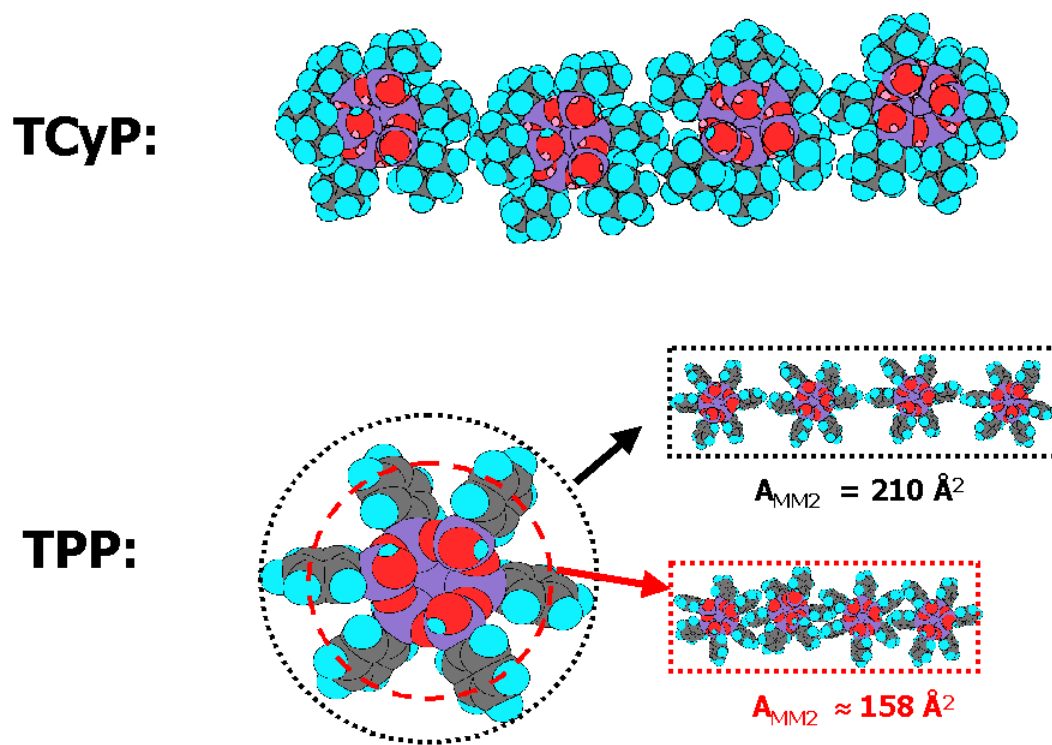


Figure 9.4: A demonstration of “interdigitating” or “interlocking” phenyl groups for TPP molecules at A/W. The space-filling models of TCyP and TPP are based on X-ray diffraction data and molecular modeling, respectively. Gray atoms are carbon, red atoms are oxygen, purple atoms are silicon, and green atoms are hydrogen. The models represent the configuration where the three silanol groups of POSS are exposed to water (out of the page). With the “interdigitating” phenyl groups, the recalculated cross-sectional area ($A_{MM2} = 158 \text{ \AA}^2 \cdot \text{molecule}^{-1}$) of TPP is smaller than the one without interdigitation ($A_{MM2} \approx 210 \text{ \AA}^2 \cdot \text{molecule}^{-1}$) and close to the experimental limiting area ($A_o = 152 \pm 8 \text{ \AA}^2 \cdot \text{molecule}^{-1}$) obtained from Π - A isotherms.

By introducing the possibility of interdigitation, several “unusual” properties of TPP at A/W can be explained. These properties include: TPP’s ability to form LB-multilayers, TPP’s smaller limiting area (A_0) relative to other trisilanol-POSS derivatives, and TPP’s cusp-free 2D→3D transition. Nonetheless, it is still difficult to explain the nearly “homogeneous” morphologies appearing during the 2D→3D transition occurring on the plateau ($47 < A < 130 \text{ \AA}^2 \cdot \text{molecule}^{-1}$) as seen in Figure 9.3. In general, after the monolayer breaks into thicker 3D structures, the density of *p*-polarized light reflected from different domains at Brewster’s angle normally should have some detectable contrast due to the thickness difference (eqs. 1.12 & 1.13). These differences are clearly observed in other POSS derivatives and lipids. However, even with the contrast enhancement provided by the “automatic gain control” mode of BAM, 3D TPP structures could not be seen in full size BAM images. At this point, several questions come to mind. Does TPP collapse by a different mechanism than other trisilanol-POSS derivatives? Does TPP have some “unusual” molecular properties, which can alter BAM contrast? These features need to be considered.

In 1959, West et al.²⁷⁵ found that phenyl substituted silanols tend to be more acidic than other alkylsilanols, arylcarbinols, and alkylcarbinols due to π bonding involving unshared electrons of O and the unfilled *d* orbital of Si. This work was done by comparing the acidity of different silanols and carbinols by measuring the frequency shift of the O-H infrared stretching band upon hydrogen bonding to the bases ether and mesitylene. Starting from that result, we can image that TPP monolayers at A/W are actually partially charged due to the dissociation of silanol groups as seen in Figure 9.5A. In other words, the cohesive energy between a TPP monolayer and a water substrate

Chapter 9

becomes much stronger than the other trisilanol-POSS derivatives. Hence, when TPP monolayers begin to collapse, those POSS molecules leaving from the condensed bottom monolayers likely take along more water molecules with them to form “damp” 3D structures on the top of the condensed monolayer. While other trisilanol-POSS derivatives may also take water to the upper layer during the 2D→3D process, their water content in 3D structures compared to TPP should be much lower due to their weaker acidity. As a suggestion for future work, the study of pH effect on the stability of different trisilanol-POSS films at A/W will be very interesting.

As a follow-up to the above-mentioned speculation about damp 3D structure formation, a speculative depiction of TPP’s 2D→3D phase transition mechanism and multilayers organization is depicted in Figure 9.5. This model tries to explain the nearly “homogeneous” morphologies of the 2D-3D coexistence region and multilayer regions of TPP at A/W. When TPP molecules are forced out of the interdigitated monolayer by lateral pressure, some water can be taken along with TPP into the upper layer (Figure 9.5B). For the sake of demonstration, we highlight the bottom half of collapsing TPP molecules with blue to match the subphase. Now the collapsed TPP and water molecules form damp 3D aggregates together on the top of the monolayer. Meanwhile, collapsed molecules (damp TPP molecules) reside on top of the hydrophobic portion of the underlying monolayer. As a result, damp 3D aggregates will separate from each other and appear as very small islands all over the surface. Due to the lateral resolution of the Mini-BAM (around 20 μm) we actually cannot easily see 3D aggregates because of their small size and smaller optical contrast. As a result, full size BAM image appear nearly “uniform” in the 2D-3D coexistence region of Figure 9.3 ($A = 90 \text{ \AA}^2 \cdot \text{molecule}^{-1}$). As the

number of damp islands increases (Figure 9.5C), the bottom monolayer is covered by numerous translucent “gel-like” 3D aggregates, which have refractive indices that are close to water than dry TPP. To support the above speculation that damp 3D aggregates actually exist on the top of the monolayers, we enlarged a central region of the BAM image in Figure 9.3, which is taken at $A = 50\text{\AA}^2 \cdot \text{molecule}^{-1}$. When we take a close look at that enlarged BAM image, bright domains (damp 3D aggregates) with sizes around $50\ \mu\text{m}$ existing in the black background (monolayer) are observed. On the basis of eq. 1.12, we believe that the “homogeneity” of TPP collapsed films is the result of smaller differences in refractive index between TPP aggregates and the monolayer/subphase than exists in other trisilanol-POSS systems.

As the suggestions for future work with TPP at A/W, X-ray and neutron reflectivity measurements, ellipsometry, and optical second-harmonic-generation (SHG) may provide more details about the collapse process. From these experiments we can obtain more information about film thickness, density, molecular alignment, and the polar ordering of TPP films. From this point of view, I would say that the research of TPP at A/W needs more effort.

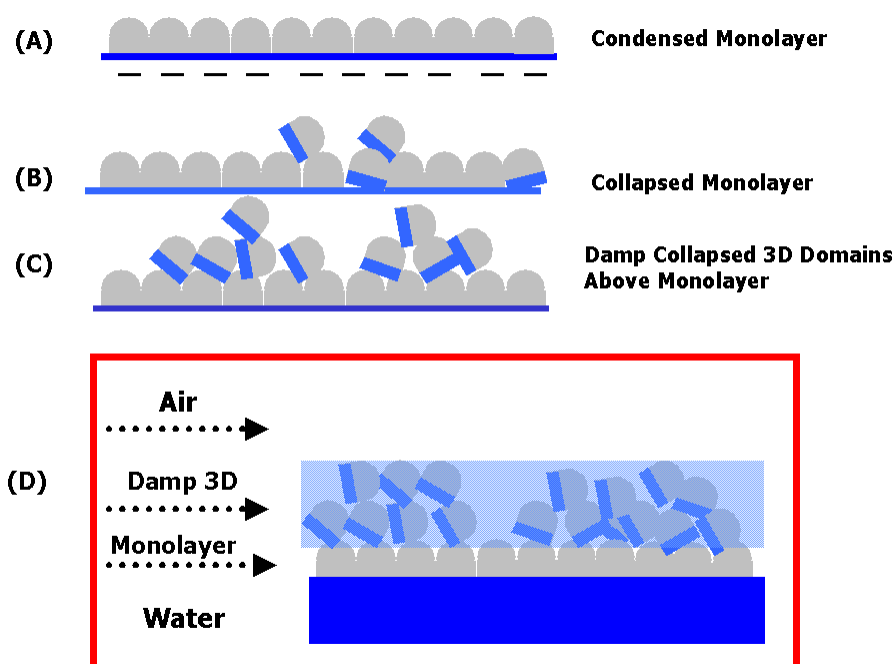


Figure 9.5: Proposed organization of TPP films at A/W: **(A)** An interlocked and condensed monolayer ($150 < A < 130 \text{ \AA}^2 \cdot \text{molecule}^{-1}$) with partially dissociated silanol groups, **(B)** a collapsing monolayer in the region near the smooth 2D→3D "turnover" point ($A \approx 130 \text{ \AA}^2 \cdot \text{molecule}^{-1}$) in the isotherm, **(C)** formation of damp collapsed 3D domains above the monolayer ($47 < A < 130 \text{ \AA}^2 \cdot \text{molecule}^{-1}$), and **(D)** "sandwich" structures for higher order multilayer formation ($A < 47 \text{ \AA}^2 \cdot \text{molecule}^{-1}$). (D) depicts TPP multilayer structures as air//damp 3D/monolayer// bulk water. In order to indicate the introduction of water into collapsed structures, the bottom parts of collapsed TPP molecules are highlighted with the same color as the water substrate (blue).

9.2.2 Fluorinated POSS Derivatives (*F*-POSS) at A/W

Fluorinated amphiphile thin films have various uses in materials science²⁷⁶ as well as emerging biomedical applications.²⁷⁷ It is very important to understand and control the structure and properties of these films, since most of these applications involve colloidal systems stabilized by monolayer films of fluorinated amphiphiles. Compared to hydrogenated chains (*H*-chains), fluorinated chains (*F*-chains) have some different properties such as greater bulkiness (cross-sectional areas of $A_{c, F\text{-chain}} \approx 28 \text{ \AA}^2$ vs. $A_{c, H\text{-chain}} \approx 18 \text{ \AA}^2$), a helical chain conformation (rather than a planar ‘zig-zag’ structure of *H*-chain), and greater stiffness. Moreover, *F*-chains are considerably more hydrophobic than *H*-chains in nature, which even leads to the formation of a stable Langmuir monolayer at A/W from a traditionally non-amphiphilic fluoroalkane, $\text{C}_{20}\text{F}_{42}$, at room temperature.²⁷⁸ In general, there are two class of well-investigated fluorinated Langmuir monolayers, which are formed either by fluorinated fatty acids and alcohol, such as $\text{C}_8\text{F}_{17}\text{COOH}$, or by semifluorinated alkanes ($\text{C}_n\text{F}_{2n+1}\text{C}_m\text{H}_{2m+1}$). With the much higher hydrophobicity of the *F*-chain, fluorinated acids and alcohol only need a minimum C_8 to form a stable monolayer, while fatty acids and alcohols need at least C_{13} . For Langmuir monolayers of semifluorinated alkanes, a major question existed: which block is in contact with the water surface in the absence of polar groups? By utilizing grazing incidence X-ray diffraction (GIXD), Huang et al.²⁷⁹ observed the organization of $\text{C}_8\text{F}_{17}\text{C}_{18}\text{H}_{37}$ Langmuir monolayers at A/W and suggested a hydrocarbon-block-down (*H*-block-down), fluorocarbon-block-up (*F*-block-up) orientation for the condensed monolayer. Meanwhile, molecular dynamics simulations of $\text{C}_8\text{F}_{17}\text{C}_{18}\text{H}_{37}$ Langmuir monolayers at A/W indicated that the monolayer structure consisted of mixed

Chapter 9

orientations with a larger portion of the molecules existing in an *H*-block-down, *F*-block-up configuration.²⁸⁰ Currently fluorinated monolayers are widely investigated as model systems in both materials and biological sciences, for 2D protein crystallization processes,²⁸¹⁻²⁸³ non-linear optical properties-based applications,^{284,285} and lubricants for microelectronics.^{286,287}

Thus far, all of the Langmuir film research we have carried out for POSS systems has focused on closed cage POSS and trisilanol-POSS derivatives. As a consequence of increasing demand for new fire retardant materials, fluorinated POSS derivatives (*F*-POSS) have emerged as potential candidates. We have investigated the interfacial properties for some *F*-POSS species. While there are now several *F*-POSS derivatives that are good candidates to form stable Langmuir films at A/W, I will only present the preliminary results for one fluorinated POSS derivative, Fluoro(13)disilanolcyclopentyl-POSS or F(13)DCpP. As seen from the molecular structure shown in Figure 9.6, F(13)DCpP simply replaces one OH group of TCpP with a long *F*-chain. Unlike semifluorinated alkanes, which only have two distinct parts with different hydrophobicity, F(13)DCpP has three parts: silanol OH polar groups, a non-polar Cp corona, and a highly hydrophobic *F*-chain. The interplay between these three groups will be the key factor that affects F(13)DCpP's phase transitions and orientations at A/W.

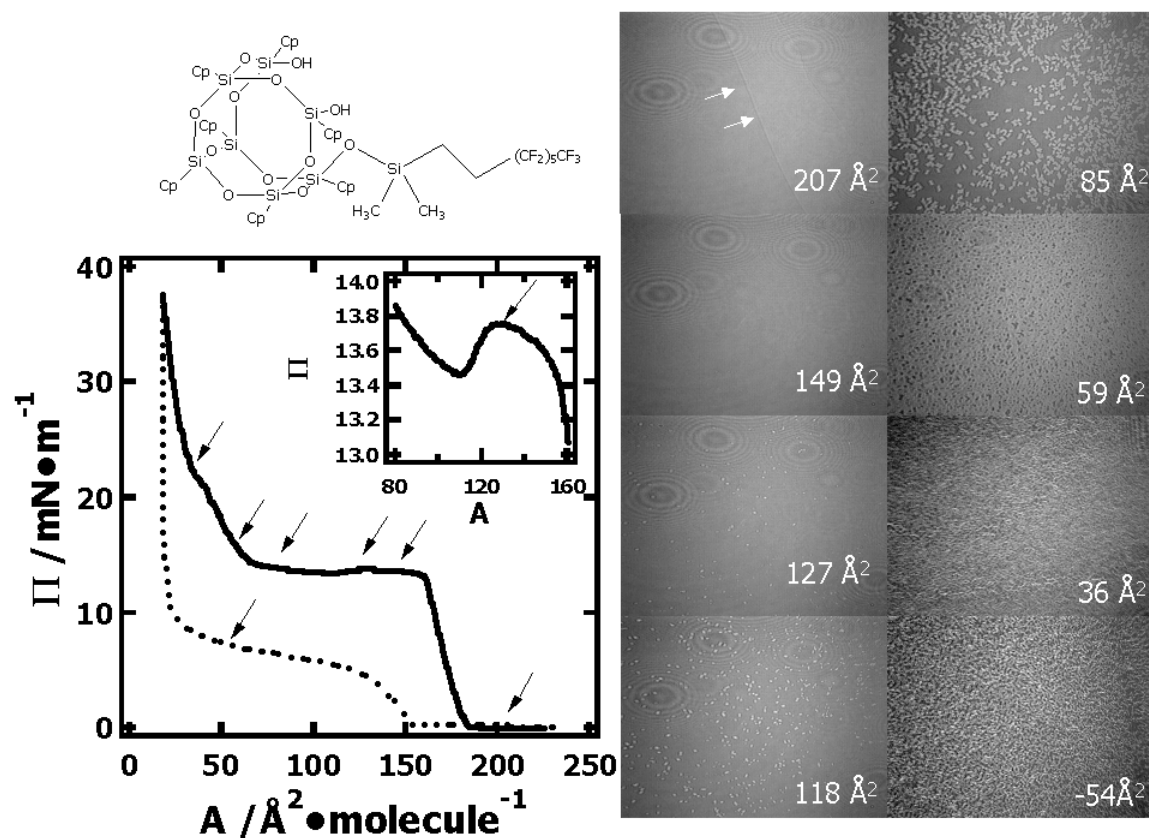


Figure 9.6: BAM images obtained from a hysteresis loop (solid curve for compression and dotted curve for expansion) for different A for a F(13)DCpP film with a constant compression/expansion rate of $20 \text{ cm}^2 \cdot \text{min}^{-1}$ at $T = 22.5 \text{ }^\circ\text{C}$. The molecular structure is shown in the upper left-hand corner of the figure. The black arrows on the Π - A isotherm correspond to the A values where the $6.4 \times 4.8 \text{ mm}^2$ BAM images were obtained. The bright arrows in the first BAM image show the boundary between coexisting liquid-like and gas-like domains.

Chapter 9

The Π - A isotherm (Figure 9.6) shows that F(13)DCpP has a similar Π - A curve to TPP (Figure 9.3). The limiting area (A_o) obtained from the isotherm is around $182 \text{ \AA}^2 \cdot \text{molecule}^{-1}$, which agrees with the modeling result ($A_{MM2} = 180 \text{ \AA}^2 \cdot \text{molecule}^{-1}$) when disilanol groups are anchored to the water surface (F -block-down or OH-down, as shown in Figure 9.7). Interestingly, F(13)DCpP has a smooth transition (no cusp) from a condensed monolayer phase ($180 < A < 160 \text{ \AA}^2 \cdot \text{molecule}^{-1}$) to a plateau ($160 < A < 130 \text{ \AA}^2 \cdot \text{molecule}^{-1}$) like TPP, whose unique interdigitating process can be attributed to its smooth transition. However F(13)DCpP molecules do not tend to interdigitate if we place several molecules close to one another. In the mean time, the BAM images taken for the plateau (Figure 9.6, $A = 160 \rightarrow 127 \text{ \AA}^2 \cdot \text{molecule}^{-1}$) show homogeneous structures and no detectable appearance of 3D aggregates. Inspired by the results from the monolayer research of semifluorinated alkanes,^{279,280} this plateau may be a 1st order phase transition plateau between two monolayer states as shown in Figure 9.7. The monolayer with F -block-down or OH-down configuration initially has a lower energy at A/W due to the existence of hydrogen bonding between silanol groups and water molecules as shown in Figure 9.7A. As the lateral pressure (Π) increases, the F -block-down state may begin to convert into the higher energy H -block-down state around $A = 160 \text{ \AA}^2 \cdot \text{molecule}^{-1}$ leading to liquid-liquid phase coexistence between F -block-down and H -block-down states as shown in Figure 9.7B. To further confirm that this is a monolayer to monolayer transition, we also investigated the temperature dependence of the Π - A isotherm for F(13)DCpP and found that with increasing temperature, the width of the plateau decreases, which can be regarded as evidence for a monolayer to monolayer phase

transition.⁵ As a suggestion for future work, we can utilize GIXD technique together with molecular dynamics simulations to validate the above speculation.

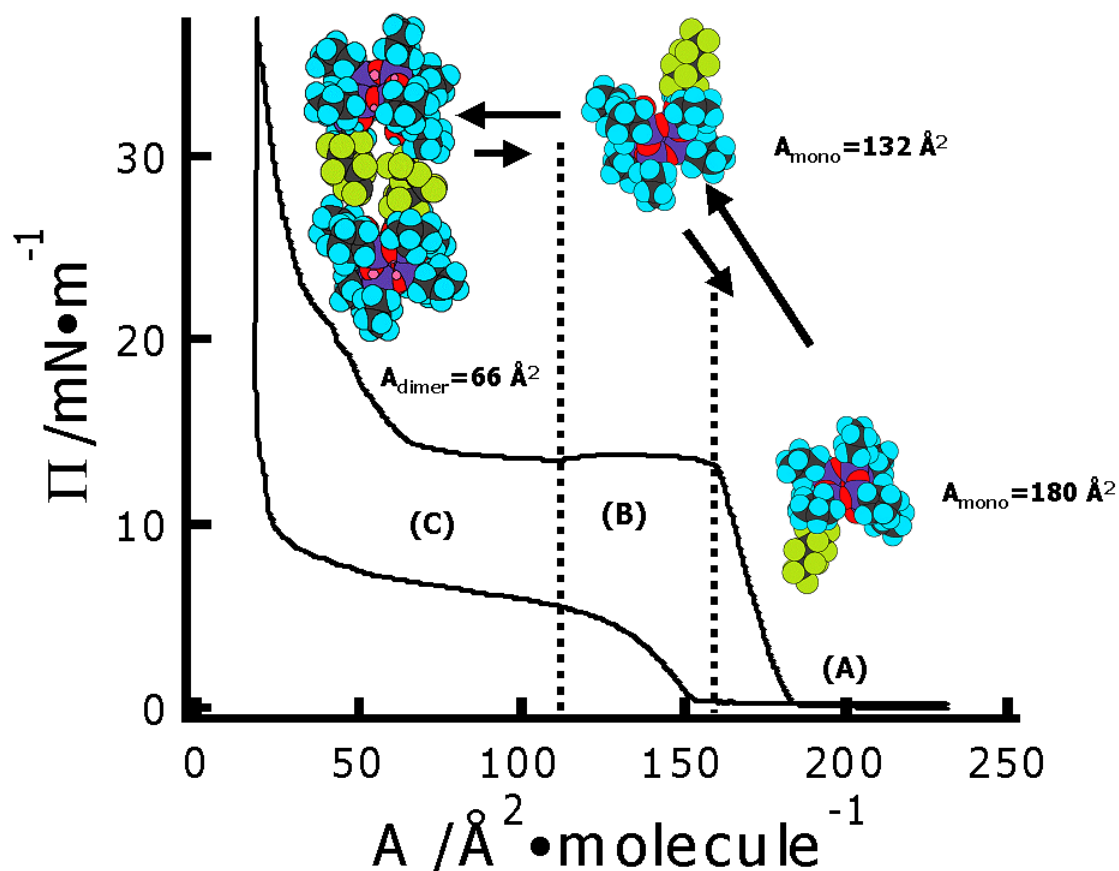


Figure 9.7: Proposed phase transitions and organization of F(13)DCpP films at A/W: **(A)** Monolayer region with an *F*-block-down (OH-down) configuration for F(13)DCpP, including G and LC states, $160 < A < 250 \text{ \AA}^2 \cdot \text{molecule}^{-1}$; **(B)** two monolayer phases coexist between *F*-block-down and *H*-block-down configurations, $130 < A < 160 \text{ \AA}^2 \cdot \text{molecule}^{-1}$; **(C)** a monolayer with an *H*-block-down configuration collapses into 3D dimer aggregates and the higher order multilayers upon further compression, $A < 130 \text{ \AA}^2 \cdot \text{molecule}^{-1}$.

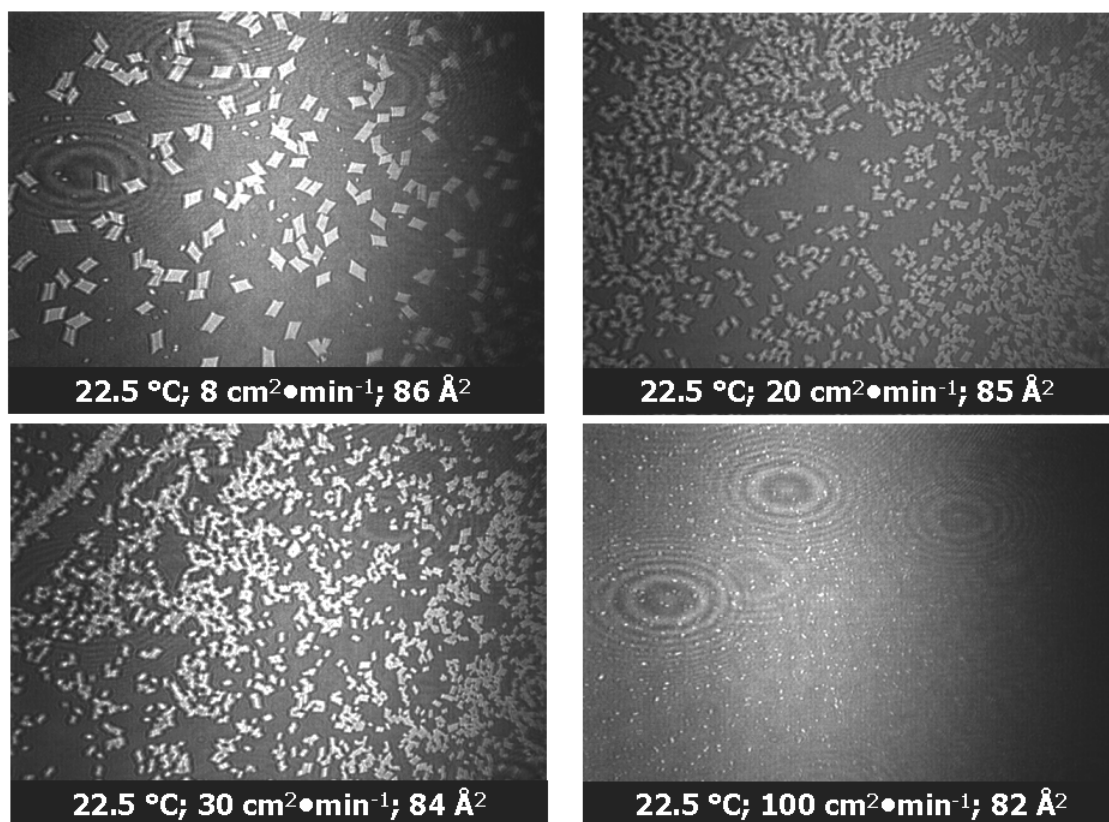


Figure 9.8: BAM images obtained at surface concentrations around $A = 85 \text{ \AA}^2 \cdot \text{molecule}^{-1}$ for F(13)DCpP films at $T = 22.5 \text{ }^\circ\text{C}$ with different compression rates: 8, 20, 30, and $100 \text{ cm}^2 \cdot \text{min}^{-1}$. All of the BAM images are $6.4 \times 4.8 \text{ mm}^2$.

The next question is, “At which surface concentration will the 2D→3D collapse point occur if the above-mentioned monolayer-monolayer transition theory is correct?” Returning to Figure 9.6, the inset Π - A isotherm from 80 to $160 \text{ \AA}^2 \cdot \text{molecule}^{-1}$ shows we actually find a cusp around $A = 130 \text{ \AA}^2 \cdot \text{molecule}^{-1}$, which is the value of the cross-sectional area for the H -block-down configuration (Figure 9.7B). More importantly, we can see some tiny bright 3D domains begin to emerge from monolayer background

(Figure 9.6, $A=127 \text{ \AA}^2 \cdot \text{molecule}^{-1}$) and confirm the occurrence of a 2D→3D collapse. Further compression results in the formation of additional 3D domains. When $A = 66 \text{ \AA}^2 \cdot \text{molecule}^{-1}$, which is one-half of the cross-sectional area of the *H*-block-down configuration, Π again rises and BAM images (Figure 9.6, $A \sim 59 \text{ \AA}^2 \cdot \text{molecule}^{-1}$) show the formation of a nearly “homogeneous” multilayer. Based upon an analysis of the isotherm and BAM images, we propose that the 3D structure appearing within $A = 60 \sim 130 \text{ \AA}^2 \cdot \text{molecule}^{-1}$ comes from F(13)DCpP dimer aggregation with a configuration as shown in Figure 9.7C.

Another interesting result comes from the morphology of 3D structures acquired at low compression rates (Figure 9.8, $8 \text{ cm}^2 \cdot \text{min}^{-1}$ at $A = 86 \text{ \AA}^2 \cdot \text{molecule}^{-1}$). In that BAM image, we can see the appearance of large “unusual” rhombus or distorted square aggregates, which have not been previously reported in the literature. To see the detail of those rhombuses, we zoom in on one rhombus and present it as Figure 9.9A with a $100 \mu\text{m}$ scale in the upper left hand corner. With the aid of its contrast-enhanced result, Figure 9.9B, we can find there actually exist three different regions: bright rhombus (multilayer) surrounded by dark strips (water substrate), and outside gray monolayers. According to Figure 9.7C, the dimers aggregates are hydrophobic in nature and it would not be surprising to see the water gaps surrounding them and separating 3D structures from monolayer regions. When we take a close look at Figures 9.9B and 9.9C, we can clearly see that there are connecting points between the multilayer and the outside monolayers located at opposite corners as indicated by two arrows in Figure 9.9B. By only incorporating monolayer asymmetrically into 3D structures, it is not surprising that the hydrophobic F(13)DCpP dimers can grow into asymmetrical domains. This

Chapter 9

conjecture may explain the “unusual” rhombus formation. As a suggestion for future work, studies of how different surface aggregation patterns arise for different *F*-POSS systems would be interesting. Meanwhile we also note that the dimer domains’ growth is strongly compression rate dependent as shown in Figure 9.8. As the compression rate increases, the sizes of the rhombuses decrease.

Figure 9.10 presents the exploratory results of the Langmuir-Blodgett (LB) and Langmuir-Schaeffer (LS) transfer of coexisting F(13)DCpP monolayer/multilayer films to solid substrates. After the films are transferred to hydrophilic glass substrates by the LB-technique, the hydrophobic rhombuses cannot maintain their morphologies and turn into “worms”. By changing the supporting surface to a hydrophobic glass, the LS-transfer traps F(13)DCpP dimer aggregates as rhombuses on the glass. For future work, one could utilize the aforementioned phase transition mechanism (Figure 9.7) as a guide to try either the LB- or the LS-transfer at different surface concentrations, by which one may obtain intact 3D domains. With the aid of electron or X-ray diffraction, further information about the crystalline order of these structures could be revealed.

While F(13)DCpP is the first *F*-POSS derivative to be investigated at A/W, there are many other *F*-POSS derivatives that can be accessed and examined by similar techniques. Two examples are Fluoro(3)disilanol-POSS and Trifluoro-POSS. Based on the effect substituents had on the aggregation behavior of trisilanol-POSS derivatives, similarly interesting results for *F*-POSS systems can be expected.

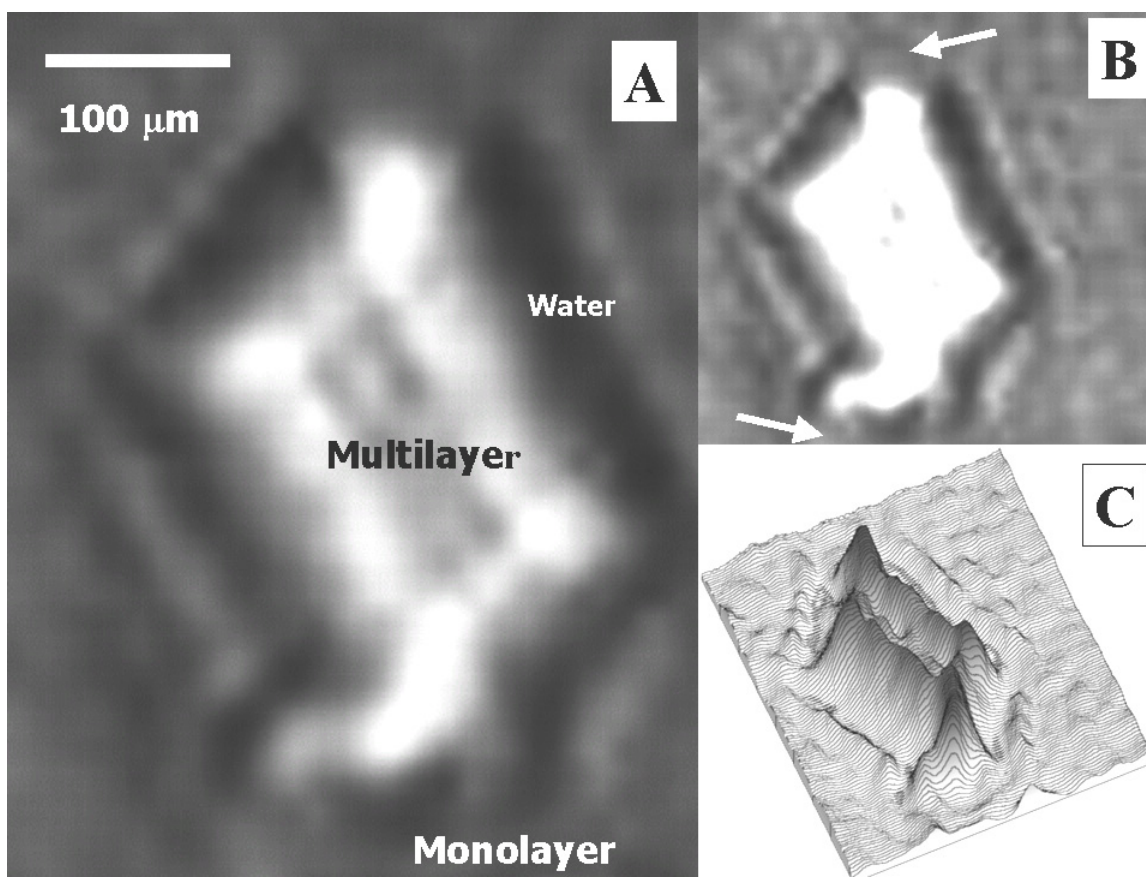


Figure 9.9: An enlarged rhombus dimer domain obtained at a low compression rate ($8\text{cm}^2\cdot\text{min}^{-1}$) at $A = 86 \text{ \AA}^2\cdot\text{molecule}^{-1}$ for a F(13)DCpP film. **(A)** Original image with a scale bar in the its upper left-hand corner; **(B)** a 2X contrast enhanced BAM image with dimensions of $0.48 \times 0.48 \text{ mm}^2$; **(C)** the surface plot generated from **(A)** showing the reflectivity or thickness difference for different regions. Two white arrows in **(B)** indicate the connection between the 3D aggregate and the outside monolayers.

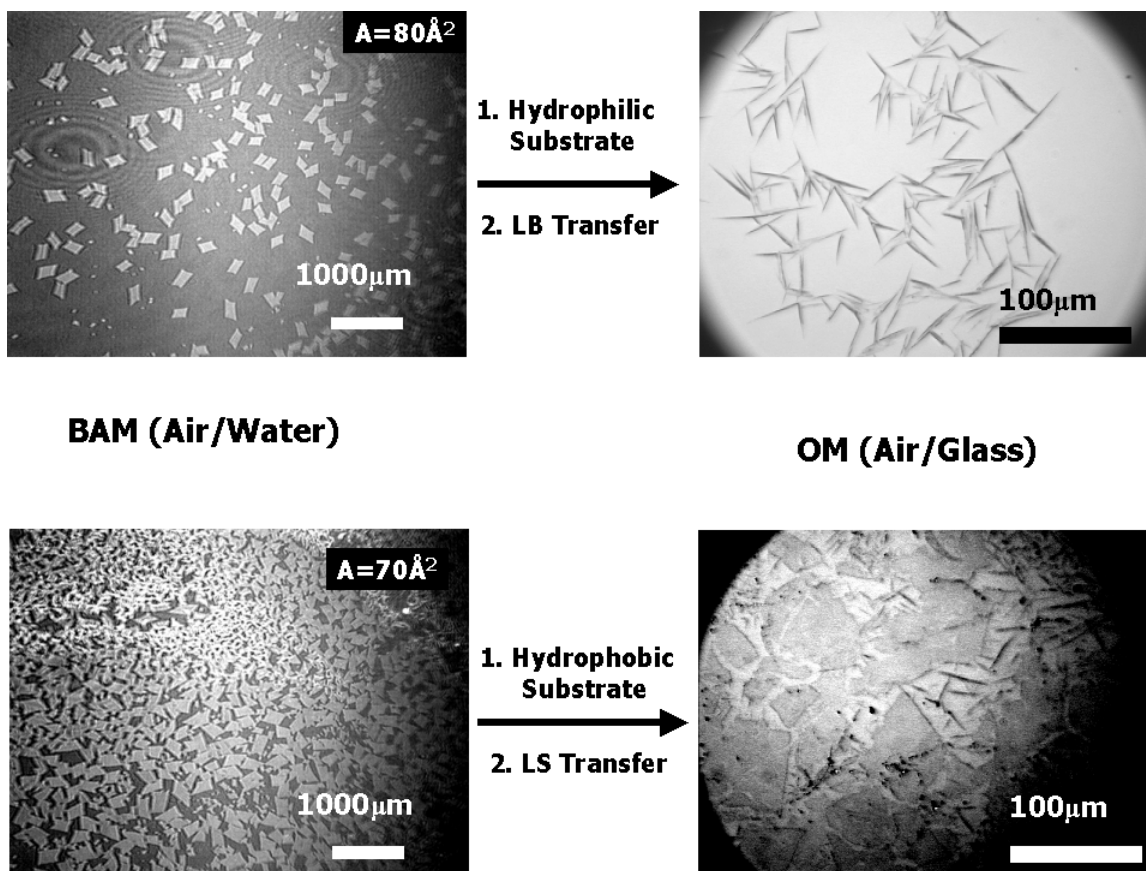


Figure 9.10: The morphology change of F(13)DCpP dimer aggregates at $A \approx 80 \text{\AA}^2 \cdot \text{molecule}^{-1}$ transferred from A/W by LB- (upper) and by LS- (lower) techniques onto hydrophilic and hydrophobic glass surfaces, respectively. To clarify the structures, the lower left-hand OM image has been increased its contrast.

Bibliography

- [1] Gaines, G. L. *Insoluble Monolayers at Liquid-Gas Interfaces*; Interscience: New York, 1966.
- [2] Swalen, J. D.; Allara, D. L.; Andrade, J. D.; Chandross, E. A.; Garoff, S.; Israelachvili, J.; McCarthy, T. J.; Murray, R.; Pease, R. F. *Langmuir* **1987**, *3*, 932.
- [3] Ulman, A. *An Introduction to Ultrathin Organic Films: From Langmuir-Blodgett to Self-Assembly*; Academic Press: Boston, 1991.
- [4] Peterson, I. R. *Mol. Electron.* **1992**, 117.
- [5] Petty, M. C. *Langmuir-Blodgett Film: An Introduction*; Cambridge University Press: Cambridge, 1996.
- [6] Petty, M. C. *Encyclopedia of Nanoscience and Nanotechnology* **2004**, *8*, 295.
- [7] Tabor, D. *J. Colloid Interface Sci.* **1980**, *75*, 240.
- [8] Dynarowicz-Latka, P.; Dhanabalan, A.; Oliveira, O. N. *Advan. Colloid Interface Sci.* **2001**, *91*, 221.
- [9] Franklin, B. *Phil. Trans. Res. Soc. (London)* **1774**, *64*, 445.
- [10] Rayleigh, L. *Proc. R. Soc. Ser. A* **1890**, *47*, 364.
- [11] Pockels, A. *Nature* **1894**, *50*, 223.
- [12] Rayleigh, L. *Phil. Mag.* **1899**, *48*, 321.
- [13] Langmuir, I. *J. Am. Chem. Soc.* **1917**, *39*, 1848.
- [14] Langmuir, I. *Trans. Faraday Soc.* **1920**, *15*, 62.
- [15] Blodgett, K. B.; Langmuir, I. *Phys. Rev.* **1937**, *51*, 964.
- [16] Morizumi, T. *Thin Solid Films* **1988**, *160*, 413.

Bibliography

- [17] Kunitake, T. *Polym. J. (Tokyo)* **1991**, 23, 613.
- [18] Sackmann, E. *Science* **1996**, 271, 43.
- [19] Rao, N. M.; Plant, A. L.; Silin, V.; Wight, S.; Hui, S. W. *Biophys. J.* **1997**, 73, 3066.
- [20] Swalen, J. D. *J. Mol. Electron.* **1986**, 2, 155.
- [21] Bilewicz, R.; Sawaguchi, T.; Chamberlain, R. V., II; Majda, M. *Langmuir* **1995**, 11, 2256.
- [22] Penner, T. L.; Motschmann, H. R.; Armstrong, N. J.; Ezenyilimba, M. C.; Williams, D. J. *Nature* **1994**, 367, 49.
- [23] Wijekoon, W. M. K. P.; Wijaya, S. K.; Bhawalkar, J. D.; Prasad, P. N.; Penner, T. L.; Armstrong, N. J.; Ezenyilimba, M. C.; Williams, D. J. *J. Am. Chem. Soc.* **1996**, 118, 4480.
- [24] Kaganer, V. M.; Mohwald, H.; Dutta, P. *Rev. Mod. Phys.* **1999**, 71, 779.
- [25] Ryley, S.; Chyla, A. T.; Peterson, I. R. *Thin Solid Films* **2000**, 370, 294.
- [26] Atkin, P. *Physical Chemistry*; 6th ed.; Freeman: New York, 1998.
- [27] Pallas, N. R.; Pethica, B. A. *Langmuir* **1985**, 1, 509.
- [28] Harkins, W. D.; Boyd, E. *J. Phys. Chem.* **1941**, 45, 20.
- [29] Overbeck, G. A.; Honig, D.; Mobius, D. *Langmuir* **1993**, 9, 555.
- [30] Dutta, P.; Peng, J. B.; Lin, B.; Ketterson, J. B.; Prakash, M.; Georgopoulos, P.; Ehrlich, S. *Phys. Rev. Lett.* **1987**, 58, 2228.
- [31] Kjaer, K.; Als-Nielsen, J.; Helm, C. A.; Laxhuber, L. A.; Moehwald, H. *Phys. Rev. Lett.* **1987**, 58, 2224.
- [32] Knobler, C. M. *Science* **1990**, 249, 870.

-
- [33] McConnell, H. M. *Annu. Rev. Phys. Chem.* **1991**, *42*, 171.
- [34] Henon, S.; Meunier, J. *Rev. Sci. Instrum.* **1991**, *62*, 936.
- [35] Honig, D.; Mobius, D. *J. Phys. Chem.* **1991**, *95*, 4590.
- [36] Haard, S.; Neuman, R. D. *J. Colloid Interface Sci.* **1981**, *83*, 315.
- [37] Langevin, D. *J. Colloid Interface Sci.* **1981**, *80*, 412.
- [38] Earnshaw, J. C.; McGivern, R. C.; Winch, P. J. *J. Phys. (Pairs)* **1988**, *49*, 1271.
- [39] Brooks, C. F.; Fuller, G. G.; Frank, C. W.; Robertson, C. R. *Langmuir* **1999**, *15*, 2450.
- [40] Rasing, T.; Shen, Y. R.; Kim, M. W.; Grubb, S. *Phys. Rev. Lett.* **1985**, *55*, 2903.
- [41] Rasing, T.; Shen, Y. R.; Kim, M. W.; Valint, P., Jr.; Bock, J. *Phys. Rev. A* **1985**, *31*, 537.
- [42] Bhattacharyya, K.; Castro, A.; Sitzmann, E. V.; Eienthal, K. B. *J. Chem. Phys.* **1988**, *89*, 3376.
- [43] Derude *Annu. Rev. Phys. Chem.* **1891**, *43*, 126.
- [44] Meunier, J. *Colloid Surf. A-Physicochem. Eng. Asp.* **2000**, *171*, 33.
- [45] Riviere, S.; Henon, S.; Meunier, J. *Phys. Rev. E* **1994**, *49*, 1375.
- [46] Henon, S.; Meunier, J. *J. Chem. Phys.* **1993**, *98*, 9148.
- [47] Braslau, A.; Deutsch, M.; Pershan, P. S.; Weiss, A. H.; Als-Nielsen, J.; Bohr, J. *Phys. Rev. Lett.* **1985**, *54*, 114.
- [48] Tabe, Y.; Yokoyama, H. *Langmuir* **1995**, *11*, 699.
- [49] Fukuto, M.; Penanen, K.; Heilmann, R. K.; Pershan, P. S.; Vaknin, D. *J. Chem. Phys.* **1997**, *107*, 5531.

Bibliography

- [50] Godovsky, Y. K.; Brezesinski, G.; Ruiz-Garcia, J.; Moehwald, H.; Jensen, T. R.; Kjaer, K.; Makarova, N. N. *Macromolecules* **2004**, *37*, 4872.
- [51] Paudler, M.; Ruths, J.; Alberti, B.; Riegler, H. *Makromol. Chem. - Macro. Chem. Phys.* **1991**, *46*, 401.
- [52] Paudler, M.; Ruths, J.; Riegler, H. *Langmuir* **1992**, *8*, 184.
- [53] Reiter, R.; Motschmann, H.; Orendi, H.; Nemetz, A.; Knoll, W. *Langmuir* **1992**, *8*, 1784.
- [54] Mendelsohn, R.; Brauner, J. W.; Gericke, A. *Annu. Rev. Phys. Chem.* **1995**, *46*, 305.
- [55] Werkman, P. J.; Schouten, A. J.; Noordegraaf, M. A.; Kimkes, P.; Sudholter, E. J. R. *Langmuir* **1998**, *14*, 157.
- [56] Gehlert, U.; Weidemann, G.; Vollhardt, D.; Brezesinski, G.; Wagner, R.; Mohwald, H. *Langmuir* **1998**, *14*, 2112.
- [57] Gehlert, U.; Vollhardt, D. *Langmuir* **1997**, *13*, 277.
- [58] Gehlert, U.; Vollhardt, D.; Brezesinski, G.; Mohwald, H. *Langmuir* **1996**, *12*, 4892.
- [59] Gehlert, U.; Weidemann, G.; Vollhardt, D. *J. Colloid Interface Sci.* **1995**, *174*, 392.
- [60] Deschenaux, R.; Masoni, C.; Stoecklievans, H.; Vaucher, S.; Ketterer, J.; Steiger, R.; Weisenhorn, A. L. *J. Chem. Soc., Dalton Trans.* **1994**, 1051.
- [61] Deschenaux, R.; Megert, S.; Zumbunn, C.; Ketterer, J.; Steiger, R. *Langmuir* **1997**, *13*, 2363.

- [62] Stuart, M. A. C.; Wegh, R. A. J.; Kroon, J. M.; Sudholter, E. J. R. *Langmuir* **1996**, *12*, 2863.
- [63] Vollhardt, D.; Melzer, V. *J. Phys. Chem. B* **1997**, *101*, 3370.
- [64] Vollhardt, D.; Melzer, V.; Fainerman, V. *Thin Solid Films* **1998**, *329*, 842.
- [65] Honig, D.; Overbeck, G. A.; Mobius, D. *Adv. Mater.* **1992**, *4*, 419.
- [66] Overbeck, G. A.; Honig, D.; Mobius, D. *Thin Solid Films* **1994**, *242*, 213.
- [67] Brezesinski, G.; Scalas, E.; Struth, B.; Mohwald, H.; Bringezu, F.; Gehlert, U.; Weidemann, G. *J. Phys. Chem.* **1995**, *99*, 8758.
- [68] Overbeck, G. A.; Honig, D.; Wolthaus, L.; Gnade, M.; Mobius, D. *Thin Solid Films* **1994**, *242*, 26.
- [69] Lauger, J.; Robertson, C. R.; Frank, C. W.; Fuller, G. G. *Langmuir* **1996**, *12*, 5630.
- [70] Friedenber, M. C.; Fuller, G. G.; Frank, C. W.; Robertson, C. R. *Langmuir* **1996**, *12*, 1594.
- [71] Friedenber, M. C.; Fuller, G. G.; Frank, C. W.; Robertson, C. R. *Macromolecules* **1996**, *29*, 705.
- [72] Mann, E. K.; Henon, S.; Langevin, D.; Meunier, J.; Leger, L. *Phys. Rev. E* **1995**, *51*, 5708.
- [73] Lautz, C.; Fischer, T. M. *J. Phys. Chem. B* **1997**, *101*, 8790.
- [74] Reda, T.; Hermel, H.; Hoeltje, H.-D. *Langmuir* **1996**, *12*, 6452.
- [75] de Mul, M. N. G.; Mann, J. A. *Langmuir* **1998**, *14*, 2455.
- [76] Weidemann, G.; Gehlert, U.; Vollhardt, D. *Langmuir* **1995**, *11*, 864.

Bibliography

- [77] Riviere, S.; Henon, S.; Meunier, J.; Schwartz, D. K.; Tsao, M. W.; Knobler, C. M. *J. Chem. Phys.* **1994**, *101*, 10045.
- [78] Bibo, A. M.; Knobler, C. M.; Peterson, I. R. *J. Phys. Chem.* **1991**, *95*, 5591.
- [79] Overbeck, G. A.; Mobius, D. *J. Phys. Chem.* **1993**, *97*, 7999.
- [80] Peterson, I. R.; Brzezinski, V.; Kenn, R. M.; Steitz, R. *Langmuir* **1992**, *8*, 2995.
- [81] Lautz, C.; Fischer, T. M.; Kildea, J. *J. Chem. Phys.* **1997**, *106*, 7448.
- [82] Durbin, M. K.; Malik, A.; Richter, A. G.; Ghaskadvi, R.; Gog, T.; Dutta, P. *J. Chem. Phys.* **1997**, *106*, 8216.
- [83] Overbeck, G. A.; Honig, D.; Mobius, D. *Biosens. Bioelectron.* **1995**, *10*, 99.
- [84] Kaganer, V. M.; Indenbom, V. L. *J. Phys. II (France)* **1993**, *3*, 813.
- [85] Edwards, D. A.; Brenner, H.; Wasan, D. T. *Interfacial Rheology: Basic Theory, Measurements and Applications*; Butterworth-Heinemann: Boston, 1991.
- [86] Schwartz, D. K.; Knobler, C. M.; Bruinsma, R. *Phys. Rev. Lett.* **1994**, *73*, 2841.
- [87] Stone, H. A. *Phys. Flu.* **1995**, *7*, 2931.
- [88] Ivanova, A. T.; Schwartz, D. K. *Langmuir* **2000**, *16*, 9433.
- [89] Mannheimer, R. J.; Schechter, R. S. *J. Colloid Interface Sci.* **1970**, *32*, 195.
- [90] Schwartz, D. K.; Knobler, C. M. *J. Phys. Chem.* **1993**, *97*, 8849.
- [91] Kurnaz, M. L.; Schwartz, D. K. *Phys. Rev. E* **1997**, *56*, 3378.
- [92] Sacchetti, M.; Yu, H.; Zograf, G. *Rev. Sci. Instrum.* **1993**, *64*, 1941.
- [93] Sacchetti, M.; Yu, H.; Zograf, G. *Langmuir* **1993**, *9*, 2168.
- [94] Wasan, D. T.; Gupta, L.; Vora, M. K. *AIChE Journal* **1971**, *17*, 1287.
- [95] Nagarajan, R.; Wasan, D. T. *Rev. Sci. Instrum.* **1994**, *65*, 2675.
- [96] Goodrich, F. C.; Chatterjee, A. K. *J. Colloid Interface Sci.* **1970**, *34*, 36.

-
- [97] Lifshutz, N.; Hegde, M. G.; Slatery, J. C. *J. Colloid Interface Sci.* **1971**, *37*, 73.
- [98] Gaub, H. E.; McConnell, H. M. *J. Phys. Chem.* **1986**, *90*, 6830.
- [99] Ghaskadvi, R. S.; Ketterson, J. B.; Dutta, P. *Langmuir* **1997**, *13*, 5137.
- [100] Ghaskadvi, R. S.; Dennin, M. *Rev. Sci. Instrum.* **1998**, *69*, 3568.
- [101] Ding, J.; Warriner, H. E.; Zasadzinski, J. A.; Schwartz, D. K. *Langmuir* **2002**, *18*, 2800.
- [102] Shahin, G. T. Ph. D dissertation; The University of Pennsylvania: Philadelphia, 1986.
- [103] Naumann, C. A.; Brooks, C. F.; Fuller, G. G.; Knoll, W.; Frank, C. W. *Langmuir* **1999**, *15*, 7752.
- [104] Fischer, P.; Brooks, C. F.; Fuller, G. G.; Ritcey, A. M.; Xiao, Y.; Rahem, T. *Langmuir* **2000**, *16*, 726.
- [105] Yim, K. S.; Brooks, C. F.; Fuller, G. G.; Winter, D.; Eisenbach, C. D. *Langmuir* **2000**, *16*, 4325.
- [106] Frank, C. W.; Naumann, C. A.; Knoll, W.; Brooks, C. F.; Fuller, G. G. *Macromol. Symp.* **2001**, *166*, 1.
- [107] Naumann, C. A.; Brooks, C. F.; Fuller, G. G.; Lehmann, T.; Ruehe, J.; Knoll, W.; Kuhn, P.; Nuyken, O.; Frank, C. W. *Langmuir* **2001**, *17*, 2801.
- [108] Naumann, C. A.; Brooks, C. F.; Wiyatno, W.; Knoll, W.; Fuller, G. G.; Frank, C. W. *Macromolecules* **2001**, *34*, 3024.
- [109] Vermant, J.; Yang, H.; Fuller, G. G. *AIChE Journal* **2001**, *47*, 790.
- [110] Brooks, C. F.; Thiele, J.; Frank, C. W.; O'Brien, D. F.; Knoll, W.; Fuller, G. G.; Robertson, C. R. *Langmuir* **2002**, *18*, 2166.

Bibliography

- [111] Hoekstra, H.; Vermant, J.; Mewis, J.; Fuller, G. G. *Langmuir* **2003**, *19*, 9134.
- [112] Vlassopoulos, D.; Terakawa, T.; Fuller, G. G. *J. Rheol.* **2003**, *47*, 143.
- [113] Luinge, J. W.; Nijboer, G. W.; Hagting, J. G.; Vorenkamp, E. J.; Fuller, G. G.; Schouten, A. J. *Langmuir* **2004**, *20*, 11517.
- [114] Lichtenhan, J. D.; Schwab, J. J.; Reinerth, W. A., Sr. *Chem. Innov.* **2001**, *31*, 3.
- [115] Bornhauser, P.; Calzaferri, G. *J. Phys. Chem.* **1996**, *100*, 2035.
- [116] Zhu, B.; Katsoulis, D. E.; Keryk, J. R.; McGarry, F. J. *Polymer* **2000**, *41*, 7559.
- [117] Brown, J. F., Jr.; Vogt, L. H., Jr.; Prescott, P. I. *J. Am. Chem. Soc.* **1964**, *86*, 1120.
- [118] Brown, J. J. F.; Vogt, J. L. H. *J. Am. Chem. Soc.* **1965**, *87*, 4313.
- [119] Feher, F. J.; Newman, D. A.; Walzer, J. F. *J. Am. Chem. Soc.* **1989**, *111*, 1741.
- [120] Biolln, C.; Tsuchida, A.; Frey, H.; Mulhaupt, R. *Chem. Mat.* **1997**, *9*, 1475.
- [121] Provatas, A.; Matisons, J. G. *Trends Polym. Sci.* **1997**, *5*, 327.
- [122] Brown, J. F., Jr. *J. Am. Chem. Soc.* **1965**, *87*, 4317.
- [123] Feher, F. J.; Weller, K. J. *Inorg. Chem.* **1991**, *30*, 880.
- [124] Feher, F. J.; Schwab, J. J.; Phillips, S. H.; Eklund, A.; Martinez, E. *Organometallics* **1995**, *14*, 4452.
- [125] Lichtenhan, J. D.; Vu, N. Q.; Carter, J. A.; Gilman, J. W.; Feher, F. J. *Macromolecules* **1993**, *26*, 2141.
- [126] Lichtenhan, J. D.; Otonari, Y. A.; Carr, M. J. *Macromolecules* **1995**, *28*, 8435.
- [127] Lichtenhan, J. D. *Comments Inorg. Chem.* **1995**, *17*, 115.
- [128] Feher, F. J.; Soulivong, D.; Eklund, A. G. *Chem. Commun.* **1998**, 399.
- [129] Fasce, D. P.; Williams, R. J. J.; Mechin, F.; Pascault, J. P.; Llauro, M. F.; Petiaud, R. *Macromolecules* **1999**, *32*, 4757.

- [130] Haddad, T. S.; Lichtenhan, J. D. *Macromolecules* **1996**, *29*, 7302.
- [131] Tsuchida, A.; Bolln, C.; Sernetz, F. G.; Frey, H.; Muelhaupt, R. *Macromolecules* **1997**, *30*, 2818.
- [132] Shockey, E.; Bolf, A. G.; Lichtenhan, J. D. *Polym. Prepr. (Am. Chem. Soc., Div. Polym. Chem.)* **1995**, *36*, 515.
- [133] Shockey, E.; Lichtenhan, J. D. *Polym. Prepr. (Am. Chem. Soc., Div. Polym. Chem.)* **1995**, *36*, 138.
- [134] Burns, G. T.; Taylor, R. B.; Xu, Y.; Zangvil, A.; Zank, G. A. *Chem. Mater.* **1992**, *4*, 1313.
- [135] White, D. A. *Adv. Ceram. Mater.* **1987**, *2*, 45.
- [136] Kamiya, K. *J. Noncryst. Solids* **1986**, *83*, 208.
- [137] Hacker, N. P. *MRS Bulletin* **1997**, *22*, 33.
- [138] Sellinger, A.; Laine, R. M. *Macromolecules* **1996**, *29*, 2327.
- [139] Sellinger, A.; Laine, R. M. *Chem. Mater.* **1996**, *8*, 1592.
- [140] Oviatt, H. W.; Shea, K. J.; Small, J. H. *Chem. Mater.* **1993**, *5*, 943.
- [141] Choi, K. M.; Shea, K. J. *J. Phys. Chem.* **1994**, *98*, 3207.
- [142] Schwab, J. J.; Lichtenhan, J. D.; Kevin, P.; Chaffee, P.; Carr, M. J.; Bolf, A. G. *Polym. Prepr. (Am. Chem. Soc., Div. Polym. Chem.)* **1997**, *38*, 518.
- [143] Schwab, J. J.; Lichtenhan, J. D.; Carr, M. J.; Chaffee, K. P.; Mather, P. T.; Romo-Uribe, A. *Polym. Mater. Sci. Eng.* **1997**, *77*, 549.
- [144] Zheng, L.; Farris, R. J.; Coughlin, E. B. *Journal of Polymer Science, Part A: Polymer Chemistry* **2001**, *39*, 2920.
- [145] Zheng, L.; Farris, R. J.; Coughlin, E. B. *Macromolecules* **2001**, *34*, 8034.

Bibliography

- [146] Zheng, L.; Kasi, R. M.; Farris, R. J.; Coughlin, E. B. *J. Polym. Sci., Part A: Polym. Chem.* **2002**, *40*, 885.
- [147] Zheng, L.; Waddon, A. J.; Farris, R. J.; Coughlin, E. B. *Macromolecules* **2002**, *35*, 2375.
- [148] Wright, M. E.; Schorzman, D. A.; Feher, F. J.; Jin, R.-Z. *Chem. Mater.* **2003**, *15*, 264.
- [149] Pyun, J.; Matyjaszewski, K.; Wu, J.; Kim, G.-M.; Chun, S. B.; Mather, P. T. *Polymer* **2003**, *44*, 2739.
- [150] Huang, J.-C.; He, C.-B.; Xiao, Y.; Mya, K. Y.; Dai, J.; Siow, Y. P. *Polymer* **2003**, *44*, 4491.
- [151] Pittman, C. U., Jr.; Li, G.-Z.; Ni, H. *Macromol. Symp.* **2003**, *196*, 301.
- [152] Leu, C.-M.; Chang, Y.-T.; Wei, K.-H. *Chem. Mater.* **2003**, *15*, 3721.
- [153] Kim, G. M.; Qin, H.; Fang, X.; Sun, F. C.; Mather, P. T. *J. Polym. Sci., Part B: Polym. Phys.* **2003**, *41*, 3299.
- [154] Gilman, J. W.; Schlitzer, D. S.; Lichtenhan, J. D. *J. Appl. Polym. Sci.* **1996**, *60*, 591.
- [155] Schwab, J.; Lichtenhan, J. D. *Appl. Organomet. Chem.* **1998**, *12*, 707.
- [156] Leu, C.-M.; Chang, Y.-T.; Wei, K.-H. *Macromolecules* **2003**, *36*, 9122.
- [157] Fu, B. X.; Gelfer, M. Y.; Hsiao, B. S.; Phillips, S.; Viers, B.; Blanski, R.; Ruth, P. *Polymer* **2003**, *44*, 1499.
- [158] Carroll, J. B.; Waddon, A. J.; Nakade, H.; Rotello, V. M. *Macromolecules* **2003**, *36*, 6289.

- [159] Fu, B. X.; Hsiao, B. S.; Pagola, S.; Stephens, P.; White, H.; Rafailovich, M.; Sokolov, J.; Mather, P. T.; Jeon, H. G.; Phillips, S.; Lichtenhan, J.; Schwab, J. *Polymer* **2000**, *42*, 599.
- [160] Laine, R. M.; Zhang, C.; Sellinger, A.; Viculis, L. *Appl. Organomet. Chem.* **1998**, *12*, 715.
- [161] Gao, F.; Culbertson, B. M.; Tong, Y.; Schricker, S. R. *Polym. Prepr. (Am. Chem. Soc., Div. Polym. Chem.)* **2000**, *41*, 580.
- [162] Jia, W. In *U.S. Pat. Appl. Publ.*; (USA). US, 2002; p 2002198282.
- [163] Ogarev, V. A. *Colloid J.* **2001**, *63*, 445.
- [164] Kobayashi, H. *Makromol. Chem. - Macro. Chem. Phys.* **1993**, *194*, 2569.
- [165] Knischka, R.; Dietsche, F.; Hanselmann, R.; Frey, H.; Muelhaupt, R.; Lutz, P. J. *Langmuir* **1999**, *15*, 4752.
- [166] Deng, J.; Polidan, J. T.; Hottle, J. R.; Farmer-Creely, C. E.; Viers, B. D.; Esker, A. R. *J. Am. Chem. Soc.* **2002**, *124*, 15194.
- [167] Deng, J.; Farmer-Creely, C. E.; Viers, B. D.; Esker, A. R. *Langmuir* **2004**, *20*, 2527.
- [168] Hottle, J. R.; Kim, H.-J.; Deng, J.; Farmer-Creely, C. E.; Viers, B. D.; Esker, A. R. *Macromolecules* **2004**, *37*, 4900.
- [169] Deng, J.; Hottle, J. R.; Polidan, J. T.; Kim, H.-J.; Farmer-Creely, C. E.; Viers, B. D.; Esker, A. R. *Langmuir* **2004**, *20*, 109.
- [170] Kim, H.-J.; Deng, J.; Lalli, J. H.; Riffle, J. S.; Viers, B. D.; Esker, A. R. *Langmuir* **2005**, *21*, 1908.

Bibliography

- [171] Deng, J.; Viers, B. D.; Esker, A. R.; Anseth, J. W.; Fuller, G. G. *Langmuir* **2005**, *21*, 2375.
- [172] Hottle, J. R.; Deng, J.; Kim, H.-J.; Farmer-Creely, C. E.; Viers, B. D.; Esker, A. R. *Langmuir* **2005**, *21*, 2250.
- [173] Gonzalez, R. I.; Phillips, S. H.; Hoflund, G. B. *J. Spacecraft Rockets* **2000**, *37*, 463.
- [174] Hoflund, G. B.; Gonzalez, R. I.; Phillips, S. H. *J. Adhes. Sci. Technol.* **2001**, *15*, 1199.
- [175] Duchateau, R.; Abbenhuis, H. C. L.; van Santen, R. A.; Meetsma, A.; Thiele, S. K. H.; van Tol, M. F. H. *Organometallics* **1998**, *17*, 5663.
- [176] Ropartz, L.; Foster, D. F.; Morris, R. E.; Slawin, A. M. Z.; Cole-Hamilton, D. J. *J. Chem. Soc., Dalton Trans.* **2002**, 1997.
- [177] Mengel, C.; Meyer, W. H.; Wegner, G. *Macromol. Chem. Phys.* **2001**, *202*, 1138.
- [178] Baney, R. H.; Itoh, M.; Sakakibara, A.; Suzuki, T. *Chem. Rev.* **1995**, *95*, 1409.
- [179] Henon, S.; Meunier, J. *Surfactant Science Series* **1999**, *83*, 109.
- [180] McConnell, H. M.; Tamm, L. K.; Weis, R. M. *Proc. Natl. Acad. Sci. U. S. A.* **1984**, *81*, 3249.
- [181] Buzin, A. I.; Godovsky, Y. K.; Makarova, N. N.; Fang, J.; Wang, X.; Knobler, C. *M. J. Phys. Chem. B* **1999**, *103*, 11372.
- [182] Von Tscharner, V.; McConnell, H. M. *Biophys. J.* **1981**, *36*, 409.
- [183] Peters, R.; Beck, K. *Proc. Natl. Acad. Sci. U. S. A.* **1983**, *80*, 7183.
- [184] Moy, V. T.; Keller, D. J.; Gaub, H. E.; McConnell, H. H. *J. Phys. Chem.* **1986**, *90*, 3198.

-
- [185] Chi, L. F.; Anders, M.; Fuchs, H.; Johnston, R. R.; Ringsdorf, H. *Science* **1993**, *259*, 213.
- [186] Losche, M.; Sackmann, E.; Mowald, H. *Ber. Bunsen-Ges. Phys. Chem. Chem. Phys.* **1983**, *87*, 848.
- [187] Stallberg-stenhagen, S.; Stenhagen, E. *Nature* **1945**, *156*, 239.
- [188] Lin, B.; Shih, M. C.; Bohanon, T. M.; Ice, G. E.; Dutta, P. *Phys. Rev. Lett.* **1990**, *65*, 191.
- [189] Bohanon, T. M.; Lin, B.; Shih, M. C.; Ice, G. E.; Dutta, P. *Phys. Rev. B* **1990**, *41*, 4846.
- [190] Duchateau, R.; Abbenhuis, H. C. L.; Van Santen, R. A.; Thiele, S. K. H.; Van Tol, M. F. H. *Organometallics* **1998**, *17*, 5222.
- [191] Gibson, M. D.; Swanson, D. R.; Eckhardt, C. J.; Zeng, X. C. *J. Chem. Phys.* **1997**, *106*, 1961.
- [192] Kampf, J. P.; Frank, C. W.; Malmstrom, E. E.; Hawker, C. J. *Science* **1999**, *283*, 1730.
- [193] Esker, A. R.; Zhang, L.-H.; Olsen, C. E.; No, K.; Yu, H. *Langmuir* **1999**, *15*, 1716.
- [194] Zhang, L.-H.; Esker, A. R.; No, K.; Yu, H. *Langmuir* **1999**, *15*, 1725.
- [195] Mann, E. K.; Henon, S.; Langevin, D.; Meunier, J. *J. Phys. II (France)* **1992**, *2*, 1683.
- [196] Corneec, M.; Narsimhan, G. *Langmuir* **2000**, *16*, 1216.
- [197] Fu, B. X.; Hsiao, B. S.; White, H.; Rafailovich, M.; Mather, P. T.; Jeon, H. G.; Phillips, S.; Lichtenhan, J.; Schwab, J. *Polym. Int.* **2000**, *49*, 437.

Bibliography

- [198] Zhang, C.; Babonneau, F.; Bonhomme, C.; Laine, R. M.; Soles, C. L.; Hristov, H. A.; Yee, A. F. *J. Am. Chem. Soc.* **1998**, *120*, 8380.
- [199] Fu, B. X.; Zhang, W.; Hsiao, B. S.; Rafailovich, M.; Sokolov, J.; Johansson, G.; Sauer, B. B.; Phillips, S.; Balnski, R. *High Perform. Polym.* **2000**, *12*, 565.
- [200] Choi, J.; Tamaki, R.; Kim, S. G.; Laine, R. M. *Chem. Mater.* **2003**, *15*, 3365.
- [201] Choi, J.; Kim, S. G.; Laine, R. M. *Macromolecules* **2004**, *37*, 99.
- [202] Voronkov, M. G.; Lavrent'yev, V. I. *Top. Curr. Chem.* **1982**, *102*, 199.
- [203] Haddad, T. S.; Lichtenhan, J. D. *J. Inorg. Organomet. Polym.* **1995**, *5*, 237.
- [204] Scott, D. W. *J. Am. Chem. Soc.* **1946**, *68*, 356.
- [205] Xu, H.; Kuo, S.-W.; Lee, J.-S.; Chang, F.-C. *Macromolecules* **2002**, *35*, 8788.
- [206] Mantz, R. A.; Jones, P. F.; Chaffee, K. P.; Lichtenhan, J. D.; Gilman, J. W.; Ismail, I. M. K.; Burmeister, M. J. *Chem. Mater.* **1996**, *8*, 1250.
- [207] Li, G. Z.; Wang, L.; Toghiani, H.; Daulton, T. L.; Koyama, K.; Pittman, C. U., Jr. *Macromolecules* **2001**, *34*, 8686.
- [208] Jakubek, V.; Liu, X.-Q.; Vohra, V. R.; Douki, K.; Kwark, Y.-J.; Ober, C. K.; Markley, T. J.; Robertson, E. A., III; Carr, R. V. C.; Marsella, J. A.; Conley, W.; Miller, D.; Zimmerman, P. *J. Photopolym. Sci. Technol.* **2003**, *16*, 573.
- [209] Waddon, A. J.; Zheng, L.; Farris, R. J.; Coughlin, E. B. *Nano Letters* **2002**, *2*, 1149.
- [210] Waddon, A. J.; Coughlin, E. B. *Chem. Mater.* **2003**, *15*, 4555.
- [211] Fox, H. W.; Taylor, P. W.; Zisman, W. A. *J. Ind. Eng. Chem.* **1947**, *39*, 1401.
- [212] Mann, E. K.; Langevin, D. *Langmuir* **1991**, *7*, 1112.
- [213] Lee, L. T.; Mann, E. K.; Langevin, D.; Farnoux, B. *Langmuir* **1991**, *7*, 3076.

-
- [214] Goodrich, F. C. *Proc. Intern. Congr. Surface Activity, 2nd, London, 1957* **1957**, *1*, 85.
- [215] Miller, A.; Moehwald, H. *J. Chem. Phys.* **1987**, *86*, 4258.
- [216] Ries, H. E., Jr.; Walker, D. C. *J. Colloid Sci.* **1961**, *16*, 361.
- [217] Gabrielli, G.; Puggelli, M.; Faccioli, R. *J. Colloid Interface Sci.* **1971**, *37*, 213.
- [218] Gabrielli, G.; Puggelli, M.; Faccioli, R. *J. Colloid Interface Sci.* **1973**, *44*, 177.
- [219] Zhu, J.; Eisenberg, A.; Lennox, R. B. *J. Am. Chem. Soc.* **1991**, *113*, 5583.
- [220] Zhu, J.; Eisenberg, A.; Lennox, R. B. *Macromolecules* **1992**, *25*, 6547.
- [221] Noll, W. *Chemistry and Technology of Silicones*; Academic Press: New York, 1968.
- [222] Hoyt, J. K.; Phillips, P.; Li, C. H.; Riffle, J. S. *Adhes. Age* **2000**, *43*, 28.
- [223] Jeon, H. G.; Mather, P. T.; Haddad, T. S. *Polym. Int.* **2000**, *49*, 453.
- [224] Leu, C.-M.; Reddy, G. M.; Wei, K.-H.; Shu, C.-F. *Chem. Mater.* **2003**, *15*, 2261.
- [225] Pellice, S. A.; Fasce, D. P.; Williams, R. J. J. *J. Polym. Sci., Part B: Polym. Phys.* **2003**, *41*, 1451.
- [226] Hoyt, J. K. Ph. D Dissertation; Virginia Tech: Blacksburg, 2002.
- [227] Jalbert, C.; Koberstein, J. T.; Hariharan, A.; Kumar, S. K. *Macromolecules* **1997**, *30*, 4481.
- [228] Joos, P.; Demel, R. A. *Biochim. Biophys. Acta* **1969**, *183*, 447.
- [229] Barnes, G. T. *J. Colloid Interface Sci.* **1991**, *144*, 299.
- [230] Sadrzadeh, N.; Yu, H.; Zografis, G. *Langmuir* **1998**, *14*, 151.
- [231] Dynarowicz-Latka, P.; Kita, K. *Advan. Colloid Interface Sci.* **1999**, *79*, 1.

Bibliography

- [232] Seoane, R.; Minones, J.; Conde, O.; Minones, J., Jr.; Casas, M.; Iribarnegaray, E. *J. Phys. Chem. B* **2000**, *104*, 7735.
- [233] Seoane, R.; Dynarowicz-Tstka, P.; Minones, J., Jr.; Rey-Gomez-Serranillos, I. *Colloid Polym. Sci.* **2001**, *279*, 562.
- [234] Seo, Y.; Esker, A. R.; Sohn, D.; Kim, H.-J.; Park, S.; Yu, H. *Langmuir* **2003**, *19*, 3313.
- [235] Bijsterbosch, H. D.; Cohen Stuart, M. A.; Fler, G. J. *J. Colloid Interface Sci.* **1999**, *210*, 37.
- [236] Xiao, S.; Nguyen, M.; Gong, X.; Cao, Y.; Wu, H.; Moses, D.; Heeger, A. J. *Adv. Funct. Mater.* **2003**, *13*, 25.
- [237] Choi, J.; Tamaki, R.; Laine, R. M. *Polym. Mater. Sci. Eng.* **2001**, *84*, 735.
- [238] McConnell, H. M. *Proc. Natl. Acad. Sci. U. S. A.* **1987**, *84*, 4719.
- [239] Hornsby, P. R. *Adv. Polym. Sci.* **1999**, *139*, 155.
- [240] Schwartz, D. K.; Garnæs, J.; Viswanathan, R.; Chiruvolu, S.; Zasadzinski, J. A. *N. Phys. Rev. E* **1993**, *47*, 452.
- [241] Kaganer, V. M.; Loginov, E. B. *Phys. Rev. E* **1995**, *51*, 2237.
- [242] Ries, H. E., Jr.; Kimball, W. A. *J. Phys. Chem.* **1955**, *59*, 94.
- [243] Ries, H. E., Jr. *Nature* **1979**, *281*, 287.
- [244] Smith, R. D.; Berg, J. C. *J. Colloid Interface Sci.* **1980**, *74*, 273.
- [245] Ries, H. E., Jr.; Swift, H. *Langmuir* **1987**, *3*, 853.
- [246] Vollhardt, D.; Kato, T.; Kawano, M. *J. Phys. Chem.* **1996**, *100*, 4141.
- [247] Lipp, M. M.; Lee, K. Y. C.; Zasadzinski, J. A.; Waring, A. J. *Science* **1996**, *273*, 1196.

-
- [248] Galvan-Miyoshi, J.; Ramos, S.; Ruiz-Garcia, J.; Castillo, R. *J. Chem. Phys.* **2001**, *115*, 8178.
- [249] Gourier, C.; Knobler, C. M.; Daillant, J.; Chatenay, D. *Langmuir* **2002**, *18*, 9434.
- [250] Meine, K.; Weidemann, G.; Vollhardt, D.; Brezesinski, G.; Kondrashkina, E. A. *Langmuir* **1997**, *13*, 6577.
- [251] Vollhardt, D.; Retter, U. *J. Phys. Chem.* **1991**, *95*, 3723.
- [252] Vollhardt, D.; Retter, U.; Siegel, S. *Thin Solid Films* **1991**, *199*, 189.
- [253] Vollhardt, D.; Retter, U. *Langmuir* **1992**, *8*, 309.
- [254] Siegel, S.; Hoenig, D.; Vollhardt, D.; Moebius, D. *J. Phys. Chem.* **1992**, *96*, 8157.
- [255] Vollhardt, D.; Retter, U. *Langmuir* **1998**, *14*, 7250.
- [256] Ybert, C.; Lu, W.; Moeller, G.; Knobler, C. M. *J. Phys. Chem. B* **2002**, *106*, 2004.
- [257] Gaines, G. L., Jr. *Langmuir* **1991**, *7*, 834.
- [258] Buzin, A. I.; Sautter, E.; Godovsky, Y. K.; Makarova, N. N.; Pechhold, W. *Colloid Polym. Sci.* **1998**, *276*, 1078.
- [259] Fang, J.; Dennin, M.; Knobler, C. M.; Godovsky, Y. K.; Makarova, N. N.; Yokoyama, H. *J. Phys. Chem. B* **1997**, *101*, 3147.
- [260] Lenk, T. J.; Lee, D. H. T.; Koberstein, J. T. *Langmuir* **1994**, *10*, 1857.
- [261] Avrami, M. *J. Phys. Chem.* **1939**, *7*, 1103.
- [262] Avrami, M. *J. Phys. Chem.* **1940**, *8*, 212.
- [263] Avrami, M. *J. Phys. Chem.* **1941**, *7*, 1103.
- [264] Jacobs, K.; Herminghaus, S.; Mecke, K. R. *Langmuir* **1998**, *14*, 965.
- [265] Mohwald, H. *Annu. Rev. Phys. Chem.* **1990**, *41*, 441.

Bibliography

- [266] Schwiegk, S.; Vahlenkamp, T.; Xu, Y.; Wegner, G. *Macromolecules* **1992**, *25*, 2513.
- [267] Maruyama, T.; Friedenber, M.; Fuller, G. G.; Frank, C. W.; Robertson, C. R.; Ferencz, A.; Wegner, G. *Thin Solid Films* **1996**, *273*, 76.
- [268] Kim, J.; McHugh, S. K.; Swager, T. M. *Macromolecules* **1999**, *32*, 1500.
- [269] de Mul, M. N. G.; Mann, J. A., Jr. *Langmuir* **1994**, *10*, 2311.
- [270] Friedenber, M. C.; Fuller, G. G.; Frank, C. W.; Robertson, C. R. *Langmuir* **1994**, *10*, 1251.
- [271] Ibn-Elhaj, M.; Moehwald, H.; Cherkaoui, M. Z.; Zniber, R. *Langmuir* **1998**, *14*, 504.
- [272] Esker, A. R.; Vastine, B. A.; Deng, J.; Ferguson, M. K.; Morris, J. R.; Satija, S. K.; Viers, B. D. *Polym. Prepr. (Am. Chem. Soc., Div. Polym. Chem.)* **2004**, *45*, 644.
- [273] Esker, A. R.; Dawson, K. J.; Huffer, S. M.; Karabiyik, U.; Deng, J.; Viers, B. D.; Ferguson-McPherson, M. K.; Morris, J. R.; Mao, M.; Ducker, W. A.; Satija, S. K. *Polym. Prepr. (Am. Chem. Soc., Div. Polym. Chem.)* **2005**, *46*, 76.
- [274] Xue, J.; Jung, C. S.; Kim, M. W. *Phys. Rev. Lett.* **1992**, *69*, 474.
- [275] West, R.; Baney, R. H. *J. Am. Chem. Soc.* **1959**, *81*, 6145.
- [276] Riess, J. G. *Tetrahedron* **2002**, *58*, 4113.
- [277] Krafft, M. P. *Adv. Drug. Deliv. Rev.* **2001**, *47*, 209.
- [278] Li, M.; Acero, A. A.; Huang, Z.; Rice, S. A. *Nature* **1994**, *367*, 151.
- [279] Huang, Z.; Acero, A. A.; Lei, N.; Rice, S. A.; Zhang, Z.; Schlossman, M. L. *J. Chem. Soc.-Faraday Trans.* **1996**, *92*, 545.

- [280] Kim, N.; Shin, S. *J. Chem. Phys.* **1999**, *110*, 10239.
- [281] Held, P.; Lach, F.; Lebeau, L.; Mioskowski, C. *Tetrahedron Lett.* **1997**, *38*, 1937.
- [282] Nuss, S.; Mioskowski, C.; Lebeau, L. *Chem. Phys. Lipids* **1999**, *103*, 21.
- [283] Lebeau, L.; Lach, F.; Venien-Bryan, C.; Renault, A.; Dietrich, J.; Jahn, T.; Palmgren, M. G.; Kuhlbrandt, W.; Mioskowski, C. *J. Mol. Biol.* **2001**, *308*, 639.
- [284] Nakahara, H.; Liang, W.; Fukuda, K.; Wang, L.; Wada, T.; Sasabe, H. *J. Colloid Interface Sci.* **1998**, *208*, 14.
- [285] Tian, Y.; Ng, Q. E.; Fendler, J. H. *Langmuir* **1998**, *14*, 3067.
- [286] Ren, Y.; Asanuma, M.; Iimura, K.-I.; Kato, T. *J. Chem. Phys.* **2001**, *114*, 923.
- [287] Fujimori, A.; Araki, T.; Nakahara, H. *J. Colloid Interface Sci.* **2002**, *247*, 351.

Curriculum Vitae

Jianjun Deng

EDUCATION

Ph. D., Polymer Physical Chemistry, May 2005

Virginia Polytechnic Institute and State University, Blacksburg, VA 24061

Dissertation: *"Interfacial Characterization of Polyhedral Oligomeric Silsesquioxane (POSS) Amphiphiles and Polymer Blends: Thermodynamics, Morphology, and Rheology"*

Advisor: Prof. Alan R. Esker

M. S., Material Science, July 1999

University of Science and Technology of China, Hefei, Anhui, P. R. China

Thesis: *"Preparation and Characterization of Novel Cd₂V₂O₇ Gas-sensing Materials"*

Advisor: Prof. Xingqin Liu

B. S., Applied Chemistry, July 1995

University of Science and Technology of China, Hefei, Anhui, P. R. China

Essay: *"Preparation and Characterization of Biodegradable Highly Water-absorbing Polymeric Materials (Hydrogels) with Co⁶⁰- γ Ray Radiation"*

Advisors: Profs. Bingxi Zhao and Wenming Chen

PROFESSIONAL RESEARCH EXPERIENCE

- 2005-** *Sr. Materials Engineer, ATD (Shanghai), Intel Co., Shanghai, China*
- 2000-2005** *Research Assistant, Dept. of Chemistry, Virginia Tech, Blacksburg, Virginia, USA*
- 1999-2000** *R&D Executive, BYD Co. Ltd., Shenzhen, China.*
- 1995-1996** *R&D and QA Engineer, San The Xing Industry Co. Xiamen, China.*

AWARDS AND HONORS

Graduate Research Excellence Award 2004, Department of Chemistry, Virginia Tech, Virginia, USA
UMCP/NIST Neutron Outreach Program Grant 2004, University of Maryland/NIST, Maryland, USA
National Science Foundation ChemBio Workshop Travel Grant 2003, NSF, Florida, USA
National Institute of Standard and Technology Summer School Travel Grant 2002, Washington D. C., USA
2nd Class Technology Progress Award 2000, BYD Company Ltd., Shenzhen, China
3rd Class Technology Progress Award 1999, BYD Company Ltd., Shenzhen, China (2 times)
Excellent Employee Award 1996, San The Xing Industry Co., Xiamen, China

PUBLICATIONS

14. "POSS: Silica "Nanoparticles" for Functional Coatings," A. R. Esker, K. J. Dawson, S. M. Huffer, U. Karabiyik, J. Deng, B. D. Viers, M. K. Ferguson-McPherson, J. R. Morris, M. Mao, W. A. Ducker, and S. K. Satija *Polym. Prepr. (Am. Chem. Soc., Div. Polym. Chem.)* **2005**, 46, 76.
13. "Phase Behavior and Viscoelastic Properties of Trisilanocyclohexyl-POSS at the Air/Water Interface," J. Deng, B. D. Viers, A. R. Esker, J. W. Anseth, and G. G. Fuller *Langmuir* **2005**, 21, 2375.
12. "Blends of Amphiphilic PDMS and Non-Amphiphilic Octaisobutyl-POSS at the Air/Water Interface," J. R. Hottle, J. Deng, H.-J. Kim, C. E. Farmer-Creely, B. D. Viers, and A. R. Esker *Langmuir* **2005**, 21, 2250.
11. "Blends of Amphiphilic Trisilanolisobutyl-POSS and Phosphine Oxide Substituted Poly(dimethylsiloxane) at the Air/Water Interface," H.-J. Kim, J. Deng, J. K. Hoyt, J. S. Riffle, B. D. Viers, and A. R. Esker *Langmuir* **2005**, 21, 1908.
10. "Unique Rodlike Surface Morphologies in Trisilanocyclohexyl Polyhedral Oligomeric Silsesquioxane Films," J. Deng, C. E. Farmer-Creely, B. D. Viers, and A. R. Esker *Langmuir* **2004**, 20, 2527.
9. "Blends of Amphiphilic PDMS and Trisilanolisobutyl-POSS at the Air/Water Interface," J. R. Hottle, H.-J. Kim, J. Deng, C. E. Farmer-Creely, B. D. Viers, and A. R. Esker *Macromolecules* **2004**, 37, 4900.
8. "Unique Interfacial Morphologies and Rheological Properties of Trisilanocyclohexyl-POSS," J. Deng, Catherine E. Farmer-Creely, Brent D. Viers, J. W. Anseth, G. G. Fuller, and A. R. Esker *Polym. Prepr. (Am. Chem. Soc., Div. Polym. Chem.)* **2004**, 45, 652.
7. "Aggregation Mechanism of Trisilanolisobutyl-POSS Langmuir Films at the Air/water Interface: Poly(dimethylsiloxane) Polarity Effects," H.-J. Kim, J. Deng, J. R. Hottle, J. K. Hoyt, J. S. Riffle, B. D. Viers, and A. R. Esker *Polym. Prepr. (Am. Chem. Soc., Div. Polym. Chem.)* **2004**, 45, 596.
6. "Langmuir-Blodgett films of POSS derivatives," A. R. Esker, B. A. Vastine, J. Deng, M. K. Ferguson, J. R. Morris, S. K. Satija, and B. D. Viers *Polym. Prepr. (Am. Chem. Soc., Div. Polym. Chem.)* **2004**, 45, 644.
5. "Polyhedral Oligomeric Silsesquioxane Amphiphiles: Isotherm and Brewster Angle Microscopy Studies of Trisilanolisobutyl-POSS at the Air/Water Interface," J. Deng, J. R. Hottle, J. T. Polidan, C. E. Farmer-Creely, B. D. Viers, and A. R. Esker *Langmuir* **2004**, 20, 109.
4. "Polyhedral Oligomeric Silsesquioxanes: A New Class of Amphiphiles at the Air/Water Interface," J. Deng, J. T. Polidan, J. R. Hottle, C. E. Farmer-Creely, B. D. Viers, and A. R. Esker *J. Am. Chem. Soc.* **2002**, 124, 15194.
3. "Model Polyhedral Oligomeric Silsesquioxane Thin Films for Coating Applications," B. D. Viers, S. Phillips, T. Haddad, A. R. Esker, J. T. Polidan, C. E. Farmer-Creely, and J. Deng *Int. SAMPE Symp. Exhib.* **2002**, 47, 1508.
2. "The Effect of Ln^{3+} ($\text{Ln} = \text{Y}, \text{Nd}$) on the Conductivity and Gas-sensing Properties of CdIn_2O_4 Semiconductor," X. Chu, X. Liu, J. Deng, and G. Meng *Sensors and Actuators, B: Chemical* **2000**, 67, 290.
1. "Preparation and Gas-sensing Properties of $\text{Cd}_2\text{V}_2\text{O}_7$," J. Deng, X. Liu, and X. Chu *Yingyong Huaxue (J. Chinese Appl. Chem.)* **1999**, 16, 52.

PRESENTATIONS

8. "Comparative Interfacial Studies of Amphiphilic PDMS/POSS Blends and Polar Amphiphilic PDMS-PO/POSS Blends at the Air/Water Interface: Poly(Dimethylsiloxane) Polarity Effects", H.-J. Kim, J. Deng, J. R. Hottle, J. K. Hoyt, J. S. Riffle, B. D. Viers, and A. R. Esker, 28th Annual Meeting of the Adhesion Society, Mobile, Alabama, 2005
7. "Phase Behavior and Rheology of Trisilanocyclohexyl-POSS POSS Langmuir Films," J. Deng, B. D. Viers, and A. R. Esker, MACRO 2004: An Update of Macromolecular Education at Virginia Tech, Blacksburg, Virginia, 2004.
6. "Comparative Interfacial Studies of Fluorinated Disilanocyclopentyl-POSS with Trisilanocyclopentyl-POSS," J. Deng, W. Yin, and A. R. Esker, Hyuk Yu Symposium, Madison, Wisconsin, 2004.
5. "Unique Interfacial Morphologies and Rheological Properties of Trisilanocyclohexyl-POSS," J. Deng, C. E. Farmer-Creely, B. D. Viers, J. W. Anseth, G. G. Fuller, A. R. Esker, 227th ACS National Meeting, Anaheim, California, 2004.
4. "Interfacial Properties of Novel Hybrid POSS Amphiphiles," J. Deng, B. A. Vastine, J. R. Hottle, A. R. Esker, S. K. Satija, and B. D. Viers, NSFCHEMIBIO Workshop: Neutron Scattering for Chemistry and Chemistry/Biology Interface, Tallahassee, Florida, 2003.
3. "Interfacial Properties of Novel Hybrid POSS Amphiphiles and their Blends with Polymers," J. Deng, H. Kim, J. Hottle, C. Farmer-Creely, B. Viers, and A. R. Esker, March Meeting of the American Physical Society, Austin, Texas, 2003.
2. "Interfacial Properties of POSS-Nanofillers," J. Polidan, J. Deng, C. Farmer-Creely, A. Esker, and B. Viers, March Meeting of the American Physical Society, Indianapolis, Indiana, 2002.
1. "POSS-Polymer Interaction in Surfactant Systems," J. Deng, B. A. Vastine, J. R. Hottle, C. E. Farmer-Creely, J. T. Polidan, B. D. Viers, and A. R. Esker, MACRO 2002: An Update of Macromolecular Education at Virginia Tech, Blacksburg, Virginia, 2002.